U.PORTO
FACULDADE DE CIÊNCIAS
UNIVERSIDADE DO PORTO

I dedicate this thesis to all my family and to my girlfriend.

U.PORTO
FACULDADE DE CIÊNCIAS
UNIVERSIDADE DO PORTO

# Special Thanks

I firstly would like to thank my parents, grandparents, uncles and my girlfriend to all the support that they gave to me and for their patience and help.

I would like to thank my supervisor Prof. Dra. Teresa Seixas, for giving me the opportunity to study and learn more about the research field of asteroids and meteorites. Without her this work would not be possible. Thankfully to Prof. Teresa Seixas, the work with meteorites started in 2011, when I have done my first extracurricular internship PEEC (Plano de Estágios Extracurriculares da FCUP), entitled “Caracterização Laboratorial de Meteoritos”, in its third edition. During my first extracurricular internship PEEC, it was possible to present two posters communications: the first was presented in the IJUP11 (Investigação Júnior da Universidade do Porto 2011) conference and was entitled “Laboratorial Characterization of Meteorites”; the second was presented in the XXI ENAA (Encontro Nacional de Astronomia e Astrofísica) conference and was entitled “Laboratorial Characterization of a Campo del Cielo meteorite”. During the work of this thesys, it was possible to present a poster communication, entitled “The early stages of the Solar System: constraints from the small icy worlds”, in the IJUP12 (Investigação Júnior da Universidade do Porto 2012) conference. In addition, it was also possible to make an oral presententation, entitled “Mineralogy of V-type near-earth objects”, in the Física2012 conference. I also would like to thank my supervisor for all the constructive comments and suggestions for this thesis.

I also would like to thank all researchers who collaborated in the RELAB and The MIT-UH-IRTF Joint Campaign for NEO Spectral Reconnaissance. All (or part) of the data utilized in this publication were obtained and made available by the The MIT-UH-IRTF Joint Campaign for NEO Reconnaissance. The IRTF is operated by the University of Hawaii under Cooperative Agreement no. NCC 5-538 with the National Aeronautics and Space Administration, Office of Space Science, Planetary Astronomy Program. The MIT component of this work is supported by NASA grant 09-NEOO009-0001, and previously by the National Science Foundation under Grant No. 0506716.

U.PORTO
FACULDADE DE CIÊNCIAS
UNIVERSIDADE DO PORTO

# Abstract

Much of our current knowledge on the formation and evolution of our Solar System is based on the study of chemical, mineralogical, and physical properties of meteorites. These are remnants of planetesimals that never formed a planet, possibly due to the gravitational influence of Jupiter, and preserve crucial information about the collisional and evolutionary processes that occurred in the early stages of the Solar System. Linking a meteorite to a specific asteroid or asteroid's group can provide important information about petrological, thermal and collisional history of asteroids. In addition, if a linkage between a meteorite and an asteroid can be established, knowing the orbital position of the asteroid allows us to argue about the mechanism that can deliver a meteorite to Earth.

Visible and near-infrared reflectance spectroscopy of meteorites, asteroids and samples of mixtures of meteorite constituent minerals provides a powerful technique to study a possible genetic linkage between meteorites and asteroids. However, reflectance spectra are not always intrinsic to surface mineralogy, as grain size effects, or surface roughness, can change the optical properties of any mineral. In the case of airless bodies like asteroids, the effects of space weathering caused by irradiation of solar wind and cosmic rays and by the bombardment of micrometeorites can redden the surface reflectance spectra and lower its albedo. In addition, the absorption features of the asteroid surface reflectance spectra can be attenuated. Hence, studying the mineralogy of asteroids is a quite arduous task. However, the V-type asteroids and the Howardites (H), Eucrites (E) and Diogenites (D) seem to share the best known meteorite-asteroid linkage. There are also possible genetic linkages that have been postulated, such as ordinary chondrites and S-type asteroids or, even more surprisingly, the recently argued possibility of the CM and CI chondrites coming from comets.

In this study, it is aimed to analyze the reflectance spectra of V-type Near Earth Objects (NEOs) and 4 Vesta taken from the publically available MIT-UH-IRTF Joint Campaign for NEO Reconaissance, and reflectance spectra of HED meteorites and intimate mineral mixtures from the RELAB database. In order to fit reflectance spectra and derive the surface composition, mineralogy and grain size, the Hapke radiative

transfer model is applied. The results of the spectral analysis and modelling corroborate the known genetic linkage between V-type asteroids and the studied HEDs. A similar linkage between several NEOs and V-type asteroids is proposed. It is also hoped to constrain some processes that took place in the early Solar System.

U.PORTO
FACULDADE DE CIÊNCIAS
UNIVERSIDADE DO PORTO

# Resumo

O nosso conhecimento sobre a formação e evolução do Sistema Solar advém do estudo das propriedades químicas, mineralógicas e físicas dos meteoritos. Estes são objetos remanescentes de planetesimais que nunca chegaram a formar um planeta possivelmente devido à ação gravítica de Júpiter e preservam informação crucial sobre os processos evolutivos e colisionais que ocorreram durante os primórdios do Sistema Solar. Estabelecendo uma ligação genética entre um meteorito e um dado asteroide ou grupo de asteroides, pode providenciar informação importante sobre a história petrológica, térmica e colisional dos asteroides. Igualmente, se tal conexão poder ser estabelecida e se a posição orbital do asteroide for conhecida, é possível argumentar-se sobre quais os mecanismos responsáveis em ejetar os meteoritos para a órbita da Terra.

A espectroscopia no visível e no infravermelho de meteoritos, asteroides e amostras de misturas de minerais constituintes dos meteoritos, é uma excelente técnica para estudar as ligações genéticas entre meteoritos e asteroides. Mas, os espectros de reflexão nem sempre são intrínsecos à superfície, pois o efeito do tamanho de grão e a rugosidade da superfície podem modificar as propriedades óticas de qualquer mineral. No caso dos asteroides, os efeitos da erosão espacial causados pela irradiação devida a raios cósmicos ou ventos solares ou até mesmo causada pelo bombardeamento de micrometeoritos pode envermelhecer o espectro de reflexão, atenuar as suas bandas de absorção e diminuir o albedo. De fato, tentar encontrar possíveis ligações genéticas entre meteoritos e asteroides pode ser uma tarefa bastante árdua. No entanto, os asteroides do tipo V e os meteoritos HED (Howardites, Eucrites e Diogenites) aparentam partilhar uma forte ligação genética, dadas as muitas semelhanças entre os seus espectros de reflexão. Existem também outras possíveis ligações genéticas que têm sido postuladas, como por exemplo a ligação entre os condritos ordinários e os asteroides do tipo S, ou ainda mais surpreendentemente a ligação entre os condritos carbonáceos CM e CI e os cometas.

Neste estudo, pretende-se analisar espectros de reflexão de Near Earth Objects (NEOs) do tipo V e do asteroide 4 Vesta, obtidos a partir da base de dados pública MIT-UH-IRTF Joint Campaign for NEO Reconaissance, e espectros de

meteoritos HED e misturas de minerais obtidos a partir da base de dados pública RELAB. É espectável conseguir-se estabelecer uma possível ligação genética entre alguns NEOs e asteroides do tipo V e os meteoritos HED. É também espectável impor-se algumas restrições em alguns processos de formação do Sistema Solar.

U.PORTO
FACULDADE DE CIÊNCIAS
UNIVERSIDADE DO PORTO

# Indices

**Page:**

U.PORTO
FACULDADE DE CIÊNCIAS
UNIVERSIDADE DO PORTO

**Page:**

U.PORTO
FACULDADE DE CIÊNCIAS
UNIVERSIDADE DO PORTO

**Page:**

U.PORTO
FACULDADE DE CIÊNCIAS
UNIVERSIDADE DO PORTO

**Page:**

U.PORTO
FACULDADE DE CIÊNCIAS
UNIVERSIDADE DO PORTO

**Page:**

U.PORTO
FACULDADE DE CIÊNCIAS
UNIVERSIDADE DO PORTO

# Indices of Figures

U.PORTO
FACULDADE DE CIÊNCIAS
UNIVERSIDADE DO PORTO

Fig.2.6 – Location of the 5112 4 Vesta family members in proper element space (Panel A: a-e plot; Panel B: a-i plot). The small blue dots represent the 5112 members of the 4 Vesta family and the red dots represent 22 V-type asteroids which are not members of the 4 Vesta family. The location of 4 Vesta is represented in both panels by the black triangle. The ellipse displays the 600m/s level of the maximum ejection velocity.

Fig.2.7 – Left: Comet Hale-Bopp. Right: Comet Halley.

Fig.2.8 – Orbit of a long period comet.

Fig.2.9 – Orbit of a short-period comet and a schematic illustration of the capture process.

Fig.2.10 – Semi-major axis vs orbital eccentricity for the Outer Solar System. The dynamical subtypes of TNOs are marked on the plot. Only three dynamical resonances with Neptune are indicated. The curve NN represents the semi-major axis of the orbit of Neptune, while the lower curve found at 40 AU represents the locus of orbits with q=40 AU. Centaurs population are also represented in this plot.

Fig.3.1 - Scanning electron micrographs of chondrules and CAIs. A. Porphyritic Olivine type I chondrule. B. Porphyritic Olivine Pyroxene type I chondrule. C. Porphyritic Pyroxene type I chondrule. D. Barred Olivine type I chondrule. E. Porphyritic Olivine type II chondrule. F. Amoeboid Olivine Aggregate. G. Fine-grained CAI with nodular texture shown in the insert. H. Hibonite-glass CAI spherule. I. Coarse-grained ultra-refractory igneous CAI E101,1, All objects are from the Efremovka carbonaceous chondrite, except H from the Murchison carbonaceous chondrite.

Fig.3.2 – Average whole-chondrite lithopile-element abundances in several chondrite groups.

Fig.3.3 – Backscattered electron images of: (a) CR chondrite PCA91082; (b) CH chondrite PCA91467.

Fig.3.4 – Chondrules of Allende Meteorite. This meteorite is classified as being a CV chondrite meteorite.

Fig.3.5 - Ordinary chondrite *NWA 869*.

U.PORTO
FACULDADE DE CIÊNCIAS
UNIVERSIDADE DO PORTO

Fig.3.6 – Photomicrographs in transmitted light with partially crossed nicols. Left: Londranite LEW88280, where orthopyroxene (opx) and olivine (ol) are marked. Right: Silicate inclusion in the IAB iron Campo del Cielo.

Fig.3.7 – Photomicrograph of a brachinite in transmitted light with partially crossed nicols: Brachina.

Fig.3.8 – Thin section photomicrographs in transmitted light with crossed polars of typical HED meteorite types. Top Left: Howardite Kapoeta consisting of mineral fragments of highly variable grain sizes. Top Right: Unequilibrated noncumulate eucrite Pasamonte showing the typical basaltic texture of plagioclase (light) and pyroxene (colored). Down: Diogenite Johnstown illustrating the highly brecciated nature of the rock that consists essentially entirely of orthopyroxene.

Fig.3.9 – Schematic model of four hypothetical impacts into the layered crust, producing different types of Eucrites.

Fig.3.10 – Mn-Cr and Al-Mg early Solar System timelines. Both chronometers are anchored to the time of 4571Myr, when most CAIs are believed to have been formed. Small planetesimals formed almost at the same time in order to preserve CAIs. The interiors of some intermediate-sized planetesimals were melted through the $^{26}$Al decay. The formation of the primary chondrules occurred within 2Myr. Chemical differentiation, formation of a stratified mantle and a core in these larger bodies ended 4565Myr ago (according to the case of 4 Vesta). Metamorphism occurred for many million years.

Fig.4.1 – Laboratory measurement of the spectral reflectivity of the Nuevo Laredo eucrite (solid line), compared to telescope data points from 4 Vesta.

Fig.4.2 – Scheme of the problematic relationship 4 Vesta – V type asteroids – HED meteorites.

Fig.4.3 - Normalized reflectance vs. Wavelenght (μm) for S-type 6 Hebe vs H5 chondrite Pantar and O-type 3628 Boznemcová vs. LL6 chondrite Manbhoom. All spectra are normalized to unity at 0.55μm. The asteroid spectra are offset by 0.5 in reflectance.

U.PORTO
FACULDADE DE CIÊNCIAS
UNIVERSIDADE DO PORTO

Fig.4.4 – Normalized reflectance vs. wavelength (μm) for M-type 16 Psyche vs. iron and enstatite chondrite meteorites (lines). By the order of increasing reflectance at 2.0μm, the meteorites are: EL6 chondrite Hvittis; ungrouped iron Babb's Mill; EH4 chondrite Abee; IIIAB iron Chulafinee. All spectra are normalized to unity at 0.55μm.

Fig.4.5 - Normalized reflectance vs. Wavelenght (μm) for G-type 19 Fortuna vs. CM chondrite LEW90500 and C-type 10 Hygiea vs. Thermally altered CI Chondrite Y-82162. All spectra are normalized to unity at 0.55μm. The asteroid spectra are offset by 0.5 in reflectance.

Fig.4.6 - TEM image of an anorthosite (An) grain from a mature lunar soil that exhibits a rim of Fe metal particles (SMFe).

Fig.4.7 – Two examples of reflectance spectra of asteroids paired with their meteoritic analogs. One possible explanation for this mismatch is the space weathering process which is thought to be responsible for the alteration of several spectral features of asteroids. Asteroids are displayed as closed triangles and meteorites as open diamonds. The top pair is offset vertically by 0.7 for clarity and show the S (IV) asteroid 7 Iris with the L6 ordinary chondrite Drake Creek. Although both objects have approximately the same mineralogy as shown by their band minima, the spectra of 7 Iris is reddened by 30% relative to Drake Creek. Also, Iris's major absorption bands are significantly reduced. The pair of 4 4 Vesta and the eucrite Jonzac also show similar mineralogy, but the band depth of 4 Vesta is reduced by 40% relative to its analog meteorite.

Fig.4.8 – Irradiance and Radiance.

Fig.4.9 – Geometrical conventions.

Fig.4.10 – Scattering by a single particle. The plane containing J and I is called the scattering plane.

Fig.4.11 – Explanatory framework of the pair (b,c).

Fig.4.12 – Empirical double HG parameters for large silicate, resin and metal particles of varied shapes, absorption coefficients and conditions of surface roughness, and containing differing densities of internal scatters. Decreasing w causes a particle to

U.PORTO
FACULDADE DE CIÊNCIAS
UNIVERSIDADE DO PORTO

Fig.5.5 – Plot of the single scattering albedo versus wavelength, for all the 14 laboratory mixtures with the following end-members: clinopyroxene and orthopyxorene.

Fig.5.6 – Plot of the single scattering albedo of the sample XP-CMP-010 (C1XP10) and their end-members (orthopyroxene (Opx) and clinopyroxene (Cpx)) versus wavelength. The selected files for orthopyroxene and clinopyroxene were PP-CMP-021 (C1PP21) and PP-CMP-030 (C1PE30), respectively. The residuals (cyan line) were translated from 0 to 1.

Fig.5.7 – Plot of the residuals of the sample XP-CMP-010 (C1XP10).

Fig.5.8 – Plot of clinopyroxene (Cpx) versus orthopyroxene (Opx) nominal and derived compositions for all seven laboratory mixtures with a grain size proportion between 0 and 45μm.

Fig.5.9 - Plot of orthopyroxene (Opx) versus olivine nominal and derived compositions for all seven laboratory mixtures with a grain size proportion between 45 and 75μm.

Fig.5.10 - Plot of anorthosite versus olivine nominal and derived compositions for all seven laboratory mixtures with a grain size proportion between 45 and 75μm.

Fig.5.11 - Plot of anorthosite versus orthopyroxene (Opx) nominal and derived compositions for all seven laboratory mixtures with a grain size proportion between 45 and 75μm.

Fig.5.12 – Reflectance spectra of all three clinopyroxenes obtained from the RELAB database.

Fig.5.13 – Single scattering albedo versus wavelength for all three clinopyroxenes.

Fig.5.14 – Plot of clinopyroxene (Cpx) versus orthopyroxene (Opx) nominal and derived compositions for all fourteen laboratory mixtures with a grain size proportion between 0 and 45μm and 70 and 145μm.

Fig.5.15 - Reflectance spectra of 4 Vesta and the four near-Earth vestoids. The reflectance spectra are incrementally shifted vertically by 0.5.

U.PORTO
FACULDADE DE CIÊNCIAS
UNIVERSIDADE DO PORTO

Fig.5.16 - Reflectance spectra of the selected ten diogenites (D), ten eucrites (E) and ten howardites (H). Eucrites' reflectance spectra are shifted vertically by 1 unity. Howardites' reflectance spectra are shifted vertically by 2 units.

Fig.5.17 - Reflectance spectra of the five V-type asteroids versus respectively HED with the closest mineralogy. A vertical shift of 1 unit is introduced between different groups of spectra.

Fig.5.18 – Plot of the derived single scattering albedos of the ten Diogenites (D), ten Eucrites (E) and ten Howardites (H). The single scattering albedo of Eucrites are shifted vertically by 1 unity, while the single scattering albedo of Howardites are shifted vertically by 2 units.

Fig.5.19 – Plot of the derived single scattering albedo of the five selected V-type asteroids. The single scattering albedo of 3908 Nyx is shifted vertically by 0,5 units, of 4055 Magellan is shifted vertically by 1 unit, of (5604) 1992 FE is shifted vertically by 1,5 units and of (6611) 1993 VW is shifted vertically by 2 units.

Fig.5.20 – Plot of the reflectance spectra of the pyroxene end-members used in this study. Reflectance spectra of Hypersthene are shifted moved vertically by 1 unity, of Augite are shifted vertically by 2 units, of Piogenite are shifted vertically by 3 units, of Enstatite are shifted vertically by 4 units, of Bronzite are shifted vertically by 5 units and of Wollastonite are shifted vertically by 6 units.

Fig.5.21 – Reflectance spectra of the selected olivine and plagioclase end-members minerals, used in this study. Reflectance spectra of Anorthite are shifted vertically by 1 unity, of Olivine Fayalite are shifted vertically by 2 units and of Olivine Forsterite are shifted vertically by 3 units.

Fig.5.22 – Reflectance spectra of the selected neutral phases used in this study.

Fig.5.23 – Best fit model results of the selected V-type asteroids. Data points represent the single scattering albedo of the samples, while the black lines represent the best obtained fits. A vertical shift of 0.5 units is introduced between different asteroids/meteorites albedos.

Fig.E7 – Derived albedo for the sample XP-CMP-014 (C1XP14) and for their extreme minerals PP-CMP-021 (C1PP21) and PP-CMP-030 (C1PE30) versus wavelength. The residuals were shifted by one unity.

Fig.E8 – Plot of the residuals of the sample C1XP14.

Fig.E9 – Derived albedo for the sample XP-CMP-015 (C1XP15) and for their extreme minerals PP-CMP-021 (C1PP21) and PP-CMP-030 (C1PE30) versus wavelength. The residuals were shifted by one unity.

Fig.E10 – Plot of the residuals of the sample C1XP15.

Fig.E11 – Derived albedo for the sample XP-CMP-016 (C1XP16) and for their extreme minerals PP-CMP-021 (C1PP21) and PP-CMP-030 (C1PE30) versus wavelength. The residuals were shifted by one unity.

Fig.E12 – Plot of the residuals of the sample C1XP16.

Fig.E13 – Derived albedo for the sample XT-CMP-033 (C1XT33) and for their extreme minerals OL-JMS-001 (C1OL01), PE-CMP-031 (C1PE31) and PA-CMP-060-B (CBPA60) versus wavelength. The residuals were shifted by 1.1 unities.

Fig.E14 – Plot of the residuals of the sample C1XT33.

Fig.E15 – Derived albedo for the sample XT-CMP-034 (C1XT34) and for their extreme minerals OL-JMS-001 (C1OL01), PE-CMP-031 (C1PE31) and PA-CMP-060-B (CBPA60) versus wavelength. The residuals were shifted by 1.1 unities.

Fig.E16 – Plot of the residuals of the sample C1XT34.

Fig.E17 – Derived albedo for the sample XT-CMP-035 (C1XT35) and for their extreme minerals OL-JMS-001 (C1OL01), PE-CMP-031 (C1PE31) and PA-CMP-060-B (CBPA60) versus wavelength. The residuals were shifted by 1.1 unities.

Fig.E18 – Plot of the residuals of the sample C1XT35.

Fig.E19 – Derived albedo for the sample XT-CMP-036 (C1XT36) and for their extreme minerals OL-JMS-001 (C1OL01), PE-CMP-031 (C1PE31) and PA-CMP-060-B (CBPA60) versus wavelength. The residuals were shifted by 1.1 unities.

U.PORTO
FACULDADE DE CIÊNCIAS
UNIVERSIDADE DO PORTO

Fig.E20 – Plot of the residuals of the sample C1XT36.

Fig.E21 – Derived albedo for the sample XT-CMP-037 (C1XT37) and for their extreme minerals OL-JMS-001 (C1OL01), PE-CMP-031 (C1PE31) and PA-CMP-060-B (CBPA60) versus wavelength. The residuals were shifted by 1.1 unities.

Fig.E22 – Plot of the residuals of the sample C1XT37.

Fig.E23 – Derived albedo for the sample XT-CMP-038 (C1XT38) and for their extreme minerals OL-JMS-001 (C1OL01), PE-CMP-031 (C1PE31) and PA-CMP-060-B (CBPA60) versus wavelength. The residuals were shifted by 1.1 unities.

Fig.E24 – Plot of the residuals of the sample C1XT38.

Fig.E25 – Derived albedo for the sample XT-CMP-039 (C1XT39) and for their extreme minerals OL-JMS-001 (C1OL01), PE-CMP-031 (C1PE31) and PA-CMP-060-B (CBPA60) versus wavelength. The residuals were shifted by 1.1 unities.

Fig.E26 – Plot of the residuals of the sample C1XT39.

Fig.E27 – Derived albedo for the sample XP-CMP-001 (C1XP01) and for their extreme minerals PP-CMP-023 (C1PP23) and PE-CMP-032 (C1PP32) versus wavelength. The residuals were shifted by one unity.

Fig.E28 – Plot of the residuals of the sample C1XP01.

Fig.E29 – Derived albedo for the sample XP-CMP-002 (C1XP02) and for their extreme minerals PP-CMP-023 (C1PP23) and PE-CMP-032 (C1PP32) versus wavelength. The residuals were shifted by one unity.

Fig.E30 – Plot of the residuals of the sample C1XP02.

Fig.E31 – Derived albedo for the sample XP-CMP-003 (C1XP03) and for their extreme minerals PP-CMP-023 (C1PP23) and PE-CMP-032 (C1PP32) versus wavelength. The residuals were shifted by one unity.

Fig.E32 – Plot of the residuals of the sample C1XP03.

U.PORTO
FACULDADE DE CIÊNCIAS
UNIVERSIDADE DO PORTO

Fig.E33 – Derived albedo for the sample XP-CMP-004 (C1XP04) and for their extreme minerals PP-CMP-023 (C1PP23) and PE-CMP-032 (C1PP32) versus wavelength. The residuals were shifted by one unity.

Fig.E34 – Plot of the residuals of the sample C1XP04.

Fig.E35 – Derived albedo for the sample XP-CMP-005 (C1XP05) and for their extreme minerals PP-CMP-023 (C1PP23) and PE-CMP-032 (C1PP32) versus wavelength. The residuals were shifted by one unity.

Fig.E36 – Plot of the residuals of the sample C1XP05.

Fig.E37 – Derived albedo for the sample XP-CMP-006 (C1XP06) and for their extreme minerals PP-CMP-023 (C1PP23) and PE-CMP-032 (C1PP32) versus wavelength. The residuals were shifted by one unity.

Fig.E38 – Plot of the residuals of the sample C1XP06.

Fig.E39 – Derived albedo for the sample XP-CMP-007 (C1XP07) and for their extreme minerals PP-CMP-023 (C1PP23) and PE-CMP-032 (C1PP32) versus wavelength. The residuals were shifted by one unity.

Fig.E40 – Plot of the residuals of the sample C1XP07.

Fig.E41 - Unnormalized reflectance spectrum of 4 Vesta compared with the reflectance spectra of ten diogenites (D), ten eucrites (E) and ten howardites (H). Reflectance spectra of: diogenites (D) are shifted vertically by 0.7; eucrites (E) are shifted vertically by 1.2; howardites (H) are shifted vertically by 2.2. All spectra are normalized by the reflectance value at 1.2μm. The abbreviature “gsp” means grain size proportion.

Fig.E42 - Unnormalized reflectance spectrum of 3908 Nyx compared with the reflectance spectra of ten diogenites (D), ten eucrites (E) and ten howardites (H). Reflectance spectra of: diogenites (D) are shifted vertically by 0.7; eucrites (E) are shifted vertically by 1.2; howardites (H) are shifted vertically by 2.2. All spectra are normalized by the reflectance value at 1.2μm. The abbreviature “gsp” means grain size proportion.

U.PORTO
FACULDADE DE CIÊNCIAS
UNIVERSIDADE DO PORTO

Fig.E43 - Unnormalized reflectance spectrum of 4055 Magellan compared with the reflectance spectra of ten diogenites (D), ten eucrites (E) and ten howardites (H). Reflectance spectra of: diogenites (D) are shifted vertically by 0.7; eucrites (E) are shifted vertically by 1.2; howardites (H) are shifted vertically by 2.2. All spectra are normalized by the reflectance value at 1.2μm. The abbreviature “gsp” means grain size proportion.

Fig.E44 - Unnormalized reflectance spectrum of (6611) 1993 VW compared with the reflectance spectra of ten diogenites (D), ten eucrites (E) and ten howardites (H). Reflectance spectra of: diogenites (D) are shifted vertically by 0.7; eucrites (E) are shifted vertically by 1.2; howardites (H) are shifted vertically by 2.2. All spectra are normalized by the reflectance value at 1.2μm. The abbreviature “gsp” means grain size proportion.

Fig.E45 - Unnormalized reflectance spectrum of (5604) 1992 FE compared with the reflectance spectra of ten diogenites (D), ten eucrites (E) and ten howardites (H). Reflectance spectra of: diogenites (D) are shifted vertically by 0.7; eucrites (E) are shifted vertically by 1.2; howardites (H) are shifted vertically by 2.2. All spectra are normalized by the reflectance value at 1.2μm. The abbreviature “gsp” means grain size proportion.

Fig.E46 – Top: Plot of the best fit obtained of a diogenite meteorite (sample MP-TXH-068-A). Down: Residuals plot of the fit of the sample MP-TXH-068-A.

Fig.E47 – Top: Plot of the worst fit obtained of a diogenite meteorite (sample MP-TXH-071-A). Down: Residuals plot of the fit of the sample MP-TXH-071-A.

Fig.E48 – Top: Plot of the best fit obtained of a eucrite meteorite (sample MB-TXH-069-B). Down: Residuals plot of the fit of the sample MB-TXH-069-B.

Fig.E49 – Top: Plot of the worst fit obtained of a diogenite meteorite (sample MP-TXH-070-D). Down: Residuals plot of the fit of the sample MP-TXH-070-D.

Fig.E50 – Top: Plot of the best fit obtained of a howardite meteorite (sample MB-TXH-053-A). Down: Residuals plot of the fit of the sample MB-TXH-053-A.

U.PORTO
FACULDADE DE CIÊNCIAS
UNIVERSIDADE DO PORTO

Fig.E51 – Top: Plot of the worst fit obtained of a howardite meteorite (sample MB-TXH-068-D). Down: Residuals plot of the fit of the sample MB-TXH-068-D.

Fig.E52 – Top: 4 Vesta single scattering albedo and its modelled curve. Down: Residuals plot of the fit.

Fig.E53 – Top: 3908 Nyx single scattering albedo and its modelled curve. Down: Residuals plot of the fit.

Fig.E54 – Top: 4055 Magellan single scattering albedo and its modelled curve. Down: Residuals plot of the fit.

Fig.E55 – Top: 5604 (1992) FE single scattering albedo and its modelled curve. Down: Residuals plot of the fit.

Fig.E56 – Top: 6611 (1993) VW single scattering albedo and its modelled curve. Down: Residuals plot of the fit.

U.PORTO
FACULDADE DE CIÊNCIAS
UNIVERSIDADE DO PORTO

# Indices of Tables

U.PORTO
FACULDADE DE CIÊNCIAS
UNIVERSIDADE DO PORTO

Table D3 – Orbital and physical properties of the five V-type asteroids, considered in this study. Orbital and physical parameters are available at http://ssd.jpl.nasa.gov/sbdb.cgi#top.

Table D4 – Set of the thirty HED meteorites, considered in this study.

Table D5 - Set of the reasonable end-members minerals with appropriate grain size proportions, considered in this study.

Table D6 – Results of the derived end-members proportions in Diogenites.

Table D7 – Results of the derived end-members proportions in Eucrites.

Table D8 – Results of the derived end-members proportions in Howardites.

Table D9 – Results of the derived end-members proportions in the selected V-type asteroids and their meteoritic analogs.

Table D10 – Derived mass fractions of the end-members found in Diogenites.

Table D11 – Derived mass fractions of the end-members found in Eucrites.

Table D12 – Derived mass fractions of the end-members found in Howardites.

Table D13 – Derived mass fractions of the end-members found in the selected V-type asteroids and their meteoritic analogs.

U.PORTO
FACULDADE DE CIÊNCIAS
UNIVERSIDADE DO PORTO

# Indices of Abbreviations

AOA: Ameboid Olivine Aggregate

AU: Astronomical Unit

CAI: Calcium-aluminum Inclusion

CCD: Charge-coupled Device

GM: Gaussian Model

HED: Howardites, Eucrites and Diogenites

HM: Hapke Model

IR: infrared

JFC: Jupiter Family of Comets

km: kilometers

kpc: kiloparsec

MAB: Main Asteroid Belt

$M_{Earth}$: Earth Masses

MGM: Modified Gaussian Model

$M_{Jupiter}$: Jupiter Masses

$M_{Sun}$: Sun Masses

Myr: Million years

NEO: Near Earth Object

NIR: near infrared

nm: nanometer

pc: parsec

U.PORTO
FACULDADE DE CIÊNCIAS
UNIVERSIDADE DO PORTO

SNC: Shergottittes, Nakhlites and Chassigny

TD: Tidal Downsizing hypothesis

TNO: Trans-Neptunian Objects

UV: ultraviolet

yrs: years

U.PORTO
FACULDADE DE CIÊNCIAS
UNIVERSIDADE DO PORTO

# Introduction

Since our ancestral, meteorites were regarded with fear and were associated to the wrath of gods. However, with the evolution of the Humankind knowledge, nowadays meteorites are regarded as crucial tools available on Earth to study and understand the early stages of the Solar System evolution. In fact, there are many philosophical questions which still remain unanswered. In particular, the question "Where do we come from?" plays an important role in the Humankind life. In this scenario, understanding the birth environment and evolution of our own Solar System can help us to better understand the formation and evolution of other known planetary systems and can also address us to questions about the origin of life.

The possible genetic linkage between a group of meteorites and a group of asteroids has been a hot topic in planetary science research, during the last few years. Several advances in our knowledge of the diversity of asteroid mineralogies have been made since the beginning of the use of charge-coupled device (CCD) detectors to obtain the visible and NIR reflectance spectra of small objects. Visible and near infrared spectroscopy of meteorites and asteroids can provide a powerful technique to study a possible genetic linkage between a meteorite and an asteroid. However, reflectance spectra are not always intrinsic to surface mineralogy as grain size effects or surface roughness can change the optical properties of any mineral. In the case of asteroids, space weathering caused by heavy micrometeorite bombardment, cosmic-rays or solar wind irradiation, can lower the albedo of the asteroids surface and redden and attenuate the absorption features of their reflectance spectra. Despite the task of establishing possible genetic linkages between meteorites and asteroids can be quite arduous, several improvements were made in order to model the effects of space weathering on reflectance spectra of meteorites. Linking a specific meteorite to an asteroid is a quite arduous task. But, the Howardites (H), Eucrites (E) and Diogenites (D) and V-type asteroids seem to share a strong relationship. Also others relationships have been postulated, such as the possible one between S-type asteroids and ordinary chondrites or the possible intriguingly one between CI and CM carbonaceous chondrites and comets.

U.PORTO
FACULDADE DE CIÊNCIAS
UNIVERSIDADE DO PORTO

In this work it is aimed to investigate the possible relationship between Howardites (H), Eucrites (E) and Diogenites (D) meteorites and some V-type Near Earth Objects (NEOs) and 4 Vesta. For this purpose, the reflectance spectra of a large number of NEOs and V-type asteroids taken from the publically available MIT-UH-IRTF Joint Campaign for NEO Reconaissance and spectra of HED meteorites and intimate mineral mixtures from the RELAB database will be analyzed. The Hapke radiactive transfer Model will be applied to derive the albedos of the asteroid and meteorite reflectance spectra samples taken from the databases cited above. The implementation of the Hapke radiactive transfer Model will be done using Microsoft Excel, following the implementation made by Quinn, D. et al. (2010) [1]. In order to derive the mineralogy of the samples, the mean least squares will be applied to fit the albedo of the sample by minimizing the residuals. This minimization process is done through the Solver package available in Microsoft Excel software. The implementation of this algorithm was previously done by Teresa M. Seixas and M. A. Salgueiro da Silva, Physics and Astronomy Department, Faculty of Sciences, University of Porto. In addition, the possible genetic linkage between several NEOs and V-type asteroids and the studied HEDs will be analyzed.

This thesis is divided into six chapters. In the first chapter, an overview about the current knowledge of the formation and evolution of the Solar System will be given. In the second chapter, a detailed description about the small objects of our Solar System (such as comets, asteroids and Trans-Neptunian Objects) will be given. In the third chapter, a detailed description about the current knowledge of meteorites classification scheme and the chronology events in the early Solar System, and their relationship with meteorites will be given. In chapter four, the postulated genetic relationships between asteroids and meteorites will be discussed and the effects of space weathering on reflectance spectra will be described. Also in chapter four, the most popular models of deconvoluting spectra will be presented. In chapter five, the results of this study will be stated and discussed. In chapter six, the conclusions of this work will be presented.

U.PORTO
FACULDADE DE CIÊNCIAS
UNIVERSIDADE DO PORTO

# 1. Formation of the Solar System

*"What we know is not much. What we don't know is immense."*

Marquis de Laplace (1749-1827)

Nowadays it is known that stars are born in clusters [2], despite some recent results from Spitzer suggesting that this scenario could not be unique [3]. The Sun was born in an open star cluster [4], perhaps in the δ-quadrant at -1.39kpc, 9.34kpc and 25.3pc along the galactic x, y and z-axis [5]**.** The birth environment of the Sun has been subject of several studies [6], where the searches for the stars which have born with the Sun – called siblings of the Sun – play an important recent role. Devoted to this thematic, during the last three years four siblings were pointed out for the first time to our knowledge: HIP28676 [7], HIP47399 [4], HIP87382 [4] and HIP92831 [8]. Identifying those stars can help us to decipher some processes which the Sun underwent in its birth's place. Of particular interest, respecting to this thematic, we can ask one enigmatic question: "How many solar siblings have a planetary system similar to our Solar System?". Answering to this question is a challenging task which still remains unsolved. However, the number of discovered exoplanets around stars has recently increased a lot [9], due to several advances in the use of the charge-coupled device (CCD) allowing us to obtain high resolution spectra of stars. The presence of planetary systems seems to be quite common around stars but, how do planetary systems form? Answering to this question is not trivial due to several puzzling phases occurred during planetary system's formation.

In this chapter, it will be explained how the Solar System has formed: from dust to planets. The chapter will start with a historical overview about the theories of the Solar System formation. Then, the most accepted theory, nowadays, will be presented.

**Keywords:** dynamics; evolution; protosun; protoplanetary nebula; chemistry; condensation; coagulation; runaway growth; oligarchic growth; ordinary growth; planetesimals; planetary embryo; planet; Solar System; disk instability; core-accretion; collisions;

## 1.1. Historical Overview

Since the antiquity that humankind tries to explain the origin of the Solar System. Aristarco de Sarmos was the first astronomer, in the ancient Greece,

proposing that the planets orbit around the Sun – heliocentric model. Because of his idea, he was charged with impiety by Cleanto. Only several centuries later, Nicolau Copernic (1473-1543) argued in his favor. Copernic proposed that: (i) the planets orbit the Sun and rotate around its rotation axis; (ii) the dimensions of the Solar System can be neglected when compared to the dimensions of the Universe. Some years later, Galileu Galilei (1564-1642) observed some planets and stars with a telescope, for the first time in the humankind history. He confirmed the Copernic theory's and then introduced the term dynamics. After this, several theories about the Solar System formation were proposed: turbulent theory (proposed by René Descartes, 1596-1650); the nebular theory (proposed by Immanuel Kant (1724-1804) and Marquis de Laplace (1749-1827)); tidal theory (proposed by Buffon (1707-1788) and later on modified by Sir James Jeans); accretion theory (proposed Alfvén and Arrhenius in the last century).

### 1.1.1. Turbulent Theory

The turbulent theory was introduced by René Descartes (1596-1650), in which the Universe was made by ether and matter. In his theory the Universe was full of swirling movements. However, this theory was discarded as it did not explain the presence of the ecliptic, later confirmed by the Newton's laws. In its theory, René Descartes introduced the term evolution.

### 1.1.2. Nebular Theory

The existence of a nebula from which the planets formed was firstly proposed by Immanuel Kant. Several years later Marquis de Laplace proposed a similar theory. He predicted that: (i) the orbits of all planets are roughly in the same plane; (ii) all planets orbit around the Sun in the same direction; (iii) all orbits have a low eccentricity, meaning that they are close to circles; (iv) all planets spin on their axis in the same direction. In his theory, the beginning point was a slowly rotating spherical nebula made of gas and dust, which were slowly collapsing due to the gravitational force (step a, in Fig. 1.1). When the nebula collapsed it spun faster and flattened along the spin axis, in order to conserve the angular momentum (step b, in Fig. 1.1). After this, maybe the nebula acquired a lenticular shape and the material found in the broadside regions was free to orbit the central mass (step c, in Fig. 1.1). As the collapse was undergoing, material was left behind in the equatorial plane forming a set of annular rings (step d, in

Fig. 1.1). In the end, each ring originated a planet. Eventually, the Sun was formed in the central region (step e, in Fig. 1.1) [11].

This theory was capable of explaining the observations made during the eighteenth century. In addition, it is capable to explain why all planets orbit around the Sun in the same direction and why their orbits are almost circles lying in the same plane, called ecliptic. However, Laplace's theory did not explain how a planet formed from a ring of material. Actually, it also did not provide an explanation for one intriguing fact: why 99.9% of the Solar System's mass is in the Sun and 99% of the Solar System's angular moments is in planets.

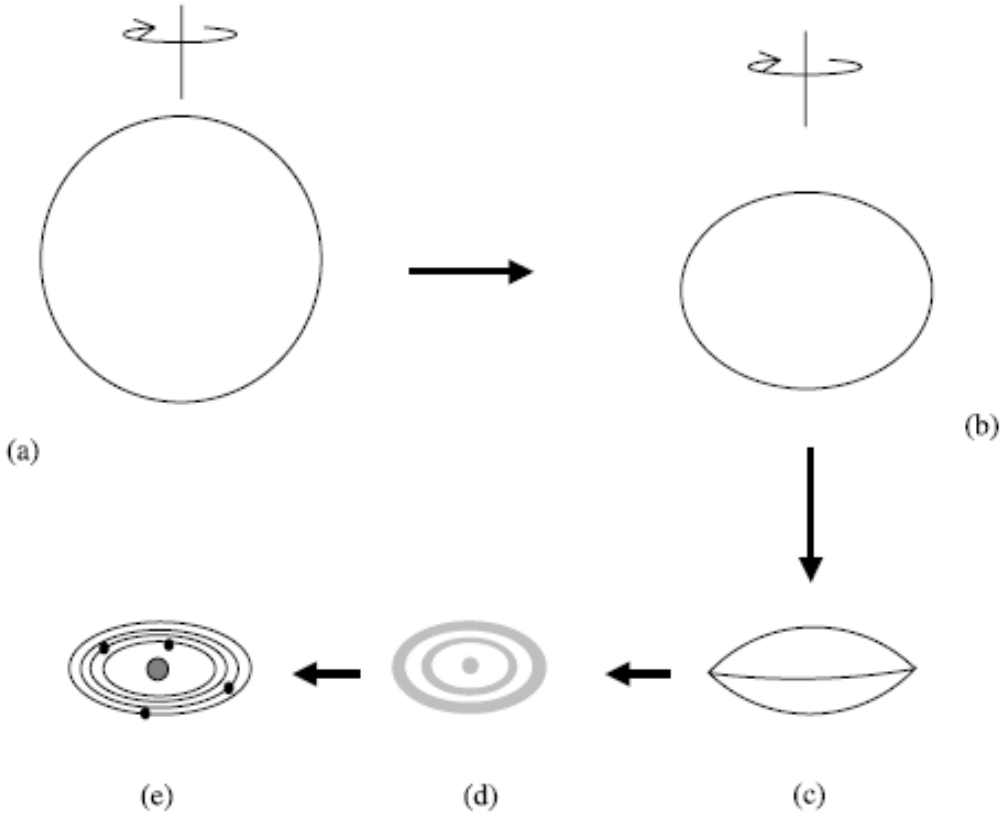


Fig.1.1 – A schematic overview of the Laplace' s nebular theory. (a) A slowly rotating and collapsing gas-and-dust sphere. (b) An oblate spheroid formed as the spin axis increased. (c) The critical lenticular form. (d) Rings were left behind in the equatorial plane. (e) Each ring originated a planet [11].

Several modifications to Laplace's theory were attempted in order to bridge the latter evidence. Berlage introduced a viscosity effect, while Hoyle and Schatzman introduced the magnetic field effect and the solar wind, respectively, attempting to give one plausible explanation which could bridge the problem of the angular momentum.

U.PORTO
FACULDADE DE CIÊNCIAS
UNIVERSIDADE DO PORTO

### 1.1.3. Tidal theory

Buffon (1707-1788) proposed that a comet shocked with the Sun, 70Myr ago. This hypothesis has no scientific fundament. But, in the beginning of the twentieth century, Sir James Jeans reformulated his theory by substituting the comet by a massive star. Jeans separated the formation of the Sun from the formation of the planets. The mechanism proposed by Sir James Jeans is illustrated in Fig. 1.2, where a massive star passing close to the Sun, raised a tide on the Sun pulling out material, which formed a filamentary structure. This filament was gravitationally unstable and as its mass was greater than the Jeans critical mass, it condensed to form planets. In the end, the planets were left in orbits around the Sun.

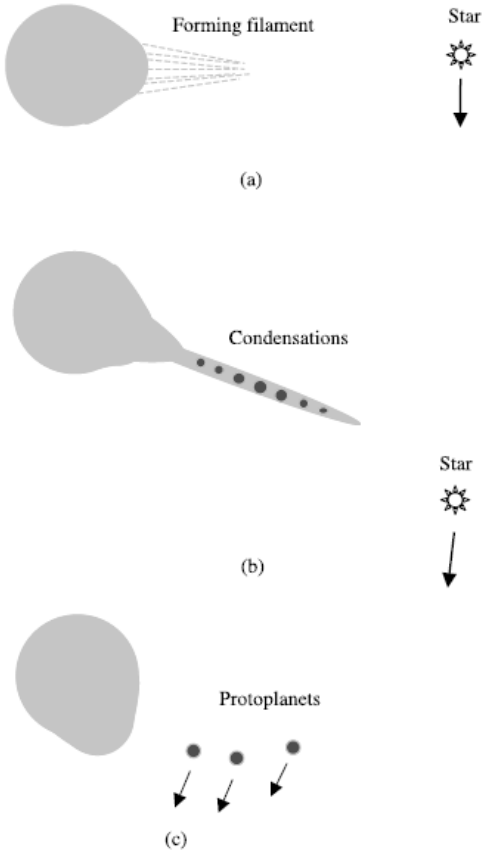


Fig.1.2 - A schematic overview of the tidal theory, modified by Sir James Jeans [11].

If this theory is correct, the presence of planetary systems around stars should be rare, which contrasts with growing up number of discovered exoplanets in the last few years.

U.PORTO
FACULDADE DE CIÊNCIAS
UNIVERSIDADE DO PORTO

### 1.1.4. Accretion theory

Alfven and Arrhenius argued that the Sun had encountered two nebulae: one composed by volatile elements and another composed by hydrogen. They proposed that the Sun accreted matter from these nebulae and several collisional processes between particles led to the formation of flows from which the planets could have formed.

## 1.2. Formation and evolution of the Solar System: Planet Formation

Modern theories about the formation and evolution of planetary systems are based on the observations of star-forming regions and numerical simulations. In the case of the Solar System, there are several observational constraints supporting the most accepted theory, which will be described in this chapter. Some key observations are:

- The Solar System contains eight large planets, with almost circular and coplanar orbits, lying in the region between 0.4-30 AU. There are also a few locations between the planets where additional large objects could exist on stable orbits.
- All planets are grouped in two distinct regions: in the inner region of the Solar System there are the volatile-poor planets while the volatile-rich planets are found further out. The Main Asteroid Belt is found between these two regions (2-4 AU). The Main Asteroid Belt is substantially depleted in mass compared to the other two regions.
- The degree of fractionation decreases with distance from the Sun: the terrestrial planets and inner-belt asteroids are highly depleted in volatiles while the outer-belt asteroids are less so and many satellites in the outer Solar System are ice rich.
- Ancient planetary surfaces, such as those of Mercury, Mars or Callisto, are covered by impact craters.
- The terrestrial planets and many asteroids have undergone differentiation.
- There is strong evidence that Saturn is highly centrally condensed, containing a core of mass of $10M_{Earth}$ and weaker evidence that Jupiter has a core of similar

mass. These cores may have masses comparable to the ones of Uranus or Neptune.

The observational evidences led the development of the Solar System formation theory postulated by Laplace, described in the last section. In this theory, planets formed from a protoplanetary nebula by pairwise accretion of small objects. A gravitational instability in some regions of this disk is added to this theory to explain the formation of the giant planets.

However, before going deeper in the description of this theory it is important to quote that the standard model only attempt to explain the planets observed in the Solar System.

### 1.2.1. The protoplanetary nebula and the first solids

The Solar System probably formed from the collapse of a fragment of a molecular cloud. When the Jeans' criterion was satisfied, the fragment of the molecular cloud collapses. These collapse may have occurred spontaneously or been triggered by an external factor, such as a supernova [12]. As the cloud fragment collapses the bulk of its mass fell to the center to form the protosun, while the remaining material formed a rotationally supported disk. The presence of this disk is constrained by the observations of young "T-Tauri" stars, with ages less than 10Myr, which have optically thick disks of gas and dust with masses of 0.001-1$M_{Sun}$ [13]. However, the question concerning to initial mass of the disk is still under debate. These disks have spectra containing absorption features caused by the presence of water ice and silicates.

According to the observations, disks are not observed around stars older than 10Myr, providing an upper limit of the solar protoplanetary nebula lifetime. But, as young stars are observed to be accreting material and due to the limited lifetime of circumstellar disks, the solar protoplanetary nebula is viewed by this model as a viscous accretion disk in which the material is transported radially inwards, ultimately falling onto the Sun [14]. However, the source of viscosity in the disk is still under debate.

Nowadays, the maximum temperature reached in the Sun's protoplanetary disk is still under current discussion. As it is constrained by the approximate isotropic

homogeneity of planetary material in the inner Solar System, most of the material in the inner regions were vaporized and mixed. As the nebula cooled and refractory material began to condense, chemistry becomes important. The sequence of the condensation of different elements can be seen in Fig. 1.3. The list along the top of Fig. 1.3 shows the 15 most abundant elements in the protoplanetary nebula. Below, there is a list of compounds in which these elements were mostly found when the nebula temperature's was around 2000K. As an illustrative example, oxygen atoms were enclosed in water molecules. The staircase found across Fig. 1.3 separates the solid phase from the gas phase. By looking down in the staircase from the top right to the bottom left we can follow the sequence in which the elements condensed as the nebula cooled [15].

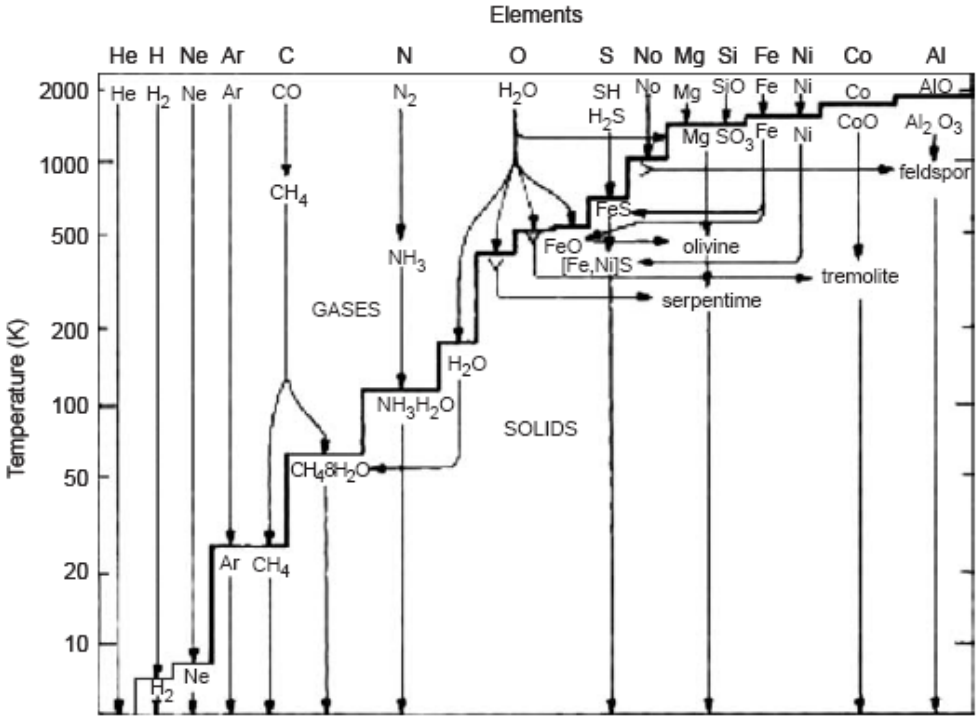


Fig.1.3 – Predictions of the sequence in which chemical species condensed in the solar nebula [15].

The first elements which condensed were metals with high boiling points as there are the cases of the calcium, aluminum and nickel. The first two cases condensed as oxides CoO and $Al_2O_3$, while nickel condensed as solid nickel. The arrows below the staircases denote how these solids reacted with other elements, which were still in the gas phase. As it can be observed by this diagram in Fig.1.3, a major quantity of aluminum ended up in the silicate mineral feldspar. The presence of

minerals like olivine and feldspar is reassuring as Earth is made by them. The others compounds with lower boiling points started to condense as the nebula cooled, even some compounds as water, ammonia and methane. The complexity of this process as a whole is evidenced by the possible routes for water molecules: it started to enter the solid phase when the temperature was still high enough by becoming incorporated in the hydrated minerals tremolite and serpentine. Furthermore, water molecules only formed pure water ice when the nebula cooled.

At this stage, in the inner region of the nebula, around 0.5% of the mass would have formed solids following any initial hot phase of the nebula evolution. These solids were mainly composed by silicates, metal and sulfides. In the outer regions, where temperatures were colder, icy materials also condensed. In this region, water ice was the most abundant. The boundary between these two regions is established by a discontinuity in the surface density of solid material called the “ice line” or “snow line”. This line would have moved inwards over time as the nebula cooled.

### 1.2.2. The origin of planetesimals

This earliest stage of planetary accretion is the most poorly understood at the present. Nowadays it is argued that planetesimals could be originated by one of the following processes: via gravitational instability or via dust grain sticking.

This stage of the nebula evolution is marked by the lacking of gas pressure support, settling dust grains and aggregates towards the midplane of the nebula, with larger objects falling faster than small ones. During this process, dust grains would have coagulated to form larger objects, increasing the rate of sedimentation. As a consequence, the solid to gas ratio in this region was increased. If the inner layer of the nebula was very thin, portions of it would become gravitationally unstable and collapsed to form solid bodies of around 1 km in diameter. These bodies are called “planetesimals”.

The formation planetesimals via gravitational instability are not so simple and are more probable to occur when the volume density of solid particles is high and their relative velocities are low. In one hand, if the disk was nonturbulent, particles would have migrated at different rates in different regions, leading to a pile up of solid material in certain regions [16]. On the other hand, particles would migrate more slowly in

regions where the volume density of particles is high, probably leading to a local increase of the solid-to-gas ratio [17]. These two factors favor the formation of planetesimals via gravitational instability.

If planetesimals were not formed through gravitational instabilities, such bodies are probably a result of a sticking process of dust grains and aggregates during collisions. Experimental studies suggest that small dust grains will stick together if they collide at velocities lower than a few meters per second [18]. This sticking process is mainly due to van de Waals forces, which are weak.

The grain growth process may have occurred in a short timescale for the objects to survive against gas drag due to the differential velocity of solid objects relative to the gas nebula.

Nowadays it is still unclear how aggregation continued for boulder-sized and larger objects. But, the presence of gas may have helped.

### 1.2.3. The formation of terrestrial planets

Once solid bodies reached a size of around 1km, gravitational interactions between them become significant. Close passages between planetesimals tended to increase their random velocities v, as a result of mutual gravitational attraction. The frequency of collisions is strongly dependent on their random velocities. In one hand, if v was high, close encounters were briefly reducing the probability of collision and thus the growth rate of planetesimals. On the other hand, if v was small during a close encounter, planetesimals remained close to each other, increasing the probability of collision. In this scenario, three growth modes may have occurred during this stage, each at different times in the solar nebula.

The early stages of accretion were marked by a “runaway growth”. Actually, if the disk was dynamically too cold, the velocity dispersion of the planetesimals,$\sigma_{rel.}$, may be inferior to their escape velocity, $v_{esp.}$. In this case a “runaway growth” begins, which means that relative mass growth of each individual object is an increasing function of its own mass M [19]:

$$\frac{1}{\mathrm{M}}\frac{\mathrm{dM}}{\mathrm{dt}} \sim \frac{\mathrm{M}^{1/3}}{\mathrm{v_{rel.}}}$$

In the “runaway growth” mode, the largest planetesimals tended acquire the smallest random velocities, due to the dynamical friction process. Hence, the largest bodies experienced strongest gravitational focusing of their trajectories and they grew more rapidly, during this stage.

Once the largest objects, become around 100 times more massive than a typical planetesimal (i.e. dubbed “planetary embryos”), the random velocities of planetesimals were mainly determined by gravitational perturbations from the embryos. So, when $\sigma_{rel} \sim v_{rel}$ the “runaway growth” slowed down and accretion continued in an “oligarchic growth” mode (in which the relative mass growth for the largest objects is proportional to $M^{-1/3}$) [20]. During this growth mode, the larger a planetary embryo was, the more it stirred up the velocities of nearby planetesimals and the slower it grew up. Gravitational interactions between planetary embryos tended to keep them in their “feeding zones” in the protoplanetary disk, where they accreted most of their mass. Hence, depending on where planetary embryos formed in the protoplanetary disk, they may have had different compositions.

The final stage of accretion is the most violent phase, marked by catastrophic collisions between planetary embryos [21]. This last stage began when the remaining planetesimals had too little mass to sustain the random velocities of planetary embryos. While the random velocities of the planetary embryos increased, their growth slowed drastically and their orbits began to cross those of their neighbors. A new growth mode began, when almost half of the total solid mass was contained in planetary embryos [22]. This growth mode is known as “orderly growth”. In this last stage, planetary embryos started to collide with each other and despite the unknown efficiency of these collisions, growth continued. However, this process is supported by numerical simulations [23]. The remaining planetesimals probably fell into the Sun or were ejected from the infant Solar System. Several impacts may have been so energetic that had completely molten each of the inner planets, originating a magma ocean which homogenized existing material and erased any chemical signatures of the earlier stages of accretion. One example of a catastrophic collision may have occurred with Mercury after it had differentiated, constraining its observed high density [24].

Due to the heat from the decay of radioactive isotopes allied with energy released from impacts, planetary embryos were differentiated once these objects

became partially molten [25]. Iron and siderophile elements (such as, platinum, palladium and gold) preferentially sank to the center to form a core, while the lighter silicates and lithophile elements formed a mantle.

As it is evidenced by the presence of siderophile elements in Earth's mantle and crust, some material was accreted as a "late veneer" when Earth's differentiation was largely complete.

However, the presence of volatile elements on Earth poses a major problem on planetary formation. As it was already described above, the inner region of the protoplanetary nebula may be too hot for the volatiles elements to condense at the same time as planetesimals were being formed. Hence, it seems likely that Earth acquired its volatile elements by accreting material which formed in regions beyond 2.5 AU, i.e. in regions where the nebula was cold enough for ices to condense. Another important aspect which has to be stated out is how Earth probably acquired water. As it constrained by the difference between the measured D/H ratio of seawater on Earth and the one's of comets, an asteroidal source is more promising to explain the origin of water on Earth. Actually, according to numerical simulations, Earth could have accreted several oceans worth of water from the asteroid belt, in particular if lunar-to-Mars size planetary embryos had formed in this region [26].

### 1.2.3.1. Origin of the Moon

One of the most intriguing properties of the Solar System is the origin of the Moon itself. Between the more than 100 moons in the Solar System, our Moon is an object of peculiar interest as the ratio between Earth's and its masses is quite large. Most of the moons in the Solar System are captured objects: see for example the case of Phobos and Deimos (moons of Mars), which are probably captured asteroids, or also the case of Triton (moon of Neptune). In addition, we can also count lots of small icy worlds orbiting Jupiter, Saturn and Uranus which are probably captured objects by the gravitational influence of these planets.

Historically, there are three theories for the origin of the Moon: the capture theory, the fission theory and the cocreation theory. In the capture theory, the Moon formed elsewhere in the protoplanetary disk and was consequently captured by the Earth's gravitational field. However, the major contradiction against this theory is the

probability of the Earth being capable of capturing such a massive object is low. In the fission theory, proposed by Charles Darwin, the Earth was originally spinning so quickly that the centrifugal force caused it to split into two. But, it does not seem that the Earth was ever spinning so fast to consider this scenario. In the last theory – cocreation theory – the Earth and the Moon formed somehow independently out of the same part of the nebula. But, the way that this happened is not clear [15].

When in the 1970s, the astronauts from Apollo's missions brought some rocks from the Moon its chemical analysis evidenced that: the Moon rock when compared to the Earth rock contains a much lower proportion of volatile substances, with low boiling points. This evidence is completely against the second and the third theories, while it seems possible in the first theory. Hence, in the 1970s these theories were completely replaced by a new theory, where the Moon was originated by some impact event with the Earth. Nowadays, it is possible to simulate this scenario: an impact between the Earth and a Mars-mass object. According to these simulations, the cores of the impacting objects quickly coalesced, while the orbital liquid and vapor debris disk solidified and consequently accreted into a single large satellite. This theory can explain why the Moon rock contains few volatile substances, as these would have boiled away in the heat produced by the impact. It also explains why the Moon has a lower density than the Earth: the Moon was formed from material coming from the Earth's mantle. According to the low iron abundance in the lunar mantle, the impact occurred close to the Earth's accumulation and differentiation, i.e. maybe a few million years after the birth of the Solar System [15].

### 1.2.4. The formation of the Giant planets

Nowadays there are two theories which try to explain the formation of giant planets: the so called "core accretion model" [27-28] and the disk instability theory [29-30].

The "standard" theory of the multistage accretionary formation of planets is the so-called core-accretion theory. However, this theory was the most popular until recently when several authors started to criticize it [31-32]. The main problem of the core-accretion model is the timescale, which is longer than estimates of the lifetime of many planet-forming disks [33]. In this scenario, the disk instability theory seems to

play an important role. It is suggested that a local gravitational Jeans-type instability of small-amplitude gravity perturbations in the disk provides a simultaneous formation of the Sun and all the planets around it.

### 1.2.4.1. Core-Accretion theory

In order to explain the inferred large core masses of Jupiter and Saturn, it was introduced the so called “core-accretion” model [27-28]. It is predicted that the giant planets formed through two distinct steps: in a first step, the formation of a roughly $\sim 10$ earth masses; in a second step, this roughly core accreted a considerable amount of gas from the disk. It is assumed that the core is formed by the same way as the terrestrial planets did (i.e. through the same collisional accumulation of planetesimals and planetary embryos that led to the formation of the terrestrial planets [34]).

### 1.2.4.2. Disk Instability theory

The idea of the giant planet formation through gravitational instability was firstly proposed by Kuiper (1951) [29] and Cameron (1978) [30]. It postulates the disintegration of a gas-and-dust protosolar nebular under the influence of local gravitational instabilities into massive clumps, which then collapse into the Sun and planets. By other words, the protoplanetary disk forms self-gravitating planetesimals through a gravitational instability of the gaseous disk, which by settling and coagulation of dust grains, form central solid cores. It is hypothesized that radiation of nearby massive stars, removes most of the protoplanets gaseous envelopes. Several numerical simulations were performed in order to argue in favor of this theory [31][35]. But, the survival of such clumps is still an unsolved issue [31].

In addition, it is important to quote that this process of gravitational instability is different from the one described above for the formation of planetesimals.

### 1.2.4.3. Observational Constraints: theory against observations

These two models seem to explain nicely the formation of the giant planets in the Solar System. However both have some advantages and disadvantages.

In the case of the core-accretion model, it has a major problem concerning to the timescales of giant planets formation. As it is observed, the limit lifetime of a typical protoplanetary disk is a few million years in regions of low-mass star formation [36]. And, even in the most optimistic case it takes around 8 million years to form Jupiter. However, recent numerical simulations argue against the timescales problem [37]. Another problem related to the core-accretion model has to do with a new generation of models of the interiors of Jupiter and Saturn [38]. According to these models, the observational constraints can be matched with considerably smaller cores than it was firstly predicted: between 0 and 12 Earth masses for the case of Jupiter and between 1 and 13 Earth masses for the case of Saturn.

In addition it seems more likely that Jupiter and Saturn can be formed in situ by the core-accretion model than Uranus and Neptune [39]. But, a promising idea is that Uranus and Neptune were formed somewhere between Jupiter and Saturn and were consequently gravitationally scattered outward to their present orbits [40].

Several advantages and disadvantages are also pointed out for the disk instability model. In this theory it is possible to form planets in less than $10^4$yr, solving the problem with timescales in the core-accretion model. Hence, giant planet formation can occur well before the disappearance of the protoplanetary disk. This evidence quotes one point favoring this model. However, the present disk instability models also have several disadvantages. As an example, they require a relatively high-mass disk (with 0.13 solar masses within 10AU), which seems more theoretical rather than observational [26].

Recently some authors argue that giant planets embryos may become convective within the first ~100 yrs of their evolution and that convection process can inhibit grain sedimentation [41]. This evidence has recently been confirmed [42]. Another objection to the disk instability model is that the disk cannot even fragment on self-bound clumps inside at least ~30 AU.

Actually, the core accretion model neither the disk instability model seems to solve nicely the question of giant planets formation. Observing the extrasolar planets at large separations (R~100AU) from their parent star cannot be explained by the core accretion model. But, they were certainly formed by gravitationally disk instability. The

core accretion model might be effective only in relatively long-lived disks found in regions devoid of high-mass star formation [43]. On the other hand, the disk instability model might form gas giant protoplanets rapidly, even in the shortest lived protoplanetary disks [43].

#### 1.2.4.4. Formation of Uranus and Neptune

As it was quoted above, it seems likely that Jupiter and Saturn formed *in situ* rather than Uranus and Neptune. In fact, long orbital periods in the outer Solar System mean that accretion occurs very slowly. The evidence that Uranus and Neptune were not formed *in situ* is also constrained by numerical simulations [45].

A more promising idea is that Uranus and Neptune formed along with the cores of Jupiter and Saturn. Such system would have remained dynamically stable until Jupiter accreted a large H/He-rich atmosphere, perturbing at least two of the other bodies into the region beyond 15 AU. According to numerical simulations, this is a robust idea which provide that cores with masses $\sim 10 M_{Earth}$ were able to survive type-I migration [46]. Gravitational interactions with planetesimals in the outer Solar System would have circularized the orbits of Uranus and Neptune, by dynamical friction.

The failure of Uranus and Neptune in capturing more than a small amount of the nebula gas, is probably due to the dispersion of the nebula, before they could accumulate massive atmospheres as it was possible in the case of Jupiter and Saturn.

### 1.2.5. The "Tidal Downsizing" hypothesis, a more plausible theory?

The tidal downsizing hypothesis (Fig.1.4) (hereafter also reported as TD hypothesis) combines some of the planet formation processes from both core-accretion and gravitational instability models. This hypothesis favors the strengths of the latter theories in spite of their weaknesses [47]. It is based in a hybrid scenario: the giant planet formation starts as in the gravitational instability model, with dust segmentation within a self-gravitating gas clump. Then, the formation continues as in the core-accretion model, with the accretion of massive metal-rich gas envelope from the inside of the giant embryo. Furthermore, solid cores left by the giant embryos disruption in the protoplanetary disk may grow further as in the core-accretion model, i.e. by accreting

smaller solid debris from the disk. Also, giant planets may also accrete more gas as well as migrate radially [47].

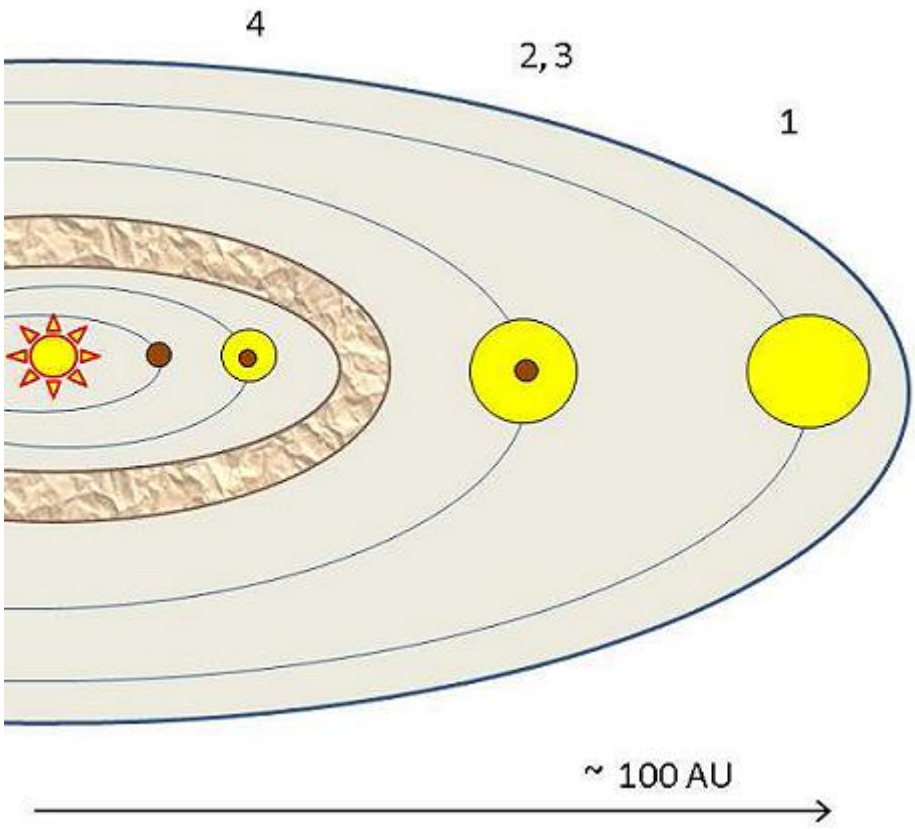


Fig.1.4 – TD hypothesis. A protostar (the central symbol) is surrounded by a massive disk of gas. The four steps stated above are schematically described in this cartoon and marked by numbers: (1) The formation of the massive clumps in the outer disk; (2) migration of the clumps close to the parent star; (3) while migrating, dust grains growths and eventually sediments into a massive solid core (brown sphere inside the gas embryo) in the center; (4) disruption of the embryo by tidal forces or by irradiation from the protostar. The brown pattern-filled donut-shaped represents the solid debris ring left from an embryo disruption. A solid core whose envelope was completely removed represents a terrestrial-like planet, in the most inward orbit of the cartoon. In the following smallest orbit a giant-like planet is represented, with its massive solid core retaining some of its gas envelope [47].

The TD hypothesis is a new combination of the earlier ideas of the gravitational instability and core-accretion models for planetary systems formation. This hypothesis is described by the following steps [47] (Fig.1.4):

1. Formation of gas clumps: a massive young protoplanetary disk fragments somewhere at larger radii of several tens to hundreds of AU on gaseous clumps with masses of a few Jupiter masses. It is estimated that the mass of the clumps is $\mathrm{M}{\sim}10\mathrm{M}_{\mathrm{Jupiter}}$ [48].

2. Contraction and Migration: the clumps cool and contract, while migrating closer to the parent star due to gravitational interactions with the surroundings gas disk.
3. Grain growth and sedimentation inside the clumps: (a) dust sediments inside the gas clumps form massive terrestrial planet cores, as earlier suggested in the gravitational instability model; (b) if the solid core becomes more massive than $\sim 10 \mathrm{M}_{\mathrm{Earth}}$, the massive gas atmosphere collapses against the solid core.
4. Disruption of giant embryos in the inner few AU due to tidal forces or by the irradiation from the star: these phenomena peel off the outer metal-poor envelope which is evolving the clump. If the tidal disruption occurs quickly, while still in step 3a, a terrestrial planet core is left. On the other hand, if it happens only in step 3b, a metal rich gas giant planet with a solid core will appear from the core.

The TD hypothesis seems to solve nicely the mainly coherent and prograde rotation of planets, which is unexpected if planets are built up by randomly oriented impacts [39]. However, several opens questions still remain unanswered about this new theory. It is aimed that in the next few years further detailed considerations may be taken in planetary system's formation, where the "Tidal Downsizing" theory can play an important role [47].

### 1.2.6. The Asteroid Belt

Another peculiar property of the Solar System remains to be explained: asteroids! It is unlikely that asteroids formed almost as they are in the present – a swarm of irregular fragments. The Widmanstätten figures argue against the formation of asteroids as individual objects. Nowadays, it is thought that in the past there were almost certainly more planetary embryos than there are planets today. Due to the gravitational forces between them, some planetary embryos were completely ejected from the solar nebula while others merged to form planets, as discussed above. The origin of asteroids is probably due to a planetary embryo in an orbit between Mars and Jupiter, which suffered a fragmentation process. In this scenario, asteroids represent the only surviving bodies from the planetesimal formation process. After their accretion, fragments of major dimensions experienced a high temperature event and consequently the disintegration of short-live time radioactive elements. As a

consequence of the latter process, a silicate crust in these bodies was formed. With the ending of this internal activity, only several collision processes in the Main Asteroid Belt could modify their characteristics: as an example, the objects with lower dimensions shocked with the ones of bigger dimensions originating a regolith in their surfaces [49].

U.PORTO
FACULDADE DE CIÊNCIAS
UNIVERSIDADE DO PORTO

# 2. Small Bodies in the Solar System

*"The clear and very uplifting lesson of all this is that we remain only dimly aware even of our immediate astronomical backyard. The Kuiper belt with its unexpected dynamical subdivisions and structures, the main-belt comets, the (perhaps) densely populated inner Oort cloud, were all completely unknown when, for example, most of the readers of this article were born. The obvious next question is "What else is out there?"."*

in Jewitt, D. (2009), *Icy bodies in the New Solar System*, Proceedings of the International Astronomical Union, IAU Symposium, 263, 14

The last 20 years have been particularly fruitful in the study of these icy objects. Due to several advances in technology it was possible to reveal the presence of such objects in regions thought to be empty. Nowadays, it is known that they carry an unimaginable fraction of scientifically useful information about the origin and the evolution of the Solar System. Firstly, the majority of these objects escaped substantial thermal alteration since its formation. Their chemical and molecular compositions may be closely to the initial conditions of the Solar System. Secondly, their number is so high and their orbits so accurate that they can be used with the purpose of mapping dynamical space parameters or to trace processes occurring in the protoplanetary disk [50].

In our Solar System, there are a countless number of small objects, ranging from planetesimals which grew up until modest sizes of a few hundreds of kms in radius to post-collisional debris. These objects are known as asteroids, comets or Trans-Neptunian Objects. They are located in the three ice reservoirs: the Oort cloud; the Kuiper Belt; and in the Main Asteroid Belt. The presence of such small bodies in our Solar System seem to be quite common in other planetary systems, as the number of known exo-Kuiper-Belts around nearby stars has recently increased from 29 to 34 [51]. As an illustrative example, the HR8799 planetary system resembles to a scaled-up version of the Solar System [52]: the presence of an asteroid belt interior to and a Kuiper Belt exterior to the recently discovered planets was inferred [53]. In this scenario, the obvious question is "What else is out there?".

In this chapter, the small icy objects of the Solar System will be described. This chapter is divided into three subsections. In the first subsection, asteroids will be presented. Then, in the second subsection, the "dirty snowballs", also known as comets and what is their role in our Solar System will be pointed out. Finally, the last subsection will be dedicated to the Trans-Neptunian Objects.

**Keywords:** asteroids; Main Asteroid Belt; taxonomy; Near Earth Asteroids; Kirkwood gaps; Trojan Asteroids; Centaurus Asteroids; 4 Vesta; Vestoids; families of asteroids; secular resonances; comets; long-period comets; short-period comets; Tisserand parameter; Oort Cloud; Trans Neptunian Objects;

## 2.1. Asteroids: Shattered Worlds

The term asteroid is applied to a peculiar class of objects, which are sufficiently non volatile not to be classified as a comet and small enough not to be classified as a planet. In addition, they were called asteroids as they seemed to be star-like points of light. Nowadays, asteroids provide our only *in situ* record of the conditions and processes that the inner portions (~1.8-3.5 AU) of the late solar nebula and the infant solar system have experienced [54]. Asteroids have irregular-shaped bodies, which in some cases they look like potatoes. Thousands of these objects orbit the Sun in the so known Main Asteroid Belt (hereafter, also reported as MAB) (Fig. 2.1), between the orbits of Mars and Jupiter [55]. Due to the several advances in technology, we are now able to get measurements of asteroid light-curves, as well as other important information such as body shapes, polar orientations or rotational periods.

Ceres was the first asteroid to be discovered in 1801 by the Italian astronomer Giuseppe Piazzi. As it was predicted by the Titius-Bode rule[1], the semi-major axis of Ceres' orbit is 2.8 AU. Ceres is the biggest known rock in the MAB, with a diameter of 950 km (around 560 miles). In 1802, a second asteroid named Pallas was discovered. Ceres and Pallas were found really close to each other suggesting that they were a result of a fragmentation process of a larger body that could be split by several collisional processes. Hence, this evidence has encouraged people to look for more possible fragments, thus leading to the discovery of Juno (1804) and 4 Vesta (1807).

[1] Titius Bode Rule: gives the mean orbital distance of the planets and which can be written in the Blagg-Richardson formulation as $r_n = r_0 \times A^n$, where $r_n$is the distance of the nth planet from the Sun (in AU), A≈ 1.73 is the mean ratio between two consecutive planetary distances and $r_0 \approx 0.21$. The MAB distance is considered as a regular planetary distance $r_5 \approx 2.8$ AU.

Nowadays, many thousands of asteroids are catalogued [56]. In Table C1 some mineralogically characterized asteroids with some meteorite affinity associated can be found.

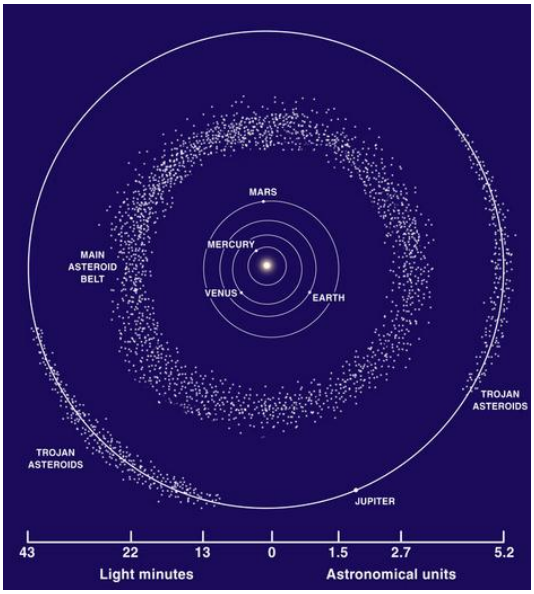


Fig.2.1 – Main Asteroid Belt and Trojan Asteroids. *Source: http://www.aerospaceweb.org/question/astronomy/q0270.shtml*

## 2.1.1. Classification of Asteroids

Asteroids can be classified by their location in the Solar System (which will be discussed in the next section of this chapter) or by their reflectance spectra. There are two taxonomic classifications, which are the most used to classify asteroids taking into account their reflectance spectra: Classification of Tholen; Classification of SMASSII. A brief description of these taxonomic classifications can be also found in Table C2.

The taxonomic classification proposed by David J. Tholen [57], in 1984, is the most commonly used to classify asteroids by their spectral type. He studied the spectra of approximately 600 asteroids, in the range between 300 nm and 1100 nm, obtained by ECAS (Eight-Color Asteroid Survey).

In this classification scheme, spectral types of asteroids are nominated by capital letters E, S, M, V, A, C, P, D and Z. Each spectral type has several linkages with a reflectance spectrum of a certain meteorite. This classification scheme tends to identify the asteroids from which different irons and stony-irons meteorites could have

been originated. This possible relationship between asteroids and irons and stony-irons meteorites will be discussed in chapter 4.

The distribution of different spectral types of asteroids is not uniform in the MAB. As an example, the abundance of the E-type asteroids decreases from 60% of all known asteroids at 1.8 AU to only 2% at 2.15 AU (Fig. 2.2). Most E-type asteroids tend to have high reflectance and relatively featureless spectra [50]. S-type asteroids are more abundant at 2.3 AU declining to 20% at 3.0 AU and reaching 0% at 3.25 AU (Fig. 2.2). The S-type asteroids have moderate albedo and are mainly composed by silicates (Fe and Mg) plus metal (Fe-Ni). This type of asteroids can represent the fusion crust of a differentiated body, in which they had experienced at least partial melting in their parent body [58]. By the analysis of S-type asteroids survey spectra, seven mineralogical subtypes of the S-taxonomy were reported: the silicate assemblages ranged from nearly monominerallic olivine (subtype S(I)) through basaltic silicates (subtype S(VII)). Only the subtype S(IV) did not require igneous processing to produce the observed assemblage [58]. C-types asteroids as well as P and D-types are the most abundant in the region between 3.0 and 5.0 AU and contain organic material such as kerogen [56]. They also contain chemically bound water, clay minerals (montmorillonite), organic polymers, magnetite and sulfides. C-type asteroids have low albedo and are mainly composed of hydrated silicates and carbon. This type of asteroids possibly has a similar composition to the solar nebula. P and D-types may also contain mixtures of various kinds of ices and other organic compounds. Only one meteorite was catalogued as being possibly linked to the D-type asteroids: Tagashi Lake meteorite, which fell on 16 of January of 2000 in British Columbia, Canada [59]. A-type asteroids are usually reported as having olivine-rich assemblages, as they only have a single absorption feature near 1.05 μm [60].

The SMASSII taxonomic classification was recently introduced by Schelte L. Bus and Richard P. Binzel, in 2002, based in SMASS (Small Main-Belt Asteroid Spectroscopic Survey) with 1447 asteroids. In their work, they obtained higher resolution spectra of asteroids comparing to ECAS. Despite their observations were only in the range between 440 nm and 920 nm, they were capable of distinguishing several particular characteristics. In order to conserve the taxonomic classification

proposed by Tholen, they catalogued 26 types of different asteroids [61]. For a comparison between these two classifications schemes, please see Table C2.

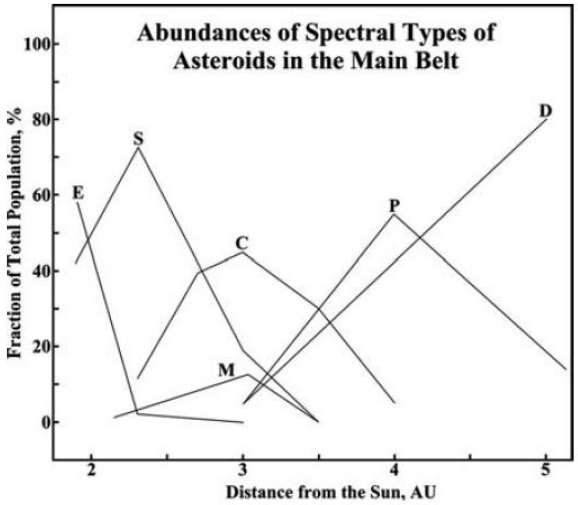


Fig.2.2 –The fraction of the total population of the different spectral types of asteroids in the MAB, varying with the distance from the Sun [62].

## 2.1.2. Orbits of Asteroids

Asteroids can also be classified based on their location within the Solar System and thus by their orbits (for further details, please check Table C3). Most asteroids orbit the Sun between 2.2 and 3.3 AU, which from the third Kepler's law corresponds to a revolution period between 3.3 to 6 years, in the so known MAB. The belt is divided in three regions taking into account the average distance (a) of asteroidal orbits: Inner Belt: $a$ < 2.5 AU; Middle Belt: 2.5 < $a$ <3.1 AU; Outer belt: 3.1 < $a$ <4.1 AU. However, asteroids can also be found close to the orbit of Jupiter (which are called Trojans), between Saturn and Uranus (which are called Centaurus) and close to Earth's orbit (also known by Near Earth Objects, also reported by the acronym NEOs).

In some regions of the MAB, some kind of gaps can be found (Fig.2.3). In 1866, Daniel Kirkwood explained these gaps for the first time to our knowledge as being a result of a resonance effect between the revolution periods of asteroids that occupied those regions and that of Jupiter. These gaps are also known as the Kirkwood gaps (Fig. 2.3). Several examples of these gaps can be counted in the MAB: the gap at 3.28 AU corresponds to a revolution period of 5.93 years, which is half of the Jupiter's period; the gap at 2.5 AU corresponds revolution period of 3.95 years, which is one

third of Jupiter's period. There are also two gaps corresponding to two-fifths and three-fifths of Jupiter's orbital period (resonance 3:1). These gaps can be explained by a simple fact: synchronous tugs from a large body on smaller particles gradually move those particles out of their orbits, like if it was "vanishing" and "cleaning" those regions. Actually a similar example to these gaps in the MAB is the Cassini division in Saturn's rings.

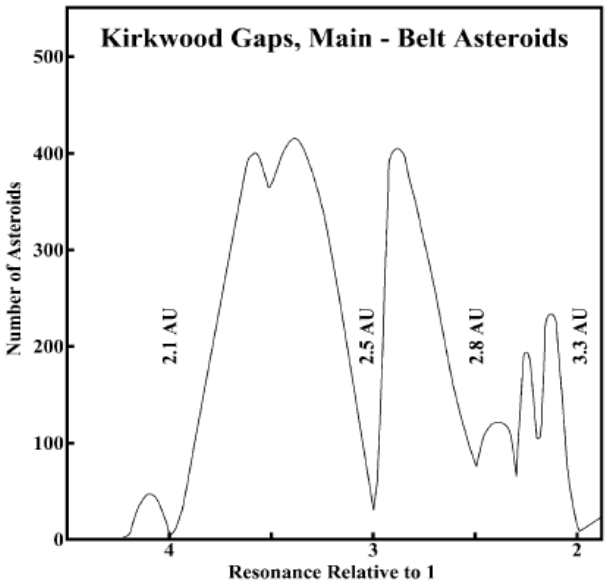


Fig.2.3 - Kirkwood gaps in the MAB [62].

The NEA's orbit the Sun in an orbit close to the Earth's one. This fact can be easily explained by the existing gaps (Fig. 2.3) in the MAB, where due to the resonance with Jupiter, these asteroids were completely pushed away from their initial orbits.

There are three known populations of NEA's: Aten, Apollo and Amores. The orbits of the asteroids from the Aten group lie inside Earth's orbits as their perihelion distance is less than 1 AU. Their diameters range from 0.2 up to 3.4 km and their reflectance spectra (C and S type) resembles to those of the stony meteorites [56]. 5604 1992 FE is one exemplar of an asteroid belonging to the Aten group, classified as a V-type asteroid. Asteroids from the Apollo group cross the Earth's and Mars orbit as their perihelion distance is less than 1 AU and their aphelion distance is greater than 1.52 AU. Their diameters range from 2 to 10 km and their reflectance spectra (S-type) link their compositions to the stony meteorites. Several asteroids, such as 1866

Sisyphus, 1685 Toro, 1864 Daedalus and 6611 (1993 VW) are exemplars of the Apollo group. The asteroids from the Amor group all have perihelion distances greater than 1 AU and aphelion distances exceeding the radius of Mars's orbit. Their diameters range from 6km up to 30km and their reflectance spectra (C and S-type) are similar to those of stony meteorites. 433 Eros, 1036 Ganymede, 3908 Nyx and 4055 Magellan are four exemplars of this group.

The Trojan asteroids are found near Jupiter's orbit, close to two points of Lagrange, oscillating around them. This group is named in allusion to the wooden horse which concealed Greek fighters. The association between the configuration of the magnetic field and the Lagrange points restricts the Trojan asteroids loosely to a comparatively small volume of space partly within and partly outside of the orbit of Jupiter. These types of asteroids contain organic matter which gives them a reddish color. The five largest Trojan asteroids are: 684 Hektor (150x300km), 911 Agamemnon (with a diameter maybe of 138km), 617 Patroclus (140km), 1437 Diomedes (possibly having a diameter of 130km) and 1172 Aeneas (125km). However, all the ten largest asteroids have diameters greater than 100km and are usually linked to the C, D and P spectral types [62].

The Centaurus asteroids are usually associated as the transition point between asteroids and the icy worlds of the Edgeworth-Kuiper belt. Their chemical compositions (spectral types C and D) are similar to those of carbonaceous chondrites but may also contain ices of volatile compounds [62].

### 2.1.3. 4 Vesta

The asteroid 4 Vesta was discovered by the German astronomer Heinrich Wilhelm Olbers in 1807 and was named 4 Vesta by the mathematician Carl Friedrich Gauss. It has an ellipsoidal shape (Fig.2.4) with an average radius of $(258 \pm 12)$ km [63] and a volume of $(7.19 \pm 0.87) \times 10^7 \mathrm{km}^3$. Its orbit has a semi-major axis of 2.362 AU, with an eccentricity of 0.089, and an inclination of 7.133$^o$. 4 Vesta has a rotation period of 5.3$^h$ and, as it turns, its reflectance spectrum appears to change, showing a heterogeneous surface. Its reflectance spectrum shows a strong band near 1000 nm, due to the presence of pyroxenes. However, its reflectance spectrum also shows

several diogenetic or even olivinic features, which are interpreted as 4 Vesta being a differentiated asteroid and also having several impact craters.

The surface of 4 Vesta shows regions with lava composed by basalt eucritic material. Its impact craters have excavated across the extrusive eucritic crust an intrusive plutonic layer or maybe a plutonic body of diogenitic composition. 4 Vesta also shows a dichotomous surface as the east hemisphere is mainly composed by pyroxene-rich in magnesium and pyroxene-poor in calcium (similar to diogenites[2]), while the west hemisphere is dominated by a pyroxene-rich in iron and calcium (similar to eucrites[2]). Also another feature which reinforces this dichotomy is: the east hemisphere is probably composed by excavated plutonic rocks (which were possibly originated due to a major impact), while the west hemisphere is possibly composed by some lava flows.

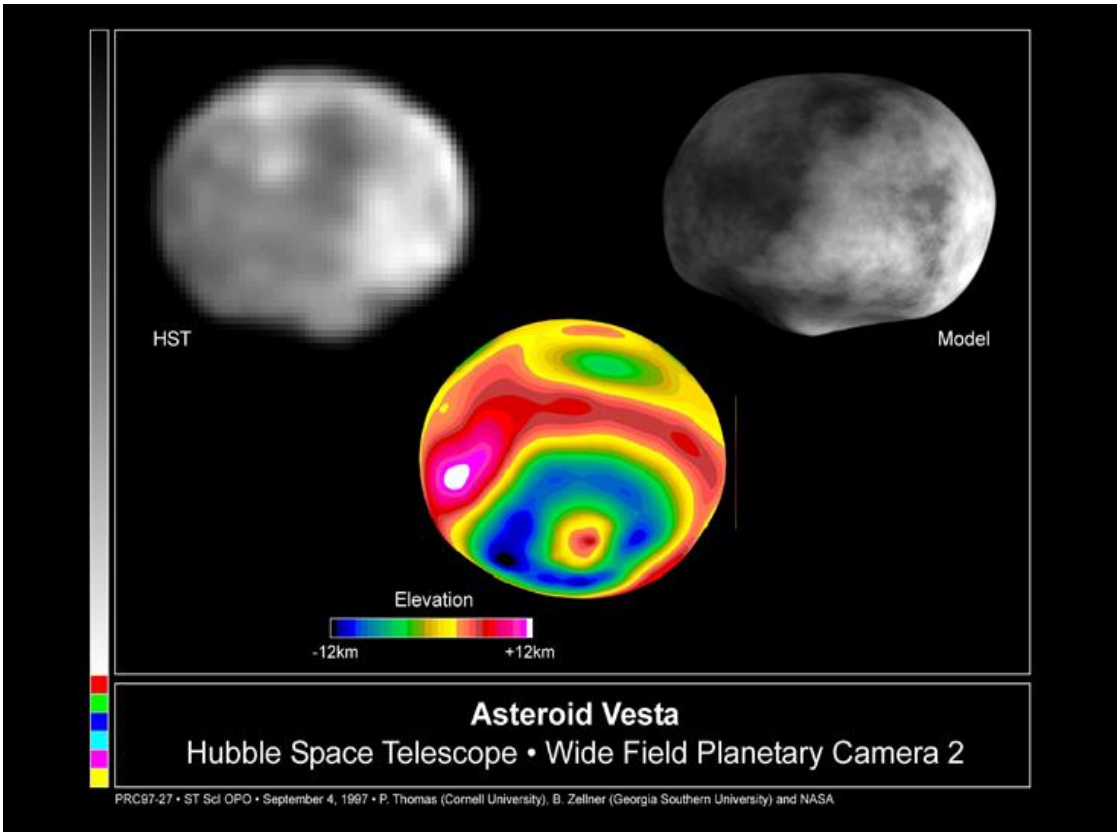


Fig.2.4 – Mapping 4 Vesta using several images captured by the Hubble Space Telescope (also known as HST). *Source:* Ben Zellner (Georgia Southern University), Peter Thomas (Cornell University) and NASA.

[2] A description about Howardites, Eucrites and Diogenites will be provided in the next chapter.

Images obtained by the HST showed a “huge” crater (Fig. 2.4) with a diameter of 460 km. This crater has a depth of around 8 km and a central peak with approximately 13 km of height. The color change rate of the crater indicates a possible transition from pyroxenes to olivines to pyroxene-rich in calcium with the topographic increasing depth of the crater [64].

According to the spectrum of 4 Vesta in the visible and IR, its surface exhibits several absorption features of Ca-low pyroxenes, which have a similar composition to eucrites [65]. It was also observed that its surface is composed by howardites. Another peculiar absorption feature centered in 506.5 nm, was observed in the 4 Vesta spectrum evidencing the presence of Ca-rich augite.

Recently, the Dawn Mission flew-by the surface of 4 Vesta. This mission belongs to NASA’s Discovery Program. Dawn’s goal is to characterize the conditions and processes of the infant Solar System, by investigating two of the largest asteroids in the MAB: 1 Ceres and 4 Vesta. In the latter case, it is aimed to verify the basaltic nature both inferred from its reflectance spectrum and from the howardites, eucrites and diogenites meteorites (which are believed to be originated from 4 Vesta). In a close future, several results about the data analysis of this mission may be found among the literature.

### 2.1.4. Families of Asteroids

Regarding the problem of the missing planet somewhere between Mars and Jupiter, a partial answer may have been finally found: during the formation of the Solar System, one or a few more planetary embryos suffered several collisions between them or bombardments that led to their fragmentation. Shock after shock, these bodies were probably reduced to a smaller size and volume. The collisional processes seem to play a very important role in the life of these small objects [66]. Actually, the so-called families of asteroids are the direct proof that these collisions really have occurred. It was first noted by Hirayama (1918) that asteroids can form prominent groupings in space of orbital elements.

Asteroid families are dynamical associations which are the individual fragments of the full or partial collisional breakup of a parent body. Such associations are properly designated by genetic families when the family members have compositions which are

consistent with derivation from a single parent body [67]. One way to identify these families is using the hierarchical clustering method (also reported in the literature as the acronym HCM) [68]. It was noted that clusters of objects appeared when the proper orbital elements are plotted in the *a-e* or *a-sin(i)* planes (where, *a* means the proper semi-major axis, *e* the eccentricity and *i* the inclination) [68]. The application of this method has been successful in identifying clumps of asteroids in the space of orbital elements: firstly, over 30 families were identified in a sample of 12487 asteroids [69]; more recently, around 50 statistically robust asteroid families were identified in a sample of around 106000 asteroids [70]. In Fig. 2.5, clumps of the Eos, Koronis and Themis families can be seen.

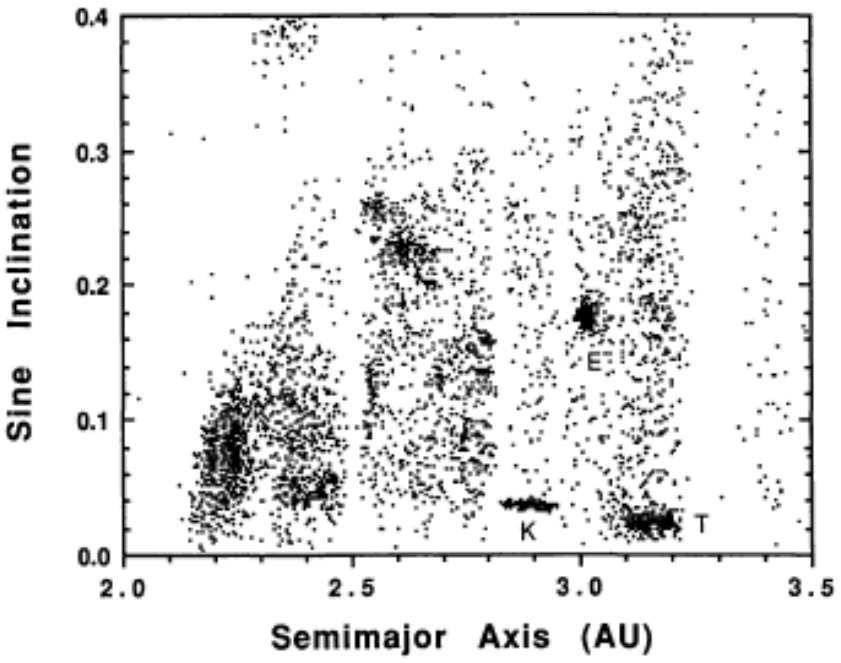


Fig.2.5 - Region of the MAB between 2AU and 3.5AU. The Eos, Koronis and Themis asteroid families are indicated by the letters E, K and T respectively. Other clumps can also be seen in this figure, which are probably additional possible families of asteroids [67].

The 4 Vesta family is one of the largest families in the inner asteroid belt. It is believed that this family was originated during a cratering event about 1 Gyr ago [71], which has excavated a basin on the surface of 4 Vesta. Nowadays, 4 Vesta family is assumed to have more than 5000 members, most of them having diameters less than 4 km (Fig 2.6) [72].

Many of the 4 Vesta family members (including 4 Vesta) show a V-type spectrum, which is characterized by a moderately steep red slope near 0.7 μm and a deep absorption band longwards of 0.75 μm. This kind of spectrum is linked with a basaltic surface composition [72].

The study of asteroid families is very useful to understand the processes that have occurred during the early ages of these small bodies. However, it is not easy to track families of asteroids and study its evolutionary behaviour. Contrarily to what was thought in the early 90s, asteroid proper elements can be significantly modified due to collisional evolution [73]. In particular, secular resonances seem to play an important role in this scenario. However, this task can be particularly fruitful when we can track and understand the evolution of several families of asteroids.

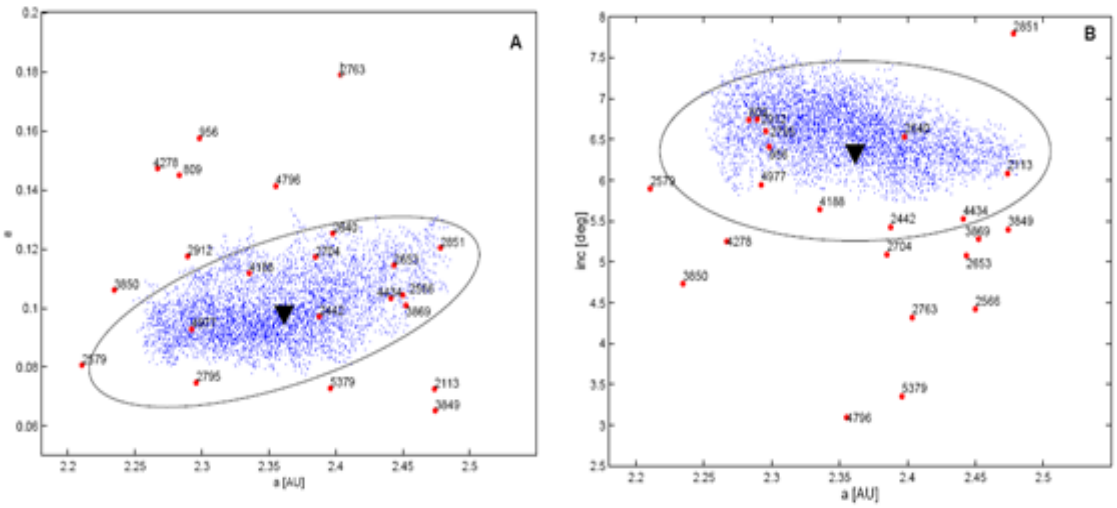


Fig.2.6 – Location of the 5112 4 Vesta family members in proper element space (Panel A: a-e plot; Panel B: a-i plot). The small blue dots represent the 5112 members of the 4 Vesta family and the red dots represent 22 V-type asteroids which are not members of the 4 Vesta family. The location of 4 Vesta is represented in both panels by the black triangle. The ellipse displays the 600m/s level of the maximum ejection velocity [72].

Families of asteroids can be used to understand:

1. the collisional history of the MAB [74];
2. collisional disruptions of large bodies (in the order of hundreds of km) [75];
3. the mineralogical structure of their parent bodies [76], as well as their thermal history and internal compositional structure [67].
4. the effects of related dust “showers” on the Earth [77];

U.PORTO
FACULDADE DE CIÊNCIAS
UNIVERSIDADE DO PORTO

## 2.2. Comets: "Dirty snowballs"

Comets are small bodies, with an irregular shape, mainly composed of water ice and small refractory dust particles. Since ancient times that comets were associated to mysticism and in some cases to the will of the gods. People regarded them with apprehension and fear. Across the centuries, there were many reports of comet events. Historically, a comet is named after the person who discovered it. Nowadays, the origin of comets provides a new area of research. Are comets linked with other planetary systems? Is there any possible linkage between comets and other bodies in the Solar System? Nowadays, these questions are still under debate.

### 2.2.1. Taxonomy of comets

When a comet approaches the Sun, the layer of water ice is heated by the solar radiation. Hence, the ice sublimates and then it is released forming a dusty atmosphere, which is called coma that surrounds the nucleus of the comet. The nucleus has a dimension of around 10km and is composed by a layer of icy water and frozen gases involving a rock. The gas and dust particles of the coma extend into a luminous tail, which is the most spectacular characteristic of a comet that can be seen with naked eye. As they can develop tails which resembles to a long hair streaming in the wind, they were called "hairy stars". In addition, the word "comet" in Greek means "long-haired" [78].

A comet has two distinct tails: the ion tail and the dust tail. The ion tails is bluish due to the emission of electromagnetic radiation by $CO^+$, $N_2^+$ and $CO_2^+$. The dust tail has a yellowish color as it reflects the sunlight. The radiation pressure exerted by the sunlight on the small particles tend to incurve the dusty tail, as it leads to reduce the orbital velocities of the particles causing them to lag behind the head of the comet. On the other hand, the ion tail is straight as the masses of the ions that are present on the ion tail are too small to suffer the gravitational action of the radiation pressure of the sunlight. In Fig. 2.7 (Left), the ion and dusty tails can be clearly seen [78].

Fig.2.7 - Left: Comet Hale-Bopp. Right: Comet Halley. Courtesy: NASA

## 2.2.2. Types of comets

Historically, comets can be divided into two classes by taking into account its revolution period P: long period comets (P>200 yrs) and the short period comets (P<200 yrs) [79]. But, this classification scheme denotes a huge disadvantage: in fact, how reliable can be the known orbital period of a long period comet? If we take as an example the comet Hale-Bopp, which is a long period comet (Fig.2.7, Left), its revolution period is of 2537 years (in Julian year)! The human average expectancy is not larger than 100 years. Hence, how can humankind have the perception of these time scales? In addition, if we go back 2000 years into the past, humankind have not had the technology that we can have nowadays to monitor and study these objects. Due to the technological advances, nowadays we can understand a bit better the small bodies in the Solar System, especially the long period comets as well as the Trans-Neptunian Objects (which will be described in the next section of this chapter).

To a first approximation, the orbit of a long period comet is established to be a parabola with an infinite period (Fig. 2.8). However, it is a challenging task to determine the orbital elements of these orbits, as a slight perturbation from a planet can turn a parabolic orbit into a long ellipse or a hyperbola. Actually, the question of such

hyperbolic orbits opens an interesting issue about the interstellar traffic: Can long period comets come from others stars in the Sun's neighborhood? The answer to this question is No! Until nowadays, no truly hyperbolic orbits have yet been detected [80]. In this scenario, the Edgeworth-Kuiper belt as well as the Oort cloud, have been postulated as being the sources of long period comets. It is important to emphasize that a description about these two structures will be given later on, in this chapter.

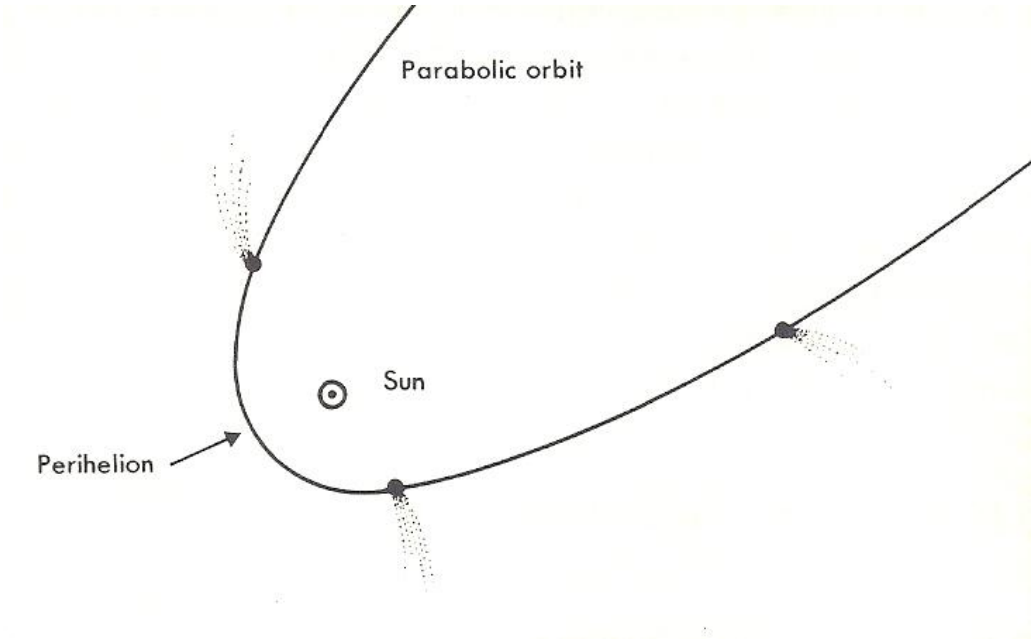


Fig.2.8 - Orbit of a long period comet [80].

Short-period comets are the result of a catastrophic perturbation by Jupiter (Fig. 2.9). Successive encounters between the comet and Jupiter tend to reduce orbital period of the comet to about 6 years and the comet will end moving within the orbit of Jupiter. This capture process originated a cluster of comets moving in the vicinity of Jupiter, forming the so called Jupiter family of comets (hereafter and also reported in the literature as the acronym JFCs). Comet Brooks is one exemplar of the JFCs. In 1886, this comet passed between the Jovian satellites and due to the gravitational influence of Jupiter, its period was reduced from 29 years to only 7.1 years. Usually a short-period orbit is like "the end of the road" for a comet. Repeated heating events by the Sun will make the comet to disintegrate and its orbit will be shortened consecutively by the effects of light pressure, the Poynting-Robertson effect [80].

As the majority of short-period comets belong to the JFCs, which have orbital period in average less than 8 years, they may have to be divided into two classes: the Jupiter-like comets with an orbital period less than 20 years [81]; and Halley-type comets, with an orbital period ranging between 20 and 200 years [82].

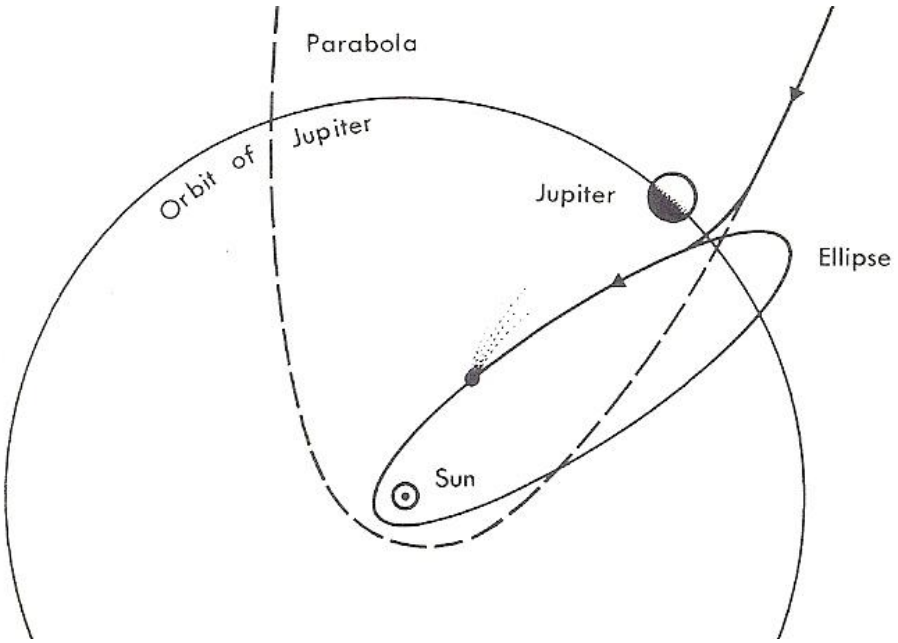


Fig.2.9 - Orbit of a short-period comet and a schematic illustration of the capture process [80].

Encke is an exemplar of the JFCs. Its period is surprisingly short: 3.3 years! This comet was discovered in 1786 and visited the Sun for the 55$^{th}$ time in 1964. Encke is a comet without a tail and the coma develops in warmth of sunlight. However, the quantity of gas and fine dust is considerably small when compared to other comets. The amount of gas and dust expelled by this comet when it passes the perihelion is considerable and it will certainly end its days due to this process [80].

### 2.2.2.1. A new classification scheme for the comets

As stated above, a classification scheme based only on the orbital period of comets alone is not very useful because the question is: How reliable can be the known orbital period of a long period comet, like the Hale-Bopp comet? Contrary to what was initially expressed [83] a classification scheme based only on the orbital period of a comet alone does not seem very useful. Hence, a new classification scheme based on certain orbital parameters of a comet was proposed [84]. Given the

perihelion q, aphelion Q and Tisserand parameter $T_P$, this new taxonomy provides an instantaneous classification for any comet-like body [84].

One way to think about comets is in terms of their Tisserand parameter, measured in relation to a certain planet. The Tisserand parameter is an approximation to the Jacobi constant (which is an exact integral of motion in the circular restricted three-body problem). The parameter is defined as:

$$T_J = \frac{a_j}{a} + 2\cos(i)\sqrt{\frac{a(1-e^2)}{a_j}} \tag{2.1}$$

where $a_j$ and $a$ are the semi-major axis of the planet and of the comet, respectively. Also $e$ and $i$ are the eccentricity and inclination of the comet's orbit. It is assumed that the inclination of Jupiter is $i = i_j = 0$.

This new classification scheme that was proposed divides comets with perihelion distances less than $\sim 4$ AU in order to include the Encke (E), short-period (SP), intermediate-period (I) and long-period (L) types [84]. The division is based on the aphelion distance (please see Table C4, for further details) and the sub-division takes into account the Tisserand parameter classes (please see Table C5, for further details), denoted by Roman-type subscripts.

SP-type comets are defined as having an aphelion distance Q ranging between 4 and 35 AU. This class includes Halley-type comets and several comets belonging to the JFCs. In order to distinguish them in the class it is used the Tisserand parameter. For example, a $SP_I$ comet is a short-period comet corresponding to a Halley-type, according to this convention.

E-type comets lie in an orbit which does not approach closer than a few Hill radii to Jupiter. The members of this class have orbital features close to the Encke's comet (Q~4.1 AU).

I-type comets have aphelia distances between 35 and 1000 AU. One exemplar of this class is the Hale-Bopp (Fig.2.7, Left), which is categorized as $I_I$ because its Tisserand parameter is 0.879.

The fourth and last class is the L-type comets. These comets have aphelion distances greater than 1000 AU. It is thought that the source of these type of comets if the Oort Cloud.

### 2.2.3. The Oort Cloud

In 1950, Jan Oort (1900-1992) noticed that the aphelion distances of several long-period comets extended to distances between 50000 and 100000 AU from the Sun [85]. He postulated that the Solar System is surrounded by a very large region of space containing a high number of objects that are bound to the Sun. The objects that belongs the Oort Cloud are composed by ices, such as water, ammonia and methane. Based on the isotropic distribution of the arrival of long-period comets, he hypnotized that this region is spherical. In honor to Jan Oort, this structure was named by *"The Oort Cloud"*. However, this region does not resemble to a cloud at all, as it is constrained by the low number of objects per unit of volume. It is thought that the objects of the Oort Cloud formed close to the Sun and then were ejected to their present location due to several gravitational interactions with the gaseous giants protoplanets.

It is estimated that the cloud contains $10^{11}$-$10^{12}$ objects [85-86]. This estimative is calculated by comparing the rate of arrival of new long period comets and the rate of erosion that is expected from external perturbations due to the combined action of passing stars allied with the torque from our own galaxy [87].

The Oort Cloud may be disturbed by the gravity of passing stars in the vicinity of the Sun. Also, it is speculated that the Sun has a dark massive planet or companion called *Nemesis* [88], which can periodically disturb the orbits of several objects in the Oort Cloud.

## 2.3. Trans-Neptunian Objects: The Outer Limit

The existence of a large number of icy objects orbiting beyond Neptune was firstly postulated by the Irish astronomer Kenneth Edgeworth and by the American astronomer Gerard Kuiper (1951). Their predictions were only confirmed in 1992, when the first Trans-Neptunian Object (1992 QB1) was discovered at a distance of 44 AU from the Sun. Until today, the number of known Trans-Neptunian Objects has not

stopped to increase. Trans-Neptunian Objects (hereafter TNOs), also known as Edgeworth Kuiper Belt (hereafter, EKB) objects, represent a population of small icy bodies orbiting beyond Neptune [89]. It is believed that these objects represent the most pristine and thermally unprocessed objects of the Solar System [90]. Their diameter varies from less than 1 km to more than 1000 kms. However, their sizes and shapes may be continuously being modified by collisional processes. It is quoted that the TNOs can provide a significant portion of NEAs [91-92]. TNOs reside in the so known Edgeworth Kuiper Belt (E-K Belt), as well as some of the Solar System dwarf planets: Pluto, Eris, Sedna, Quaoar, Ixion and Varuna.

TNOs can be divided dynamically in several classes: Classical, Resonants, Scattered and Extended scattering disk objects (Fig.2.10) [90]. Classical objects are characterized by having orbits with low inclination and eccentricities ($e \lesssim 0.2$). Also its semi-major axis lies between 42 and 48 AU, so they are dynamically stable in timescales of Gyr as they approach to Neptune. Resonant objects are trapped in resonances with Neptune. They are usually found near the 3:2 mean motion resonance. The most famous resonant TNO is 134430 Pluto. Scattered objects are characterized by having a high inclination as well as high eccentricities ($e \sim 0.5$, please see Fig. 2.12). Their perihelion distance is found near 35 AU and numerical simulations showed that their orbits are unstable on Gyr timescales due to perihelion interactions with Neptune. The Extended scattering disk objects are located out of interacting gravitational encounters with Neptune. These are the most intriguing TNOs objects: their orbits suggest the existence of another force or perturbation by an unknown planet (Nemesis?), by a passing star or by several resonant effects, which lifted their perihelion to the outer planetary domain. In Fig. 2.12 the Centaurus population is also represented. As it was explained above in the first section of this chapter, Centaurus are found in orbits between Jupiter and Neptune and they are probably ejected objects from the E-K belt or the MAB. As they strongly interact with the giant planets, their lifetime is short: in average ~10 Myr [93].

The total mass of the TNOs can be estimated based on their observed size distribution and by assuming that their bulk composition is 1.0 $g.cm^{-3}$. Hence, the resulting total mass of TNOs is around 0.30 $M_{Earth}$ [89].

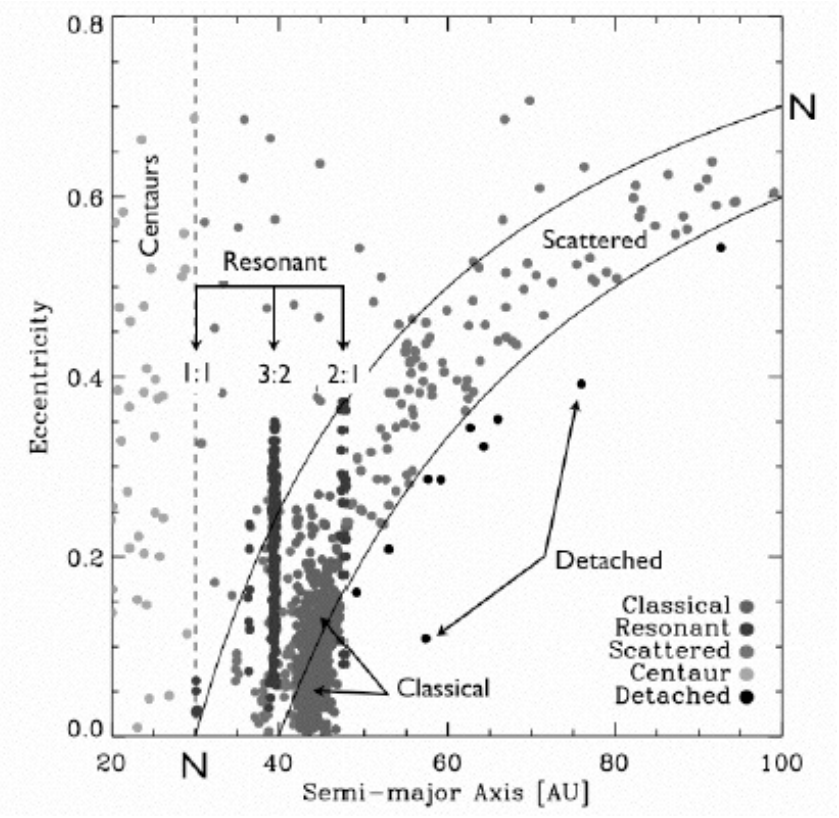


Fig.2.10 – Semi-major axis vs orbital eccentricity for the Outer Solar System. The dynamical subtypes of TNOs are marked on the plot. Only three dynamical resonances with Neptune are indicated. The curve NN represents the semi-major axis of the orbit of Neptune, while the lower curve found at 40 AU represents the locus of orbits with q=40 AU. Centaurus population are also represented in this plot [50].

The colors of TNOs vary from grey to different tonalities of brown or red, depending on the deposits that cover their surface. TNOs are mainly composed by mixtures of water ice and refractory particles with admixtures of frozen methane, ammonia and oxides of carbon [89].

The state of knowledge about TNOs is nowadays in a lower level respecting to the MAB. However, it is hoped that in the future more and more questions will come: *"this is the main rule of the game of knowledge."* [94].

U.PORTO
FACULDADE DE CIÊNCIAS
UNIVERSIDADE DO PORTO

# 3. Meteorites

*"All known meteorites are fragments of either asteroids, the Moon, or Mars, with the former dominating. They display a large diversity of texture and mineralogy. Most are ancient, dating from the first 10 million years of the solar system formation. They trace key stages of its evolution, such as the composition of the initial interstellar medium, the early stages of the Sun's protostellar collapse, disk formation, dust condensation and coagulation, thermal processing, and planetesimal and planet formation."*

in Perryman, M. (2011), *The Origin of the Solar System*, arXiv:1111.1286

Meteorites provide us important tools to understand the evolutive processes that occurred during the infant solar system. In particular, they enable us to understand the chemical, physical and mineralogical properties of the near-earth objects (NEOs) as well as objects in the asteroid belt [95-97].

Solid bodies with extraterrestrial origin that penetrate and reach Earth's surface are called meteorites. It is important to clearly distinguish between a *fall* and a *find* of a meteorite: meteorites are considered falls if they can be associated with an observed fall event and find if it cannot be associated with a recorded fall event. A meteorite is a fragment of an asteroid or a comet that can have different sizes and shapes. . Several perturbations in the orbit of an asteroid, due to the gravitational influence of Jupiter, can make the asteroid go through the inner regions of the Solar System and cross Earth's orbit. As an evidence of this fact are the cases of the 4 Vesta fragments.

Meteorites are named taking into account the location where they were recovered. As an example, the Allende meteorite fell in Allende (Mexico). The number of known meteorites is currently growing up through the discovery of new samples in the hot [98] and cold deserts [99]. As numerous samples are found in the same location, these meteorites are given names and numbers. The increasing number of meteorite finds, allied with the beginning of the use of charge-coupled device (CCD) detectors to obtain the visible and NIR reflectance spectra of small objects, enables us to understand the diversity of asteroid mineralogies.

U.PORTO
FACULDADE DE CIÊNCIAS
UNIVERSIDADE DO PORTO

This chapter will mainly provide a description about the classification of meteorites. In addition, a final section describing the chronology of events in the early Solar System and their relation with meteorites will be presented.

**Keywords:** meteorites; chondrites; nonchondrites; textures; primitive achondrites; differentiated achondrites; carbonaceous chondites; ordinary chondrites; enstatite chondrites; stony-irons; irons; clan; grouplet; chondrules; oxidation state; breccias; refractory inclusions; CAIs; AOAs; thermal metamorphism; HED's; Howardites; Diogenites; Eucrites;

## 3.1. Classification of meteorites

In the 1860s, G. Rose drew the first lines of the picture of the current classification scheme of meteorites. Rose was the first to split stones into chondrites and nonchondrites. Nowadays, based on the bulk composition and textures, meteorites can be separated into two major categories: chodrintes and nonchondrites meteorites. The latter contain the primitive achondrites and the differentiated meteorites. The main goal of a scheme classification is to divide meteorites into classes that seem to share the same origin or formation history. Indeed, it can reveal possible genetic linkages between meteorites of the same class. The chondrites and nonchondrites meteorites are classified in classes, such as: carbonaceous, ordinary, enstatite, R, achondrites, stony-iron and irons. These classes of meteorites are also divided in groups, as for example the enstatite chondrites are divided into two groups: EH and EL. For a more detailed review of the basis of this classification scheme, please see Table C6. Also for a detailed review of the meteorite groups and the number of their registered falls or finds, please see Tables C7 and C9.

### 3.1.1. Chondrite Meteorites

Chondrites are the oldest rocks known in the Solar System, providing the best clues about the physical and chemical processes which have occurred during the infant solar nebula. The term chondrite comes from the greek word for seed, referencing the ameboid olivine aggregates (also reported as the acronym AOAs) and Ca-Al rich inclusions (also reported as the acronym CAIs), which will be explained later on. Chondrites have formed about 4.6 Myr ago and their abundances of nonvolatile elements are close to those in the solar photosphere.

Chondrites are mainly composed of four major components: chondrules, FeNi-metal, refractory inclusions (which can be CAIs or AOAs) and some fine grained size material. It is commonly accepted that the refractory inclusions, chondrules as well as the FeNi-metal were formed in the solar nebula due to condensation and evaporation processes that have occurred at high temperatures. Several CAIs, FeNi-metal and chondrules were subsequently melted during some heating processes. However, some CAIs and metals in some chondrites appear to have escaped these high temperatures in the solar nebula.

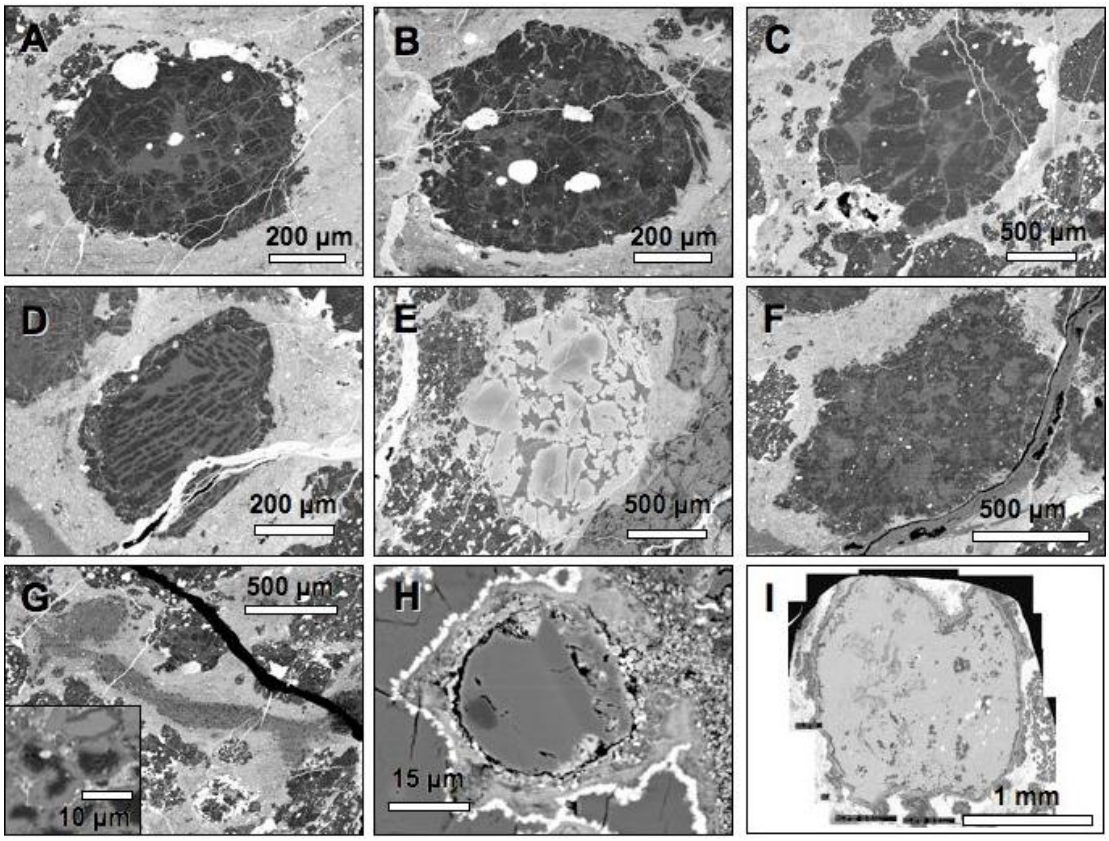


Fig.3.1 - Scanning electron micrographs of chondrules and CAIs. A. Porphyritic Olivine type I chondrule. B. Porphyritic Olivine Pyroxene type I chondrule. C. Porphyritic Pyroxene type I chondrule. D. Barred Olivine type I chondrule. E. Porphyritic Olivine type II chondrule. F. Amoeboid Olivine Aggregate. G. Fine-grained CAI with nodular texture shown in the insert. H. Hibonite-glass CAI spherule. I. Coarse-grained ultra-refractory igneous CAI E101,1, All objects are from the Efremovka carbonaceous chondrite, except H from the Murchison carbonaceous chondrite [107].

Chondrules are 100 µm to 10 mm spherules of once melted silicates. They are mainly composed by ferromagnesian olivine and pyroxene minerals embedded in a Ca-Al-rich glassy mesostatis of close-to-feldspathic compositions. Based on their textural

and chemical properties, different groups of chondrules are pointed out (Fig.3.1). There are two major groups of chondrules: type-I chondrules showing the presence of reduced iron as sulfides, magnesian olivine or pyroxene; type II chondrules containing oxidized Fe entering the structure with silicates.

Chondrites are divided into five classes that share similar mineralogy, petrography, isotopic properties and chemical composition; carbonaceous chondrites, ordinary chondrites and enstatite chondrites. Some chondrites are also classified into two additional groups: the R and K groups. The R group (also known as Rumuruti-like) and K group (also known as Kakangari-like) are quite different from the other chondrites, suggesting that they represent two additional groups. The K chondrites are a small group as only two meteorites are catalogued. This group is also designated as a grouplet. Indeed, the three major classes of chondrites are the carbonaceous class (hereafter, also reported as C-class), the ordinary class (hereafter, also reported as O-class) and the enstatite class (hereafter, also reported as E-class).

These major classes also contain several groups. In the C-class there are eight groups: CI (also known as Ivuna-like), CM (also known as Mighei-like), CO (also known as Ornans-like), CR (also known as Renazzo-like), CH (also known as ALH85085-like), CB (also known as Bencubbin-like), CV (also known as Vigarano-like) and CK (also known as Karoonda-like). The letters designating the group are usually associated with a particular chondrite. The only exception is the CH group, where the “H” refers to high metal abundance and high iron concentration [101]. The O-class is divided in three groups: H, L and LL. The letters designating these groups refer the bulk content of iron: the H group possesses a high content of iron; the L group possesses a low content of iron; the LL group has a low content of metallic iron compared to the total iron bulk content, as well as a total low bulk content of iron. The E-class is divided into two groups: EH and EL. These two groups have different metallic iron bulk content. But, there is a meteorite that is classified as an enstatite which is not catalogued in one of these groups: LEW87223 [102]. Several groups of the chondritic meteorites have similar chemical, mineralogical and isotopical properties, which constitute “clans”. As an example, the H, L and LL groups are chemically and isotopically similar, so these three groups form a clan. Four other clans are also reported: EH-EL clan, CM-CO clan, CV-CK clan and CR-CH-CB clan.

U.PORTO
FACULDADE DE CIÊNCIAS
UNIVERSIDADE DO PORTO

### 3.1.1.1. Oxidation state and bulk oxygen isotopic compositions

Chondrites show a wide range of oxidation states that were almost certainly due to both combined asteroidal and nebular processes [103-104]. The oxidation state is characterized taking into account the distribution of iron along with its three usual oxidation states: 0 (FeNi-metal and Fe-sulfides), 2 (silicates) and 3 (oxides). The oxidation state of the chondrites increases as follows: E-class, O-class, C-class+R. The K group is in the intermediate position between the E and O classes.

In the C-class, the oxidation state increases as follows: CB-CH-CR-CO-CV-CK-CM-CI. In the E-class the oxidation state increases from H to L to LL as denoted in the ratio $\frac{\mathrm{Fe}}{\mathrm{Fe+Mg}}$ of their olivine and pyroxene.

Oxygen has three stable isotopes synthesized in stars: $^{16}O$, $^{17}O$ and $^{18}O$. $^{16}O$ is formed during the fusion of four He nuclei during its burning in supernovae. But, $^{17}O$ and $^{18}O$ are secondary isotopes which are formed from $^{16}O$ and $^{14}N$, respectively. Oxygen isotope abundances in meteorites can help us to understand several physical and chemical processes occurred during the formation of our Solar System. Average values for $\delta^{17}O$[3] can be found in Table C8.

### 3.1.1.2. Petrologic type

Chondritic meteorites are also classified in petrologic types [105]. This classification scheme yields a guide to the degree of thermal and aqueous alteration suffered by the chondrite. They are divided into six petrologic or petrographic types: type 1 represents the higher degree of aqueous alteration in relation to the type 2; type 3 is the less modified by secondary processes; the sequence from type 3 to 6 denotes an increasing degree of chemical equilibrium. In the C-class: CI are classified as being of petrologic type 1; CM are classified as being of petrologic type 1 or 2, however most of CM chondrites are petrologic type 2 with fully hydrated matrices and variably altered chondrules, CAIs, etc; both CO and CV are classified as petrologic types 3 or 4; both CB and CH are classified as petrologic type 3; CR are classified as being of petrologic type 1 or 2, but the majority of them are classified as type 2. All the others (meaning

[3] The conventional way to express the variations in abundances of isotopes in terms of isotopic ratios, in relation to an arbitrary standard called SMOW (standard mean ocean water), is as follows: $\delta^{17}O = \left[\frac{(^{17}O/^{16}O)_{\mathrm{sample}}}{(^{17}O/^{16}O)_{\mathrm{SMOW}}} - 1\right] \times 1{,}000$.

the CK, L, LL, H, EH, EL and R), exception made of the K group which is classified as petrologic type 3, are classified as being of petrologic types between 3 to 6.

### 3.1.1.3. Refractory inclusions

Refractory inclusions are the oldest objects in our Solar System, with a Pb isotope age of 4.567 Gyr [106]. There are three roughly families of refractory inclusions: coarse-grained Ca-Al-rich inclusions; fine-grained Ca-Al-rich inclusions; amoeboid olivine aggregates.

Calcium-aluminum rich inclusions (also reported in the literature as CAIs) are submillimiter to the centimeter sized clasts presented in chondritic meteorites (Fig.3.1). Their mineralogy is usually described as a “primary” and “secondary”. The term “primary” reports to a phase when the inclusions were formed by direct condensation melt solidification or solid-state recrystallization. The term “secondary” is used for any phase that texturally seems to be replacing another phase. Several minerals are present in the CAIs: corundum, hibonite, grossite, perovskite, melilite, spinel, Al-Ti-diopside, anorthite and forsterite. The coarse-grained family of CAIs has magmatic textures and crystal sizes ranging from roughly 10 μm to 1 mm, whereas the fine-grained family of CAIs consists of aggregates of 20-50 μm nodules [107]. The magmatic texture presented in the coarse-grained CAIs is indicative of crystallization from a melt process.

AOAs are irregular shaped objects, which have fine grain sizes (tipically 5-20 μm) [107] that reside in a few percent of type 2-3 carbonaceous chondrites. They do not appear to show mineralogical and isotopic differences among groups.

### 3.2.1.4. Thermal metamorphism

Thermal metamorphism affected most of the chondritic classes and plays an important role in the classification scheme developed for chondrites. It is known that thermal metamorphism modified substantially the characteristics of the chondrite meteorites and in particular it changed textural integration and recrystallization, mineral equilibrium, destruction of primary minerals, and growth of secondary minerals [108]. Several heat sources have been proposed to be the cause of thermal metamorphism,

such as: accretional or collisional heating; radioactive decays ($^{26}$Al and $^{60}$Fe); or, electromagnetic induction.

### 3.2.1.5. Properties of the Chondrites meteorites

In this section, the mineralogical and geochemical compositions of the chondrites meteorites classes will be described. For a summarized review of chondrites compositions and some genetic linkages between groups, please see Table C8. Carbonaceous chondrites are characterized by whole-chondrite refractory-litophile elements abundances (Fig.3.2).

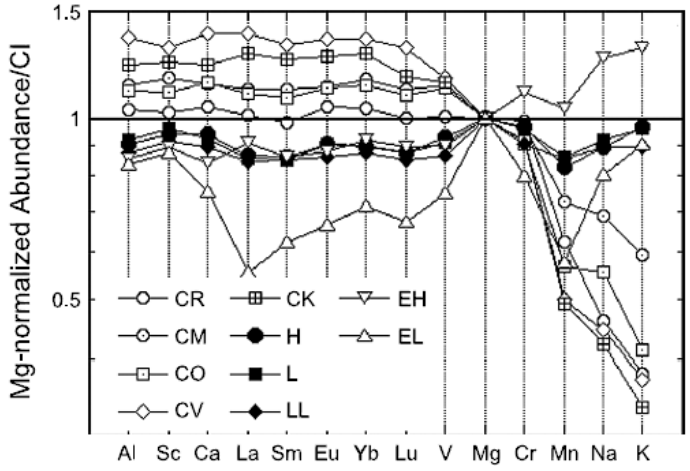


Fig.3.2 - Average whole-chondrite lithopile-element abundances in several chondrite groups [109].

CI chondrites are the most compositionally primitive rocks in the Solar System, having bulk composition close to that of the solar photosphere. This group has long been cited as the most classical example of asteroidal aqueous alteration as they contain minerals like phyllosilicates, sulfates and hydroxides. They have experienced extensive brecciation on their asteroidal parent bodies that have originated mixing of compositionally distinct lithic clasts on the sub-mm and mm scale [109].

CM chondrites are a complex group of meteorites that have experienced aqueous alteration and brecciation [110-112]. A detailed discussion is currently undergoing as the major controversies of the CM chondrites are the relationship between aqueous alteration and brecciation as well as the local and timing when aqueous alteration has occurred [110-112]. Despite it has been argued by some

authors that the aqueous alteration occurred in their parent body environment [111], it is proposed that CM chondrites may have experienced some kind of preaccretionary alteration in the solar nebula [112].

CM chondrites have bulk and oxygen isotopic [113] compositions different from the others C-class chondrites. They have a clastic texture, which is actually a peculiar characteristic of many CM chondrites, due to the brecciation occurred in their parent body caused by the fragmentation of their primary texture. They also have relatively small chondrules ($\sim 300$ μm).

*C*O chondrites have experienced limited aqueous alteration through an event of low temperature. But, it is argued that this kind of meteorites may also have experienced aqueous alteration allied with metamorphism [114]. The CO chondrites include several typical features, such as abundant small and rounded chondrules ($\sim$150 μm) [115] or secondary altered minerals in chondrules and CAIs which are similar to those on the CV chondrites (like, as an example, ferrous olivine or nepheline) [116]. As stated above, the CM and CO chondrites belong to the same clan. In order to link these two classes of meteorites, three characteristics were taken into account: chondrules are similar in size and anhydrous minerals have similar compositions; refractory-litophile element abundances are similar; O-isotopic composition of high-temperature minerals is similar.

CR chondrites (Fig.3.3) are reported to be the most primitive meteorites [117] as evidenced by its large range with a positive Ni vs Co trend and its solar Ni/Co ratio. They have experienced little or no thermal metamorphism, but they show variable degrees of aqueous alteration as it is evidenced by the variation in the extent of alteration of chondrules mesostasis. Usually CR chondrites contain abundant phyllosilicates, carbonates, magnetite and sulfides [118]. However, this group of meteorites has low abundance of CAIs and AOAs.

CB chondrites are metal-rich chondritic meteorites that are notoriously distinguished from the others groups by their particular characteristics [117]: very high metal abundances; almost exclusively barred textures of chondrules; large depletion in moderately-volatile litophile elements; large enrichement in heavy N. This group includes the following meteorites: Bencubbin, Gujba, Weatherford, Hammadah al

Hamra (HH) 237, and Queen Alexandra Range (QUE) 94411 which is paired with QUE94627 [119].

CB chondrites have been divided into two subgroups due to the petrologic and chemical differences among CB chondrites: $CB_a$ which includes Bencubbin, Weatherford and Gujba; $CB_b$ which includes HH237 and QUE94411 [119]. This division among this group is based on FeNi-metal abundances, CAI abundances, chondrules sizes and nitrogen isotopic compositions.

CH chondrites (Fig.3.3) are characterizes by small chondrules (<50-100 μm) and CAI sizes (as for example the average diameter of 90 μm in Acfer 182), abundant chondrules, large depletions of some refractory and volatile elements and abundant occurrence of silica minerals [120].

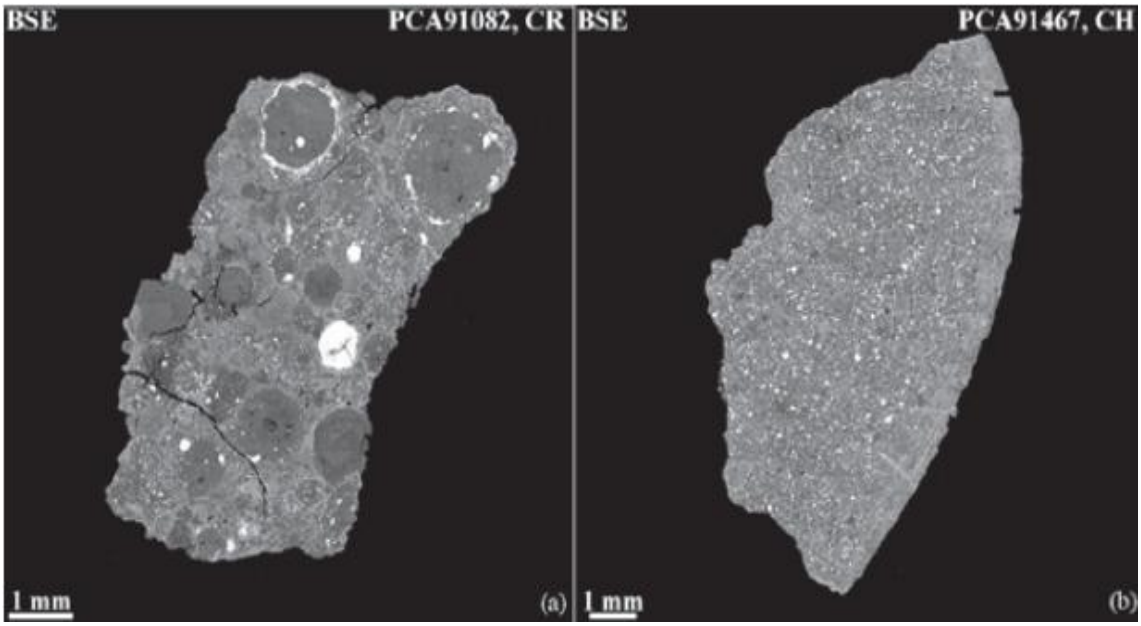


Fig.3.3 - Backscattered electron images of: (a) CR chondrite PCA91082; (b) CH chondrite PCA91467 [121].

CV chondrites (Fig.3.4) are usually considered rocks characterized by condensates formed in the nebula. The high abundance of CAIs and AOAs as well as chondrules and grains of magnesian silicates are similar to those predicted by the equilibrium condensation models. Hence, these components are thought to be primitive nebular condensates. Several secondary minerals are present in the CV group, as for example ferrous olivine, pyroxenes, magnetite, Ni-rich metal or FeNi-sulfides. The CV chondrites were firstly divided into two subgroups: oxidized ($CV_{OX}$) and reduced ($CV_{red}$).

Subsequently, they were subdivided into three subgroups which experienced different styles of alteration: oxidized Bali-like ($CVO_{xB}$), oxidized Allende-like ($CVO_{xA}$), and reduced ($CV_R$) [122].

Fig.3.4 - Chondrules of Allende Meteorite. This meteorite is classified as being a CV chondrite meteorite. *Source:* Wikipedia.

CK chondrites are highly oxidized meteorites that have abundant magnetite, high nickel content in sulfides and trace amounts of FeNi-metal [123]. CAIs and AOAs are rare in this group of the C-class. They contain a large abundance of matrix and large chondrules (700-1000 μm).

Ordinary chondrites (Fig.3.5) may have important clues about the origin and formation of our Solar System. They are originated in the inner asteroid belt and comprise the majority (around 85%) of the known meteorites [124]. They are distinguished from each other by the differences in bulk chemical and isotopic composition, chondrules size as well as by the oxidation state [125]. They are characterized by: high abundance of FeO-rich chondrules being frequent while the aluminum-rich chondrules are rare; CAIs and AOAs are rare or even absent; a large range in the degree of metamorphism (varying from petrologic type 3 to 6). H, L and LL chondrites differ in the amount of total iron, of iron metal and iron oxide in the silicates. Their siderophile element abundances decreases and the oxidation state increases as

follows: H-L-LL. In addition, H chondrites have Highest total iron and metal content, L chondrites have Lower total iron and metal content and LL chondrites have Low total iron and Low metal.

Fig.3.5 - Ordinary chondrite *NWA 869*. *Source:* Wikipedia.

Enstatite chondrites are highly reduced meteorites denoting a high presence of enstatite, contrarily to the olivine which is depleted or completely absent. They are divided into two groups based on the iron content: Fe-rich EH and the Fe-poor EL [126]. Enstatite meteorites show a unique mineralogy (e.g. oldhamite (CaS), osbornite (TiN), pyrite ($(Ni,Fe)_x(Si,P)$), etc.) suggestive of a very reduced environment where they were formed [127]. They are also characterized by the rarity of CAIs, contrarily to the abundance of chondrules.

## 3.2.2. Nonchondrite Meteorites

Nonchondrite meteorites were formed from chondritic materials by several processes such as planetary melting or fractionation that caused their bulk compositions to differ in different degrees from chondritic materials. Since the melting degree that these meteorites suffered is highly variable, they are usually divided into two types: primitive achondrites and differentiated. The nonchondrite meteorites can be divided into three groups: achondrites, stony-irons and irons. The achondrites group is currently divided into two broad categories: primitive achondrites, which include the acapulcoites, the londranites and the winonaites; differentiated achondrites, which include the angrites, aubites, brachinites, ureilites, HED, Martian and Lunar. The stony-

irons type includes the mesosiderites and pallasites groups. The irons type includes the IAB, IC, IIAB, IIC, IID, IIE, IIIAB, IIICD, IIIE, IIIF, IVA and IVB groups.

The differentiated achondrites show igneous textures and sometimes these were modified by impact or thermal metamorphism. These textures also have highly fractioned lithophile, siderophile, chalciophile and atmophile elements. The primitive achondrites show metamorphic textures, possibly modified by impacts. This nomenculature “primitive achondrite” was introduced with the goal of distinguish members which have bulk chondritic composition but achondritic texture formed due to low degrees of melting [128]. They have siderophile, chalciophile and atmophile elements in their composition, which are moderately fractioned. For a summarized review of achondrites compositions and some genetic linkages between groups, please see Table C8.

Three clans were recognized among achondrites: the acapulcoite-londranite clan, the winonaite-IAB iron silicate inclusion clan and the brachinites.

### 3.2.2.1. Primitive Achondrites

As described above, the primitive achondrites type can be divided into three groups: acapulcoites, londranites [129-130] and winonaites.


Fig.3.6 - Photomicrographs in transmitted light with partially crossed nicols. Left: Londranite LEW88280, where orthopyroxene (opx) and olivine (ol) are marked. Right: Silicate inclusion in the IAB iron Campo del Cielo [121].

Acapulcoites and londranites (Fig.3.6) have approximately chondritic bulk compositions, recrystallized textures, chondritic mineralogy and planetary-type rare gases. They are mainly composed of orthopyroxene, olivine, Cr-diopside, Na-plagioclase, FeNi-metal, schreibersite, troilite, whitlockite, Cl-apatite, chromite and graphite [131]. Acapulcoites differ from londranites in several characteristics, such as: small grain sizes, abundant Fe, Ni-FeS as μm-sized veins and plagioclase that have escaped from partial melting. Usually, acapulcoites are fine-grained size (150-230 μm) with more or less chondritic abundances of olivine, pyroxene, plagioclase, metal and troilite. On the other hand, londranites are coarse grained (540-700 μm) and are also characterized by the depletion in troilite and plagioclase [132].

Winonaites have approximately chondritic mineralogy and chemical composition. They can contain mm-to-cm sized regions with different textures and/or mineralogies. These regions include plagioclase, diopside-rich, coarse grained olivine-rich areas and/or calcic pyroxenes [133]. On the other hand, they also exhibit recrystallized textures and reduced mineral chemistries. Winonaites have experienced partial melting and show evidence for brecciation and metamorphism on the precursor body. It is known that winonaites are linked to the IAB irons (Fig.3.6) by the oxygen isotopic and mineral composition, as it was reported above about the winonaite-IAB iron silicate inclusion clan [134]. They may also be related to the IIICD irons [135].

### 3.2.2.2. Differentiated Achondrites

Differentiated achondrites are divided into seven subgroups, where the HED seem to be the most interesting group as there is strong evidence that they originated in the same parent body (a detailed discussion about this topic can be found in the next chapter). The others six reported groups are: angrites, aubites, brachinites, ureilites, Martian (SNC) and Lunar meteorites.

Angrites are in between the oldest differentiated achondrites and are crucial references for Solar System chronology [134]. They are medium to coarse-grained (up to 2-3 mm) igneous rocks, usually associated with a basaltic composition. Their composition mainly consists of Ca-Al-Ti-rich, pyroxene, calcium-rich olivine, anorthite and plagioclase [132]. Oxygen isotopic compositions of angrites are similar to those of HED meteorites, brachinites and mesosiderites.

Aubites typically are highly reduced enstatite pyroxenites. Almost all aubites are fragmental, except in some cases that are regolith breccias as it is evidenced by their high contents of noble gases implanted by the solar wind [136]. Their compositions mainly consist of FeO-free enstatite, but it also contains plagioclase, FeO-free diopside and forsterite. Aubites have close affinities with the E-class of chondrites and are sometimes referred to as enstatite achondrites.

Brachinites (Fig.3.7) are essentially made of olivine (typically 74-98%). However, others minerals can also be found: augite (4-15%), plagioclase (0-10%), some traces of orthopyroxene, chromite (0.5-2%), Fe-sulfides (3-7%), few amount of phosphate and FeNi-metal. The differences in petrology and geochemical compositions among the different brachinites propose that they possibly were not formed by the same process [132].

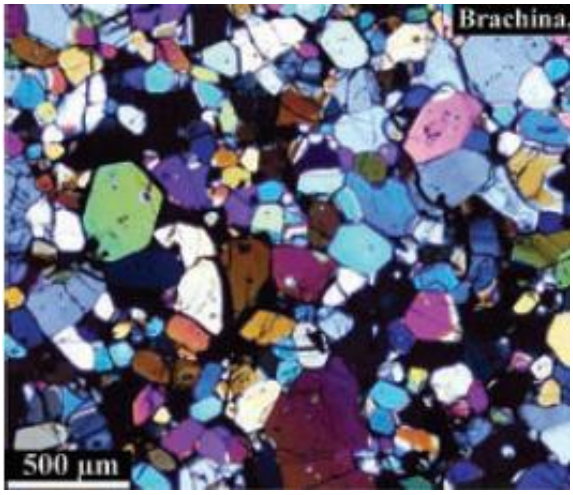


Fig.3.7 - Photomicrograph of a brachinite in transmitted light with partially crossed nicols: Brachina [121].

Ureilites are mainly composed by olivine, pyroxene and <10% dark interstitial material such as carbon, metal sulfides and minor fine-grained silicates [132]. Several characteristics differentiate ureilites from the other differentiated achondrites: high content of CaO in olivine and pigeonite; high $Cr_2O_3$ contents in olivine; high carbon contents; and a large range in oxygen isotopic compositions.

The martian meteorites is also know by the acronym SNC, which means S for Shergottites, N for Nakhlites and C for Chassigny. They are volcanic or subvolcanic rocks. Due to their highly fractionated compositions and young crystallization ages

(possibly 180 Myr), it seem that they are derived from a planet-size body. They were linked to Mars, as several similarities between the isotopic composition of nitrogen and noble gases of the martian atmosphere and the one's found in some shegorttites were reported.

### 3.2.2.3. HED's

The letters from the acronym HED refers to the Howardites, Eucrites and Diogenites, respectively (Fig.3.8).

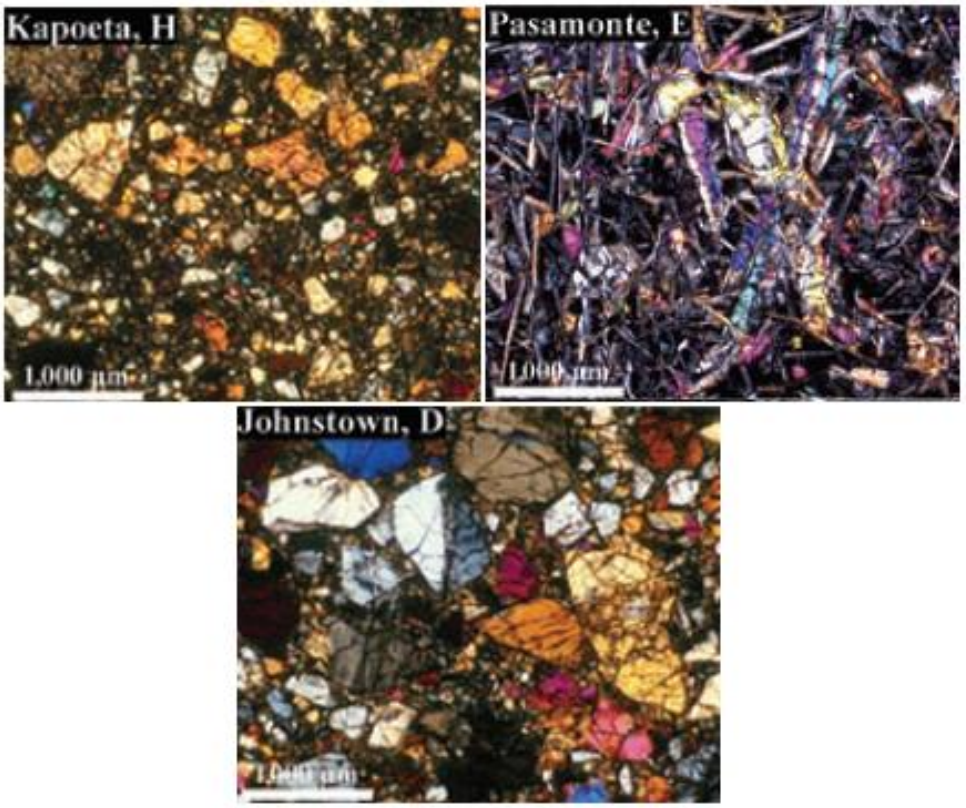


Fig.3.8 – Thin section photomicrographs in transmitted light with crossed polars of typical HED meteorite types. Top Left: Howardite Kapoeta consisting of mineral fragments of highly variable grain sizes. Top Right: Unequilibrated noncumulate eucrite Pasamonte showing the typical basaltic texture of plagioclase (light) and pyroxene (colored). Down: Diogenite Johnstown illustrating the highly brecciated nature of the rock that consists essentially entirely of orthopyroxene [121].

Eucrites (Fig.3.8) are the most common type of achondrites. They have a dark fusion crust and their interior is calcium-rich presenting a brown tonality. They are named after a Greek word meaning "easily distinguished", as they are easily distinguish from chondrites. Eucrites are also reported as the "extraterrestrial basalts"

because they are volcanic rocks of magmatic origin, probably representing the surface of their parent body (Fig.3.9). They are primarly composed by Calcium-poor pyroxenes, piogenite and anorthite. However, other accessory minerals can also be present, such as silica, ilminite, chromite, troilite or fayalitic olivine.

According to their mineralogical composition they can be divided into three subclasses: noncumulate eucrites, cumulate eucrites and polymict eucrites. Noncumulate eucrites formed due to a quickly cooling of lava flows and most were then metamorphosed (Fig.3.9). Cumulate eucrites are coarse-grained gabbros and many of them are unbrecciated. They probably formed in a region of around 8km depth (Fig.3.9). Polymict eucrites are polymict breccias mainly composed by eucritic material, but they also contain less than 10vol.% of a diogenitic component in the form of orthopyroxene.

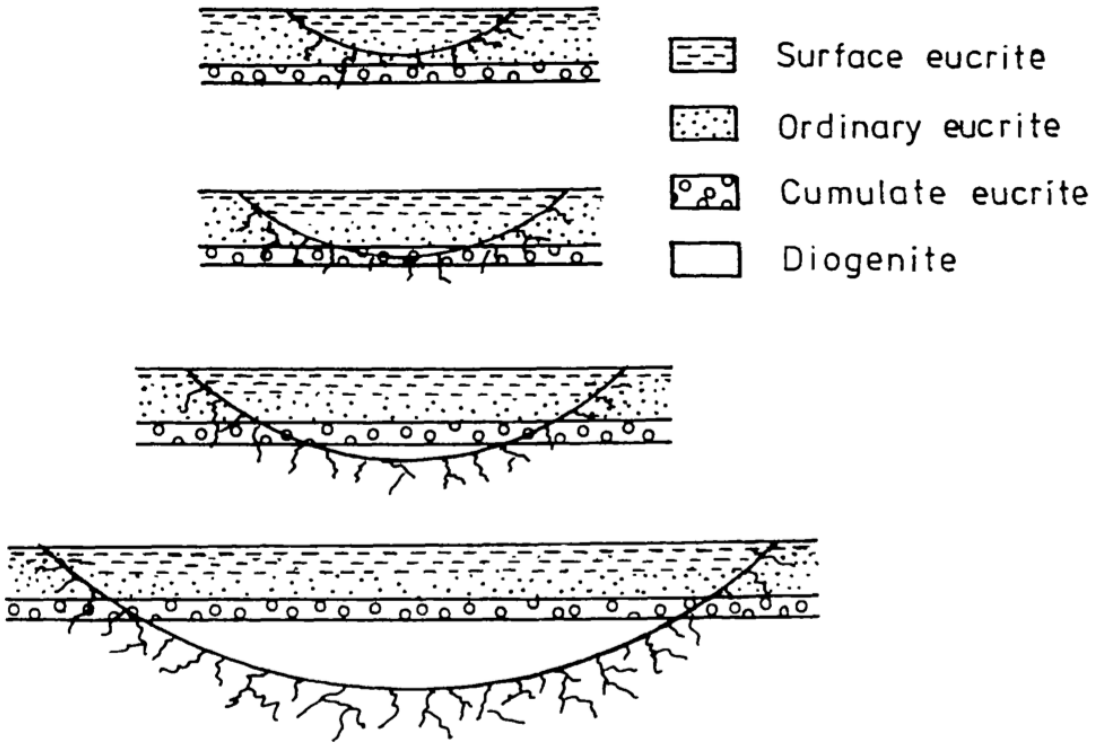


Fig.3.9 - Schematic model of four hypothetical impacts into the layered crust, producing different types of Eucrites. The crustal layers from bottom to top are arranged as follows: (1) Mg-rich diogenite layer with mainly orthopyroxene; (2) cumulate eucrites with Mg-rich inverted with piogenite and calcic plagioclase; (3) ordinary eucrites; (4) surface lava flows with chemically zoned pyroxene [137].

Diogenites were maybe formed in an interior layer of a differentiated asteroid, probably in a Fe-rich mantle (Fig.3.9). They are mainly composed by Magnesium-rich orthopyroxenes. However, other minerals such as olivine, cyclopyroxene, chromite, plagioclase, FeNi-metal, troilite and a silica phase are also present in lesser quantities [138]. Olivine is a minor phase while troilite, metal and silica are accessory phases in many diogenites. Diopside occurs as exsolution products. Plagioclase can be present in some members while phosphates are rare accessory members.

Howardites are named after Edward Howard, a renowned British chemist of the 18$^{th}$ century and one of the pioneers in the study of meteorites. They have broken faces revealing a grey interior. Actually, they are regolith polymitic breccias mainly composed by eucritic and diogenitic debris components. In addition, they also contain abundant impact-melt clasts and breccias fragments [139]. It seems that howardites were material exposed in the surface of their parent body, as it is evidenced by the presence of sputtering gases by solar wind.

### 3.2.2.4. Irons

Irons and stony-irons seem to be originated in the same asteroid, which have experienced high temperature events to completely differentiate. Iron meteorites are usually classified based on their chemical and structural properties. Some determinations of the most volatile siderophile elements as gallium and germanium, resolved only four groups [140], designated by Roman numerals I-IV (ordered by the decreasing content of these two elements). Letters were also added in order to distinguish additional groups. However, not all groups seem to be independent, leading to this (and sometimes confusing) nomenclature. In some cases, some groups have a combination of two letters after their Roman numeral, as for example the IAB or IIICD group. Several chemical characteristics indicate that magmatic iron meteorite groups formed by fractional crystallization, maybe in the cores of differentiated asteroids. Of the 12 groups of iron meteorites, the most enigmatic groups are the IAB and the IIICD groups. Only these two groups have broad ranges in nickel and some trace elements, which are difficult to explain by a simple fractional crystallization process or by a metallic core. For a summarized review of irons compositions and some genetic linkages between groups, please see Table C8.

U.PORTO
FACULDADE DE CIÊNCIAS
UNIVERSIDADE DO PORTO

### 3.2.2.5. Stony-irons

Stony-iron meteorites are divided into two groups: mesosiderites and pallasites.

Mesosiderites are breccias mainly composed of roughly proportions of silicates and FeNi-metal plus troilite. They can be divided into three petrologic classes, taking into account the orthopyroxene abundance: the content of orthopyroxene increases from A (basaltic) to C (orthopiroxinite), with an intermediate state B (more ultramafic).

Pallasites are essentially composed of an amount of silicate (olivine), metal and troilite. Based on the differences of silicate mineralogy, composition, metal and isotopic composition there are three types of pallasites that can be recognized: the main group; the Eagle Station grouplet (with high Ni, Ge, and Ir and siderophiles in the metal and high content of fayalitic olivine [141]); the pyroxene-pallasite grouplet [132].

## 3.3. The chronology of events in the early Solar System

The chronology of the early Solar System has been extensively studied in the last decade, using the isotopic composition of several radiogenic elements in meteorites [142]. For example, several decays have been used in studying the origin and evolution of the terrestrial planets. In order to date the CAIs formation, we can point out the following decays presented in the literature: $^{7}$Be to $^{7}$Li; $^{10}$Be to $^{10}$B; $^{26}$Al to $^{26}$Mg; $^{41}$Ca to $^{41}$K; $^{129}$I to $^{129}$Xe; $^{244}$Pu to $^{136}$Xe. The latter two decays can also be used to date the chondrules chronology.

In the middle 80's, the following chronology of events in the early Solar System was proposed [143]:

4.568 Gyrs ago: Beginning of the collapse of the presolar cloud, formation of "anomalous" CAIs before incorporation of radionuclides of stellar origin;

4.567 Gyrs ago: CAI formation during a few $10^5$ years;

4.566 Gyrs ago: Chondrule formation stars and lasts for 1-2 Myrs;

4.565 – 4.564 Gyrs ago: Accretion of chondritic planetesimals, large scale melting in the parent body of differentiated HED meteorites (postulated as being 4 Vesta, which is discussed in the next chapter).

However, during the last few years several modifications and additions were made in the latter chronology (Fig.3.10).

Using bulk high precision Al-Mg dating, it was possible to establish a relative chronology for CAI and chondrules formation [144]. Also, using the Mn-Cr chronometer it was possible to date the formation of CAIs ~4571 Myr ago [145]. Nowadays it is believed that CAIs formed probably during an embedded phase and during the initial phase of cloud collapse [146] and the formation of the first small planetesimals. However, an early and swift formation of planetesimals is necessary in order to prevent the rapid loss of CAIs into the Sun.

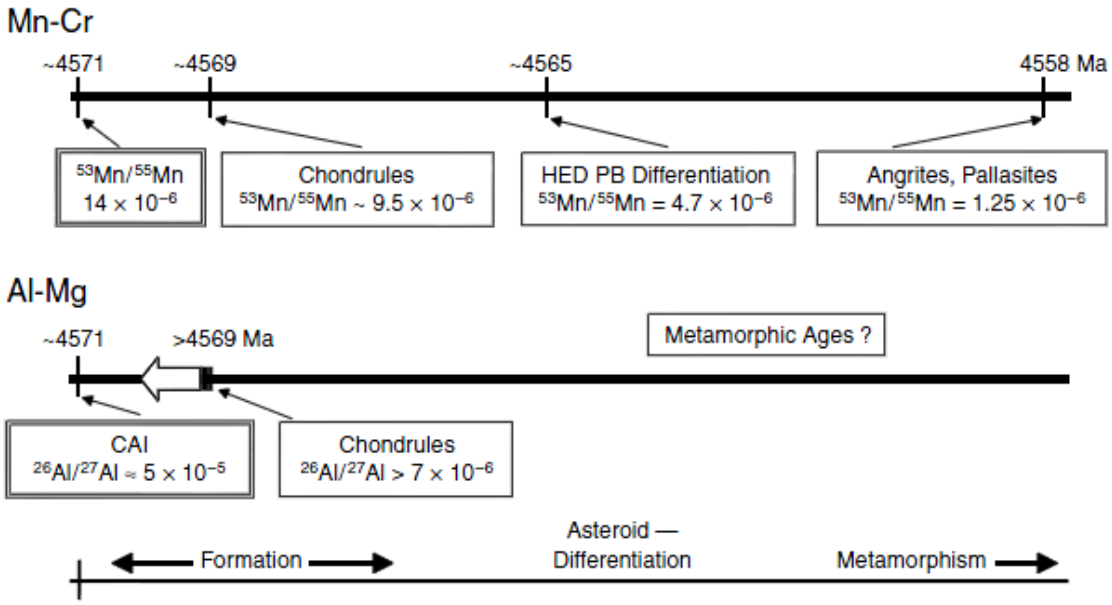


Fig.3.10 - Mn-Cr and Al-Mg early Solar System timelines. Both chronometers are anchored to the time of 4571Myr, when most CAIs are believed to have been formed. Small planetesimals formed almost at the same time in order to preserve CAIs. The interiors of some intermediate-sized planetesimals were melted through the $^{26}Al$ decay. The formation of the primary chondrules occurred within 2Myr. Chemical differentiation, formation of a stratified mantle and a core in these larger bodies ended 4565Myr ago (according to the case of 4 Vesta). Metamorphism occurred for many million years [145].

Al-Mg and Mn-Cr chronometers are consistent in dating the primary chondrules formation within the first ~2 Myr (Fig.3.10) of the Solar System history [145]. Their formation may be concluded around 4569 Myr ago. It seems that this time was an era of intense thermal processing in the inner Solar System materials due to the decay of $^{26}Al$. Later collisional disruption distributed chondrules to their meteorite parent bodies.

Proposed mechanisms for chondrules formation include the interaction with the infant Sun, through jets or solar flares at distances less than 0.1 AU (the so-called X-wind model, which is also reported to explain the formation of CAIs) [146]. However, the most accepted theory for chondrules formation is the so-called “shock model”, in which chondrules formed in solar nebula shocks [146-147]. Several mechanisms were proposed for producing shock fronts inside the solar nebula [148] however their origin is still under debate. Identifying the mechanism responsible for the production of shock fronts can help us to understand the way that chondrules formed.

Chemical differentiation, formation the core and a stratified mantle was concluded no later than ~4565 Myr ago [145]. Also during this time, the H chondrite and enstatite chondrites parent bodies cooled below the temperature where isotopic closure occurs. The formation of pallasites occurred 4558 Myr ago and their younger age mark the time when either the interiors of their parent bodies cooled or the parent bodies were disrupted to allow rapid cooling of the exposed interior [145]. It is clear that accretion, accumulation of heat and chemical differentiation on larger asteroids occurred during a period of ~6 Myr.

Understanding the chronology of the events occurred in the early stages of the Solar System can help us to accomplish the puzzling task of understanding the steps beyond the planetary formation. But, it is important to note that the various chronometers and measurements presented in the literature are not always consistent with each other.

U.PORTO
FACULDADE DE CIÊNCIAS
UNIVERSIDADE DO PORTO

# 4. The parent body search

*"Asteroids investigations can provide a "map" to complement the meteorite "clock"."*

in Graffey, M. J., Burbine, T. H. and Binzel, R. P. (1993), *Asteroids spectroscopy: Progress and perspectives*, Meteoritics, 28, 2, 161-187

As the number of known meteorites is rapidly growing up through the discovery of large concentrations of meteorites in the hot and cold deserts, this reports us to an intriguing question: "Where do meteorites come from?". Several evidences indicate that the major source of meteorite is the inner asteroid belt. However, linking a meteorite to a specific body has been a challenging task through the past years. With the advances in the use of the charge-coupled device (CCD) detectors, it is possible to obtain visible and near-infrared reflectance spectra of smaller and smaller objects [96]. The main advantage is that it may be possible to determine parent or source bodies for particular meteorites. A parent body is the body from which the meteorite acquired its current chemical composition and mineralogical characteristics, while a source body is a fragment of the parent body by which the meteorite was completely shielded from cosmic rays for most of the Solar System's history [96]. The postulated parent or source bodies for almost all groups of meteorites can be found in Table C9.

Establishing linkages between asteroids and meteorites are of crucial importance as they allow us to understand the compositional and thermal gradients in the solar nebula. A key of interest is the very earliest history of nebular solids, which provide important constraints on nebular conditions and processes that are the ground truth for astrophysical models of nebular evolution.

In the past decade, the strong relationship between the HED meteorites and the asteroid 4 Vesta was reinforced [149-150]. Linkages between ordinary chondrites and S-type asteroids, CM chondrites and C-type asteroids and irons as well as enstatite chondrites and M-type asteroids have been subject of discussion.

In this chapter we will discuss the linkages that asteroids and comets may share with meteorites as well as methods to identify and study their relationships. In addition, we will describe how space weathering can play an important role in the identification

of possible linkages between asteroids and meteorites. Finally, the model for deconvulting reflectance spectra, which will be used in this study, will be presented: the Hapke Radiative Transfer Model.

**Keywords:** parent bodies; source bodies; 4 Vesta; Vestoids; HEDs; comets; space weathering; albedo; reflectance; absorption band; valence band; conduction band; Hapke Model; bidirectional;

## 4.1. The meteorite-parent body relationship

Historically, it has been an arduous task linking telescopic measurements of asteroids with laboratorial measurements of meteorites. Such linkages provide physical constraints in order to develop and/or test sophisticated models of the origin and evolution of our Solar System. Long-running modeling studies of the dynamical evolution of the MAB as well as long-running spectral investigations of asteroid compositions, finally converged to yield a clear view of the asteroid-meteorite linkages. However it is interesting to note the enormous disparity between the 100 to 150 postulated parent bodies or source bodies and the approximately number of known asteroids [151]: 1000000!

In the following subsections it will be pointed out a number of postulated asteroid-meteorite linkages for several groups of meteorites. As it was referred above, the postulated parent or source bodies for almost all groups of meteorites can be found in Table C9.

### 4.1.1. HED's-4 Vesta-Vestoids

Asteroid 4 Vesta is the only known asteroid with a diameter larger than 400 km which has a basaltic crust. It is believed that the geological history of 4 Vesta occurred in the first 10 Myr of the Solar System [152]. It should be noted that basalts are rocks formed in the interior of a planet, during a stage of high temperatures and pressures and later brought to the surface. Hence, the study of basalts provides information about: the formation and differentiation of a body; the mineralogy and chemistry of its formation region in the interior of the body; thermal history and characteristics of the parent body aside from the process of the formation of magma and its evolution.

The link between the HED meteorites and 4 Vesta was originally based on the similarities between the composition of the HEDs and the surface of 4 Vesta, as it is evidenced by spectroscopy (Fig.4.1).This linkage was first established through spectroscopy in the visible and NIR [153]. The surface of 4 Vesta exhibits absorption features typical for low-Ca pyroxene that are similar in composition to certain basaltic achondrites (i.e. eucrites). Such evidence can be seen in Fig.4.1. However, this relationship was early questioned [154]. The main problem is stating how HEDs were transported from the MAB into Earth.

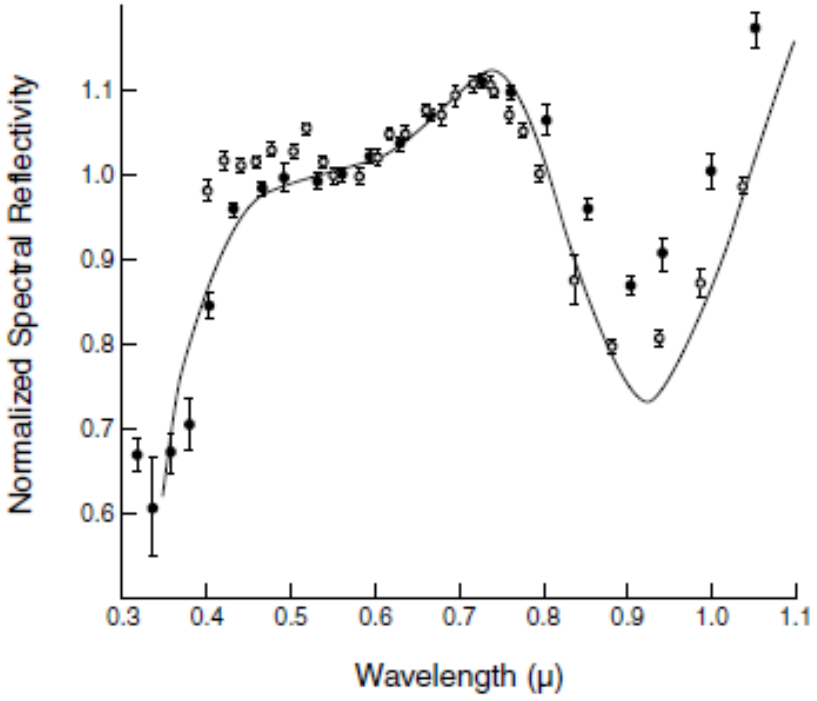


Fig.4.1 – Laboratory measurement of the spectral reflectivity of the Nuevo Laredo eucrite (solid line), compared to telescope data points from 4 Vesta [64].

As stated in the second chapter, 4 Vesta shows a huge crater with a diameter of ~460 km. Such evidence contributed to the development of a hydrodynamic model where a ~42 km stricks the basaltic surface of 4 Vesta [155]: if the impact velocity is 5,4 km/s, fragments with several diameters will be released with an injection velocity of 600 m/s without modifying the structure of 4 Vesta's crust. According to this model, the fragments would be both originated in crust and superior layer of the mantle. These fragments constitute, nowadays, the so known "4 Vesta family". Currently, more than 40 vestoids <10 km in diameter with 4 Vesta-like spectral features are known that fall

inside 2.5 AU, also known as the Kirkwood gap defined by 3:2 jovian resonance. Others fragments were brought to the secular resonance $\nu_6$. Both resonances can modify the eccentricity of 4 Vesta's fragments and only a few of them remained in orbits close to Earth (NEO's). Some collisional processes which occurred later brought some of these fragments into Earth. A schematic representation of this scenario is represented in Fig.4.2. Hence, the transport problem stated above is now solved.

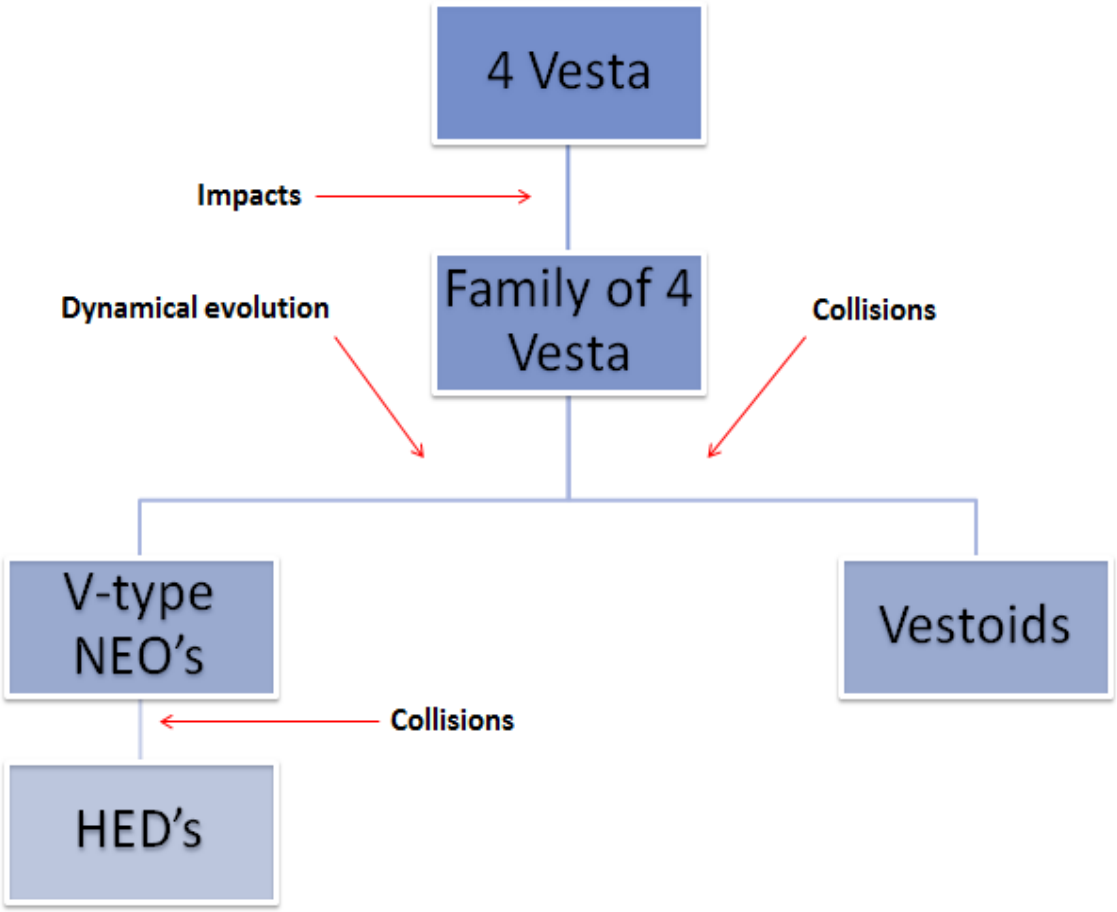


Fig.4.2 - Scheme of the problematic relationship 4 Vesta - V type asteroids - HED meteorites.

But, can HED meteorites be originated from another source in the MAB other than 4 Vesta? The only other large asteroid known in the MAB with a basaltic surface that has no known dynamical link to 4 Vesta, the vestoids, and any family or nearby large asteroid is 1459 Magnya [156]. This scenario seems to be quite unlikely since the delivery efficiency of fragments from 1459 Magnya to near-Earth orbits, located at 3.15 AU, is much less than the one's of 4 Vesta and Vestoids.

U.PORTO
FACULDADE DE CIÊNCIAS
UNIVERSIDADE DO PORTO

## 4.1.2. Ordinary Chondrites

Ordinary chondrites are the most common type of meteorites falling on Earth. Such evidence requires an efficient delivery mechanism.

The first asteroid proposed as having a similar visible spectrum to ordinary chondrites was 3628 Boznemcova (Fig.4.3) [157]. However the NIR spectrum of this asteroid shows an unusual bowl-shaped 1-μm feature unlike any measured meteorite spectrum from 1.2 to 1.5 μm [149].

Several lines of evidence show that S(IV)-type asteroids are the parent bodies of the ordinary chondrites. S(IV) asteroids include many of the largest asteroids in the MAB: 3 Juno, 6 Hebe, 7 Iris and 11 Parthenope. 6 Hebe is located near both $\nu_6$ and 3:1 resonances, so is suggested as being a major source of ordinary chondrites meteorite flux [158]. The silicate portion assemblage of 6 Hebe is consistent with the silicates in H chondrites. Hence, 6 Hebe is stated as being the probable parent body of the H chondrites (Fig.4.3). The L- and LL-chondrites parent bodies remain to be identified, but they probably reside among the S(IV) asteroids, located near the 3:1 and $\nu_6$ resonances [159]. It is argued that L-chondrites are almost certainly originated in an asteroid family, due to the strong clustering of shock waves near 500 Myr. Among the families located near the 3:1 and $\nu_6$ resonances, the Maria Family seems to be the best candidate.

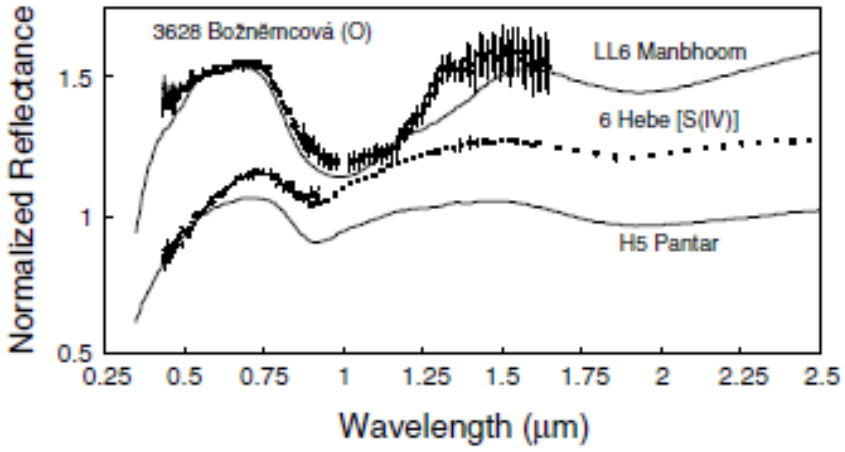


Fig.4.3 - Normalized reflectance vs. Wavelenght (μm) for S-type 6 Hebe vs H5 chondrite Pantar and O-type 3628 Boznemcová vs. LL6 chondrite Manbhoom. All spectra are normalized to unity at 0.55μm. The asteroid spectra are offset by 0.5 in reflectance [96].

It was hoped that the mission NEAR *Shoemaker* to S(IV)-asteroid 433 Eros, answered many of the scientific community doubts about the composition of the S-type asteroids. The olivine-to-pyroxene composition derived from band area ratios and elemental ratios derived from X-ray measurements of 433 Eros are consistent with ordinary chondrites [96]. But, the S:Si and Fe:Si ratio derived from X-rays and γ-rays, respectively, are depleted in relation to the ordinary chondrites. Linking 433 Eros to a specified meteorite group is strongly dependent on our understanding about the physical and chemical processes that affect asteroid regoliths.

### 4.1.3. Iron meteorites and Enstatite chondrites

M asteroids are characterized by moderate visual albedos (~0.10 to 0.30) as well as relatively featureless spectra and red spectral slopes. These spectral features are similar to those of irons and enstatite chondrites. Hence M asteroids are postulated as being the probable parent bodies of these two groups of meteorites [96].

The spectrum of an iron meteorite (Fig.4.4) is characterized by a red slope and a moderate albedo (~0.10-0.30). Enstatite chondrites also have relatively featureless spectra (Fig.4.4) with red slopes and moderate albedos [96].

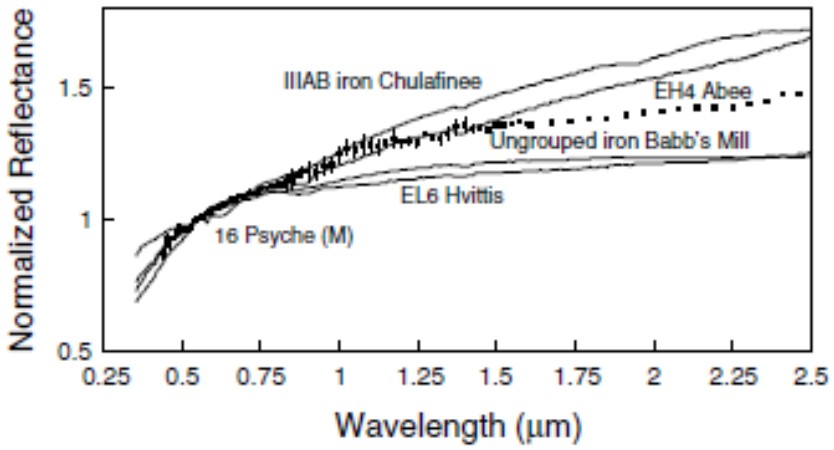


Fig.4.4 - Normalized reflectance vs. wavelength (μm) for M-type 16 Psyche vs. iron and enstatite chondrite meteorites (lines). By the order of increasing reflectance at 2.0μm, the meteorites are: EL6 chondrite Hvittis; ungrouped iron Babb's Mill; EH4 chondrite Abee; IIIAB iron Chulafinee. All spectra are normalized to unity at 0.55μm [96].

Metallic Fe has the same reflectance features in this wavelength region (Fig.4.4) as M asteroids. Hence, M asteroids have been historically identified as the disrupted cores of differentiated objects, which have had their silicates removed. But,

enstatite chondrites have similar reflectance features to metallic Fe and were then proposed as meteoritic analogs to M asteroids [96].

### 4.1.4. CM and CI carbonaceous chondrites

CM chondrites spectrally show several characteristics (Fig.4.5): low visible albedos (~0.04); relatively strong UV features; a number of weak features between 0.6 and 0.9 μm; relatively featureless spectra between 0.9 and 2.5 μm.

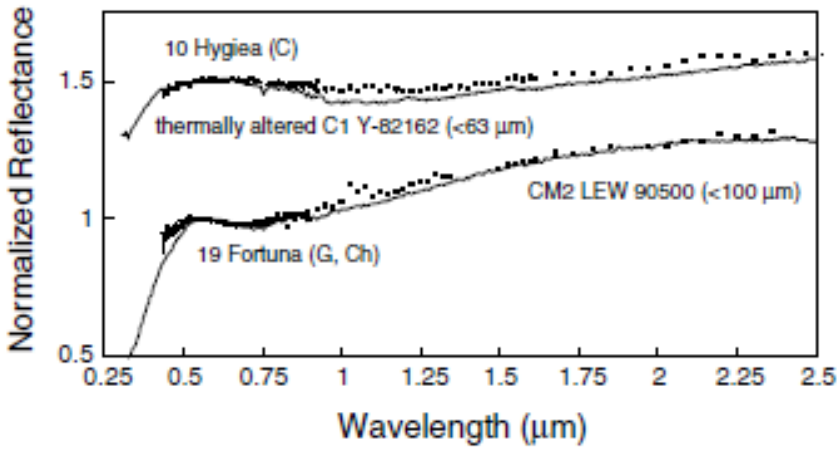


Fig.4.5 - Normalized reflectance vs. Wavelenght (μm) for G-type 19 Fortuna vs. CM chondrite LEW90500 and C-type 10 Hygiea vs. Thermally altered CI Chondrite Y-82162. All spectra are normalized to unity at 0.55μm. The asteroid spectra are offset by 0.5 in reflectance [96].

CM and CI chondrites have been linked to the C-type asteroids due to the low albedos and relatively featureless spectra [96]. Two particular asteroids have been identified as possible parent bodies: 13 Egeria and in particular 19 Fortuna [160]. Both asteroids have similar spectral slopes to CM chondrites in the range between 0.7 and 2.5 μm. In addition, both asteroids show a relatively strong 3-μm feature.

However, is it possible that CM and CI meteorites come from the outer Solar System? Actually, two solutions are possible: there are no meteorites coming from other sources than asteroids, or cometary meteorites are so similar to several asteroidal meteorites that are impossible to distinguish them [161]. However it seems quite improbable that no cometary meteorites exist, or it should exists some unknown powerful mechanism which is preventing them to reach Earth. But, according to dynamical studies indeed show that JFCs can find direct and indirect dynamic routes to Earth [161]. Hence, in this scenario, CM and CI carbonaceous chondrites are the best

plausible candidates of being cometary meteorites as they are rare, dark, have an unfractionated chemical composition, are rich in volatile elements and are rich in light elements (H, C, N and O) [161]. Actually it is argued in the literature, based on studies comparing the available information on chemistry and petrology of comets, that CM and CI chondrites can be samples of extinct cometary nuclei [158]:

*"We would argue, however, that there is a continuum between comets and asteroids rather than a sharp distinction. This continuum is easy to understand as the cometary (ice-rich) or asteroidal (ice-poor) nature of a given object depends on its position at formation relative to the snowline. There is no reason for the snowline to have always occupied the same location in the protoplanetary accretion disk, nor to define an abrupt transition between water-poor and water-rich objects. Type 1 and 2 carbonaceous chondrites might be sample the continuum between asteroids and* comets. The answer to our question is therefore Yes."

In Gounelle, M., Morbidelli, A., Bland, P. A., Spurny, P., Young, E. D. and Septhon, M. (2008), *Meteorites from the outer Solar System?*, The Solar System Beyond Neptune, M. A. Barucci, H. Boehnhardt, D. P. Cruikshank, and A. Morbidelli (eds.), University of Arizona Press, Tucson, 592, 538

### 4.1.5. Others Meteorites Groups

The parent bodies of CV and CO chondrites are probably among the K asteroids. Due to their low fall frequency on Earth (less than 1%), the probable parent bodies of these groups of meteorites are located far away from an efficient Earth-delivery resonance. S asteroids are the postulated parent bodies for the acapulcoites, ureilites, londranites, winonaites and angrites. Also due to their low fall frequency on Earth, their parent bodies may be located somewhere far away from the efficient Earth-delivery resonances. The NEA 3103 Eger, which is maybe derived from the Hungaria family, is the postulated parent body of aubites. Brachinites and pallasites are probably derived from the A-type asteroids, while mesosiderites are probably derived from M-type asteroids. Spectral features of the CK, CR and R carbonaceous chondrites are currently too poorly known to look for a probable parent body. However, CR and CK are cited in the literature as being linked to the C-type asteroids, while R-type asteroids

are cited as being linked to the A- or S-type asteroids. These genetic linkages between asteroids and meteorites can be found in Table C9.

## 4.2. Space weathering

Since the discovery of the possible linkage between 4 Vesta and the HED's meteorites, several studies aimed to link other meteoritic classes to asteroids as it was discussed in the last section. But, in some cases, the spectra of some types of asteroids do not fit well the spectra of their meteoritic analogs (Fig.4.7). This difference between some asteroid-types and their meteoritic analogs has long been cited to be caused by "space weathering" [162]. Space weathering is the amount of physical and chemical alterations which occur in the material exposed in the surface of an airless body. Nowadays it is currently accepted that space weathering can be a key modifier of visible and near infrared reflectance spectra of an airless body. It is believed that space weathering is caused by vapor recondensation after either ion sputtering or impact by micrometeorites [163]. One result of space weathering is the production of submicroscopic metallic iron (SMFe) in the regolith of airless bodies (Fig.4.6). Also, in the literature some authors use the phrase "nanophase metallic iron" (abbreviated $npFe^0$) to refer to the carrier of the space weathering [164].

Space weathering was firstly proposed to occur on the Moon, as it was not understood why the lunar soil becomes darker and spectrally redder with time [165]. It was argued that space weathering was responsible for redden the spectral slope, obscuring absorption bands and lowering the albedo of the Moon [164]. In addition, the characteristic magnetic spin resonance of the lunar regolith is thought to be due to space weathering. The latter facts were later confirmed when astronauts of the Apollo's mission brought back some lunar soil, which through laboratorial studies provided crucial information on the space weathering process on the Moon. However, space weathering effects on asteroids are still not well understood because we do not have soil samples of asteroids yet available for laboratorial studies.

Asteroid types which show evidences of space weathering include the S, A, Q and V-types. The effects of space weathering on these types of asteroids are summarized on Table C12. It is also presented their probable meteoritic analogs and

inferred space weathering effects. In Fig.4.7, the space weathering effects are evidenced for S- and V-type asteroids [162].

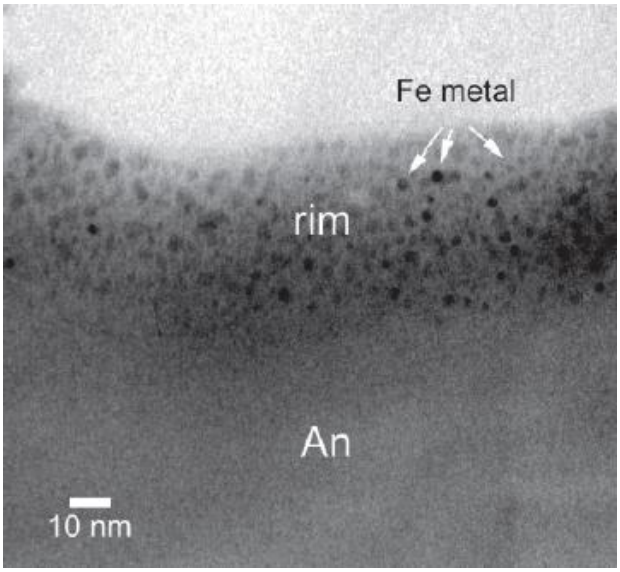


Fig.4.6 - TEM image of an anorthosite (An) grain from a mature lunar soil that exhibits a rim of Fe metal particles (SMFe) [162].

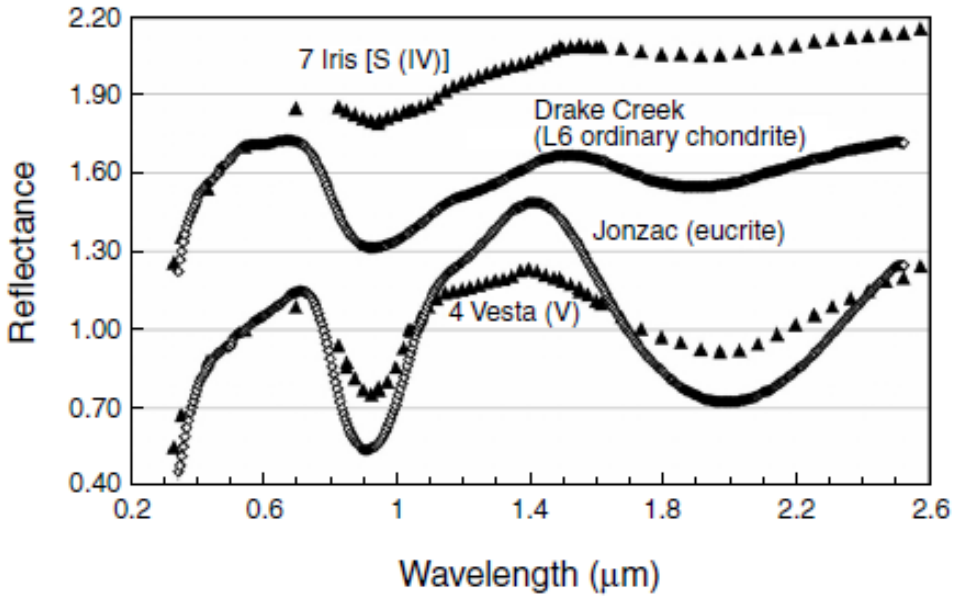


Fig.4.7 – Two examples of reflectance spectra of asteroids paired with their meteoritic analogs. One possible explanation for this mismatch is the space weathering process which is thought to be responsible for the alteration of several spectral features of asteroids. Asteroids are displayed as closed triangles and meteorites as open diamonds. The top pair is offset vertically by 0.7 for clarity and show the S (IV) asteroid 7 Iris with the L6 ordinary chondrite Drake Creek. Although both objects have approximately the same mineralogy as shown by their band minima, the spectra of 7 Iris is reddened by 30% relative to Drake Creek. Also, Iris's major absorption bands are significantly reduced. The pair of 4 4 Vesta and the eucrite Jonzac also show similar mineralogy, but the band depth of 4 Vesta is reduced by 40% relative to its analog meteorite [162].

The Q-type asteroids, for which ordinary chondrites are postulated as being their meteoritic analogs, denote on their spectra evidences of band suppression and albedo reduction. The red continuum slope and modest band suppression evidenced on the spectra of A-type asteroids are consistent of olivine weathering. In the case of V-type asteroids (Fig.4.7), the largest asteroid 4 Vesta shows a reduction in band depth evidencing the presence of space weathering, despite the band centers and shapes of the 4 Vesta and Jonzac eucrite spectra are similar. But, the strongest evidence of space weathering in asteroids is found among the S-type asteroids. Despite the spectral band center of 7 Iris (Fig.4.7) shows a similar mineralogy to the Drake Creek L6 ordinary chondrite, the weathering process seems to produce differences in band depth, red slope and albedo [162].

## 4.3. Spectra Modelling: The Hapke Radiative Transfer Model

In the visible and near-infrared regions, the reflectance spectra of meteorites show several absorption features, which are function of the composition and crystalline structure of the absorbing materials. Aiming to establish a possible linkage between parent body and source body, studying the reflectance spectra of meteorites can be an important tool to accomplish this hard task. However, how can we study the reflectance spectra of meteorites? In fact, this is possible through remote sensing of reflectance spectra, by inferring the surface mineralogy of asteroids and meteorites. But, to describe the absorption features it is necessary to understand the physics which controls them. Hence, the Hapke Radiative Transfer Model (hereafter also reported as the acronym HM) [166] will be described in this section.

### 4.3.1. Hapke Radiative Transfer Model

The Hapke radiative transfer model provides a method to derive the composition and mineralogy of a surface as well as the size of its particles, through its reflectance spectra. If the surface optical constants are available, the analysis of the reflectance spectra can be made with high accuracy. The optical constants are fundamental properties of a mineral and are independent of the size and shape of the particle. The refraction index *m*, is defined as follows:

$$m = n + ik \tag{4.1}$$

where *n* denotes the real refraction index and *k* denotes the complex refraction index.

The spectral signatures found in absorption spectra or in reflectance spectra of mafic minerals, in the near-infrared regions are dominated by variations of *k* [1].

### 4.3.1.1. Concepts and Definitions

In this section several concepts and definitions will be introduced, such as: the difference between radiance and irradiance; the geometrical notation for the incident, emergent and phase angles of a light beam; the definitions of cross sections, efficiencies, particle scattering albedo and espat function. These definitions and concepts will be useful later to understand the basis of the Hapke Model.

#### 4.3.1.1.1. Radiance and Irradiance

In the radiation field, where the light is uncollimated, it is important to distinguish between radiance and irradiance.

The amount of power at position *r* crossing unit area (*dS*) perpendicular to the direction of propagation $\Omega$, travelling into unit solid angle about $\Omega$ (denoted by $d\Omega$), is called the radiance (Fig.4.8). The radiance will be denoted by $I(\Omega, \mathrm{r})$.

The irradiance term refers to the radiative power per unit of area of a collimated light beam (Fig.4.8). It is usually denoted by *J*.

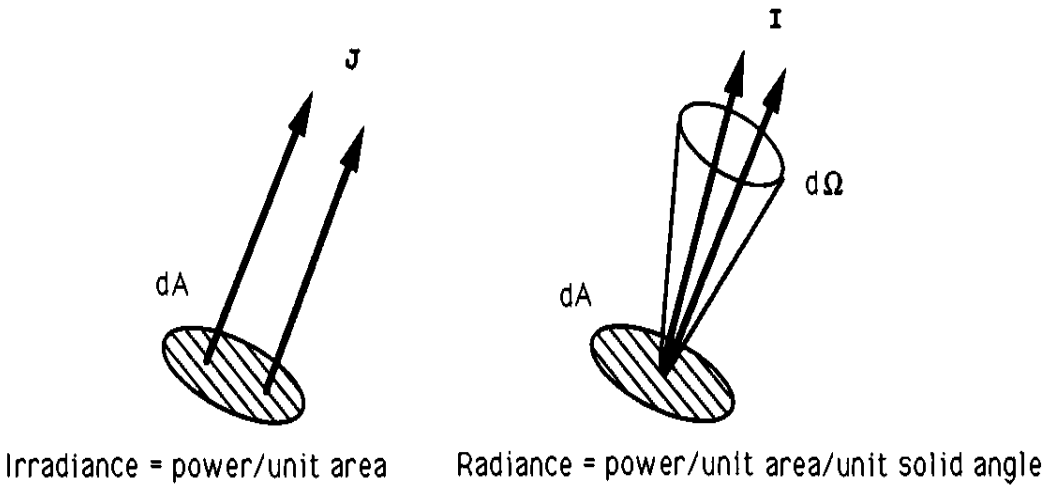


Fig.4.8 - Irradiance and Radiance [166].

U.PORTO
FACULDADE DE CIÊNCIAS
UNIVERSIDADE DO PORTO

#### 4.3.1.1.2. Geometric Notions

Let's assume that a light beam is focused on a semi-infinite medium. There are two crucial geometrical conventions, which are related to the latter assumption: the incident angle $(i)$ and the emergent angle $(e)$ (Fig.4.9). Let $\vec{n}$ be the unitary vector normal to the surface *ΔA*, in Fig.4.9.

The incident direction $\vec{\imath}$ of the light beam can be decomposed in two angles (Fig.4.9):

1. The incident angle *i*: is defined as the angle between the $\vec{n}$ and the incident direction;
2. The azimuth angle $\varphi_i$: is defined as the angle between the North direction and the projection of $\vec{\imath}$ on the surface;

After scattered by the surface, several rays of light will emerge through the surface in a certain direction $\vec{e}$, called the emergent direction. As in the case of the incident direction, $\vec{e}$ can be decomposed in two angles (Fig.4.9):

1. The emergence angle *e*: is defined as the angle between $\vec{n}$ and the emergent beam;
2. The azimuth angle $\varphi_e$: is defined as the angle between the North direction and the projection of $\vec{e}$ on the surface;

There are some aditional angles which can be defined from the ones described above, such as:

1. The phase angle: it is the angle between the incident and emergent beams;
2. The diffusion angle θ: it is the complementary angle of *g* ($\theta = \pi - g$);
3. The azimuth angle relative to $\varphi$: it is the angle between the projections of $\vec{\imath}$ and $\vec{e}$ ($\varphi = |\varphi_e - \varphi_i|$);

A relation between the phase and the azimuth angles can be derived through spherical trigonometry:

$$\cos(g) = \cos(e)\cos(i) + \sin(e)\sin(i)\cos(\varphi) \qquad (4.2)$$

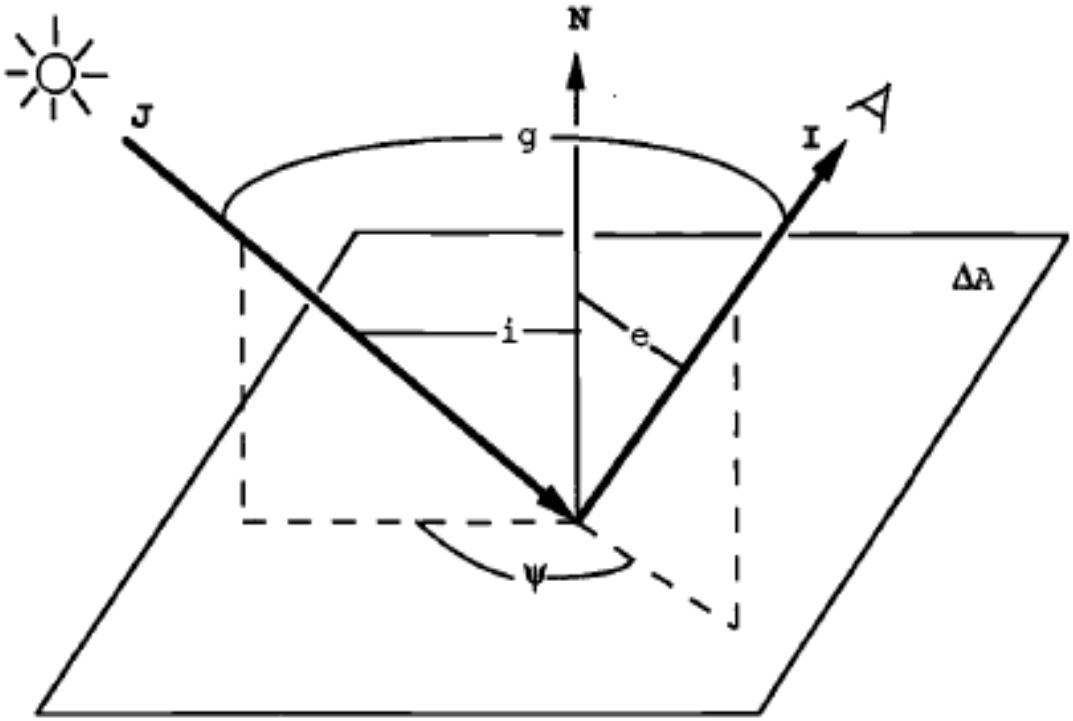


Fig.4.9 - Geometrical conventions [166].

A commonly used notation in the literature when referring to the cosine of the incident and emergence angles is the following:

$$\mu_0 = \cos(i) \tag{4.3}$$

$$\mu = \cos(e) \tag{4.4}$$

The plane containing $\vec{n}$ and $\vec{i}$ is called the incident plane, and that containing $\vec{n}$ and $\vec{e}$ is called the emergence plane.

## 4.3.1.1.3. Cross sections and efficiencies

Let $P_E$ be the total power of the incident irradiance $J$, which is affected by the particle. The extinction cross section is defined as the ratio between $P_E$ and $J$:

$$\sigma_E = \frac{P_E}{J} \tag{4.5}$$

However, a certain portion of the total power is scattered into all directions and the remaining is absorbed by the particle (Fig.4.10). Let $P_S$ be the scattered power and $P_A$ be the absorbed power. Hence:

$$P_E = P_A + P_S \tag{4.6}$$

The scattering cross section, $\sigma_S$, is defined as:

$$\sigma_S = \frac{P_S}{J} \tag{4.7}$$

In addition, the absorption cross section is defined as:

$$\sigma_A = \frac{P_A}{J} \tag{4.8}$$

Rewriting equation 4.6, using 4.5, 4.7 and 4.8 in leads to:

$$\sigma_E = \sigma_A + \sigma_S \tag{4.9}$$

Considering, now, a particle with radius *a*, its geometrical cross-sectional area *σ*, is defined as:

$$\sigma = \pi a^2 \tag{4.10}$$

Hence, the extinction, scattering and absorption efficiencies are, respectively defined as:

$$Q_A = \frac{\sigma_A}{\sigma} \tag{4.11}$$

$$Q_E = \frac{\sigma_E}{\sigma} \tag{4.12}$$

$$Q_S = \frac{\sigma_S}{\sigma} \tag{4.13}$$

Where:

$$Q_E = Q_S + Q_A \tag{4.14}$$

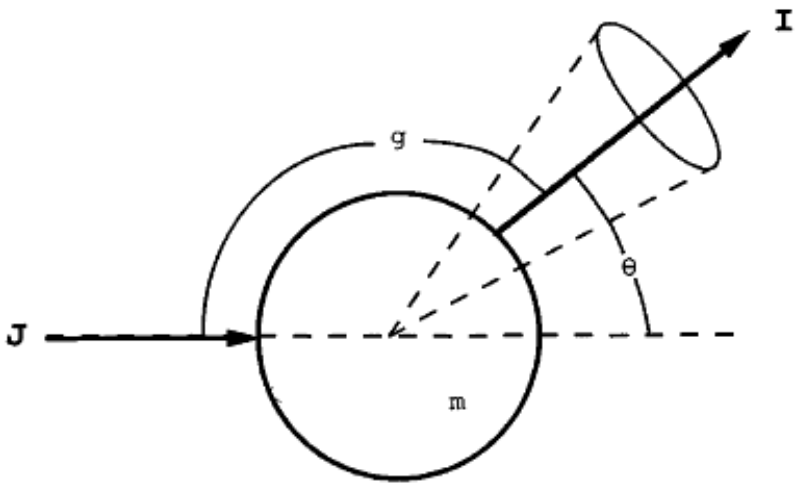


Fig.4.10 - Scattering by a single particle. The plane containing J and I is called the scattering plane [166].

### 4.3.1.1.4. Particle Scattering Albedo and Espat Function

The particle single scattering albedo *w*, is defined as the ratio between the total scattered power and the total power that is removed from the wave:

$$w = \frac{P_S}{P_E} = \frac{\sigma_S}{\sigma_E} = \frac{Q_S}{Q_E} \tag{4.15}$$

In addition, a parameter related to the single scattering albedo is the so-called particle espat function:

$$W = \frac{Q_A}{Q_S} = \frac{1-w}{w} \tag{4.16}$$

In general, the efficiencies and the single-scattering albedo are functions of the wavelength.

### 4.3.1.1.5. Physics of absorption mechanisms

When a light beam is focused on a material, where the refraction index changes, part of the light is reflected while the other is absorbed by the medium. When the photons collide with an absorber medium, they are absorbed according to the Beer-Lambert Law.

Let's consider an isotropic and homogeneous medium with a thickness *dl*. Let $I_0$ be the intensity measured of a light beam before crossing that medium, and $I_1$ the intensity of the light beam measured after crossing that medium. In addition, let τ be the attenuation coefficient and *c* its concentration.

By crossing the homogeneous and isotropic medium, the intensity of the light beam decreases by a factor of $\tau = \frac{1}{\alpha c}$, where $\alpha = \frac{4\pi m}{\lambda}$ is called the dispersion relation. Hence:

$$I_1 = I_0 \alpha c . dl \tag{4.17}$$

Integrating equation 4.17 for a medium of finite thickness gives:

$$I_1 = I_0 e^{-\alpha c l} \tag{4.18}$$

The equation 4.18 is called the Beer-Lambert law.

However, what are the mechanisms responsible for the absorption?

Actually, absorption in the near ultraviolet, visible and near-infrared regions of the spectrum can occur by several mechanisms, but most can be classified as transitions in which single electrons are induced by the radiation to jump from a lower state of energy to one of higher energy. These transitions can be described in terms of the band model of electrons in a solid [166]. In this model, the system has several wide continuous bands in which the electrons can exist, separated by gaps. The highest energy band, in which the electron states are all occupied, is denominated by valence band, while the lowest energy band in which not all states are occupied is called the conduction band. If an electron is excited from the valence band to the conduction band, it leaves an ion with an excess of positive charge behind it. This positively charged electron vacancy is called a hole [166].

This overview of bands occupied by electrons and holes gives rise to a rich variety of ways by which light can be absorbed. In particular, the most commonly process which is responsible for the absorption features in minerals spectra, is the electronic transition between electron shells which are not completely filled in transition elements. Usually, in an isolated ion the orbital states in the partly filled shell are degenerate. Hence, the electrons have the same probability of residing in any state.

But, if the ion is in a solid, the electric field created due to the surrounding ions is not isotropic. As a consequence, this nonisotropy removes the degeneracies and the orbitals in the shell have different energy levels. In this scenario, an electron can move from a lower level of energy to a higher level of energy when a photon is absorbed. This mechanism is usually called the crystal-field absorption [166]. The energy levels are characterized by the valence state of the atom (as for example, $Fe^{2+}$ or $Fe^{3+}$), by their coordination number, by the type of ligands formed, or by the metal-ligand interatomic distance.

Absorption bands due to crystal-field transitions typically occur in the visible and near-infrared regions. In particular, the $Fe^{2+}$ bands near 1 and 2 μm and the $Fe^{3+}$ band near 0.86 μm have important applications in geochemical remote sensing. As an ion is able to produce different absorptions, it is possible to identify specific minerals in spectroscopy.

### 4.3.1.2. Radiative Transfer Equation

The formalism which is usually used to calculate how the intensity of an electromagnetic wave changes due to emission, absorption and scattering processes, as the wave crosses a complex medium is known as the radiative transfer equation. The main hypothesis of this formalism is to suppose that the medium heterogeneities emit and scatter the radiation independently [166].

The radiative transfer equation is written as:

$$-\mu_e \frac{\partial I(\tau,\Omega)}{\partial \tau} = -I(\tau,\Omega) + \frac{w(\tau)}{4\pi}\int_0^{4\pi} I(\tau,\Omega')\, p(\tau,\Omega',\Omega) d\Omega' +$$

$$+ J\frac{w(\tau)}{4\pi} p(\tau,\Omega_0,\Omega) e^{-\tau/\cos(i)} + F_T(\tau,\Omega)^4 \quad (4.19)$$

With several precautions, the theory of the radiative transfer can be applied to two mediums of particular importance in remote sensing: atmospheres and planetary regoliths. However, if the particles do not have a regular shape and if they are not uniformly spaced, the application of this theory can give erroneous results [166].

[4] A deduction of this equation can be found in Hapke (1993) [164], pages 151-155.

U.PORTO
FACULDADE DE CIÊNCIAS
UNIVERSIDADE DO PORTO

### 4.3.1.3. Particle Phase Function

The particle phase function ($p(g)$) is also called the single-particle angular-scattering function [166].

Let us suppose that a light beam with irradiance $J(\Omega, r)$ travels in a direction $\Omega_0$ and it is scattered by a particle at a position *r*, according to a diffraction pattern $I(\Omega, r)$. The particle phase function describes the angular distribution in which $P_S$ is scattered [166]. It is defined as:

$$I(\Omega) = Jw\frac{p(g)}{4\pi} \tag{4.20}$$

If the particle scatters isotropically, $p(g) = 1$. As the power which is scattered into all directions must be equal to $P_S$, $p(g)$ may obey the following condition of normalization:

$$\int_0^{4\pi} p(g)d\Omega = 4\pi \tag{4.21}$$

However, for spherical particles, the scattered power is independent of the azimuth angle. Hence, the condition of normalization may be written as follows:

$$\frac{1}{2}\int_0^{\pi} p(g)\sin(g)\,dg = 1 \tag{4.22}$$

The exact solution of the radiative transfer equation (Equation 4.19) was obtained for homogeneous and perfectly spherical particles through Mie theory [166]. The Mie solutions depend only on two parameters: the particle refraction index ($m = n + ik$) relative to its surroundings medium and the ratio, which will be defined as *X*, between the size of the particle and the wavelength of the incident radiation:

$$X = \frac{2\pi a}{\lambda} = \frac{\pi D}{\lambda} \tag{4.23}$$

where *a* is the particle's radius, *D* is the particle's diameter and *λ* is the wavelength of the incident radiation.

If $X \ll 1$ or $a \ll \lambda$: the Rayleigh region. In this region, if the incident light beam is unpolarized, the particle phase function is written as follows:

$$p(g) = \frac{3}{4}\left(1 + cos^2(g)\right) \tag{4.24}$$

For $X \sim 1$ or $a \sim \lambda$: the resonance regime. The behaviours of the efficiencies and of the particle phase function are complicated and vary from case to case.

If $X \gg 1$ or $a \gg \lambda$: the geometric-optics regime. In this region, the parts of the front waves separated by a distance of the order of the radius are nearly independent, so that what happens to one part has very little influence on the other part. In this case, the propagation of the wave can be treated as if it was made up of independent bundles of rays that are refracted and reflected by the sphere. The particle phase function for this regime is quite complicated and it is not mentioned here.

Until now, only spherical particles have been considered. However, spherical particles are only idealizations of real particles. In fact, real particles have an irregular shape. In this scenario it is not possible to derive a unique expression for the particle phase function. So, some empirical relations may be used, as the Legendre polynomials or the Henyey-Greenstein functions [166].

The Legendre polynomial representation of the particle phase function is:

$$p(g) = \sum_{j=0}^{\infty} b_j P_j(g) \tag{4.25}$$

where $b_j's$ are constants and $P_j's$ are the Legendre polynomials of order $j$. The combination of $b_j's$ must satisfy the condition of normalization given by equation 4.22. Equation 4.25 is useful when single scattering is not far from the isotropic and only the first terms are important.

Henyey e Greenstein (1941) introduced another empirical relation for the particle phase function:

$$p(g) = \frac{1 - g^2}{(1 + 2\xi \cos(g) + g^2)^{3/2}} \tag{4.26}$$

where $\xi$ represents the cosine of the asymmetry factor[5]. This parameter describes the anisotropy of the scattering. If $\xi$ is negative, it represents a backward scattering, while if $\xi$ is positive, it represents a forward scattering. Equation 4.26 is also known as the Henyey-Greenstein function or HG function.

Alternatively, it is sometimes used a double HG function, having two parameters: one related to the back-scattering lobe and another related to the forward scattering lobe (Fig.4.11). McGuire and Hapke (1995) [167] introduced an expression for the double HG function:

$$p(g) = \frac{1+c}{2}\frac{1-b^2}{1-2b\cos(g)+b^2} + \frac{1-c}{2}\frac{1-b^2}{1-2b\cos(g)+b^2} \qquad (4.27)$$

where parameter *b* is related to the lobes amplitude, varying between 0 and 1, and parameter *c* quantifies the dominant direction (Fig.4.12). The double HG function given by McGuire and Hapke (1995) [167] is widely used in practice as it can model particles with various shapes.

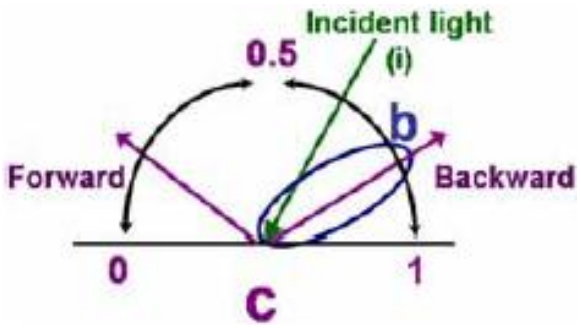


Fig.4.11 - Explanatory framework of the pair (b,c) [168].

McGuire and Hapke (1995) [167] modelled many kinds of particles with the double HG function, given by equation 4.27 and summarized their *b* and *c* parameters in a plot, shown in Fig.4.12.

However, if the particles that we aim to model are highly absorbing, as the transmitted light can be neglected, there are two other alternative expressions for the

[5] The cosine of the asymmetry factor is defined the mean value of the cosine of the diffusion angle $\theta$: $\xi = \langle cos(\theta) \rangle = -\frac{1}{2}\int_0^\pi cos(g)p(g)\,sin(g)dg$

particle phase function. But, these two expressions are not mentioned here as they are not commonly used.

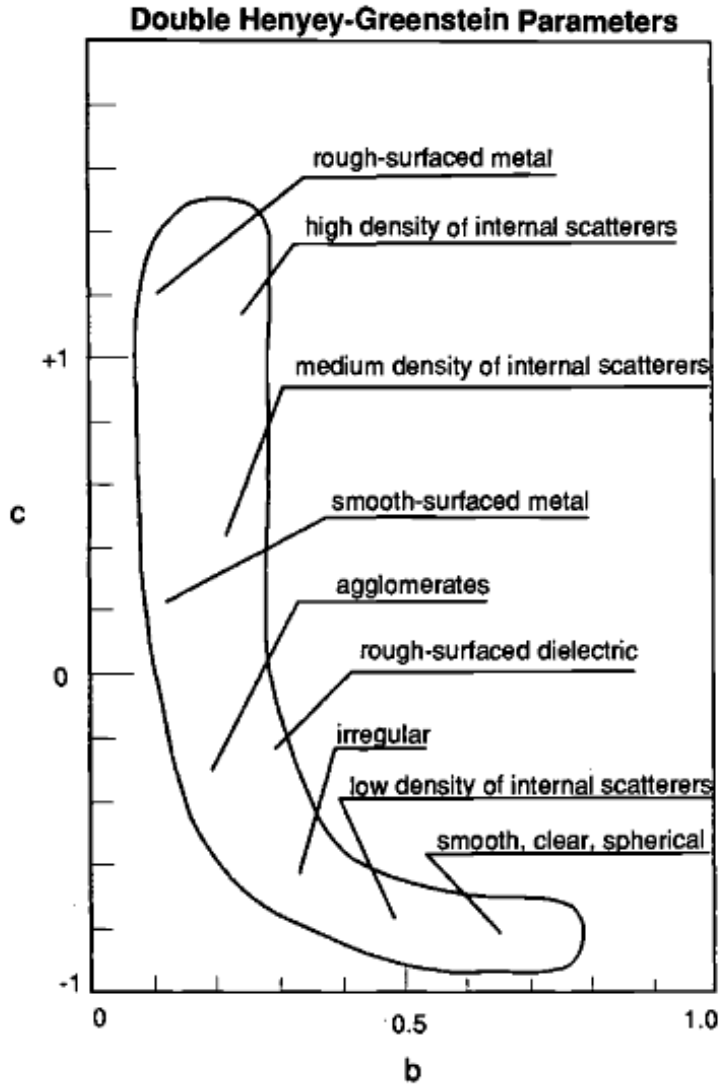


Fig.4.12 – Empirical double HG parameters for large silicate, resin and metal particles of varied shapes, absorption coefficients and conditions of surface roughness, and containing differing densities of internal scatters. Decreasing w causes a particle to move a short distance in a direction away from either end toward the center of the L-shape area. Almost any change that is made to a particle that is initially clear, smooth-surfaced and spherical decreases *b* and increases *c* [166].

## 4.3.1.4. Reflectance

As defined by Hapke (1993) [166], the term reflectance is the fraction of light that is diffusively scattered or reflected by a rough surface. A similar term, reflectivity, is the fraction of light which is specularly reflected from a smooth surface.

Depending on the geometry, there are many kinds of reflectances. But, two adjectives are used preceding the term reflectance that aim to characterize the geometry: the first term refers to the degree of collimation of the source, and the second that of the detector. The most commonly used adjectives are: directional, conic and hemispherical. If the preceding adjectives are the same, the prefix –bi is used. In this theme, Hapke (1993) [166] gives a summarized description about various kinds of reflectances and the corresponding symbols used (Fig.4.13).

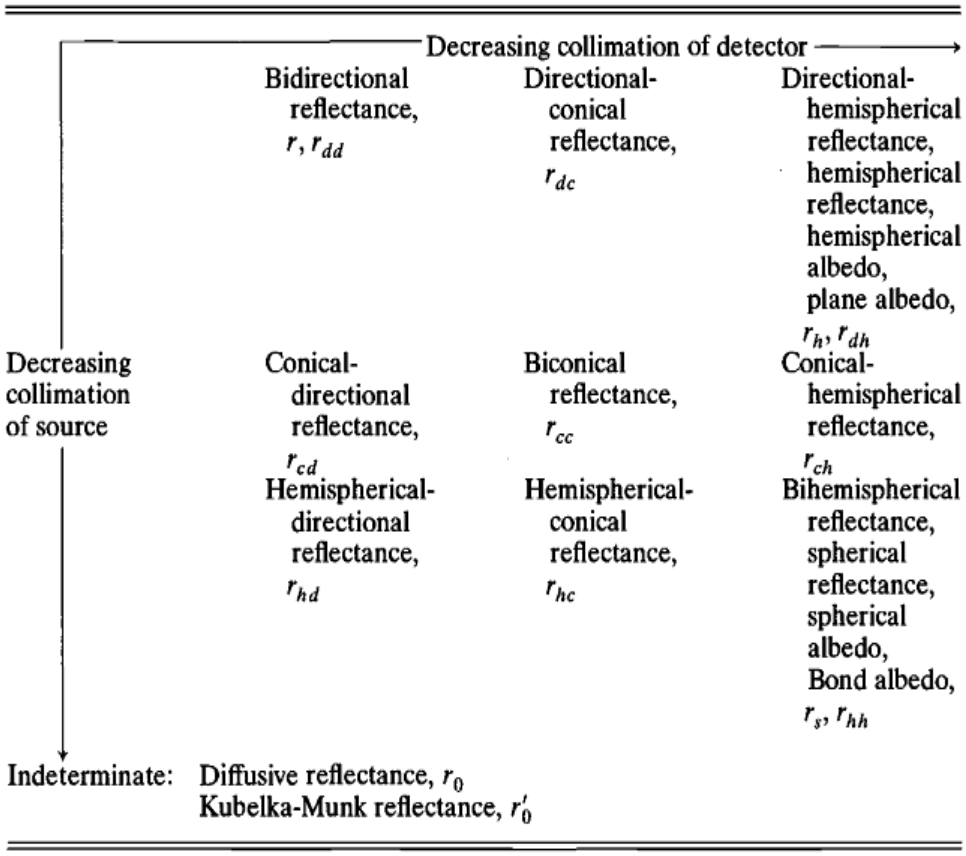


Fig.4.13 - Types of reflectances and their symbols [166].

The most commonly used reflectance is the bidirectional reflectance ($r(e,i,g)$), which refers to the fraction of light that is scattered into a direction *e*, when the surface is illuminated by a collimated light beam in the direction *i*.

## 4.3.1.4.1. Empirical relations of reflectance

The simplest empirical relation of the bidirectional reflectance is the Lambert Law [166], where the reflectance is proportional to the cosine of the incident angle:

$$r_L(i,e,g) = \frac{1}{\pi} A_L \mu_0 \tag{4.28}$$

where $A_L$ is denominated as the Lambert albedo constant. If a certain surface has $A_L = 1$, it is called a perfectly diffuse surface.

The Lambert Law gives good results when it is applied to surfaces where the albedo is high, but completely fails when the surfaces are dark.

Another empirical relation of the reflectance is the Minnaert's Law [166], which is a generalization of the Lambert Law. In 1941, Minnaert's proposed that the bidirectional reflectance can be derived from the expression:

$$r_M(i,e,g) = A_M \mu_0^{\nu} \mu^{\nu-1} \tag{4.29}$$

where $A_M$ is denominated as the Minnaert's albedo constant and $\nu$ represents the Minnaert's index. If $\nu = 1$, from equation 4.29, the Minnaert's Law is reduced to the Lambert's Law, where $A_M = \frac{A_L}{\pi}$.

The Minnaert's Law describes the variation of scattering of many surfaces over a limited range of angles.

### 4.3.1.4.2. Scattering Hapke's Law

The Hapke scattering theory is an approximate solution of the radiative transfer equation (Equation 4.19) for a semi-infinite surface, when it is illuminated by a collimated light beam with an irradiance *J* and a fixed incident angle *I* [166]. The radiation that is detected in the emergence angle *e*, is according to equation 4.19:

$$I = \int_0^{\infty} \left[ \frac{w(\tau)}{4\pi} \int_0^{4\pi} P(\tau, \Omega, \Omega') I(\tau, \Omega')\, d\Omega' + F(\tau, \Omega) \right] e^{-\tau/\mu} \frac{d\tau}{\mu} \tag{4.30}$$

where *F* is the source function: $F(\tau,\Omega) = \frac{w(\tau)J}{4\pi} p(\tau,g) e^{-\tau/\mu_0}$ (4.31) . The term $\int_0^{4\pi} P(\tau,\Omega,\Omega') I(\tau,\Omega')\, d\Omega' + F(\tau,\Omega)$ is the term due to the scattering across the optical depth *τ*.

Assuming that *p* and *w* are independent of *τ* and integrating equation 4.30 it is obtained that:

$$I_d = J\frac{w}{4\pi}\frac{\mu_0}{\mu+\mu_0}p(g) \tag{4.32}$$

where $I_d$ is the intensity of the scattered light. But, as the bidirectional reflectance is defined as the ratio between the intensity of the scattered light and the irradiance *J*:

$$r_d = \frac{I_d}{J} = \frac{w}{4\pi}\frac{\mu_0}{\mu+\mu_0}p(g) \tag{4.33}$$

If $p(g) = 1$, from equation 4.33:

$$r_d = \frac{w}{4\pi}\frac{\mu_0}{\mu+\mu_0} \tag{4.34}$$

Equation 4.34 is known as the Lommel-Seelinger Law.

Let us consider now a simple surface composed by particles that scatter light independently and isotropically [166]. The exact solution of this medium was derived by Ambartsumian (1958), based on the fact that adding a new thin layer to this surface will not change the reflectance. The reflectance of this medium is:

$$r(e,i,g) = \frac{w}{4\pi}\frac{\mu_0}{\mu+\mu_0}H(\mu_0)H(\mu) \tag{4.35}$$

where $H(x = \mu)$ is the *Ambartsumian-Chandrasekhar H-function*, which satisfies the following integral equation:

$$H(x) = 1 + \frac{w}{2}xH(x)\int_0^1 \frac{H(x')}{x+x'}dx' \tag{4.36}$$

The multiple scattering reflectance ($r_m$) is obtained by subtracting the total reflectance (equation 4.35) to the Lommel-Seelinger Law (equation 4.34):

$$r_m(e,i,g) = \frac{w}{4\pi}\frac{\mu_0}{\mu+\mu_0}[H(\mu_0)H(\mu) - 1] \tag{4.37}$$

Hapke (1993) [166] derived an approximate solution for equation 4.36, based on simple assumptions in solving the transfer radiative equation:

$$H(x) \approx \frac{1+2x}{1+2\Upsilon x} \tag{4.38}$$

where $\Upsilon = \sqrt{1-w}$ (4.39).

However, Hapke (1993) [166] also derived an accurate approximation for the *Ambartsumian-Chandrasekhar function*. Equation 4.36 can be rewritten in the following way:

$$H(x) = \left[1 - \frac{w}{2} x \int_0^1 \frac{H(y)}{x+y} dy\right]^{-1} \tag{4.40}$$

Solving equation 4.39, Hapke (1993) [166] obtained the following approximation for equation 4.36:

$$H(x) = \left[1 - [1-\gamma]x\left[r_0 + \left(1 - \frac{1}{2}r_0 - r_0 x\right) ln\left(\frac{1+x}{x}\right)\right]\right]^{-1} \tag{4.41}$$

where $r_0 = \frac{2}{1+\sqrt{1-w}} - 1$ (4.42).

More recently, Hapke (2002) [169] presented a better accurate version of the approximate solution for equation 4.36. Linearizing equation 4.36, Hapke (2002) [169] obtained that:

$$H(x) \approx \left[1 - wx\left(r_0 + \frac{1-2r_0 x}{2} ln\left(\frac{1+x}{x}\right)\right)\right]^{-1} \tag{4.43}$$

where $r_0 = \frac{1+\Upsilon}{1-\Upsilon} = \frac{1-\sqrt{\alpha(\alpha+s)}}{1+\sqrt{\alpha(\alpha+s)}}$ (4.44), where *s* represents the internal scattering coefficient of the particle near its surface.

The bidirectional reflectance of Hapke is obtained by the sum of equations 4.34 and 4.37:

$$r_H(e,i,g) = r_d + r_m = \frac{w}{4\pi}\frac{\mu_0}{\mu+\mu_0}[p(g) + H(\mu_0)H(\mu) - 1] \tag{4.45}$$

Equation 4.45 is a good approximation for dark surfaces or medium which scatter the light isotropically.

However, in laboratorial samples, the reflectance denotes a non linear growth for small values of *g*, near the opposition. The non linear peak that is evidenced is

called the opposition effect. This phenomenon is only found in dark surfaces which are porous and particulate and where the mutual blocks between the particles cause a shadow that is superior to the wavelength of the incident light beam: *Shadow-hiding opposition effect (SHOE).*

This opposition effect was studied by Hapke (1993) [166]. As only the single scattering is affected, Hapke (1993) [166] introduced a new term in equation 4.34:

$$r_d = \frac{w}{4\pi}\frac{\mu_0}{\mu+\mu_0}\mathrm{p(g)[1+B_S(g)]} \tag{4.46}$$

where $B_S(g)$ is the term due to the opposition effect and is defined as follows:

$$\mathrm{B_S(g)} = \frac{\mathrm{B_{S0}}}{1+\frac{1}{\mathrm{h_S}}\tan\left(\frac{\mathrm{g}}{2}\right)} \tag{4.47}$$

Finally, the expression of the Hapke bidirectional reflectance is obtained by replacing equations 4.46 and 4.37 in equation 4.45:

$$r_H(e,i,g) = r_d + r_m = \frac{w}{4\pi}\frac{\mu_0}{\mu+\mu_0}\left[[1+\mathrm{B_S(g)}]p(g) + H(\mu_0)H(\mu) - 1\right] \tag{4.48}$$

### 4.3.1.5. The equivalent slab approximation for $Q_S$

The internal transmission coefficient, *Θ*, lists the fraction of light that enters into a particle and the fraction of light that reaches the opposite surface, after transmitted. The internal transmission coefficient is defined as follows:

$$\Theta = \frac{2\mathrm{n}^2}{(\alpha\,\mathrm{D})^2}\left\{\exp\left(-\alpha\,\mathrm{D}\left(1-{}^{1}\!/_{\mathrm{n}^2}\right)^{1/2}\left(1+\alpha\,\mathrm{D}\left(1-{}^{1}\!/_{\mathrm{n}^2}\right)\right)\right) - \exp(-\alpha\,\mathrm{D})[1+\alpha\,\mathrm{D}]\right\}$$ [6] (4.49)

where $D = 2a$ represents the diameter of the particle.

[6] A deduction of this expression can be found on Hapke (1993) [164], page 98.

Let $< D >$ be the mean path length travelled by the light beam. It represents the thickness of a slab, that will have the same value of Θ, when $\alpha -> 0$. For the slab: $\Theta = e^{-\alpha D} \approx 1 - \alpha < D >$ (4.50).

Expanding equation 4.49 in powers of $\alpha D$:

$$< D >= \frac{2}{3}\left(n^2 - \frac{1}{n}(n^2 - 1)^{3/2}\right) D \tag{4.51}$$

where $< D >$ is the mean distance travelled by all rays of light during a single transit of the particle.

If the internal transmission coefficient of a particle near to its surface is equal to zero $(s = 0)$: $\Theta = e^{-\alpha D}$ (exponential model).

If $s > 0$, the scattering occurs between the particles or close to their surfaces. In this case, the internal transmission coefficient is given by:

$$\Theta = \frac{r_0 + \exp\left(-< D > \sqrt{\alpha(\alpha + s)}\right)}{1 - r_0 \exp\left(-< D > \sqrt{\alpha(\alpha + s)}\right)} \text{ (Internal Scattering Model)} \tag{4.52}$$

In the case of planetary regolith particles, where $a >> \lambda$, the extinction efficiency is: $Q_E = 1$. Hence, the albedo *w*, can be defined as follows:

$$w = \frac{Q_S}{Q_E} = \frac{Q_S}{Q_S + Q_A} = Q_S \tag{4.53}$$

According to the equivalent slab model, a good approximation for $Q_S$, when the incident light is unpolarized, consists in replacing the spherical particle by a slab, with adequate optical constants (Fig.4.14).

Let $S_E$ and $S_I$ be defined as the external and internal reflectance Fresnel coefficients of a surface, respectively. According to Hapke (1993) [166], an empiric approximation for $S_E$, can be written as:

$$S_E \approx \frac{(n-1)^2 + k^2}{(n+1)^2 + k^2} + 0.05 \tag{4.54}$$

The latter equation (4.54) gives good results (Fig.4.15) for $k^2 \ll 1$ and $1.2 \lesssim n \lesssim 2.2$. On the other hand, the internal reflectance of a surface can be approximated by:

$$S_I \approx 1 - \frac{4}{n(n+1)^2} \tag{4.55}$$

The latter equation (4.55) also gives good results (Fig.4.15) for $k^2 \ll 1$ and $n \gtrsim 3$.

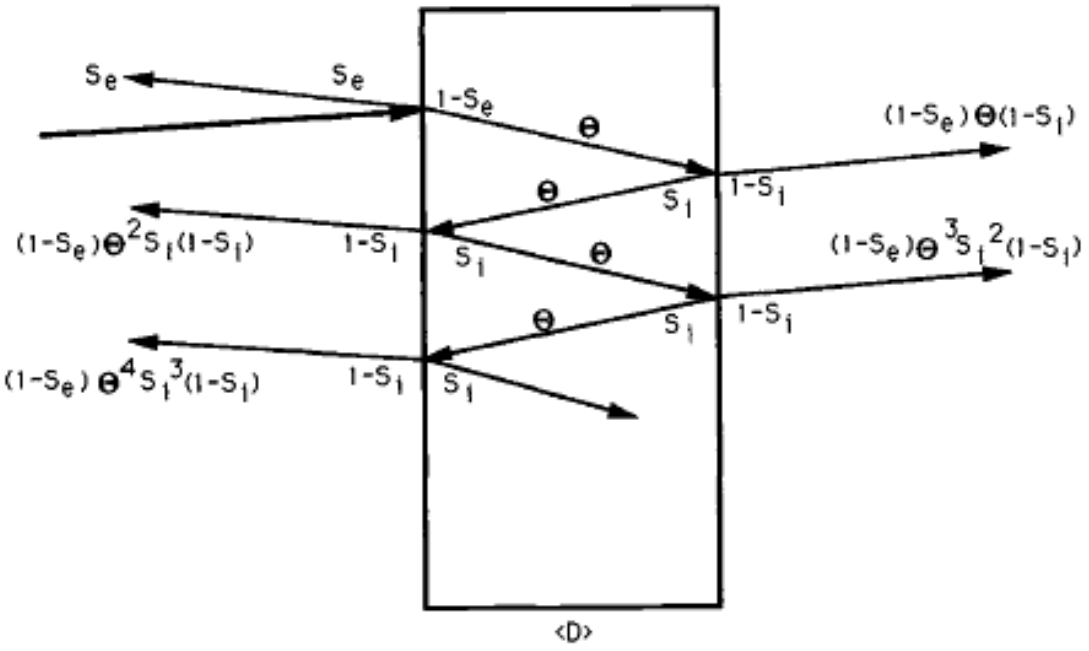


Fig.4.14 - Scheme of the equivalent slab model for $Q_S$ [166].

In Fig.4.14 there are two quantities that have not been defined yet: $S_E$ and $S_I$.

Returning to Fig.4.14, during the first passage through the particle, a fraction of light $S_I$ is internally reflected and the remaining 1-$S_I$ is refracted through the surface. This process continues as it is evidenced in Fig.4.14. Due to spherical symmetry of the problem, the reflection coefficients are the same for each order of internal reflection.

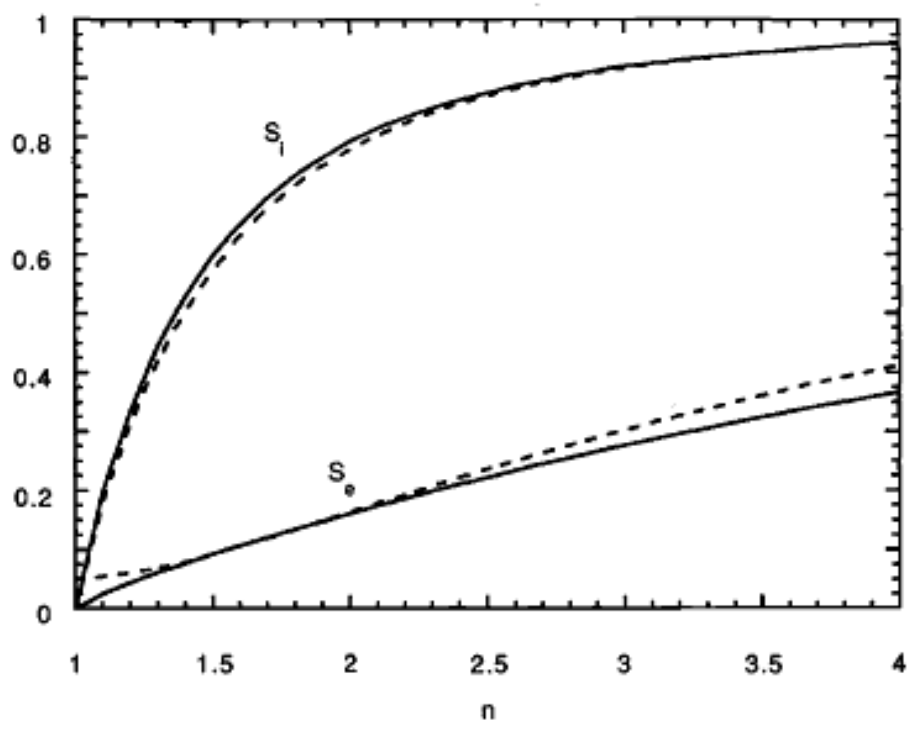


Fig.4.15 - External ($S_E$) and Internal ($S_I$) surface reflectance coefficients versus the refractive index for $k << 1$. The solid lines denote the exact expressions while the dashed lines denote the approximations results [166].

Hence, the total fraction of light emerging from the surface is:

$$Q_S = S_E + (1 - S_E)\Theta(1 - S_I) + (1 - S_E)\Theta S_I\,\Theta(1 - S_I) + (1 - S_E)\Theta S_I\,\Theta S_I\,\Theta(1 - S_I) + \cdots$$

$$Q_S = S_E + (1 - S_E)\Theta(1 - S_I)[1 + S_I\,\Theta + (S_I\,\Theta)^2 + \cdots]$$

$$Q_S = S_E + (1 - S_E)\frac{(1 - S_I)}{(1 - S_I\Theta)}\Theta \tag{4.56}$$

Due to the spherical symmetry of the problem, $S_E = S_I$. So, from equation 4.56:

$$Q_S = S_E + (1 - S_E)\frac{(1 - S_E)}{(1 - S_E\Theta)}\Theta \tag{4.57}$$

From equation 4.57, the absorption efficiency can also be obtained:

$$Q_A = 1 - Q_S = (1 - S_E)\frac{1 - \Theta}{1 + S_E\Theta} \tag{4.58}$$

U.PORTO
FACULDADE DE CIÊNCIAS
UNIVERSIDADE DO PORTO

## 4.4. Computation of the Hapke Model and justification of the parameters used

The Hapke Model is usually cited as a two step model. First, the reflectance spectra are converted into single scattering albedo, where the effects of geometry are removed. Second, the single scattering albedo is converted into optical constants, where the grain size of the sample particles is removed. However, for the purpose of this study, the Hapke Model will be only used to derive the single scattering albedo of the meteorite samples from their reflectance spectra. Hence, only the first step of the Hapke Model will be computed.

The radiance coefficient is derived through the bidirectional reflectance expression of Hapke (1993) [166]:

$$r_H(e,i,g) = r_d + r_m = \frac{w}{4\pi}\frac{\mu_0}{\mu+\mu_0}\left[[1+\mathrm{B_S(g)}]p(g) + H(\mu_0)H(\mu) - 1\right] \qquad (4.59)$$

The bidirectional reflectance of Hapke (1993) [166] is derived as function of six parameters: the albedo *w*, the cosines of the incident and emergence angles ($\mu_0$ and $\mu$, respectively), the opposition effect $B_S(g)$, the particle phase function $p(g)$ and the *Ambartsumian-Chandrasekhar* functions ($H(\mu_0)$ e $H(\mu)$).

The opposition effect can be set to 0 for phase angles greater than 15º. In this study, the phase angles are 30º and so the opposition effect can be neglected [170].

The particle phase function used is the one given by the second order Legendre polynomials:

$$p(g) = 1 + b\cos(g) + c(1.5cos^2(g) - 0.5) \qquad (4.60)$$

where $b = -0.4$ and $c = 0.25$, which are the appropriate average values for forward scaterring minerals [170].

$H(x)$ is the *Ambartsumian-Chandrasekhar* function. In this work it will be used the approximation derived by Hapke (1993) [166]: Eq.4.41.This approximation is an accurate approximation derived by Hapke (1993) [166] that was later confirmed to give results close to the exact solutions one's [171].

The first step of the Hapke Model described above was implemented using Microsoft Excel [1]. It was shown that the implementation of this model in Microsoft Excel also gives accurate results, when compared to other software implementations, such as Matlab or IDL [1]. In addition, the implementation of this model in Excel can be accessible to all people that have Microsoft Office installed in their computers.

The first step of this compositional model was coded using Visual Basic for Applications (VBA), available on Microsoft Excel software [1]. Firstly, the *w* value is derived through an optimization process to find the radiance coefficient which matches the spectral measurements. This optimization process is done through a table of values of $r_c$ and *w*. For accuracy, $r_c$ is calculated for 1000 values of *w*, varying stepwise from 0 to 1. A linear interpolation between adjacent values is made in order the increase the accuracy. The VLOOKUP() function is used to find the nearest values to the spectral measurements and the corresponding single scattering albedo is output. This process is repeated for each wavelength [1].

In Fig.4.17 a general view of the input spreadsheet of the Hapke Model implementation is presented. Reflectance spectrum of a sample is input into the spreadsheet as two columns of data (columns highlighted in orange), one containing wavelength and the other containing the corresponding reflectance measurement. The ID of the sample is input into the spreadsheet into cells B1, B2 and B3 (cells highlighted in red). Model variables' are grouped in the green box: green colored cells represent sample specific values; orange colored cells represent assumptions of the Hapke Model. The buttons, displayed in Fig.4.17, are used to run the Hapke Model by steps, which are coded using VBA. The button called "Chart 1: Reflectance vs Wavelength" is used to obtain the plot of the input data. The button called "Clear Chart 1" is used to clear the created plot of the input data. The button called "Solving for Albedo" is used to solve the first step of the Hapke Model, which calculates the single scattering albedo from the input reflectance data, for each wavelength, through the optimization process described above. The button called "Clear Albedo Calculations" is used to clear all the calculations done in the first step of the model. The button called "Chart2: Albedo vs Wavelength" is used to obtain the plot of the derived single scattering albedo versus wavelength. The button "Clear Chart 2" is used to clear the single scattering albedo versus wavelength plot.

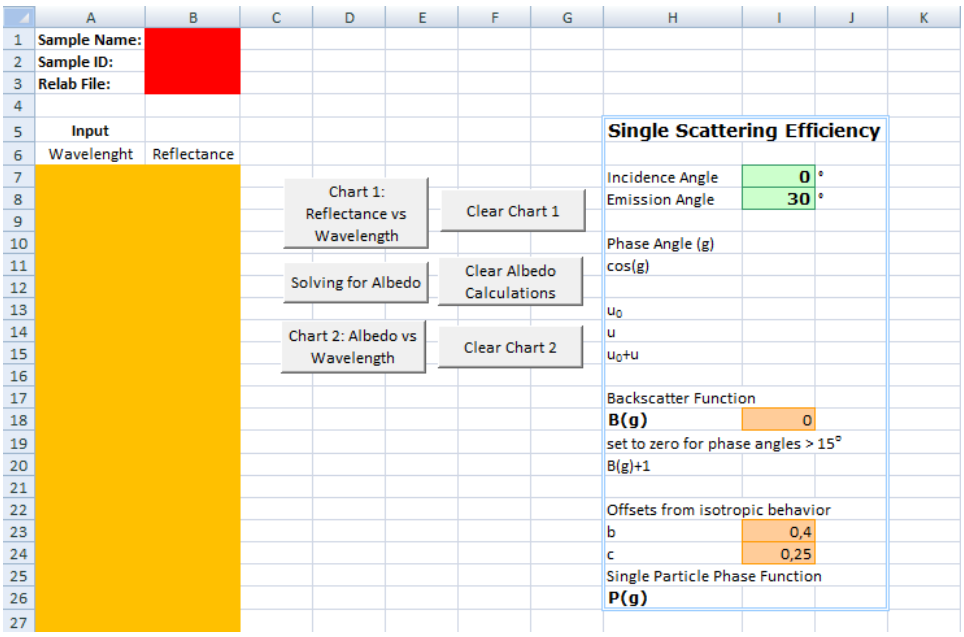


Fig.4.17 - Input parameters for the Hapke Model spreadsheet. Red colored cells represent the identification of the sample, orange colored cells represent the input spectra data, green colored cells represent sample specific values and orange colored cells represent assumptions of the Hapke Model.

## 4.5. Compositional Determination using the Solver tool in Microsoft Excel

The mineralogical composition of a sample can be derived by fitting its single scattering albedo curve through the linear combination of reasonable end-member minerals and minimizing the sum of the residuals's squares $\chi^2$ (i.e. by minimizing the difference between the single scattering albedo' and the modelled curves through the method of least squares). But, it is important to note that any mixing model is strongly dependent on the choice of end-members. If end-members are not constrained, then derived model abundances must be viewed as an estimate of possible composition and not as a unique determination.

This process was also implemented using Microsoft Excel software (authors: Teresa M. Seixas and M. A. Salgueiro da Silva, Physics and Astronomy Department, Faculty of Sciences, University of Porto, 2010). A resulting demo spreadsheet is shown in Fig.4.18.

U.PORTO
FACULDADE DE CIÊNCIAS
UNIVERSIDADE DO PORTO

| | A | B | C | D | E | F | G | H | I | J | K |
|---|---|---|---|---|---|---|---|---|---|---|---|
| 1 | RELAB ID: | | | | | Parameters | | | Sum Square | | |
| 2 | RELAB Sample: | | | | | xA | xB | | 0 | | |
| 3 | | | | | | 1 | 1 | | | | |
| 4 | RELAB ID: | | | | | | | | | | |
| 5 | RELAB Sample: | | | | | | | | | | |
| 6 | Mineral: | | | | | | | | | | |
| 7 | Grain size: | | | End-members | | Mixture | | | | | |
| 8 | | | wavelength (microns) | w(A) | w(B) | w | | wcalc | wcalc-w | (wcalc-w)^2 | |
| 9 | RELAB ID: | | | | | | | 0 | 0 | 0 | |
| 10 | RELAB Sample: | | | | | | | 0 | 0 | 0 | |
| 11 | Mineral: | | | | | | | 0 | 0 | 0 | |
| 12 | Grain size: | | | | | | | 0 | 0 | 0 | |
| 13 | | | | | | | | 0 | 0 | 0 | |
| 14 | | | | | | | | 0 | 0 | 0 | |
| 15 | | | | | | | | 0 | 0 | 0 | |
| 16 | | | | | | | | 0 | 0 | 0 | |
| 17 | | | | | | | | 0 | 0 | 0 | |
| 18 | | | | | | | | 0 | 0 | 0 | |
| 19 | | | | | | | | 0 | 0 | 0 | |
| 20 | | | | | | | | 0 | 0 | 0 | |
| 21 | | | | | | | | 0 | 0 | 0 | |
| 22 | | | | | | | | 0 | 0 | 0 | |
| 23 | | | | | | | | 0 | 0 | 0 | |

Fig.4.18 – General overview of the demo spreadsheet developed in Microsoft Excel, to derive the mineralogical composition of laboratory mixtures.

In Fig.4.18 the highlighted cells in orange represent the identification of the samples. The single scattering albedo for the sample and end-members must be placed in the columns which are highlighted in yellow and purple, respectively. The range of wavelength must be placed in the column highlighted in cyan. Highlighted in grey there are two initial estimates of the end-members proportions presented in the sample. The sum of the residuals is highlighted in green. In column H, the modelled single scattering albedo is derived. In column I, the residuals are derived. In column J, the square of the residuals is calculated. The derivations presented in cells highlighted in grey and columns H, I and J are changed each time the Solver is applied until the minimal solution (i.e. the lowest of the residuals' sum) is found.

U.PORTO
FACULDADE DE CIÊNCIAS
UNIVERSIDADE DO PORTO

# 5. Results and Discussion

In this study it is aimed to test the hypothesis that a mixture of HED meteorites can simulate the spectra of V-type asteroids. Or, by other words, it is aimed to investigate if HED meteorites are genetically linked to V-type asteroids. In order to investigate this possibility, it is needed to derive the mineralogical composition of the chosen HED meteorites and V-type asteroids. So, firstly the Hapke radiative transfer model will be applied to derive the single scattering albedo of the chosen samples. After this task accomplished, the mineralogical composition of the chosen samples will be derived through the Solver implementation, described in the last chapter.

Nowadays, it is currently known that asteroids's surfaces are exposed to impacts of interplanetary meteor bombardment. Hence, their surfaces are thought to be composed by fine-grained particles that are mixtures of rock minerals. However, the particles sizes are not yet known, despite some evidences show that grain sizes may be coarser than on the lunar regolith. Hence, it is reasonable to accept that grain sizes on asteroids will vary between 30 and 300 μm, as the lunar regolith grain sizes range between 10 and 50 μm [172]. But, finer-grained particles tend to coat coarser-grain particles, making the finer grains of the mixture more important. So, it is also aimed in this study to infer about the grain sizes of asteroids's particles, through meteorites. It is important to quote that the effects of space weathering will not be modelled in this study.

In this section, the results of this study will be presented. In addition, a discussion about the obtained results will be done. However, before applying the procedure described in the last chapter to derive the mineralogical compositions of HED meteorites and of V-type asteroids, it is important to check if this procedure is giving accurate results. Hence, to build confidence, its application was firstly tested in several laboratory mixtures. Their mineralogical compositions will be derived through this procedure and will be compared with their nominal compositions. After this step accomplished, the same procedure will then be applied to derive the mineralogical compositions of HED meteorites and of V-type asteroids.

U.PORTO
FACULDADE DE CIÊNCIAS
UNIVERSIDADE DO PORTO

## 5.1. Laboratory Mixtures of Minerals

A set of laboratory mixtures of minerals were selected and analyzed from the RELAB database (Reflectance Experiment Laboratory [173], available at http://www.planetary.brown.edu/relab), containing low-Ca pyroxenes (orthopyroxenes), high-Ca pyroxenes (clinopyroxenes) and olivine. The set of laboratory mixtures were selected from Duffard et al. (2005) [174] and are listed in Table D1. Their spectra range in wavelength between 0.3 and 2.6 μm, and were obtained with a 0.005 μm sampling resolution. The RELAB instrument is designed to simulate the diverse viewing geometries in remote telescopic measurements. A 30° incident angle and a 0° emission angle (measured from the vertical) were the default parameters for the measured spectra. The details of RELAB and how the spectra were obtained are described in the RELAB users' manual. The reflectance spectra of these mixtures are presented in Figs.5.1-5.3. Please note that laboratory mixtures presented in the next plots are identified by the RELAB file name. If it is aimed to know the RELAB sample ID, check Table D1.

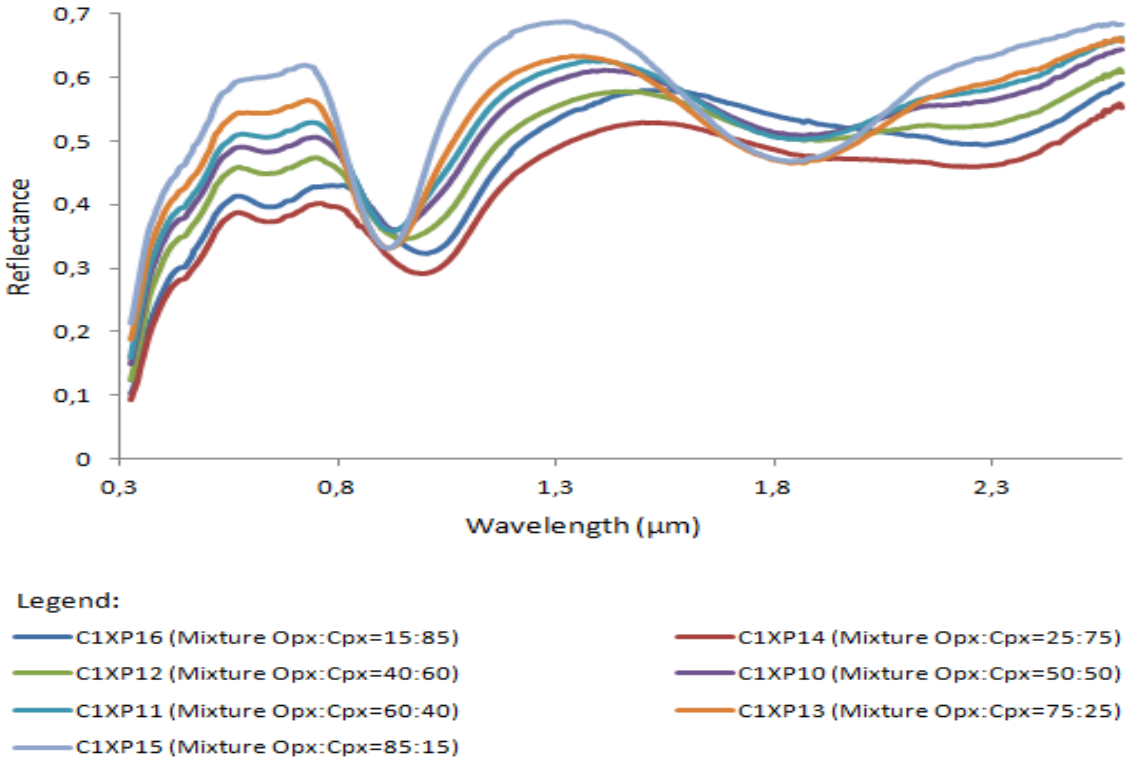


Fig.5.1 - Reflectance spectra of the seven laboratory mixtures of orthopyxorene and clinopyroxene obtained from the RELAB database, with a grain size proportion ranging between 0-45μm.

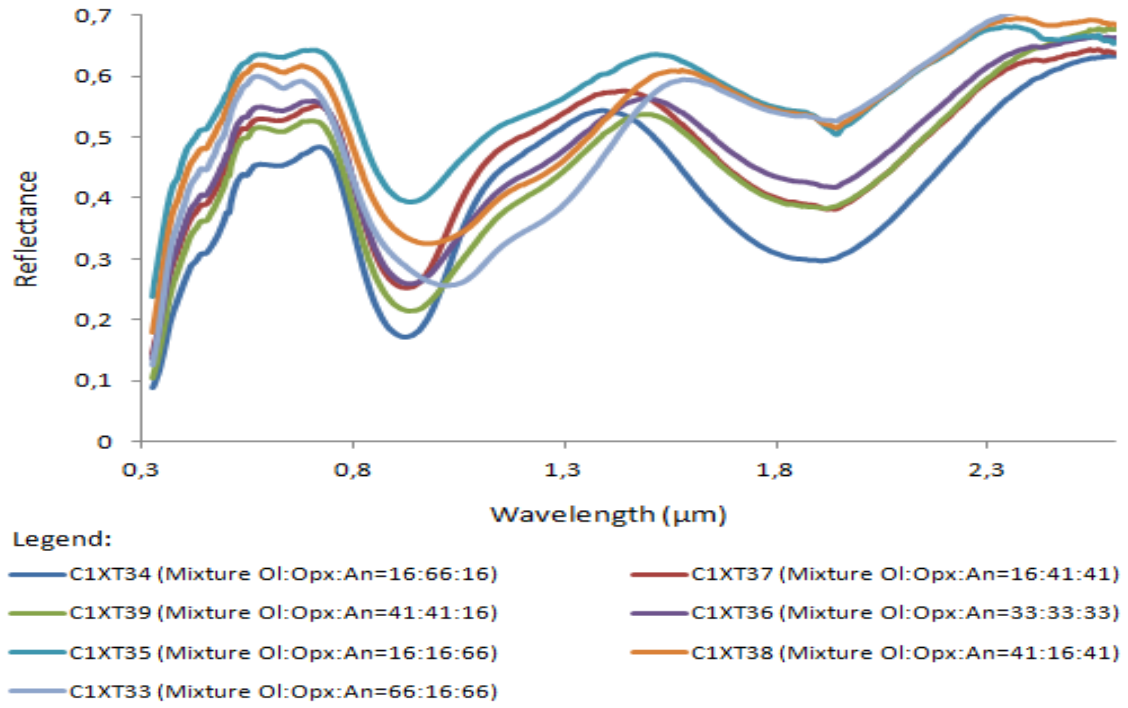


Fig.5.2 - Reflectance spectra of the seven laboratory mixtures of olivine, orthopyxorene and anorthosite obtained from the RELAB database, with a grain size proportion ranging between 45-75µm.

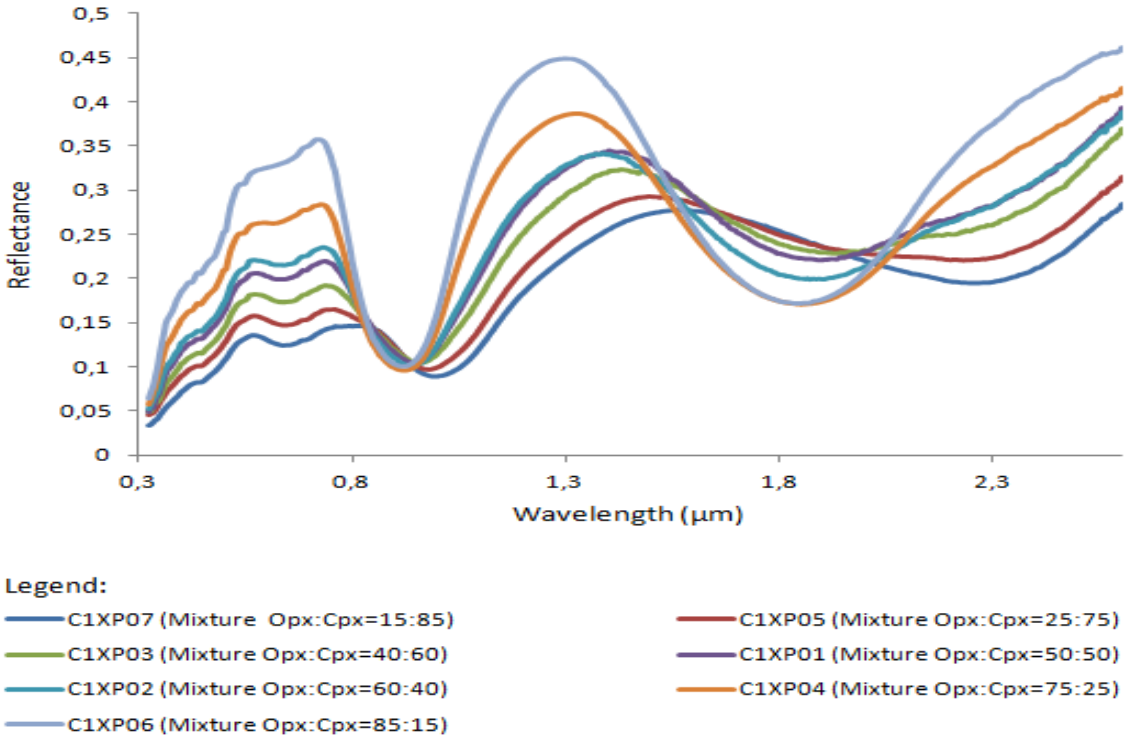


Fig.5.3 - Reflectance spectra of the seven laboratory mixtures of olivine, orthopyxorene and anorthosite obtained from the RELAB database, with a grain size proportion ranging between 70-145µm.

The Hapke radiative transfer model was applied to derive the single scattering albedo of all selected samples. The derived single scattering albedo are plotted in Figs.5.4-5.5

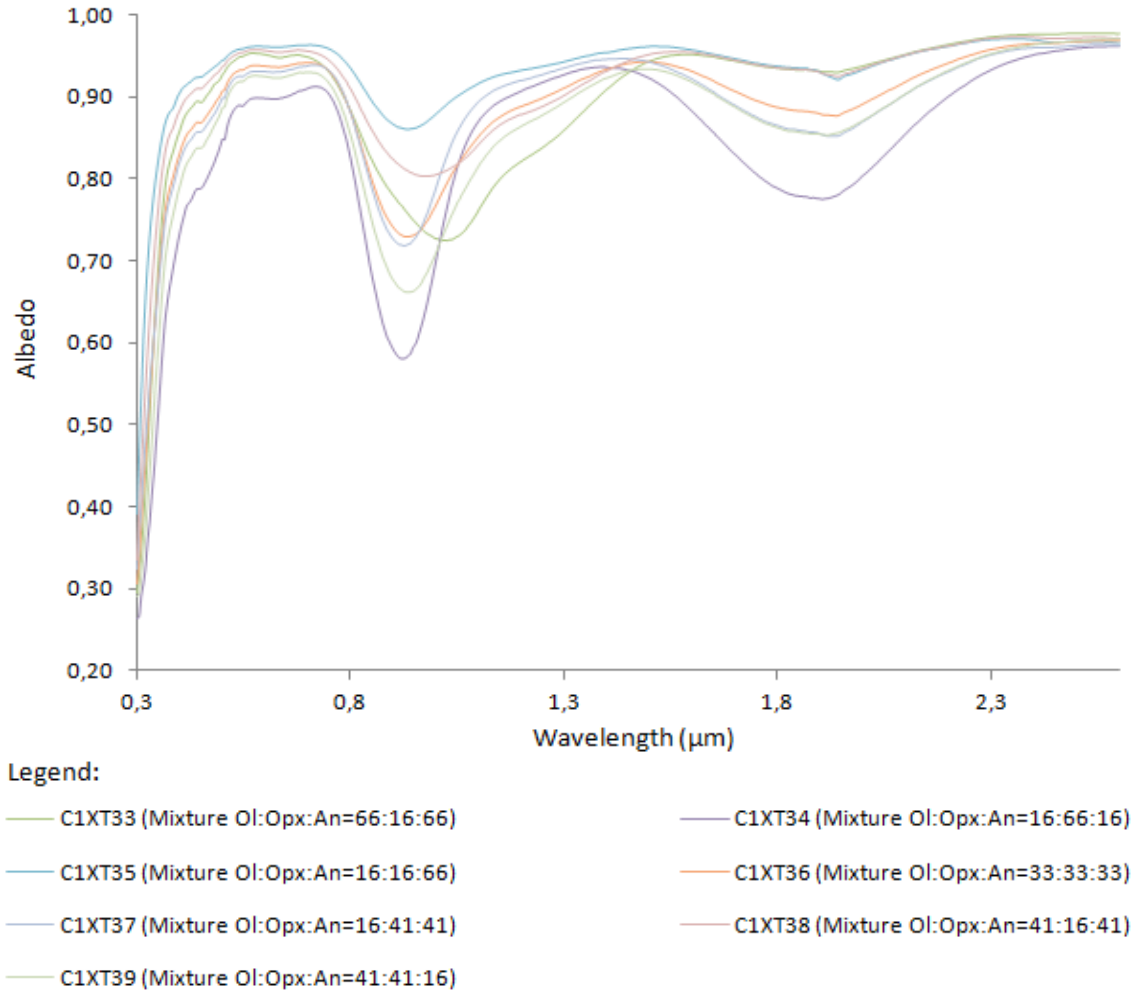


Fig.5.4 - Plot of the single scattering albedo versus wavelength, for all the 7 laboratory mixtures with the following end-members: anorthosite, orthopyxorene and olivine.

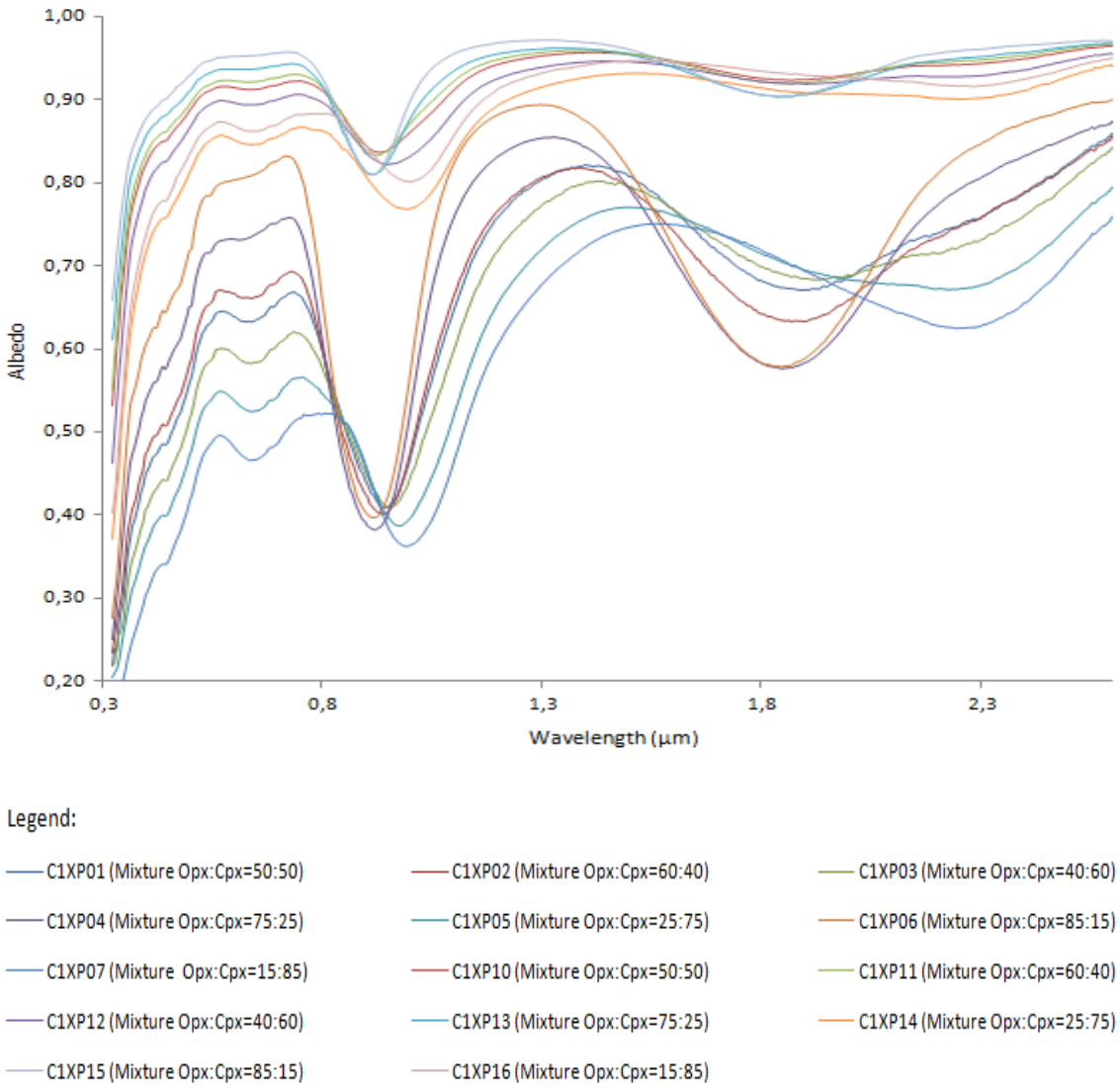


Fig.5.5 - Plot of the single scattering albedo versus wavelength, for all the 14 laboratory mixtures with the following end-members: clinopyroxene and orthopyxorene.

After having derived the single scattering albedo for all the 21 laboratory mixtures samples, it is aimed to derive their mineralogical compositions. For this purpose, eight end-member minerals were selected from the RELAB database, which are listed in Table D2. For these eight selected end-members, the single scattering albedo was also derived through the Hapke radiative transfer model. Afterwards, the mineralogical compositions of all the 21 laboratory mixtures were derived using the process described in the last chapter. The derived mineralogical compositions for all the 21 laboratory mixtures are listed in Table D1.

The single scattering albedo and the fitted curve, of the sample XP-CMP-010, are presented in Fig.5.6. In addition, the selected end-members are also presented. The cyan line in Fig.5.6 represents the residuals, which seem to be almost flat. However, observing Fig.5.7 the residuals shows some little variations, evidencing the regions where the single scattering albedo was worst fitted. As it can be seen from Fig.5.7, the worst fitted region is found roughly between 0.3 and 0.6 μm. The plots including the single scattering albedo, the fitted curves and the end-members and the residuals' plot, for all the others 20 laboratory mixtures can be found in Fig.E1 to Fig.E40 (Section E).

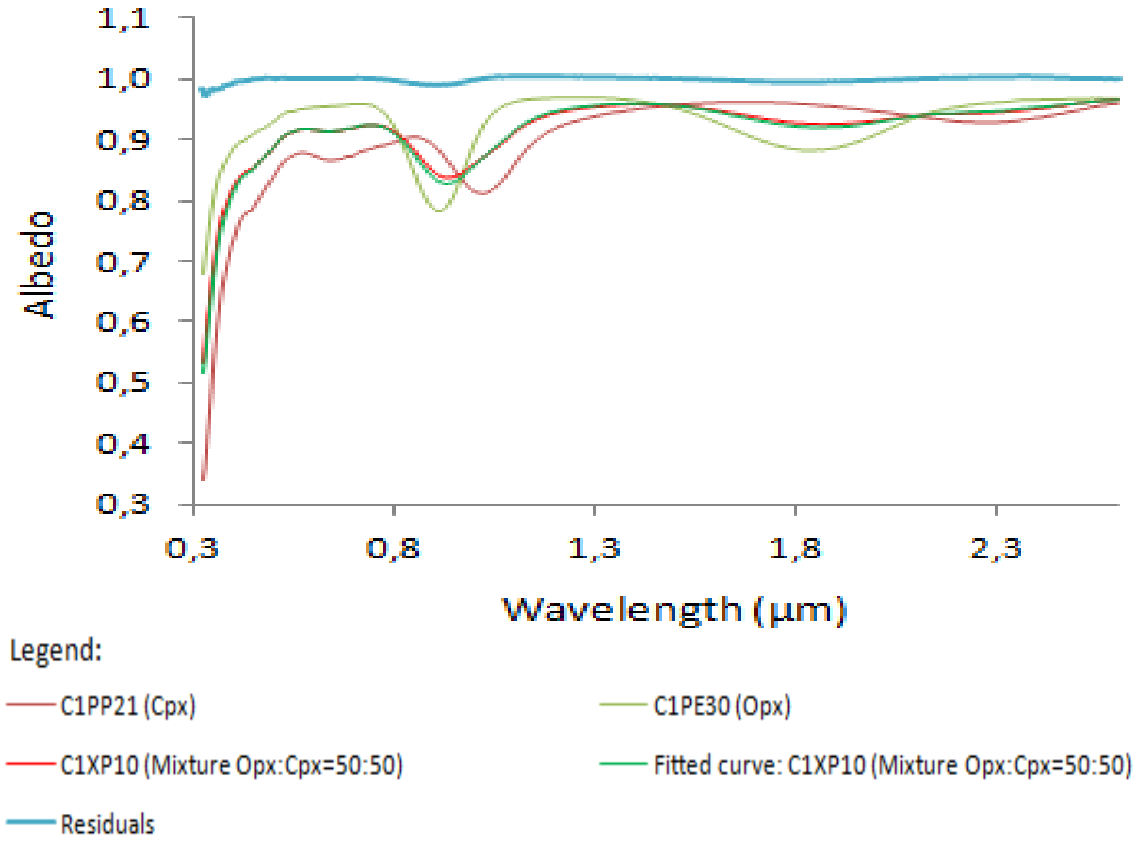


Fig.5.6 – Plot of the single scattering albedo of the sample XP-CMP-010 (C1XP10) and their end-members (orthopyroxene (Opx) and clinopyroxene (Cpx)) versus wavelength. The selected files for orthopyroxene and clinopyroxene were PP-CMP-021 (C1PP21) and PP-CMP-030 (C1PE30), respectively. The residuals (cyan line) were translated from 0 to 1.

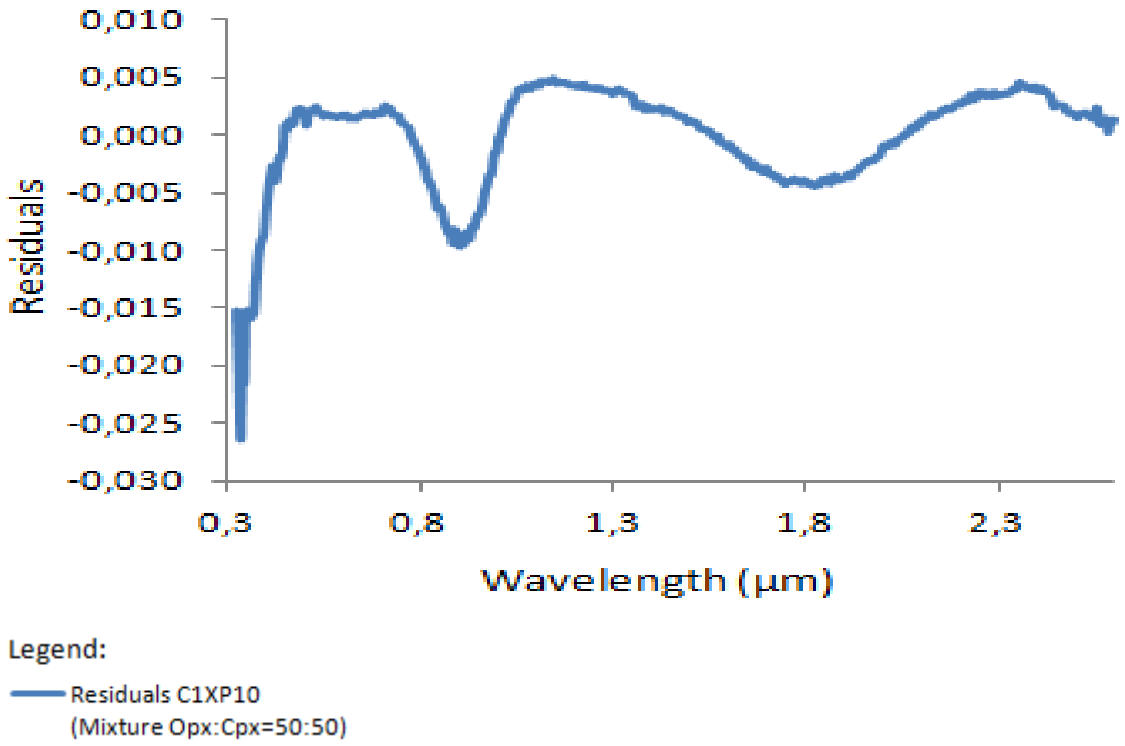


Fig.5.7 - Plot of the residuals of the sample XP-CMP-010 (C1XP10).

All single scattering albedo of the laboratory mixtures with a grain size proportion between 0 and 45µm were well fitted. The only exception is the case of the sample XP-CMP-014, as constrained by the residuals in Fig.E.4. For these seven laboratory mixtures, their nominal and derived compositions are plotted in Fig.5.8. In addition, the problem stated above about the derived composition for the sample XP-CMP-014, seems to be supported by Fig.5.8. It is evidenced a little discrepancy between the nominal and derived compositions for this sample. In the case of the laboratory mixtures with a grain size proportion between 45 and 75µm, only the single scattering albedo' of the samples XT-CMP-033 (Fig.E13), XT-CMP-035 (Fig.E17) and XT-CMP-038 (Fig.E23) seem to be well fitted as it constrained by their residuals. In all the other cases, the absorption feature found near 2 µm is not perfectly fitted, as evidenced by the samples residuals'. However, the absorption feature found near 1 µm seems to be well fitted in all the samples. For these seven laboratory mixtures, their nominal and derived compositions are plotted in FigS.5.9- 5.11.

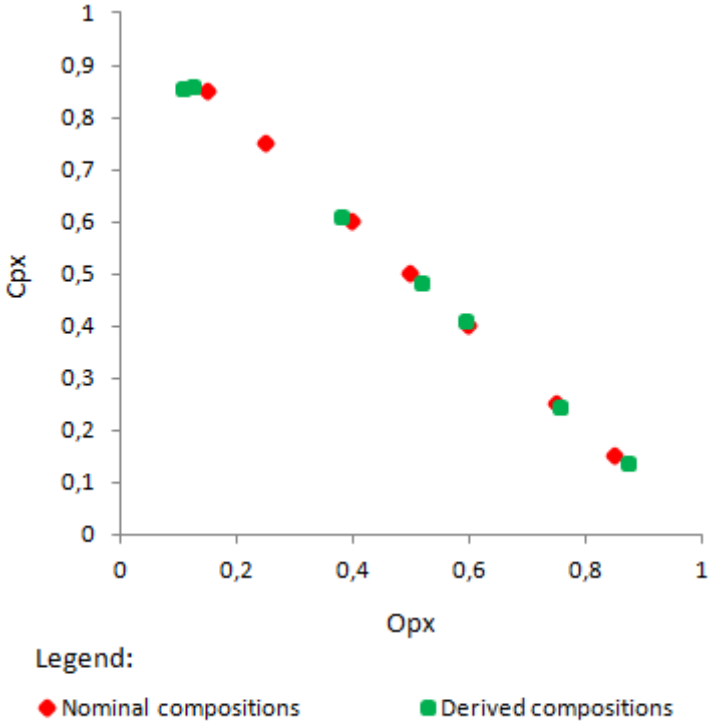


Fig.5.8 - Plot of clinopyroxene (Cpx) versus orthopyroxene (Opx) nominal and derived compositions for all seven laboratory mixtures with a grain size proportion between 0 and 45µm.

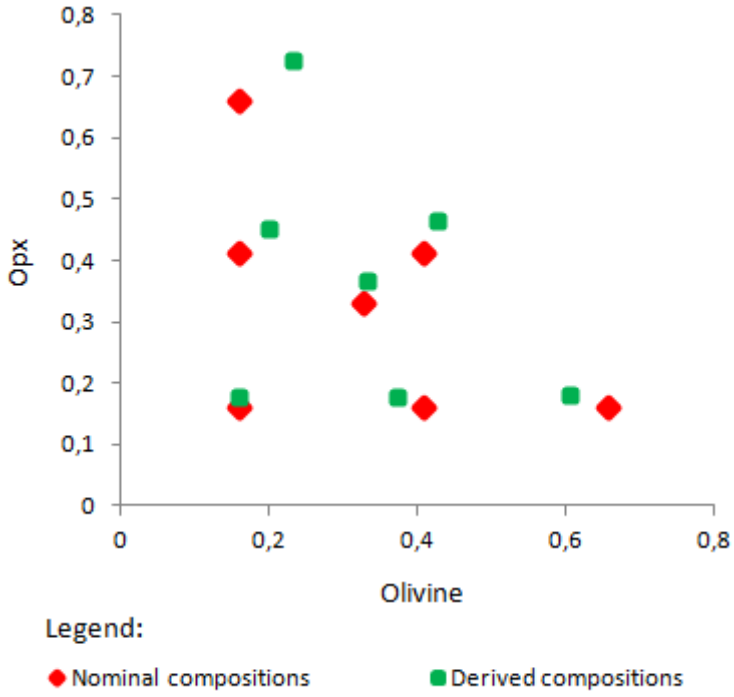


Fig.5.9 - Plot of orthopyroxene (Opx) versus olivine nominal and derived compositions for all seven laboratory mixtures with a grain size proportion between 45 and 75µm.

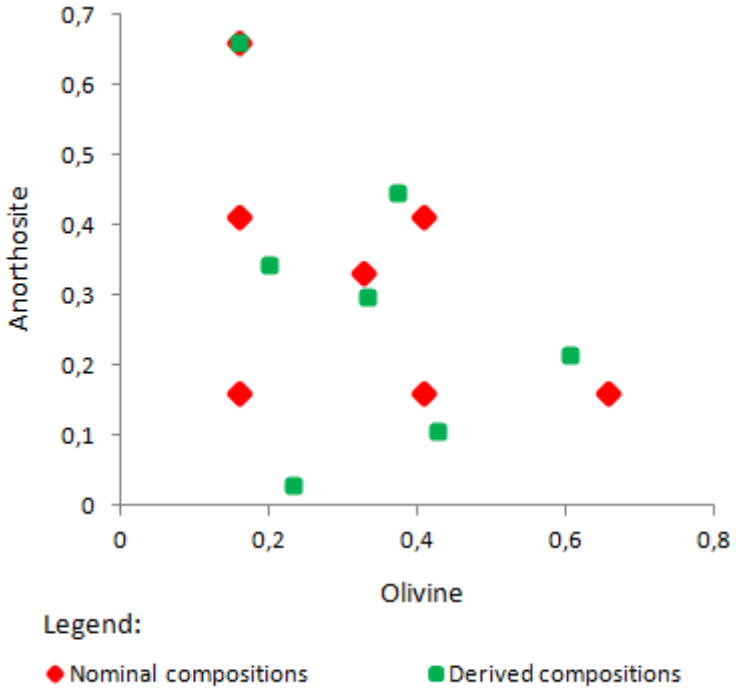


Fig.5.10 - Plot of anorthosite versus olivine nominal and derived compositions for all seven laboratory mixtures with a grain size proportion between 45 and 75μm.

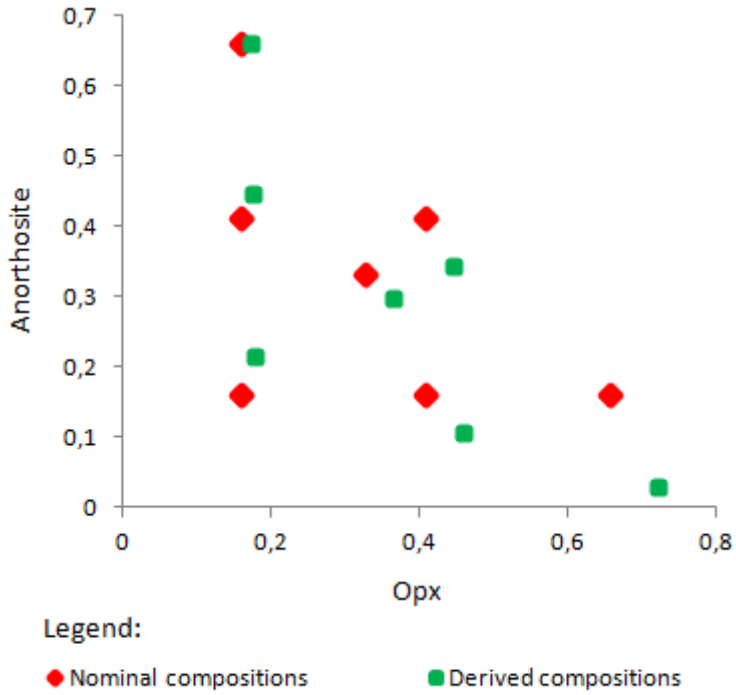


Fig.5.11 - Plot of anorthosite versus orthopyroxene (Opx) nominal and derived compositions for all seven laboratory mixtures with a grain size proportion between 45 and 75μm.

According to Fig.5.9, the derived mineralogical compositions, for orthopyroxene and olivine, seem to be close to the nominal compositions. However, only the case of the sample XT-CMP-034 shows a little discrepancy between the derived and nominal compositions. Actually, the single scattering albedo of this sample is not well fitted, as it is also constrained by its residuals' plot (Fig.E16). In addition, this discrepancy is also evidenced in Fig.5.10 and Fig.5.11. In all the others samples, the derived mineralogical compositions, for anorthosite and olivine (Fig.5.10) and for anorthosite and orthopyroxene (Fig.5.11), seem to be close to the nominal compositions.

In all laboratory mixtures with a grain size proportion between 70 and 145 μm the single scattering albedo seems to be well fitted, as evidenced by their residuals. However, in some samples, the residuals show some variance near the 1 μm absorption band. This can be due to the effects of the grain size proportion: in fact, the grain size proportion of the chosen end-members is 70 to 125 μm, inferior to the ones of the selected samples. Actually, it is also important to quote the effect of the grain size proportion of the end-members in the derivation of the mineralogical composition of the mixtures. The grain size proportion of the end-members may be similar to the ones of the selected laboratory mixtures. However, in this case none end-members with a grain size proportion between 70 and 145 μm were found in the RELAB database. Only end-members with close values of the grain size proportion between 70 and 125 μm were found.

In Fig.5.12 and 5.13 the effect of the grain size proportions are evidenced. In Fig.5.12, the reflectance spectra of all three clinopyroxenes, selected from the RELAB database, are plotted. It can be seen that as the grain size proportion increases, the reflectance spectra decreases. In Fig.5.13, the single scattering albedo versus wavelength is plotted, for all three clinopyroxenes. It can be also seen that as the grain size proportion increases, the derived albedo decreases. Hence, if the grain size proportions are not taken into account the derived mineralogical composition may be completely meaningful.

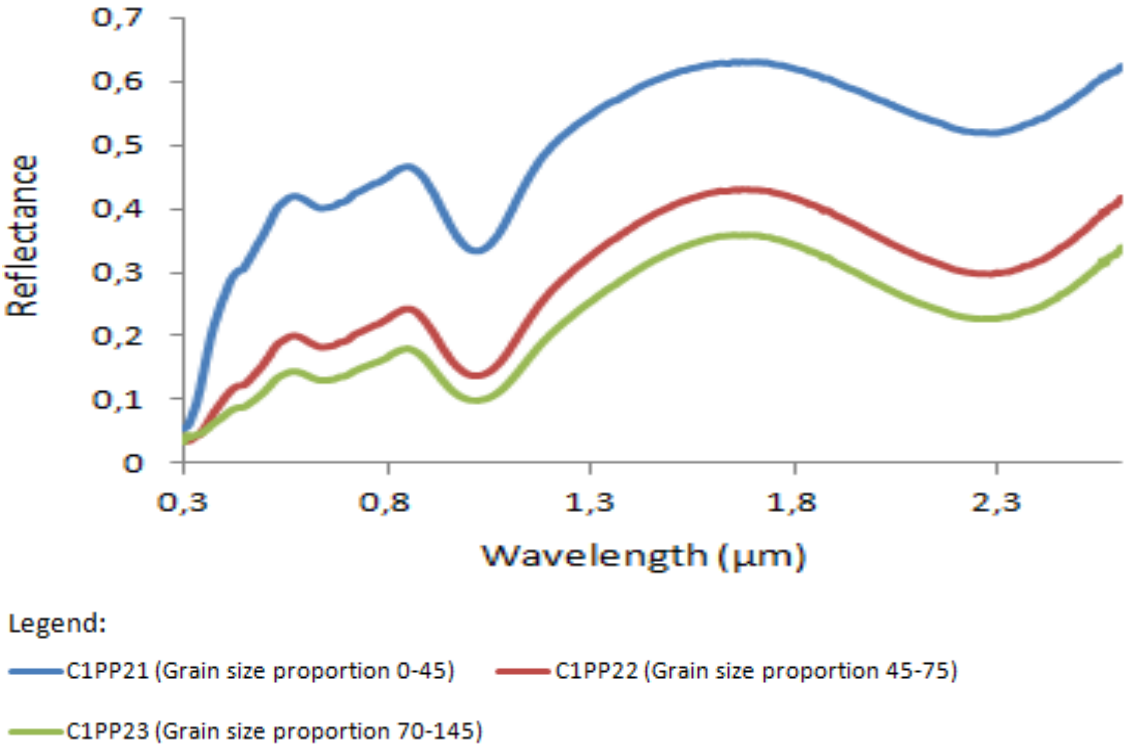


Fig.5.12 - Reflectance spectra of all three clinopyroxenes obtained from the RELAB database.

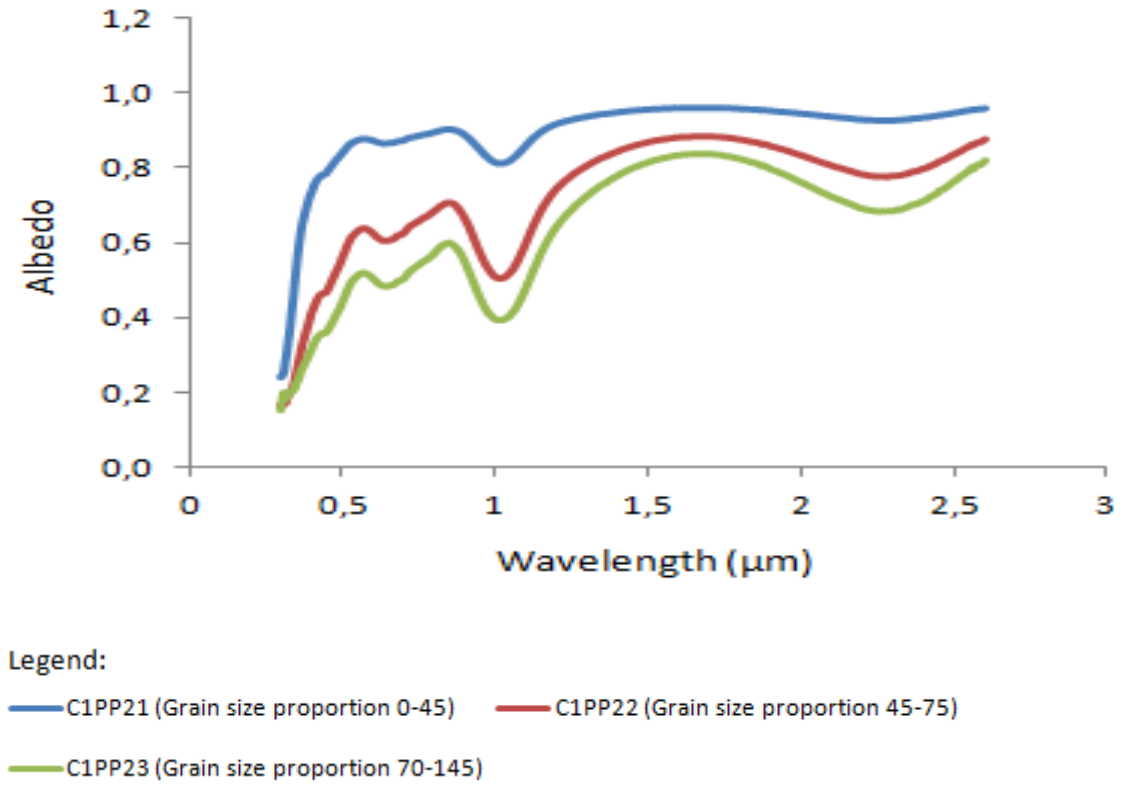


Fig.5.13 - Single scattering albedo versus wavelength for all three clinopyroxenes.

For all these seven laboratory mixtures, their nominal and derived mineralogical compositions are plotted in Fig.5.14. As it is evidenced by Fig.5.14, the derived mineralogical compositions for the orthopyroxene seem to be underestimated in some cases.

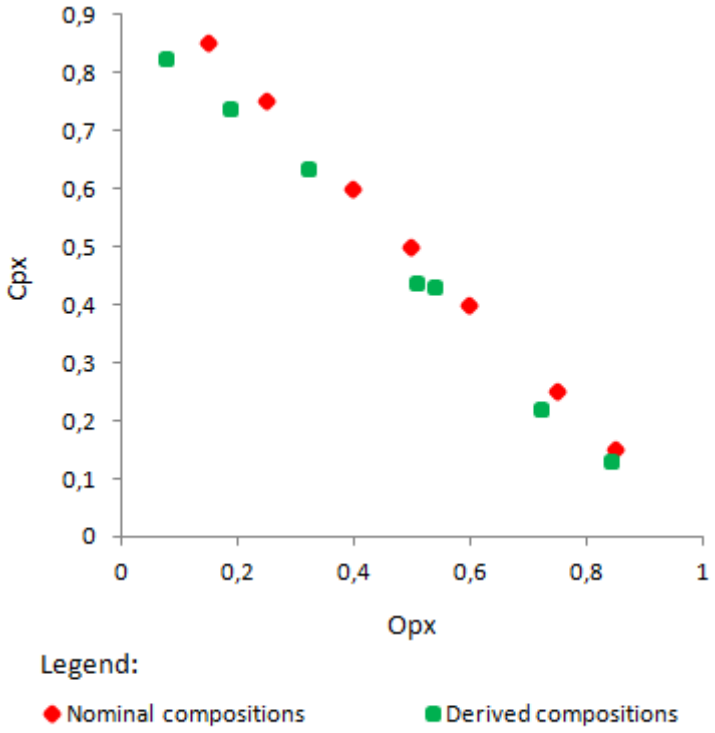


Fig.5.14 - Plot of clinopyroxene (Cpx) versus orthopyroxene (Opx) nominal and derived compositions for all fourteen laboratory mixtures with a grain size proportion between 0 and 45µm and 70 and 145µm.

As supported by the results of this test, the applied procedure to derive the mineralogical composition of samples seems to give good results. Hence, this procedure fulfilled the confidence tests.

## 5.2. Mineralogy of HED meteorites and of V-type Asteroids

In this section it is aimed to analyse spectroscopic features of HED meteorites and compare with the V-type asteroids. To obtain information about the mineralogical composition of asteroids, studying their reflectance spectra in the visible and NIR is a powerful technique. In this spectral range (0-4-2.6 µm), there are several absorption features which can be easily identified to infer about the presence of several minerals in the surface of an asteroid. Through a medium resolution spectrograph, the

reflectance spectrum of an asteroid can be obtained. As the obtained spectrum is due to the Sun's reflected light from the asteroid, it must be corrected by extracting the Sun light component. The resulting spectrum only has information about the asteroid's surface.

For the purpose of this study, a set of five V-type asteroids were obtained from "The MIT-UH-IRTF Joint Campaign for NEO Spectral Reconnaissance" [175], available online at http://smass.mit.edu/minus.html. It is an ongoing joint observing program for routine measurement of Near Earth Objects (NEO) spectra, conducted by MIT, University of Hawai and the NASA Infrared Telescope Facility (IRTF). A low-to-medium resolution NIR spectrograph and imager called SpeX, is used to obtain 0.8 to 2.5 microns spectra of NEO. When available, visible wavelength data from SMASS survey are also included. Normalization is at 0.55 μm, when visible wavelength data are available. If not, normalization is made near 1.21 μm. The selected set of asteroid is listed in Table D3. When needed, the geometric albedo values listed in Table D3 were used to "unnormalize" the asteroid spectra. The reflectance spectra of the selected five V-type asteroids are presented in Fig.5.15.

In addition, a set of ten Howardites, ten Eucrites and ten Diogenites were obtained from the RELAB database [173]. Their reflectance spectra range in wavelength between 0.3 and 2.6 μm, and were obtained with a 0.005 μm sampling resolution. The thirty selected HED meteorites are listed in Table D4. The reflectance spectra of the selected HED meteorites are presented in Fig.5.16.

All selected asteroids (Fig.5.15) have the pyroxene and possibly olivine and plagioclase characteristics absorption features of the HED meteorites (Fig.5.16). The pyroxene features are due to the presence of $Fe^{2+}$ ions in the M2 crystallographic site. All selected V-type asteroids (Fig.5.15) and HED meteorites (Fig.5.16) have strong pyroxene bands centered near ~0.9 μm and ~1.9 μm. All of the four V-type near-Earth Vestoids (meaning 3908 Nyx, 4055 Magellan, (5604) 1992 FE and (6611) 1993 VW) have strong absorption edges. 3908 Nyx, 4055 Magellan and (5604) 1992 FE have peaks near ~1.3 μm, while (6611) 1993 VW have a peak near ~1.4 μm. The 1.2 μm absorption band, attributed to $Fe^{2+}$ in the M1 crystallographic site, is not visually distinctive in the selected V-type asteroids. In addition, the absorption feature found near ~0.9 μm, can also be indicative of the presence of olivine. The olivine spectrum is

dominated by a complex absorption feature centered near ~1.0 μm. For further details about the crystallographic sites and spectroscopic features of pyroxene, olivine and plagioclase, check section B.3.

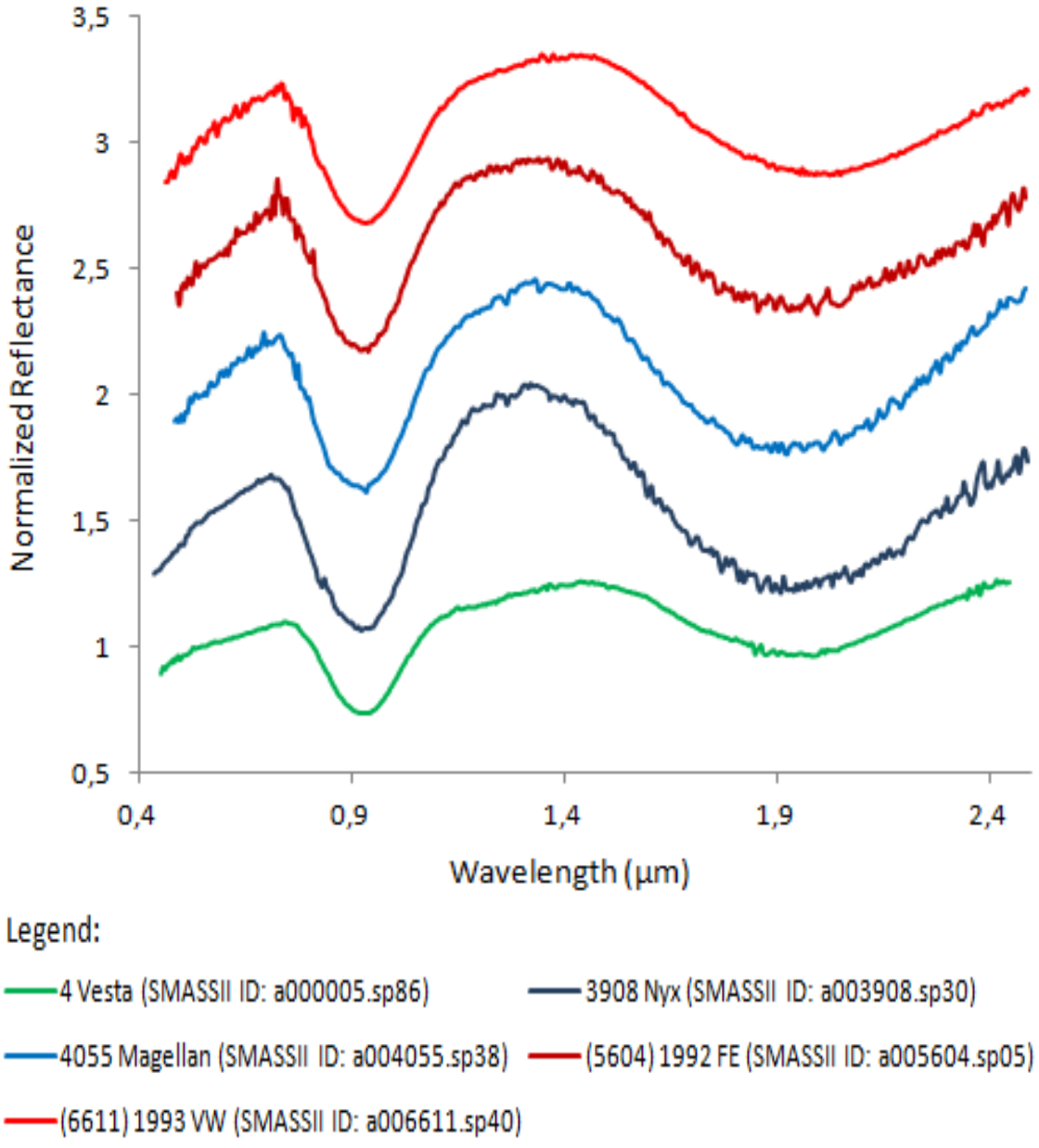


Fig.5.15 - Reflectance spectra of 4 Vesta and the four near-Earth vestoids. The reflectance spectra are incrementally shifted vertically by 0.5.

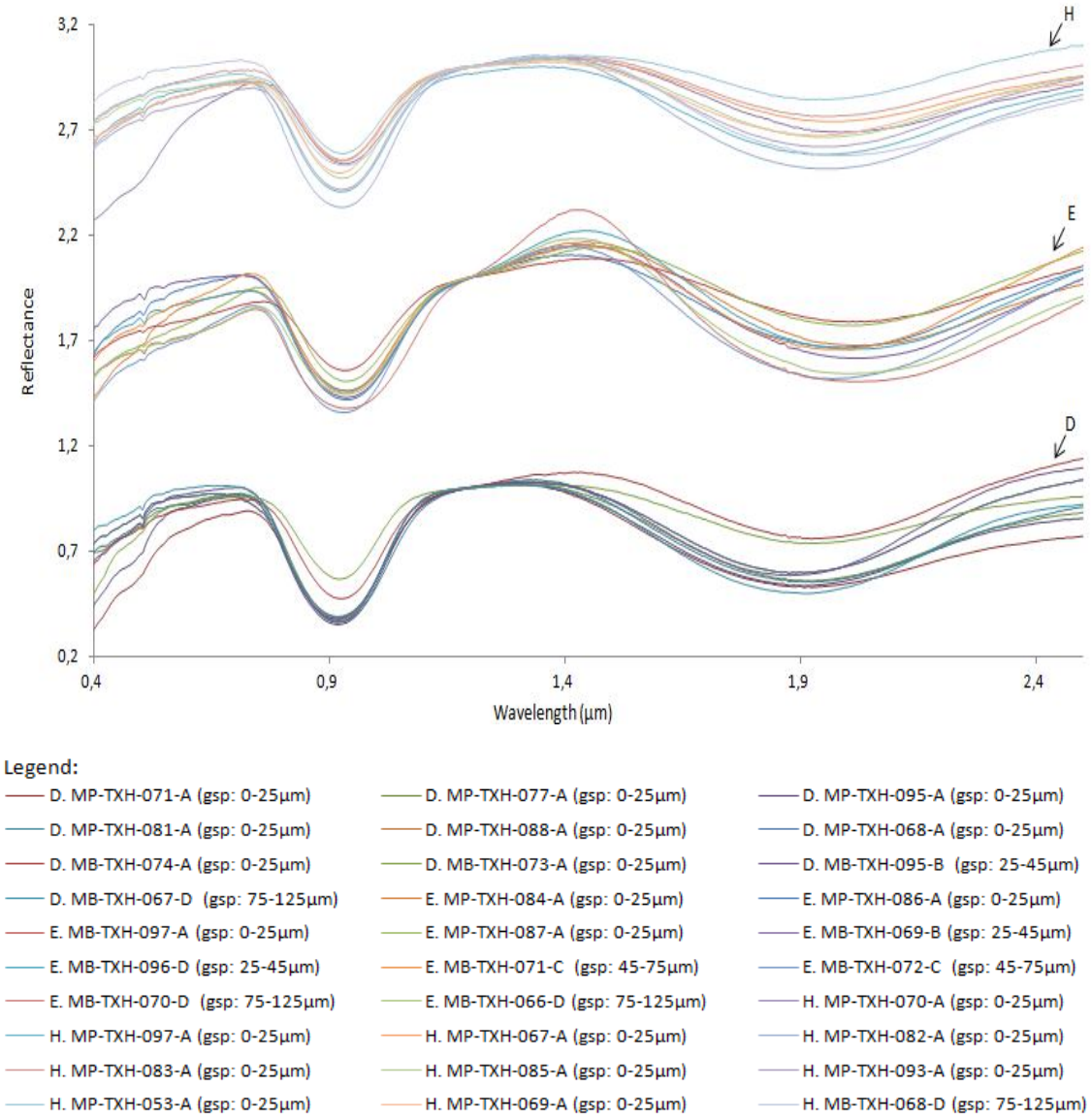


Fig.5.16 - Reflectance spectra of the selected ten diogenites (D), ten eucrites (E) and ten howardites (H). Eucrites' reflectance spectra are shifted vertically by 1 unity. Howardites' reflectance spectra are shifted vertically by 2 units.

There are some interesting techniques to analyze the spectroscopic features in the reflectance spectra of asteroids and compare them with meteorites. One interesting technique is to compare meteorites spectra with asteroids spectra. The first step is to identify the mineralogy of an asteroid, by comparing their reflectance spectra with ones' of meteorites taken from reflectance spectra databases. Hence, the reflectance spectra of HED meteorites were compared with the ones' of the selected V-type asteroids (Figs.E41- E45).

The mineralogies of the five selected V-type asteroids are quite similar to the ones of the HED meteorites (Fig.5.17). As it is quoted in the literature, 4 Vesta has a mineralogical composition similar to howardites [176]. This fact is constrained by Fig.5.17. In addition, the mineralogical compositions of the near Earth vestoids (6611) 1993 VW and (5604) 1992 FE were identified as being close the ones' of howardites. 4055 Magallen seems to have a similar mineralogy to eucrites. Finally, 3908 Nyx were identified to be similar to the ones' of diogenites. This fact seems to contradict the lack of identified vestoids with mineralogies similar to diogenites in the NEA [177].

Also, this method provided us possible particle sizes on the selected asteroids' surfaces, as they are currently unknown.

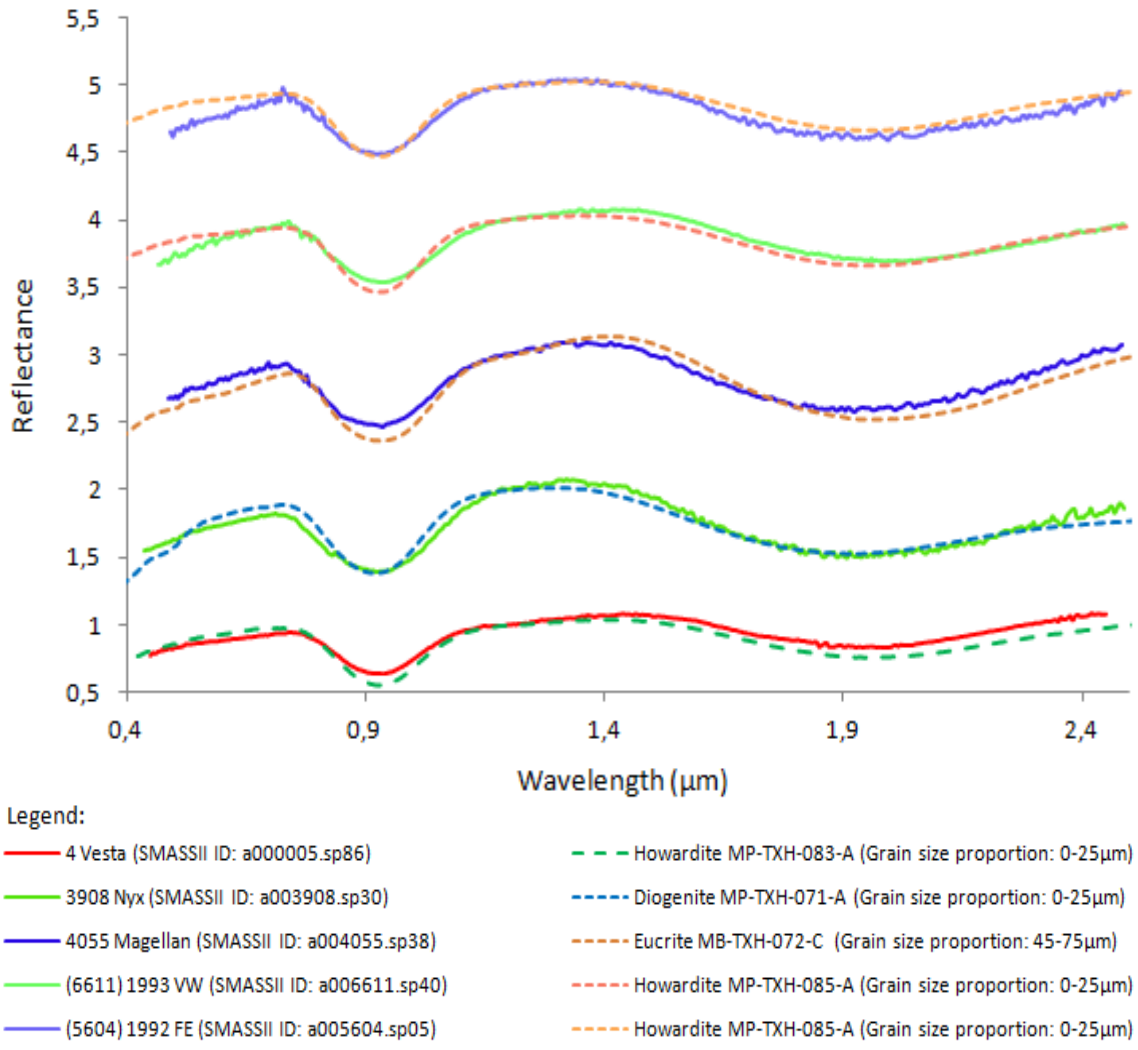


Fig.5.17 - Reflectance spectra of the five V-type asteroids versus respectively HED with the closest mineralogy. A vertical shift of 1 unit is introduced between different groups of spectra.

Another interesting technique to study the mineralogy of asteroids and meteorites is to construct a mixing model, which deconvolutes their reflectance spectra. As it was already referred above, the mixing model constructed in this study is based on the Hapke's theory of the reflectance of particulate surfaces. Then, assuming reasonable end-members minerals choices, the developed Solver application in Microsoft Excel can be applied to derive the mineralogical compositions of asteroids and meteorites.

In order to infer the mineralogical compositions of the selected V-type asteroids and HED meteorites, their single scattering albedo may be derived through the application of the Hapke Model. The derived single scattering albedos of the HED meteorites are plotted in Fig.5.18. However, in the case of the selected V-type asteroids, information about the viewing geometry is not provided in the literature. Hence, their single scattering albedos must be approximated by the measured reflectance, assuming that reflectance can be calibrated through their geometric albedo. It is supposed that the reflectance is proportional to the albedo, where the proportionality factor is independent of the wavelength. The approximated single scattering albedos of the V-type asteroids are plotted in Fig.5.19.

A set of reasonable end-members minerals, with appropriate grain sizes proportions, were taken from the RELAB database [173]. This selection took into account the typical mineralogy of HED meteorites and V-type asteroids, which was pointed out above. Hence, several types of pyroxenes and two types of olivine and plagioclase were selected. Some spectrally neutral phases were also included in this modeling process, to reduce the spectral contrast of the pure mineral end-members. These neutral phases, including several opaque and anisotropic minerals, have no absorption features and may help improving the fit of the single scattering albedo. Also, neutral phases are usually chosen to account for inappropriate end-member grain sizes. The set of selected end-members minerals, are listed on Table D5. For further details about pyroxenes, olivine and plagioclase, check section B3.

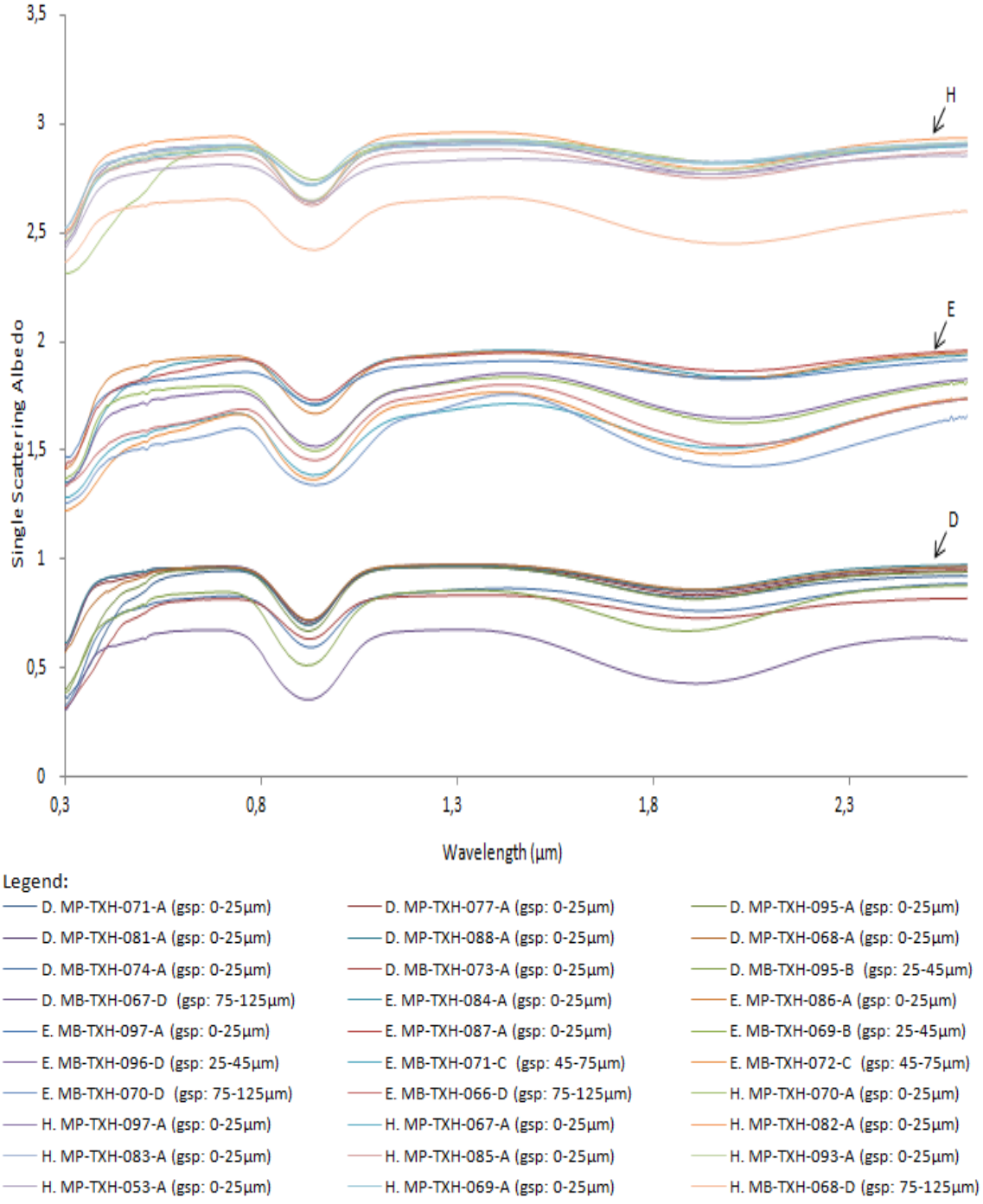


Fig.5.18 – Plot of the derived single scattering albedos of the ten Diogenites (D), ten Eucrites (E) and ten Howardites (H). The single scattering albedo of Eucrites are shifted vertically by 1 unity, while the single scattering albedo of Howardites are shifted vertically by 2 units.

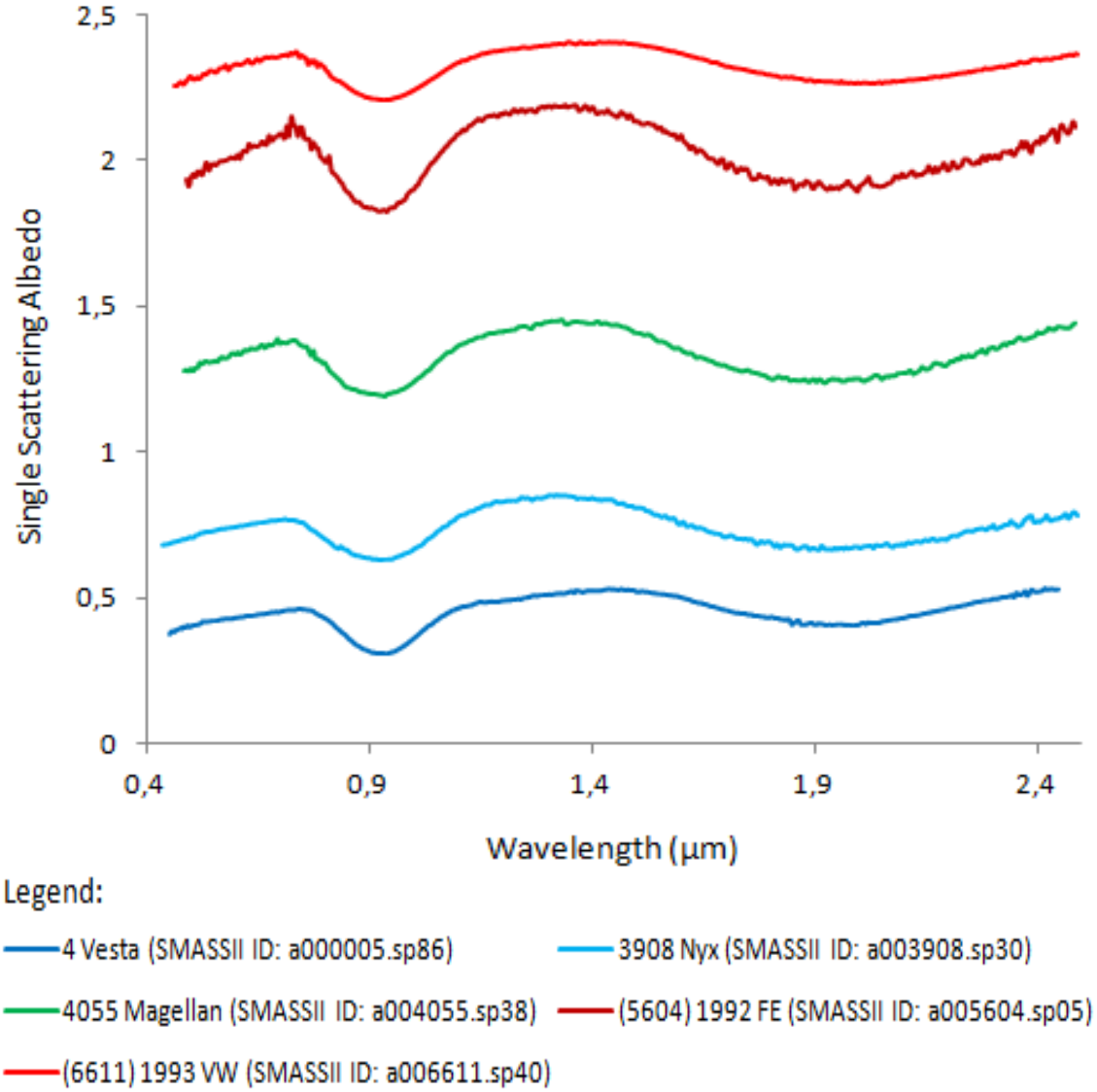


Fig.5.19 - Plot of the derived single scattering albedo of the five selected V-type asteroids. The single scattering albedo of 3908 Nyx is shifted vertically by 0,5 units, of 4055 Magellan is shifted vertically by 1 unit, of (5604) 1992 FE is shifted vertically by 1,5 units and of (6611) 1993 VW is shifted vertically by 2 units.

In Fig.5.20 the reflectance spectra of the selected pyroxene end-members for the mixing model are plotted.

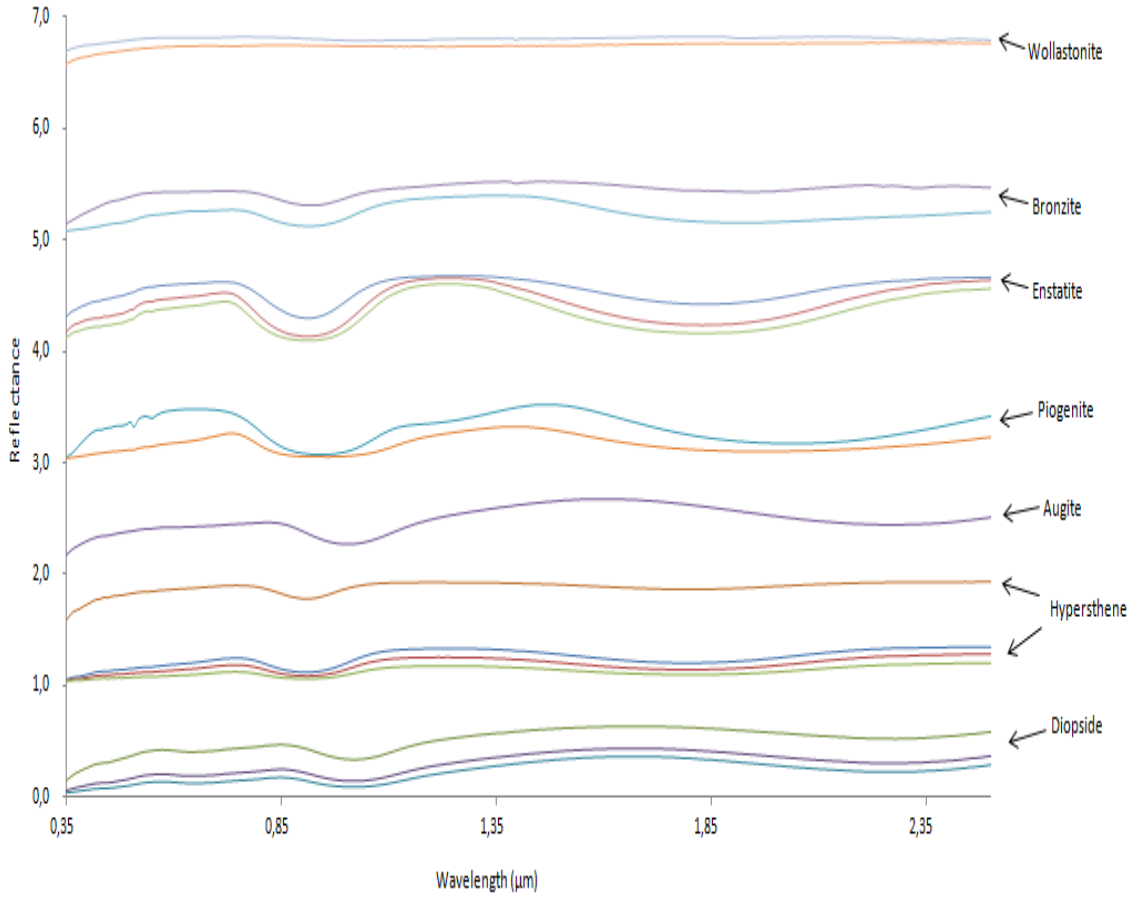


Legend:

- Diopside PP-CMP-021 (Grain size proportion: 0-45µm)
- Diopside PP-CMP-022 (Grain size proportion: 45-75µm)
- Diopside PP-CMP-023 (Grain size proportion: 75-125µm)
- Hypersthene PP-TXH-038-A (Grain size proportion: 0-25µm)
- Hypersthene PP-TXH-038-B (Grain size proportion: 0-25µm)
- Hypersthene PP-TXH-038-C (Grain size proportion: 45-75µm)
- Hypersthene PP-TXH-038-D (Grain size proportion: 75-125µm)
- Augite AG-TJM-010 (Grain size proportion: 0-45µm)
- Piogenite DL-CMP-008-A (Grain size proportion: 0-45µm)
- Piogenite LR-CMP-180 (Grain size proportion: 0-125µm)
- Enstatite PE-CMP-030 (Grain size proportion: 0-45µm)
- Enstatite PE-CMP-031 (Grain size proportion: 45-75µm)
- Enstatite PE-CMP-032 (Grain size proportion: 75-125µm)
- Bronzite JB-JLB-236 (Grain size proportion: 0-45µm)
- Bronzite PP-EAC-052 (Grain size proportion: 45-90µm)
- Wollastonite PX-EAC-003 (Grain size proportion: 0-45µm)
- Wollastonite SR-JFM-070-A (Grain size proportion: 45-150µm)

Fig.5.20 - Plot of the reflectance spectra of the pyroxene end-members used in this study. Reflectance spectra of Hypersthene are shifted moved vertically by 1 unity, of Augite are shifted vertically by 2 units, of Piogenite are shifted vertically by 3 units, of Enstatite are shifted vertically by 4 units, of Bronzite are shifted vertically by 5 units and of Wollastonite are shifted vertically by 6 units.

In Fig.5.21 the reflectance spectra of the selected olivine and plagioclase end-members for the mixing model are plotted.

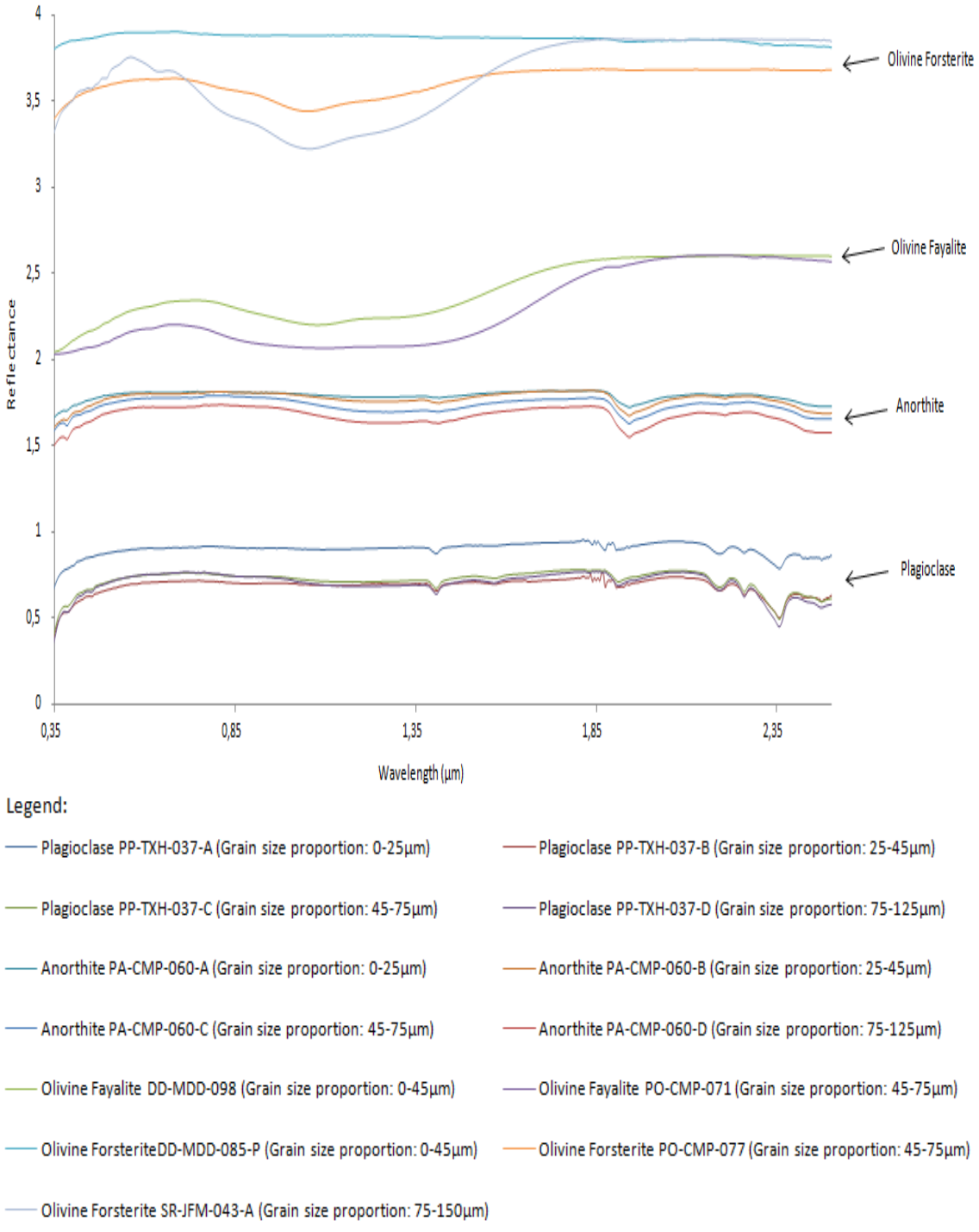


Fig.5.21 - Reflectance spectra of the selected olivine and plagioclase end-members minerals, used in this study. Reflectance spectra of Anorthite are shifted vertically by 1 unity, of Olivine Fayalite are shifted vertically by 2 units and of Olivine Forsterite are shifted vertically by 3 units.

In Fig.5.22 the reflectance spectra of the selected neutral phases for the mixing model are plotted.

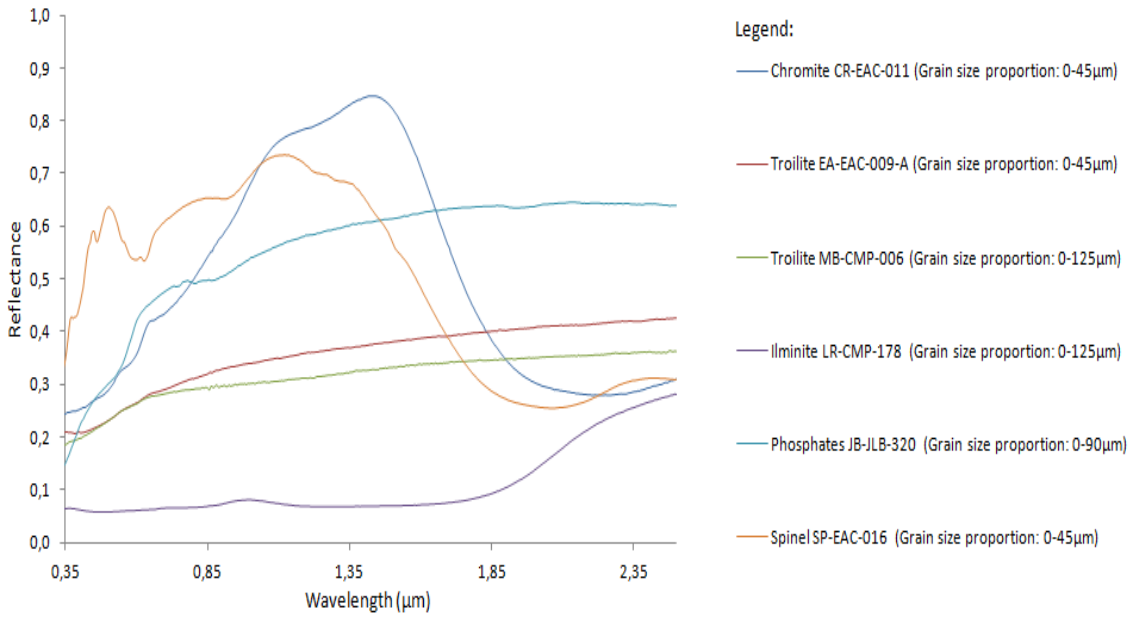


Fig.5.22 - Reflectance spectra of the selected neutral phases used in this study.

However, if a certain sample is considered to have opaque or anisotropic minerals in its composition, others than the selected ones', which originate a smooth curve that can be viewed as a spectrum background curve, a low degree polynomial can be added to the single scattering albedo modeling. For a given sample, its single scattering albedo can be modelled as follows:

$$w(\lambda) = \sum_{i=1}^{n_m} x_i w_i(\lambda) \tag{5.1}$$

where, *w* represents the single scattering albedo, *x* represents the i-th mineral compositional proportion and $n_m$ represents the number of plausible end-members which may be present on the sample.

But, if a low degree polynomial is considered, then the single scattering albedo albedo is modelled as follows:

$$w(\lambda) = \sum_{i=1}^{n_m} x_i w_i(\lambda) + Pol_n(\lambda) \tag{5.2}$$

where,

$$Pol_n(\lambda) = A_0 + A_1\lambda + A_2\lambda^2 + \cdots + A_n\lambda^n \quad (5.3)$$

Parameters $A_k$ (k=0,1,2,….,n) and the compositional mineral proportions are fitted in the Solver application. In this study, a third degree (n=3) polynomial will be considered.

In the modeling process, it must be guaranteed that the sum of the end-members minerals compositions ($x_i$) is 1. In order to better fit the individual selected V-type asteroids and HED meteorites, the piogenite and enstatite end-members with different granulometries, were considered in the modeling process. The derived compositions for the selected Diogenites, Eucrites and Howardites are listed in Tables D6, D7 and D8, respectively. In addition, the derived compositions for the selected V-type asteroids and their meteoritic analogs are listed in Table D9. In this study, the term “meteoritic analog” refers to a certain meteorite which is inferred, from Fig.5.17, to have the closest mineralogy to a certain V-type asteroid. In all cases, the results of the lowest $\chi^2$ found, is reported. In Fig.E46 the best obtained fit of diogenites, meaning the fit of the sample MP-TXH-068-A, and its residuals plot are presented. In Fig.E47 the worst obtained fit of diogenites, meaning the fit of the sample MP-TXH-071-A, and its residuals plot are presented. In Fig.E48 the best obtained fit of eucrites, meaning the fit of the sample MB-TXH-069-B, and its residuals plot are presented. In Fig.E49 the worst obtained fit of diogenites, meaning the fit of the sample MP-TXH-070-D, and its residuals plot are presented. In Fig.E50 the best obtained fit of diogenites, meaning the fit of the sample MP-TXH-053-A, and its residuals plot are presented. In Fig.E51 the worst obtained fit of diogenites, meaning the fit of the sample MP-TXH-068-D, and its residuals plot are presented.

In Fig.5.23, it is shown the best fit results of the mixing model simulations of the five selected V-type asteroids. In addition, in Fig.E52 to E56 their obtained fits and respectively residuals plot and background curve are presented. It can be seen from Fig.5.23, that these results are good matches for all of the selected asteroids. In Fig.5.24, the reflectance spectrum of 4 Vesta and the reflectance spectra of the chosen appropriate end-members are presented. The appropriate end-members minerals chosen to fit the reflectance spectrum of 4 Vesta are listed in Table D9.

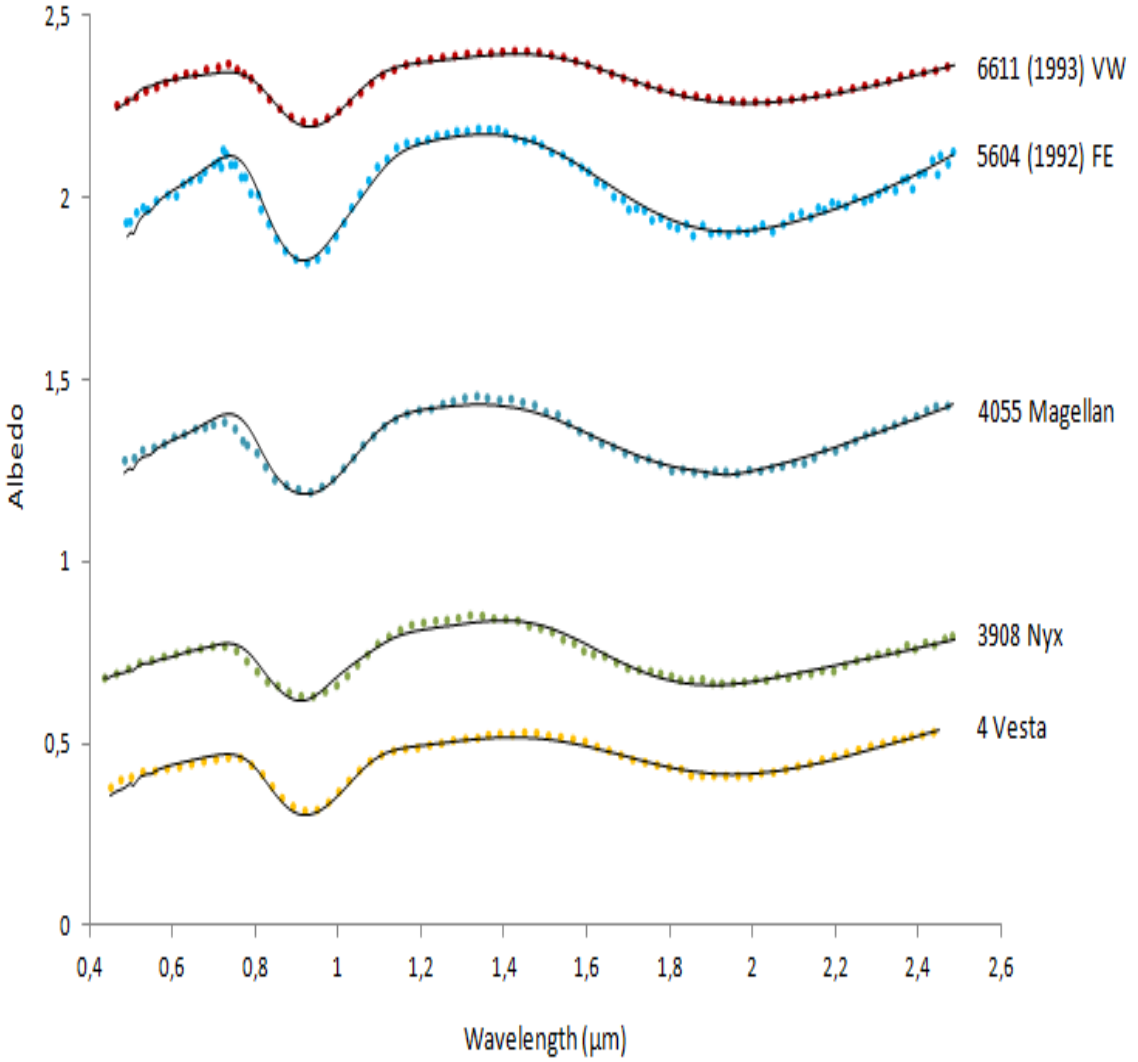


Fig.5.23 - Best fit model results of the selected V-type asteroids. Data points represent the single scattering albedo of the samples, while the black lines represent the best obtained fits. A vertical shift of 0.5 units is introduced between different asteroids/meteorites albedos.

On the other hand, if the particle grain sizes ($d_i$) and each mineral density ($\rho_i$) are known, the respectively HED meteorites and V-type asteroids mass fractions can be derived through the following expression:

$$M_i = \frac{\rho_i d_i x_i}{\sum_{k=1}^{n_m} \rho_k d_k x_k} \tag{5.4}$$

The derived mass fractions of selected Diogenites, Eucrites and Howardites are listed in Tables D10, D11 and D12, respectively. In addition, the derived mass

fractions for the selected V-type asteroids and their meteoritic analogs are listed in Table D13.

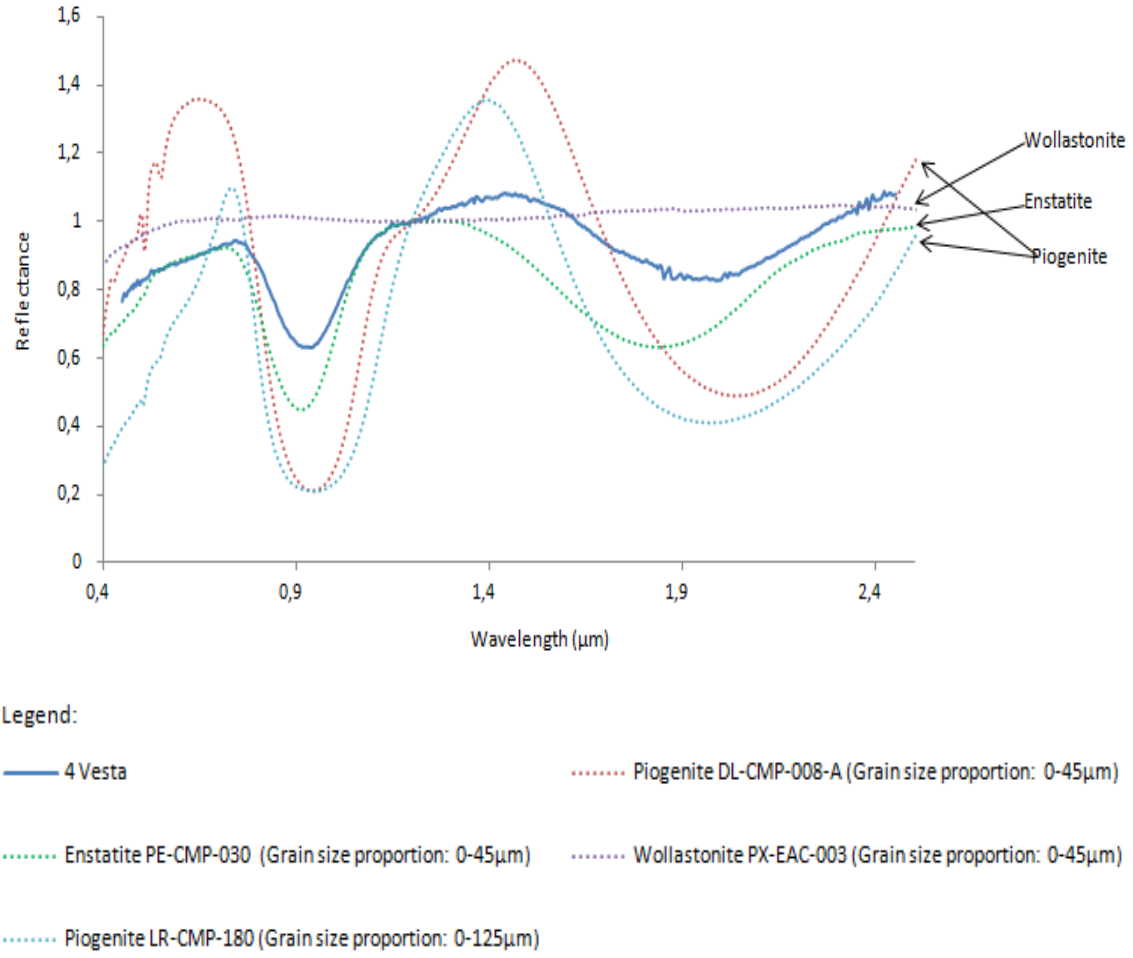


Fig.5.24 – Plot of the reflectance spectrum of 4 Vesta with its appropriate end-members minerals found in this study. All spectra are normalized by the reflectance value at 1.2µm.

In Fig.5.25 is presented a plot of the derived high-Ca pyroxenes vs derived low-Ca pyroxenes in this study, for all the selected HED meteorites and V-type asteroids.

The derived mass fractions indicate that the surface mineralogies of the studied V-type asteroids are indeed composed by a mixture of pyroxenes (Fig.5.25). In addition, the mineralogies of the selected HED meteorites are composed by a mixture of pyroxenes and in some cases some traces olivine are also present. It is also important to quote that the derived mass fractions of the selected HED meteorites and V-type asteroids may not be unique, as mixing models are highly on the choice of end-members.

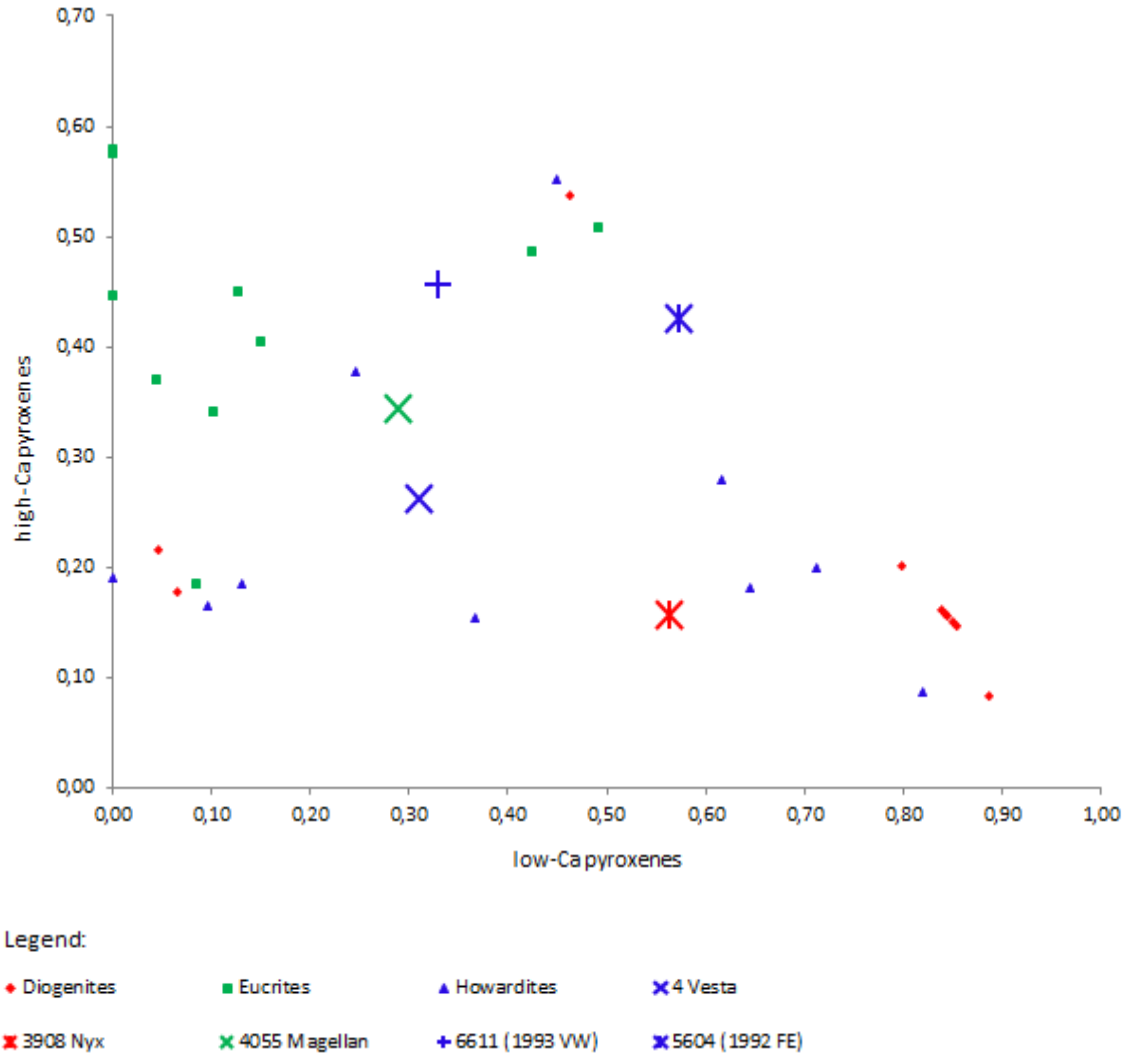


Fig.5.25 - Plot of the low-Ca pyroxenes content vs high-Ca pyroxenes content, of all thirty HED meteorites and all five V-type asteroids.

The derived mass fractions of diogenites indicate that their mineralogies are mainly dominated by magnesian orthopyroxenes, consistent with the mineralogical composition found in the literature for this type of meteorites. Chromite is a minor phase being found in only three samples: MP-TXH-081-A, MP-TXH-088-A and MB-TXH-095-B. Troilite is an accessory phase, which was found in only one sample: MB-TXH-074-B. Anorthite was also found in one sample: MB-TXH-067-D. It is also important to quote that the added low-degree polynomial to the modelling process, can model the presence of chromite, troilite or silica, as these minerals do not have any absorption feature as function of the wavelength.

The derived mass fractions of eucrites indicate that their mineralogies are mainly dominated by piogenite and enstatite. Minor phases of chromite were found in two samples: MB-TXH-069-B and MB-TXH-096-D. Accessory phases such as troilite and phosphates were also found. Troilite were found in three samples: MB-TXH-097-A, MB-TXH-096-D and MB-TXH-070-D. Phosphates were found in only one sample: MP-TXH-084-A. These mineralogies are in agreement with the literature, however fayalitic olivine and Ca-rich plagioclase (anorthite) were not found in these samples, according to the results of this study. In addition, as it was referred above in the case of diogenites, the added low-degree polynomial can model the presence of minerals such as troilite or chromite.

The derived mass fractions of howardites indicate that their mineralogies are mainly dominated by diogenitic and eucritic material (Fig.5.25), being consistent to the mineralogies found in the literature.

These results strengths the relationship between HED meteorites and V-type Near Earth Asteroids. Indeed, they strength the relationship between 4 Vesta, HED meteorites and Vestoids (Fig.5.25). As pointed out in the literature and confirmed in this study, 4 Vesta has a reflectance spectrum that can be matched very well with the spectrum of a howardite [176]. The derived mineralogies of 4 Vesta and of howadirte MP-TXH-083-A also tend to strength this idea. As constrained by the derived mineralogies of 4055 Magellan, (5604) 1992 FE and (6611) 1993 VW and their postulated HED meteoritic analogs in this study, all of them have pyroxene mineralogies consistent with eucrites or howardites (Fig.5.25) [177], supporting the links established in Fig.5.17. Finally, the only near-Earth vestoid with pyroxene mineralogy consistent with diogenites is 3908 Nyx (Fig.5.25). This evidence contradicts the fact that none near Earth vestoids have pyroxene mineralogies consistent with diogenites [177]. In addition, as it can be seen from Fig.5.17, the reflectance spectrum of 3908 Nyx can be matched by the spectrum of a diogenite (MP-TXH-071-A).

As none of the studied near-Earth Vestoids are composed only by one type of pyroxenes, this is suggestive of the absence of a quickly cooling of their surfaces.

The wide range of the studied V-type Near Earth Asteroids mineralogies points towards one direction: they are not originated from different parent bodies, but they

almost certainly come from different layers of 4 Vesta, which was excavated by a huge collision. In fact, 4 Vesta has a huge crater in the South Polar Region, probably originated by a big collision. This collision eventually ejected a big amount of material into 4 Vesta neighborhood. Some ejected fragments were re-accumulated and formed small bodies, which show a howardite type spectra (i.e composed by eucritic and diogenitic material). These bodies would have formed the howardite type family of asteroids. If this collision excavated enough material until it reached inner layers close to the mantle of 4 Vesta, traces of olivine may be present in some Vestoids and HED meteorites. If true, this evidence may favor the ocean magma model of 4 Vesta interior [178]. Actually, in the near-Earth Vestoid (6611) 1993 VW, a small amount of fayalitic olivine was found. If the latter assumption is true, then (6611) 1993 VW can be originated from the inner layers close to the mantle of 4 Vesta.

Despite being suggested in the literature that Vestoids may come from different layers of 4 Vesta, the near-Earth Asteroids 3908 Nyx and 4055 Magellan can be ejected fragments of the disruption of a 4 Vesta clone and not 4 Vesta itself [179]. This can be a good hypothesis, but such a clone body is still unknown. These two near-Earth Vestoids are also referred as being dynamically too young to have been originated in the same event as the Vesta family did [180]. However, the derived mineralogies of the studied near-Earth Vestoids do not point towards this direction.

The silicate mineralogy inferred for the studied V-type Near Earth Asteroids requires that their parent body or parent bodies suffered early igneous differentiation in their histories [181], producing a basaltic surface lithology. In fact, the presence of high-Ca pyroxenes in asteroids can act as a tracer of their igneous history. Several minerals, such as troilite, high-Ca orthopyroxenes and plagioclase were all preferentially incorporated in early partial melts from a chondritic precursor and depleted from residues of partial melting [181]. Hence, the parent body of HED meteorites and Vestoids, which is reported as being 4 Vesta, may be a differentiated asteroid.

U.PORTO
FACULDADE DE CIÊNCIAS
UNIVERSIDADE DO PORTO

# 6. Conclusion

In this work, a set of five V-type asteroids and thirty HED meteorites reflectance spectra were obtained from public databases. These spectra were modelled to test the hypothesis that HED meteorites may be linked to Vestoids and 4 Vesta. Their spectra were modelled through the application of a mixing model, based on the Hapke theory, with reasonable end-members pointed out in the literature. All end-member spectra were obtained from the RELAB public database and were constrained to samples with grain sizes less than 125 μm. The Hapke Model was coded using Visual Basic for Applications, available in Microsoft Excel software, to derive the single scattering albedo of the selected samples. Then, a Solver application was developed to model the derived single scattering albedo of the chosen samples, using reasonable end-members choices, by minimizing the sum of squares of the residuals.

Firstly, to gain confidence, this procedure was applied to a set of laboratory mixtures of minerals, containing low-Ca pyroxenes, high-Ca pyroxenes and olivine. Their reflectance spectra were obtained from the RELAB database. With the exception of few cases, the derived compositions almost matched the nominal compositions. Then, fulfilled the confidence test, this procedure was applied to the selected samples of V-type asteroids and HED meteorites.

The results of this study strengthened the hypothesis of a genetic linkage between V-type asteroids and HED meteorites. In addition, they indicate that the studied near-Earth Vestoids may come from different layers of 4 Vesta or another, still unknown, 4 Vesta-like body. According to the detected presence of fayalitic olivine in (6611) 1993 VW, this near-Earth Vestoid can come from the inner layers close to the mantle of 4 Vesta. The presence of olivine found in (6611) 1993 VW and some HED meteorites, may favor the ocean magma computational model of 4 Vesta interior. These near-Earth Vestoids were probably originated from a huge collision suffered by 4 Vesta or a 4 Vesta-like body.

In this study, it was possible to identify a near-Earth Vestoids with pyroxene mineralogy consistent with diogenites: 3908 Nyx. This evidence confirmed that it was possible to link a near-Earth Vestoids with diogenites. However, the apparent difficulty in linking diogenites with V-type asteroids could not be confirmed or refuted by the

results of this study. The remaining studied near-Earth Vestoids were identified as having pyroxene mineralogies consistent with eucrites and howardites, confirming what is pointed out in literature [177]. On the other hand, the pyroxene mineralogy of 4 Vesta was confirmed as being consistent with howardites.

The derived silicate mineralogy of the studied near-Earth Vestoids indicates that their parent body (probably 4 Vesta) may be a differentiated asteroid [181].

It is hoped in the future to apply this procedure to study other types of asteroids and meteorites or even comets. These studies can give us clues about the processes that took place in the infant Solar System. So far, the mineralogical composition and internal structure of the primitive Earth is still unknown. Understanding several processes that took place in the infant Solar System can teach us crucial steps of its formation history.

Due to the recently increasing number of discovered exoplanets, the question of how do planetary systems formed comes to our mind. It is interesting to note that to study these planets, we still need to study their host star. However, due to the advances in technology, in a close future, several Earth-like exoplanets will be probably found. By studying their mineralogies, this will probably leave us one step closer to understand the formation of Earth-like planets.

In the zoo of known exoplanets, by understanding the formation of their planetary systems, Humankind will be one step closer to understand the nature and origin of life.

U.PORTO
FACULDADE DE CIÊNCIAS
UNIVERSIDADE DO PORTO

# References:

[1] Quinn, D. P., Gillis-Davis, J. J. and Lucey, P. G. (2010), *Using Microsoft Excel for Hapke Modeling: A Technique to Simplify Calculations of Optical Constants and Reflectance Spectra*, 41st Lunar and Planetary Science Conference, held March 1-5, 2010 in The Woodlands, Texas. LPI Contribution No. 1533, 2426-2427

[2] Lada, C. J. and Lada, E. A. (2003), *Embedded Clusters in Molecular Clouds,* ARAA, 41, 57-115

[3] Bressert, E., Bastian, N., Gutermuth, R. (2011), *Do All Stars in the Solar Neighborhood Form in Clusters?*, arXiv:1102.0565v1

[4] Bobylev, V., V., Bajkova, A. T., Myllari, A. and Valtonen, M. (2010), *Searching for possible siblings of the sun from a common cluster based on stellar space velocities*, Astronomy Letters, 37, 8, 550-562

[5] Portegies Zwart, S. F. (2009), *The Lost Siblings of the Sun*, ApJ, 696, 1, L13-L16

[6]Adams, F. C. (2010), *The Birth Environment of the Solar System*, ARAA, 48, 47-85

[7] Brown, Anthony G. A., Portegies Zwart, S. F., Bean, J. (2010), *The quest for the Sun's siblings: an exploratory search in the Hipparcos Catalogue*, MNRAS, 407, 1, 458-464.

[8] Batista, S. F. A. and Fernandes, J. (2012), *Lost siblings of the Sun: revisiting the FGK potential candidates*, New Astronomy, 17, 514-519

[9] *Butler, R. P., Wright, J. T., Marcy, G. W., Fischer, D. A., Vogt, S. S., Tinney, C. G., Jones, H. R. A., Carter, B. D., Johnson, J. A., McCarthy, C., Penny, A. J.* (2006), *Catalog of nearby Exoplanets*, ApJ, 646, 1, 505-522

[10] McBride, N., Moore, E. A., Widdowsen, M. and Wright, I. (2003), *An Introduction to the Solar System,* Cambridge Press Uni, ISBN: 0521837359

[11] Coole, G. H. A. and Woolfson, M. M. (2002), *Planetary Science – The Science of planets around stars* , Institute of Physics Publishing Bristol and Philadephia, ISBN: 075030815 X, pp.168-189

[12] Cameron A. G. W. (1962), *The formation of the Sun and planets*, Icarus 1, 13–69

[13] Strom, S. E. (1994), *The early evolution of stars*, Revista Mexicana de Astronomia y Astrofisica, 29, 23 - 29

[14] Lynden-Bell D. and Pringle J. E. (1974), *The evolution of viscous discs and the origin of the nebula variables,* MNRAS, 168, 603–637

[15] Eales, S. (2009), *Planets and Planetary Systems*, Wiley-Blackwell, ISBN: 978-0-470-01692-3, pp.141-157

[16] Youdin, A. N. and Shu, F. H. (2002), *Planetesimal Formation by Gravitational Instability*, ApJ, 580, 1, 494-505

[17] Goodman, J. and Pindor, B. (2000), *Secular Instability and Planetesimal Formation in the dust layer,* Icarus, 148, 2, 537-549

[18] Poppe, T., Blum, J. and Henning, T. (2000), *Analogous Experiments on the Stickiness of Micron-sized Preplanetary Dust*, ApJ, 533, 1, 454-471

[19] Wetherill, G. W., Stewart, G. R. (1989), *Accumulation of a swarm of small planetesimals*, Icarus, 77, 330-357

[20] Kobuko, E. and Ida, S. (1998), *Oligarghic growth of protoplanets,* Icarus, 131, 171-178

[21] Agnor, C. B., Canup, R. M. and Levison H. F. (1999), *On the character and consequences of large impacts in the late stage of terrestrial planet formation*, Icarus, 142, 1756-1771

[22] Kokubo E. and Ida S. (1998), *Oligarchic growth of protoplanets,* Icarus, 131, 171–187

[23] Alexander S. G. and Agnor C. B. (1998), *N-body simulations of late stage planetary formation with a simple fragment model*, Icaurus, 113-124

[24] Wetherill, G. W. (1988), *Accumulation of Mercury from planetesimals,* IN: Mercury (A89-43751 19-91). Tucson, AZ, University of Arizona Press, 1988, p. 670-691

[25] Tonks, W. B. and Melosh H. J. (1992), *Core formation by giant impacts*, Icarus, 100, 2, 326-346

[26] *Morbidelli, A., Chambers, J., Lunine, J. I., Petit, J. M., Robert, F., Valsecchi, G. B. and Cyr, K. E.* (2000), *Source regions and time scales for the delivery of water to Earth,* Meteoritics & Planetary Science, 35, 6, 1309-1320

[27] Mizuno, H. (1980), *Formation of the Giant Planets*, Progress of Theoretical Physics, 64, 2, 544-577

[28] *Pollack, J. B., Hubickyj, O., Bodenheimer, P. Lissauer, J. J., Podolak, M., Greenzweig, Y.* (1996), *Formation of the Giant Planets by Concurrent Accretion of Solids and Gas*, Icarus, 124, 1,62-85

[29] Kuiper, G. P. (1951), *On the origin of the Solar System*, Proceedings of the National Academy of Sciences of the United States of America, 37, 1, 1-14

[30] Cameron, A. G. W. (1978), *Physics of the primitive solar accretion disk*, Moon and the Planets, 18, 5-40

[31] Boss, A. P. (2002), *Evolution of the Solar Nebula. V. Disk Instabilities with varied thermodynamics*, ApJ, 576, 462-472

[32] Boss, A. P. (2003), *Rapid formation of outer giant planets by disk instability*, ApJ, 599, 577-581

[33] Feigelson, E. D. & Montmerle, T. (1999), *High-Energy Processes in Young Stellar Objects*, ARAA, 37, 363-408

[34] Wetherill, G. W. (1990), *Formation of the earth*, Annual Review Earth and Planetary Science, 18, 205-256

[35] Boss, A. P. (1998), *Evolution of the Solar Nebula IV. Giant Gaseous protoplanets formation*, ApJ, 503, 923-937

[36] *Briceño, C., Vivas, A. K., Calvet, N., Hartmann, L., Pacheco, R., Herrera, D., Romero, L., Berlind, P., Sánchez, G., Snyder, J. A., Andrews, P.* (2001), *The CIDA-QUEST Large-Scale Survey of Orion OB1: Evidence for Rapid Disk Dissipation in a Dispersed Stellar Population*, Science, 291, 5501, 93-97

[37] Hubickyj, O., Bodenheimer, P., Lissaeur, J. J. (2004), *Evolution of gas giant planets using the core accretion model*, RevMexAA (Serie de Conferencias), 22, 83-86

[38] *Guillot, T., Gautier, D., Hubbard, W. B.* (1997), *NOTE: New Constraints on the Composition of Jupiter from Galileo Measurements and Interior Models*, Icarus, 130, 2, 534-539

[39] Levison, H. F. & Stewart, G. R. (2001), *Remarks on Modeling the Formation of Uranus and Neptune*, Icarus, 153, 1, 224-228

[40] Thommes, E. W., Duncan, M. J., Levison, H. F. (2002), *The Formation of Uranus and Neptune among Jupiter and Saturn*, AJ, 123, 5, 2862-2883

[41] *Wuchterl, G., Guillot, T., Lissauer, J. J.* (2000), *Giant Planet formation*, Protostars and Planets IV, 1081

[42] *Helled, R., Podolak, M., Kovetz, A.* (2008), *Grain sedimentation in a giant gaseous protoplanet*, Icarus, 195, 2, 863-870

[43] Boss, A. P. (2002), *Formation of gas and ice giant planets*, Earth and Plant. Sci. Letters, 202, 3-4, 513-523

[44] Boss, A. P. (1997), *Giant planet formation by gravitational instability*, Science, 276, 5320, 1836-1839

[45] Thomes, E. W., Duncan, M. J. and Levison H. F. (2003), *Oligarchic growth of giant planets,* Icarus, 161, 431-455

[46] Thomes, E. W., Duncan, M. J. and Levison H. F. (1999), *The formation of Uranus and Neptune in the Jupiter-Saturn region of the Solar System,* Nature, 402, 635-638

[47] Nayakshin, S. (2010), *Formation of planets by tidal downsizing of giant planet embryos*, MNRAS, 408, 1, 36-40

[48] *Boley, A. C., Hayfield, T., Mayer, L., Durisen, R. H.* (2010), *Clumps in the outer disk by disk instability: Why they are initially gas giants and the legacy of disruption*, Icarus, 207, 2, 509-516

[49] *Morbidelli, A., Bottke, W. F., Nesvorný, D., Levison, H. F.* (2009), *Asteroids were born big*, Icarus, 204, 2, 558-573

[50] Jewitt, D. (2009), *Icy bodies in the New Solar System*, Proceedings of the International Astronomical Union, IAU Symposium, 263, 3-16

[51] Nilsson, R., Liseau, R., Brandeker, A., Olofsson, G., Pilbratt, G. L., Risacher, C., Rodmann, J., Augereau, J.-C., Bergman, P., Eiroa, C., Fridlund, M., Thébault, P., White, G. J. (2010), *Kuiper Belts around nearby stars*, A&A, 518, A40

[52] Marois, C., Macintosh, B., Barman, T., Zuckerman, B., Song, I., Patience, J., Lafrenière, D., Doyon, R. (2008), *Direct Imaging of Multiple* Planets *Orbiting the Star HR 8799*, Science, 322, 5906, 1348-1352

[53] Chen, H. C., Sheehan, P., Watson, D. M., Puravankara, P. M., Najita, J. R. (2009), *Solar System analogs around IRAS-Discovered Debris Disk*, ApJ, 701, 2, 1367-1372

[54] Gaffey, M.J., Cloutis, E.A., Kelley, M.S., Reed, K.L. (2002), *Mineralogy of asteroids*. In: Bottke, W.F., Cellino, A., Paolicchi, P., Binzel, R.P. (Eds.), Asteroids III. University of Arizona Press, Tucson, pp. 183–204.

[55] Chapman, CR (1999), *Asteroids*, In: Beatty J. K., Petersen, C. C., Chaikin, A., *The New Solar System*, 4th edn. 337-350. Cambridge University Press, Cambridge, UK

[56] Hartmann WK (2005), *Moons and planets*, 5th edn., Brooks/Cole, Belmont, CA

[57] Tholen, D. J. (1984), *Asteroid taxonomy from cluster analysis of Photometry,* Ph.D. Thesis Arizona Univ., Tucson

[58] Gaffey, Michael J., Burbine, Thomas H., Piatek, Jennifer L., Reed, Kevin L., Chaky, Damon A., Bell, Jeffrey F., Brown, R. H. (1993), *Mineralogical variations within the S-type asteroid class*, Icarus, 106, 573-602

U.PORTO
FACULDADE DE CIÊNCIAS
UNIVERSIDADE DO PORTO

[59] Hiroi, T., Zolensky, M. E., Pieters, C. M. (2001), *The Tagish Lake Meteorite: A Possible Sample from a D-Type Asteroid*, Science, 293, 5538, 2234-2236

[60] Cruikshank, D. P. and Hartmann, W. K. (1984), *The meteorite-asteroid connection: Two olivine-rich asteroids*, Science, 223, 281-283

[61] Bus S. J., Vilas F., Barucci M. A., (2002), *Visible-Wavelength Spectroscopy of Asteroids*, Asteroids III, W. F. Bottke Jr., A. Cellino, P. Paolicchi, and R. P. Binzel (eds), University of Arizona Press, Tucson, 169-182

[62] Faure, G. and Mensing, T. M. (2007), *Introduction to Planetary Science, The Geological Perspective,* Springer, ISBN-13 978-1-4020-5233-0, 13, 261-280

[63] Thomas, P.C., Binzel, R.P., Gaffey, M.J., Storrs, A.D., Wells, E. N., Zellner, B.H. (1997), *Impact excavation on asteroid 4 Vesta: Hubble Space Telescope results.*, Science, 277, 1492-1495.

[64] Keil, K. (2002), *Geological History of Asteroid 4 Vesta: The "Smallest Terrestrial Planet"*, Asteroids III, W. F. Bottke Jr., A. Cellino, P. Paolicchi, and R. P. Binzel (eds), University of Arizona Press, Tucson, 573-584

[65] McCord, T. B., Adams, J. B., Johnson, T. V. (1970), *Asteroid Vesta: Spectral reflectivity and compositional implications*, Science, 168, 3938, 1145-1147

[66]Lemaitre, A. (2005), *Asteroid family classification from very large catalogues*, Dynamics of Populations of Planetary Systems, Proceedings of IAU Colloquium #197, held 31 August - 4 Spetember, 2004 in Belgrade, Serbia and Montenegro. Edited by Z. Knezevic and A. Milani. Cambridge: Cambridge University Press, 135-144

[67] Gaffey, M. J., Burbine, T. H., Binzel, R. P. (1993), *Asteroid spectroscopy: progress and perspectives*, Meteoritics (ISSN 0026-1114), 28, 2, 161-187

[68] Zappala, V., Cellino, A., Farinella, P., Knezevic, Z. (1990), *Asteroid families. I - Identification by hierarchical clustering and reliability assessment*, AJ (ISSN 0004-6256), 100, 2030-2046

[69] Zappala, V., Bendjoya, Ph., Cellino, A., Farinella, P., Froeschle, C. (1995), *Asteroid families: Search of a 12,487-asteroid sample using two different clustering techniques.*, Icarus, 116, 291-314

[70] Nesvorný, D., Jedicke, R., Whiteley, R. J., Ivezić, Ž. (2005), *Evidence for asteroid space weathering from the Sloan Digital Sky Survey*, Icarus, 173, 1, 132-152

[71] Marzari, F., Cellino, A., Davis, D. R., Farinella, P., Zappala, V., Vanzani, V. (1996), *Origin and evolution of the Vesta asteroid family.*, A&A, 316, 248-262

[72] Carruba, V., Michtchenko, T. A., Roig, F., Ferraz-Mello, S., Nesvorný, D. (2005), *On the V-type asteroids outside the Vesta family. I. Interplay of nonlinear secular resonances and the Yarkovsky effect: the cases of 956 Elisa and 809 Lundia*, A&A, 411, 2, 819-829

[73] O'Brien, D. P. and Greenberg, R. (2005), *The collisional and dynamical evolution of the main-belt and NEA size distributions*, Icarus, 178, 1, 179-212

[74] Bottke, W. F., Durda, D. D., Nesvorný, D., Jedicke, R., Morbidelli, A., Vokrouhlický, D., Levison, H. F. (2005), *Linking the collisional history of the main asteroid belt to its dynamical excitation and depletion*, Icarus, 179, 1, 63-94

[75] Durda, D. D., Bottke, W. F., Nesvorný, D., Enke, B. L., Merline, W. J., Asphaug, E., Richardson, D. C. (2007*), Size-frequency distributions of fragments from SPH/N-body simulations of asteroid impacts: Comparison with observed asteroid families*, Icarus, 186, 2, 498-516

[76] Cellino, A., Bus, S. J., Doressoundiram, A., Lazzaro, D. (2002), *Spectroscopic Properties of Asteroid Families*, Asteroids III, W. F. Bottke Jr., A. Cellino, P. Paolicchi, and R. P. Binzel (eds), University of Arizona Press, Tucson, 633-643

[77] Farley, K. A., Vokrouhlický, D., Bottke, W. F., Nesvorný, D. (2006), *A late Miocene dust shower from the break-up of an asteroid in the main belt*, Nature, 439, 7074, 295-297

[78] Faure, G. and Mensing, T. M. (2007), *Introduction to Planetary Science, The Geological Perspective,* Springer, ISBN-13 978-1-4020-5233-0, 13, 421-440

[79] Duncan, M., Quinn, T., Tremaine, S. (1988), *The origin of short-period comets*, ApJ, 328, 69-73

[80] Hawkins, G. H. (1964), *Meteors, Comets and Meteorites*, McGraw-Hill Book Company, 106-129

[81] Fernandez, J. A. (1985), *Dynamical capture and physical decay of short-period comets*, Icarus, 64, 308-319

[82] Carusi, A., Kresak, L., Perozzi, E., Valsecchi, G. B. (1987), *High-Order Librations of Halley-Type Comets*, A&A, 187, 899-905

[83] Fernandez, J. A. and Gallardo, T. (1994), *The transfer of comets from parabolic orbits to short-period orbits: Numerical studies*, A&A, 281, 3, 911-922

[84] Horner, J., Evans, N. W., Bailey, M. E., Asher, D. J. (2003), *The populations of comet-like bodies in the Solar system*, MNRAS, 343, 4, 1057-1066

[85] Oort, J. H. (1950), *The structure of the cloud of comets surrounding the Solar System, and a hypothesis concerning its origin*, Bull. Astron. Inst. Neth., 11, 91-110

[86] Francis, P. J. (2005), *The Demographics of Long-Period Comets*, ApJ, 635, 2, 1348-1361

[87] Higuchi, A., Kokubo, E., Kinoshita, H., Mukai, T. (2007), *Orbital Evolution of Planetesimals due to the Galactic Tide: Formation of the Comet Cloud*, AJ, 134, 4, 1693-1706

[88] Bailey, M. E. (1984), *Astronomy: Nemesis for Nemesis?*, Nature, 311, 5987, 602-603

[89] Faure, G. and Mensing, T. M. (2007), *Introduction to Planetary Science, The Geological Perspective,* Springer, ISBN-13 978-1-4020-5233-0, 13, 409-420

[90] Barucci, M. A. and Peixinho, N. (2006), *Trans-Neptunian objects' surface properties*, Asteroids, Comets, Meteors, Proceedings of the 229th Symposium of the International Astronomical Union held in Búzios, Rio de Janeiro, Brasil August 7-12, 2005, Edited by Daniela, L.; Sylvio Ferraz, M.; Angel, F. Julio Cambridge: Cambridge University Press, 2006., 171-190

[91] Ipatov, S. I. and Mather, J. C. (2006), *Migration of small bodies and dust to near-Earth space*, Advances in Space Research, 37, 1, 126-137

[92] Weissman, P.R., Bottke, W.F. Jr., & Levison, H.F. 2002, in: W.F. Bottke Jr., A. Cellino, P. Paolicchi, & R.P. Binzel (eds.), Asteroids III, Univ. of Arizona: Tucson, 669-686

[93] Horner, J., Evans, N. W., Bailey, M. E. (2004), *Simulations of the population of Centaurs - I. The bulk statistics*, MNRAS, 354, 3, 798-810

[94] Bagatin, A. C. (2006), *Collisional evolution of asteroids and Trans-Neptunian objects*, Asteroids, Comets, Meteors, Proceedings of the 229th Symposium of the International Astronomical Union held in Búzios, Rio de Janeiro, Brasil August 7-12, 2005, Edited by Daniela, L.; Sylvio Ferraz, M.; Angel, F. Julio Cambridge: Cambridge University Press, 2006., 335-350

[95] Safronov, V. S. (1969), *Evolution of the Protoplanetary Cloud and Formation of the Earth and Planets*, Moscow: Nauka; English transl. NASA TTF-677 [1972].

[96] Burbine T. H., McCoy T. J., Meibom A., Gladman B., Keil K. (2002), *Meteoritic parent bodies: Their number and identification*. In: Bottke, W. F. Jr., Cellino, A., Paolicchi, P., Binzel, R. P. (Eds), Asteroids III. University of Arizona Press, Tucson, 653–667

[97] R. Hutchinson, I. P. Williams, S. S. Russel (2001), *Theories of planet formation: constraints from the study of meteorites*, Phil. Trans. R. Soc. Lond. A, 359, 1787, 2077-93

[98] Bischoff, A. & Geiger, T. (1995), *Meteorites for the Sahara: Find locations, shock classification, degree of weathering and pairing*, Meteoritics (ISSN 0026-1114), 30, 1, 113-122

[99] Sephton, M. A., Bland, P. A., Pillinger, C. T., Gilmou, I. (2004), *The preservation state of organic matter in meteorites from Antarctica*, Meteoritics & Planetary Science, 39, 5, 747-754

[100] Heide, F. (1964), *Meteorites*, The University of Chicago Press, 2nd edition, 61-67

[101] Bischoff A., Palme H., Schultz L., Weber D., Weber H., and Spettel B. (1993), *Acfer 182 and paired samples, an ironrich carbonaceous chondrite: similarities with ALH85085 and relationship to CR chondrites.*, Geochim. Cosmochim. Acta 57, 2631–2648.

[102] Grossman J. N., MacPherson G. J., and Crozaz G. (1993), *LEW 87223: a unique E chondrite with possible links to H chondrites*, Meteoritics 28, 358

[103] Rubin A. E., Fegley B., and Brett R., (1988), *Oxidation state in chondrites,* In Meteorites and the Early Solar System (eds.J. F. Kerridge and M. S. Matthews), University of Arizona Press, Tucson, 488–511.

[104] Krot A. N., Fegley B., Palme H., and Lodders K. (2000), *Meteoritical and astrophysical constraints on the oxidation state of the solar nebula*, In Protostars and Planets IV (eds. A. P. Boss, V. Manning, and S. S. Russell), University of Arizona Press, Tucson, 1019–1055

[105] Van Schmus W. R. and Wood J. A. (1967), *A chemicalpetrologic classification for the chondritic meteorites*, Geochim. Cosmochim. Acta 31, 747–765

[106] Connelly, J. N., Amelin, Y., Krot, A. N., Bizzarro, M. (2008), *Chronology of the Solar System's Oldest Solids*, ApJ, 675, 2, 121-124

[107] Aléon, J. (2008), *Meteorites and the physico-chemical conditions in the early solar nebula*, eprint arXiv:0809.1735

[108] Huss, G. R., Rubin, A. E., Grossman, J. N. (2006), *Thermal Metamorphism in Chondrites*, Meteorites and the Early Solar System II, D. S. Lauretta and H. Y. McSween Jr. (eds.), University of Arizona Press, Tucson, 943, 567-586

[109] Weisberg, M. K., McCoy, T. J., Krot, A. N. (2006), *Systematics and Evaluation of Meteorite Classification*, Meteorites and the Early Solar System II, D. S. Lauretta and H. Y. McSween Jr. (eds.), University of Arizona Press, Tucson, 943, 19-52

[110] Zolensky, M. and McSween, H. Y. Jr. (1988), *Aqueous Alteration*, IN: Meteorites and the early solar system (A89-27476 10-91). Tucson, AZ, University of Arizona Press, 114-143

[111] McSween, H. Y. Jr. (1987), *Aqueous alteration in carbonaceous chondrites - Mass balance constraints on matrix mineralogy*, GCA (ISSN 0016-7037), 51, 2469-2477

[112] Metzler, K., Bischoff, A., Stoeffler, D. (1992), *Accretionary dust mantles in CM chondrites - Evidence for solar nebula processes*, GCA (ISSN 0016-7037), 56, 7, 2873-2897

[113] Clayton R. N. and Mayeda T. K. (1999), *Oxygen isotope studies of carbonaceous chondrites*, Geochim. Cosmochim. Acta 63, 2089–2104.

[114] Rubin A. E. (1998), *Correlated petrologic and geochemical characteristics of CO3 chondrites*, Meteorit. Planet. Sci., 33, 2, 385–391

[115] Rubin A. E. (1989), *Size-frequency distributions of chondrules in CO3 chondrites*, Meteoritics ISSN 0026-1114), 24, 179-189

[116] Russell S. S., Huss G. R., Fahey A. J., Greenwood R. C., Hutchison R., Wasserburg G. J. (1998), *An isotopic and petrologic study of calcium–aluminum-rich inclusions from CO3 chondrites*, GCA, 62, 689–714

[117] Krot, A. N., Meibom, A., Weisberg, M. K. and Keil, K. (2002), *The CR chondrite clan: Implications for early solar system processes*, Meteoritics & Planetary Science, 37, 11, 1451-1490

[118] Weisberg, M.K., Prinz, M., Clayton, R. N., Mayeda, T. K. (1993), *The CR (Renazzo-type) carbonaceous chondrite group and its implications*, in Geochim. Cosmochim. Acta 57, 7, 1567-1586

[119] Weisberg, M. K., Prinz, M., Clayton, R. N., Mayeda, T. K., Sugiura, N., Zashu, S., Ebihhara, M. (2001), *A new metal-rich chondrite grouplet,* Meteorite Planetary Scince, 36, 3, 401-418

[120] Weisberg, M. K., Prinz, M. and Nehru, C. E. (1988), *Petrology of ALH85085*: *a chondrite with unique characteristics*, Earth and Planet. Sci. Letters (ISSN 0012-821X), 91, 1-2, 19-32

[121] Davies, A. M. (2005), *Meteorites, Comets and Planets*, Elsevier, 1

[122] Weisberg, M. K., Prinz, M., Clayton, R. N., Mayeda, T. K. (1997), *CV3 chondrites, three subgroups, not two (Abstract),* Meteorites & Planet. Sci., 32, 138-139

[123] Geiger, T. and Bischoff, A. (1995), *Formation of opaque minerals in CK chondrites*, Planetary and Space Science, 43, 485-498

[124] Grady, M. M. (2000), *Catalogue of meteorites*, ISBN 0521663032, Cambridge, UK: Cambridge University Press, 696

[125] Rubin A. E. (2005), *Relationships among intrinsic properties of ordinary chondrites: Oxidation state, bulk chemistry, oxygen-isotopic composition, petrologic type, and chondrule size,* GCA, 69, 20, 4907-4918

[126] Sears, D. W. G., Grossman, J. N. and Wasson, J. T. (1982), *The compositional classification of chondrites: II. The enstatite chodrinte groups*, Geochim. Chosmochim. Acta 46, 597-608

[127] Brearly, A. J. and Jones, R. H. (1998), *Chondritic meteorites.*, in Planetary Materials, Reviews in mineralogy (ed. J. J. Papike), Mineralogical Society of America, Washington DC, 36, chap.3, 313-398

[128] Prinz M., Nehru C. E., Delaney J. S., and Weisberg M. (1983), *Silicates in IAB and IIICD irons, winonaites, lodranites and Brachina: a primitive and modified-primitive group*, In Lunar Planet. Sci. XIV. The Lunar and Planetary Institute, Houston, 616–617

[129] Prinz M., Waggoner, D.G. and Hamilton, P.J. (1980), *Winonaites: a Primitive Achondritic Group Related to Silicate Inclusions in IAB Irons*, Lunar Planet. Sci. XI, 902-904

[130] Kimura, M., Tsuchiyama, A., Fukuoka, T. and Imura, Y. (1992), *Antarctic primitive achondrites Yamato-74025, -75300, and -75305: Their mineralogy, thermal history and the relevance to winonaite*, Sixteenth Symposium on Antarctic Meteorites. Proceedings of the NIPR Symposium, No. 5, held June 5-7, 1991, at the National Institute of Polar Research, Tokyo. Editor in Chief, Keizo Yanai, with Hideyasu Kojima, Noboru Nakamura, Nobuo Takaoka, Hiroshi Takeda, and Yoshio Yoshida. Published by the National Institute of Polar Research, 165-190

[131] McCoy, T. J., Keil, K., Clayton, R. N., Mayeda, T. K., Bogard, D. D., Garrison, D. H., Huss, G. R., Hutcheon, I. D. and Wieler, R. (1996), *A petrologic, chemical and isotopic study of Monument Draw and comparison with other acapulcoites: evidence for formation by incipient partial melting,* GCA, 60, 14, 2681-2708

[132] Mittlefehldt, D. W., McCoy, T. J., Goodrich, C. A. and Kracher, A. (1998), *Non-chondritic meteorites from asteroidal bodies,* In Planetary materials, Reviews in Mineralogy (ed. J. J. Papike), Mineralogical Society of America, Washington DC, 36, charpter 4, 414-495

[133] Benedix, G. K., McCoy, T. J., Keil, K., Bogard, D. D. and Garrisson, D. H. (1998), *A petrologic study of winonaites: evidence for early partial melting, brecciation, and metamorphism,* GCA, 62, 2535-2553

[134] Benedix, G. K., McCoy, T. J., Keil, K. and Love, S. G. (2000), *A petrologic study of the IAB iron meteorites: constraints on the formation of the IAB-winonaite parent body,* Meteorit Planet. Sci., 35, 6, 1127-1141

[135] Connelly, J. N., Bizzarro, M., Thrane, K., Baker, J. A. (2008), *The Pb Pb age of Angrite SAH99555 revisited*, GCA, 72, 19, 4813-4824

[136] Keil, K. (1989), *Enstatite meteorites and their parent bodies*, Meteoritics (ISSN 0026-1114), 24, 195-208

[137] Takeda, H. (1997), *Mineralogical records of early planetary processes on the HED parent body with reference to Vesta*, Meteorit. Planet. Sci., 32, 843

[138] Bowman, L. E., Spilde, M. N. and Papike, J. J. (1997), *Automated energy dispersive spectrometer modal analysis applied to diogenites*, Meteorit. Planet. Sci., 32, 6, 869-875

[139] Pun, A., Keil, K., Taylor, G. J. and Wieler, R. (1998), *The Kapoeta howardite: implications for the regolith evolution of the howardite-eucrite-diogenite parent body*, Meteorit. Planet. Sci., 33, 4, 835-851

[140] Lovering, J. F., Nichiporuk, W., Chodos, A. and Brown, H. (1957), *The distribution of gallium, germanium, cobalt, chromium and copper in iron and stony-iron meteorites in relation to nickel content and structure*, GCA, 11, 4, 263-278

[141] Scott, E. R. D. (1977), *Pallasites - Metal composition, classification and relationships with iron meteorites*, GCA 41, 349-360

[142] McKeegan, K. D. and Davis, A. M. (2005), *Meteorites, Comets and Planets: Treatise on Geochemistry*, Edited by A. M. Davis. Executive Editors: H. D. Holland and K. K. Turekian. Elsevier B. V., Amsterdam, The Netherlands, 1, 431-460

[143] McKeegan, K. D., Walker, R. M., Zinner, E. (1985), *Ion microprobe isotopic measurements of individual interplanetary dust particles*, Geochimica et Cosmochimica Acta (ISSN 0016-7037), 49, 1971-1987

[144] Connelly, J. N., Amelin, Y., Krot, A. N., Bizzarro, M. (2008), *Chronology of the Solar System's Oldest Solids*, ApJ, 675, 2, 121-124

[145] Shukolyukov, A., Lugmair, G. W. (2002), *Chronology of Asteroid Accretion and Differentiation*, Asteroids III, W. F. Bottke Jr., A. Cellino, P. Paolicchi, and R. P. Binzel (eds), University of Arizona Press, Tucson, 687-695

[146] Shu, F. H., Shang, H., Gounelle, M. and Glassgold, A. E. (2001), *The origin of chondrules and refractory inclusions in chondritic meteorites,* ApJ, 548, 1029-1050

[147] Desch, S. J., Connolly, H. C., Jr. (2002), *A model of the thermal processing of particles in solar nebula shocks: Application to the cooling rates of chondrules*, Meteoritics & Planetary Science, 37, 2, 183-207

[148] Morris, M. A. & Desch, S. J. (2010), *Thermal Histories of Chondrules in Solar Nebula Shocks*, ApJ, 722, 2, 1474-1494

[149] Binzel R.P., Harris A.W., Bus S.J., and Burbine T.H. (2001), *Spectral Properties of Near-Earth Objects: Palomar and IRTF Results for 48 Objects Including Spacecraft Targets (9969) Braille and (10302) 1989 ML.*, Icarus, 151, 2, 139-149

[150] Drake, M.J. (2001), *The eucrite – Vesta story*, Meteoritics & Planetary Science, 36, 4, 501-513

[151] Ivezić, Ž., Tabachnik, S., Rafikov, R., Lupton, R. H., Quinn, T., Hammergren, M., Eyer, L., Chu, J., Armstrong, J. C., Fan, X., Finlator, K., Geballe, T. R., Gunn, J. E., Hennessy, G. S., Knapp, G. R., Leggett, S. K., Munn, J. A., Pier, J. R., Rockosi, C. M., Schneider, D. P., Strauss, M. A., Yanny, B., Brinkmann, J., Csabai, I., Hindsley, R. B., Kent, S., Lamb, D. Q., Margon, B., McKay, T. A., Smith, J. A., Waddel, P., York, D. G., the SDSS Collaboration (2001), *Solar System Objects Observed in the Sloan Digital Sky Survey Commissioning Data*, ApJ, 122, 5, 2749-2784

[152] Lugmair, G. W. and Shukolyukov, A. (1998), *Early solar system timescales according to 53Mn-53Cr systematics*, GCA, 62, 2863-2886

[153] McCord, T. B., Adams, J. B., Johnson, T. V. (1970), *Asteroid Vesta: Spectral Reflectivity and Compositional Implications*, Science, 168, 3938, 1445-1447

[154] Wasson, J. T. and Wetherill, G. W. (1979), *Dynamical chemical and isotopic evidence regarding the formation locations of asteroids and meteorites*, In: Asteroids. (A80-24551 08-91) Tucson, Ariz., University of Arizona Press, 926-974

[155] Asphaug, E. (1997), *Impact origin of the Vesta family*, Meteoritics & Planetary Science, 32, 6, 965-980

[156] Lazzaro, D., Michtchenko, T., Carvano, J. M., Binzel, R. P., Bus, S. J., Burbine, T. H., Mothé-Diniz, T., Florczak, M., Angeli, C. A., Harris, Alan W. (2000), *Discovery of a Basaltic Asteroid in the Outer Main Belt*, Science, 288, 5473, 2033-2035

[157] Binzel, R. P., Xu, S., Bus, S. J., Skrutskie, M. F., Meyer, M. R., Knezek, P., Barker, E. S. (1993), *Discovery of a Main-Belt Asteroid Resembling Ordinary Chondrite Meteorites*, Science, 262, 5139, 1541-1543

[158] Farinella, P., Gonczi, R., Froeschle, Ch., Froeschle, C. (1993), *The injection of asteroid fragments into resonances*, Icarus (ISSN 0019-1035), 101, 2, 174-187

[159] Gaffey, M. J. and Gilbert, S. L. (1998), *Asteroid 6 Hebe: The probable parent body of the H-Type ordinary chondrites and the IIE iron meteorites*, Meteoritics & Planetary Science, 33, 6, 1281-1295

[160] Burbine, T. H. (1998), *Could G-class asteroids be the parent bodies of the CM chondrites?*, Meteoritics & Planetary Science, 33, 2, 253-258

[161] Gounelle, M., Morbidelli, A., Bland, P. A., Spurny, P., Young, E. D., Sephton, M. (2008), *Meteorites from the outer Solar System?*, The Solar System Beyond Neptune, M. A. Barucci, H. Boehnhardt, D. P. Cruikshank, and A. Morbidelli (eds.), University of Arizona Press, Tucson, 592, 525-541

[162] Clark, B. E., Hapke, B., Pieters, C., Britt, D. (2002), Asteroid Space Weathering and Regolith Evolution, Asteroids III, W. F. Bottke Jr., A. Cellino, P. Paolicchi, and R. P. Binzel (eds), University of Arizona Press, Tucson, 585-599

[163] Sasaki, S., Nakamura, K., Hamabe, Y., Kurahashi, E. and Hiroi, T. (2001), *Production of iron nanoparticles by laser irradiation in a simulation of lunar-like space weathering*, Nature, 410, 6828, 555-557

[164] Hapke, B. (2001), *Space weathering from Mercury to the asteroid belt*, Journal of Geophysical Research, 106, E5, 10039-10074

[165] Gold, T. (1955), *The Lunar surface,* MNRAS, 115, 585-604

[166] Hapke, B. (1993), *Theory of Reflectance and Emittance Spectroscopy*, Cambridge University Press, 1st edition

[167] McGuire, A. F. and Hapke, B. (1995), *An Experimental Study of Light Scattering by Large, Irregular Particles*, *Icarus*, 113, 134-155

[168] Jehl, A. (2008), *Etude photométrique de la surface de Mars à partir de la caméra HRSC à bord de la sonde Mars Express : Préparation aux observations orbitales multi-angulaires en exploration planétaire.*, PhD Thesys, 20.

[169] Hapke, B. (2002), *Bidirectional reflectance spectroscopy. 5. The coherent backscatter opposition effect and anisotropic scattering.* Icarus, 157, 523-534

[170] Mustard, J. F. and C. M. Pieters (1989), *Photometric phase functions of common geologic materials and applications to quantitative analysis of mineral mixture reflectance spectra*, JGR, 94, 13, 619-634

[171] Hiroi, T. (1994), *Recalculations of the isotropic H-functions*, Icarus, 109, 313-317

[172] Clark, B. E., Bus, S. J., Rivkin, A. S., McConnochie, T., Sanders, J., Shah, S., Hiroi, T. and Shepard, M. (2004), *E-type asteroid spectroscopy and compositional modeling*, JGR, 109, doi: 10.1029/2003JE002200

[173] Pieters, C. M. and Hiroi, T. (2004), *RELAB (Reflectance Experiment Laboratory): A NASA multi-user spectroscopy facility,* LPS, 35, Abstract #1720 (CDROM)

[174] Duffard, R., Lazzaro, D. and De Léon, J. (2005), *Revisiting spectral parameters of silicate-bearing meteorites*, Meteor. & Planet. Sci. 40, 3, 445-459

[175] Rayner, J. T., Tooney, D. W., Onaka, P. M., Denault, A. J., Stahlberger, W. E., Vacca, W. D., Cushing, M. C. and Wang, S. (2003), *"SpeX: A Medium-Resolution 0.8-5.5 micron Spectrograph and Imager for the NASA Infrared Telescope Facility"*, PASP 115, 362

[176] Hiroi, T., Binzel, R. P., Sunshine, J. M., Pieters, C. M. and Takeda H. (1995), *Grain sizes and mineral compositions of surface regoliths of Vesta-like asteroids.* Icarus, 115, 374-386

[177] Burbine, T. H., Buchanan, P. C., Dolkar, T. and Binzel, R. P. (2009), *Pyroxene mineralogies of near-Earth vestoids*, MPS, 44, 9, 1331-1341

[178] Righter, K. and Drake, M. J. (1997), *A magma ocean on Vesta: Core formation and petrogenesis of eucrites and diogenites*, MPS, 32, 929-944

[179] Cruikshank, D. P., Tholen, D. J., Bell, J. F., Hartmann, W. K. and Brown, R. H. (1991), *Three basaltic earth-approaching asteroids and the source of the basaltic meteorites*, Icarus, 89, 1-13

[180] Migliorini, F., Morbidelli, A., Zappala, V., Gladman, B. J., Bailey, M. E. and Cellino, A. (1997), Vesta fragments from v6 and 3:1 resonances: Implications for V-type NEAs and HED meteorites, MPS, 32, 903-916

[181] Sunshine, J. M., Bus, S. J., McCoy, T. J., Burbine, T. H., Corrigan, C. M. and Binzel, R. P. (2004), *Hgh-calcium pyroxene as an indicator of igneous differentiation in asteroids and meteorites*, MPS, 39, 8, 1343-1357

U.PORTO
FACULDADE DE CIÊNCIAS
UNIVERSIDADE DO PORTO

# Annexes:

# A. Glossary

*Achondrites:* are types of meteorites which do not contain chondrules.

*Albedo:* is the fraction of incident light that an object reflects.

*Anhydrous minerals:* are minerals which do not have water in their chemical composition.

*Aqueous Alteration:* is a process in which changes to minerals occurs through reactions with water.

*Atmophile elements:* represent one group of the Goldschmidt classification. They remain mostly on or above the surface because they are liquids and/or gases at temperatures and pressures found on the surface. The atmophile elements are: H, C, N and noble gases.

*Breccias:* are fragmented rocks.

*Calchophile elements:* represent one group of the Goldschmidt classification. They remain on or close to the surface as they combine readily with sulfur and/or some other chalcogen other than oxygen, forming compounds which do not sink into the core. The calchopile elements are: Ag, As, Bi, Cd, Cu, Ga, Ge, Hg, In, Pb, Po, S, Sb, Se, Sn, Te, Tl and Zn.

*Charge-coupled device (CCD):* is a small semiconductor chip that serves as a light detector by emitting electrons when it is struck by light. A computer uses the pattern of electron emission to form images.

*Chondrites:* are types of meteorites which contain chondrules. They are composed by primitive aggregates of the early Solar System material.

*Chondrules:* are small spherical rocks usually with less than 1mm in diameter. They are one of the chondrites constituents.

U.PORTO
FACULDADE DE CIÊNCIAS
UNIVERSIDADE DO PORTO

*Clans:* is a relatively new classification scheme of meteorites used as a higher order classification than group, but less than class. It is defined to report chondrites that have chemical, mineralogical and isotopic similarities and were thought to have formed in the same local region o the solar nebula. Clans may represent materials which have experienced different secondary histories such as brecciation, oxidation or reduction, and/or hydrothermal alteration.

*Class:* consists of two or more groups of meteorites which share primary whole-rock chemical and O-isotopic properties.

*Clasts:* is a rock fragment or gain resulting from the breakdown of larger rocks.

*Cometary meteorites:* is a term used for referring meteorites coming from objects of the outer Solar System.

*Differentiation:* is a process which separates distinct constituents of planetary bodies due to their physical and chemical behavior. This process has occurred on planets, dwarf planets, natural satellites and on the asteroid 4 Vesta, dividing these bodies into several layers where the heavier material are found in the inner layer and the less dense material are found near the superficial layer.

*Diffraction:* is the spreading of light upon passing the edge of an object.

*Diogenitic material:* is material which has a similar composition to diogenites.

*Edgeworth-Kuiper Belt:* is a region of the Solar System which lies roughly between the orbit of Neptune and 50AU. It is composed by small bodies as the Main Asteroid Belt and several remnants from the Solar System's formation. The Edgeworth-Kuiper Belt objects are mainly composed by "ices", such as methane, ammonia and water.

*Eucritic material:* is material which has a similar composition to eucrites.

*Feeding zone:* is a region delimited by $\sim 10 - 12$ Hill radii, from where planetary embryos accreted most of their masses.

*Fractionation:* is a separation process in which a quantity of a mixture is divided into smaller quantities, changing the composition according to the gradient.

U.PORTO
FACULDADE DE CIÊNCIAS
UNIVERSIDADE DO PORTO

*Gabbro:* is a large group of dark, intrusive mafic igneous rocks chemically equivalent to basalt.

*Group:* is the most basic and significant unit used in meteorite taxonomy. It is defined as a minimum of five unpaired chondrites with similar petrologic (chondrules size, modal abundances and mineral compositions), whole-rock chemical and O-isotopic characteristics.

*Grouplet:* is defined as only having between two and four meteorites catalogued.

*Hill radius:* corresponds to the largest distances at which a planet can possess a moon. It is defined as: $\mathrm{R_H} = \mathrm{a} \times \sqrt[3]{\frac{\mathrm{M_{Planet}}}{3 \times \mathrm{M_{Sun}}}}$, where *a* corresponds to the semi-major axis of the orbit of the planet, $M_{Planet}$ to the mass of the planet and $M_{Sun}$ to the mass of the Sun.

*Igneous textures:* are the igneous rocks textures. Igneous rocks are formed through the cooling and solidification of magma or lava.

*Lagrange points:* the mathematician Joseph-Louis de Lagrange discovered the existence of special points close to an orbital system of two massive objects. They mark five regions where the combined gravitational pull of the two large masses provides precisely the centripetal force to orbit with them.

*Lithification:* is a process in which sediments compact under pressure, expel connate fluids and gradually become solid rock.

*Litophile elements:* represent one group of the Goldschmidt classification. They are elements which are on or close to the surface of planetary bodies as they combine readily with oxygen and do not sank into the core region. The litophile elements are: Al, At, B, Ba, Be, Br, Ca, Cl, Cr, Cs, F, I, Hf, K, Li, Mg, Na, Nb, O, P, Rb, Sc, Si, Sr, Ta, Th, Ti, U, V, Y, Zr, W and Lanthanides.

*Kirkwood gaps:* are regions in the Main Asteroid Belt where asteroids were scattered. These regions are gaps in the distribution of asteroids in the Main Asteroid Belt and are caused by resonances with Jupiter.

*Mafic Mineral:* is reported to a mineral which belongs to the silicate group. This kinds of minerals is rich in magnesium and iron.

U.PORTO
FACULDADE DE CIÊNCIAS
UNIVERSIDADE DO PORTO

*Matrix:* is the embedded medium between chondrules, grain, etc., in meteorites.

*Mesostatis:* is the very last stage in the formation of an igneous rock.

*Metamorphism:* is the solid-state recrystallization of pre-existing rocks due to changes in physical and chemical conditions.

*Oort Cloud:* is probably a spherical region which may lie roughly at distances larger than 50.000 AU. This cloud is also referred as the probable reservoir of long-period comets.

*Planetary embryos*: are objects with Lunar to Martian masses, precursors of the terrestrial planets. These objects are expected to have formed in the terrestrial planets zone or in the Main Asteroid Belt region.

*Planetesimal:* are solid bodies of around 1km in diameter, formed by particles which stuck together during the earlier stages of the Solar System.

*Plutinos:* are TNOs that share the same 3:2 resonance as Pluto does with Neptune. Their eccentricities range between 0.1 and 0.3. Their color varies from blue/neutral to very red. Their sizes range from a few kms to a few thousands of kms. Plutinos have a semi-major axis within $39.5 < a < 40.5$ AU.

*Poyting-Robertson effect*: is a process by which solar radiation causes a dust grain to slowly spiral into the Sun.

*Probable parent body:* is an asteroid with the appropriate surface mineralogy and whose orbital locations allow the delivery of fragments in abundances comparable to the fall of the particular meteorite type.

*Reflectance spectrum:* is a spectrum which shows the proportion of light by a surface over a range of wavelengths. Several minerals in the surface reflect light in characteristic ways, so the reflectance spectrum of a body provides information about its mineralogical composition.

*Regolith:* is a layer which covers the surfaces terrestrial planets, moons and several asteroids. It is mainly composed by dust, soil and broken rocks.

U.PORTO
FACULDADE DE CIÊNCIAS
UNIVERSIDADE DO PORTO

*Regolith breccias:* is one type of breccias. They contain solar-gas-bearing dust grain in their matrices.

*Secular resonances:* occurs when the frequency of variation of the longitude of pericenter ω(g), or longitude of the node Ω(s), becomes almost equal to an eigenfrequency of the system of coupled planetary orbits.

*Sedimentation:* is the deposition of particles carried by a fluid flow.

*Siderophile elements:* represent one group of the Goldschmidt classification. They are the high density transition metals which tend to sink into the core regions, because they dissolve readily in iron. The siderophile elements are: Au, Co, Fe, Ir, Mn, Mo, Ni, Os, Pd, Pt, Re, Rh and Ru.

*Snowline*: corresponds to the radius in the protoplanetary disk beyond water ice can be present. Water ice only forms at temperatures below 180K, so the snowline fell near 3AU in the early solar nebula. Actually, this fact is consistent with the water-rich asteroids (also known as the C-class asteroids), which are found essentially in the outer asteroid belt.

*Space weathering:* is a term used for some processes that act on any body exposed to the harsh space environment. These processes include exposure to the galactic and solar cosmic rays, to the bombardment of micrometeorites or irradiation from solar wind particles. Space weathering plays an important role in changing the physical and optical properties of the surface of several planetary objects.

*Texture:* is the physical appearance of a meteorite, such as grain size, shape, arrangement and pattern at macroscopic and microscopic feature level.

*Type-I migration*: happens when the gravitational attraction of overdense regions exerts a torque on the planet which changes its orbit. Torqueses due to gas orbiting inside and outside the planet have opposite signs but, in general, unequal magnitude, such that a planet is likely to lose angular momentum and drift inwards.

*Yarkovsky effect:* is a force that acts on a rotating body in space. It is caused by the anisotropic emission of thermal photons, which carry momentum. Its influence is higher in smaller asteroids.

*Widmanstätten pattern*: is a remarkable pattern of octaehedrites, which is caused by a minor degenerative process in the octahedral crystal during the annealing process.

U.PORTO
FACULDADE DE CIÊNCIAS
UNIVERSIDADE DO PORTO

# B. Minerals

In this section, a briefly glossary of minerals is provided. This section is divided into three subsections as follows: Mineral Groups, where the groups of minerals are described; Glossary of Minerals, where the minerals pointed out in chapter 3 will be described; Minerals used in this study, where a briefly description of the minerals used in this study will be given.

## B.1. Mineral Groups

A mineral is a solid body which formed due to the chemical and physical interaction in a geological ambient. They are classified taking into account their crystalline structure and chemical composition. However, some minerals can share the same chemical composition but they can be quite different in the way that their atoms and molecule are distributed in space (e.g. the graphite and the diamante). The physical properties of minerals are a result of their chemical composition and structural features. Some physical properties can be stated out, such as: their color, crystalline structure, cleavage, density or magnetism.

According to the chemical composition of minerals, they can be classified into the following groups:

1. Silicate Group: In this group, minerals are mainly composed by silicon and oxygen, with the addition of cations like magnesium, iron or calcium.
2. Carbonates, Nitrates and Borates Group: Salts of three acids are included in this group: nitric acid ($H[NO_3]$), carbonic acid ($H_2[CO_3]$) and boric acid ($H_3[BO_3]$).
3. Sulphides Group: sulphides consist essentially on sulfuric acid salts ($H_2S$). The most frequent metals in these compounds are: iron (Fe), cobalt (Co), nickel (Ni), copper (Cu), silver (Ag), zinc (Zn), mercury (Hg) and lead (Pb). The sulfur can be replaced by some quite similar elements, such as: selenium (Se), tellurium (Te), arsenic (As), antimony (Sb) or bismuth (Bi).
4. Halide salts Group: Halide salts are composed by the following elements: fluorine (F), chlorine (Cl), bromine (Br) and Iodine (I).
5. Oxides and Hydroxides Group: Oxides are a result of an oxidation reaction. In this case, oxygen can be combined with other elements. In the case of

hydroxides, the atom of oxygen can be replaced by the hydroxide group OH. Several elements tend to aggregate to oxygen, as for example: silicon (Si), magnesium (Mg), aluminum (Al), sodium (Na), calcium (Ca), potassium (K) or iron (Fe).

6. Sulfates and Chromates Group: Salts of two acids are included in this group: sulfuric acid ($H_2[SO_4]$) and chromic acid ($H_2[CrO_4]$).
7. Phosphates, Arsenates and Vanadates Group: This group is mainly composed by the salts of the phosphoric acid ($H_3[PO_4]$), where due to their crystal-chemical affinity the salts of the arsenic acid ($H_3[AsO_4]$) and the vanadic acid ($H_3[VO_4]$).
8. Organic compounds Group.
9. Native elements Group.

## B.2. Glossary of minerals

Hereafter the minerals pointed out in chapter 3, will be briefly described.

*Anorthite:* Belongs to the Silicate Group of minerals. It is a compositional variation of feldspar plagioclase. Its chemical formula is $Ca[Al_2Si_2O_8]$.

*Apatite:* Belongs to the Phosphates, Arsenates and Vanadates Group. Its chemical formula is $Ca_5[(F,Cl,OH)|(PO_4)_3]$.

*Augite:* Belongs to the Silicate Group. It is an intermediate mineral of the solid solution series of the pyroxenes group.

*Chromite:* Belongs to the Oxides and Hydroxides Group. Its chemical formula is $FeCr_2O_4$.

*Corundum:* Crystalline phase of the aluminum oxide ($Al_2O_3$).

*Diopside:* It is a monocyclic mineral, belonging to the pyroxenes group. Its chemical formula is $MgCaSi_2O_6$.

*Enstatite:* Enstatite is a pyroxenic silicate mineral. Its chemical formula is $Mg_2[Si_2O_6]$.

*Forsterite:* It is a terminal member of the solid solution series of olivine-rich in magnesium. Its chemical formula is $Mg_2SiO_4$.

*Graphite:* It is the stable form of carbon on Earth's surface.

*Grossite*: Belongs to the Oxides and Hydroxides Group. Its chemical formula is $CaAl_4O_7$.

*Hibonite*: Belongs to the Oxides and Hydroxides Group. Its chemical formula is $(Ca,Ce)(Al,Ti,Mg)_{12}O_{19}$.

*Magnetite:* Belongs to the Oxides and Hydroxides Group. It is a ferromagnetic mineral and its chemical formula is $Fe_3O_4$.

*Melilite:* Belongs to the Silicates Group. Its general chemical formula is $(Ca,Na)_2(Mg,Al,Fe)[Si_2O_7]$.

*Nepheline:* Belongs to the Silicates Group. Its chemical formula is $KNa_3[AlSiO_4]_4$.

Oldhamite: Belongs to the Silicates Group. Its chemical formula is (Ca,Mg,Fe)S.

*Olivine:* Belongs to the Silicates Group. The ratio of iron and magnesium changes between two endmembers of the solid solution series: forsterite (Mg-endmember) and fayalite (Fe-endmember). Its chemical formula is $(Mg,Fe)_2[SiO_4]$.

*Orthopyroxene:* It is common in mafic igneous rocks and also found in some high grade metamorphic rocks. Its chemical formula is $(Mg,Fe,Ca)(Mg,Fe,Al)(Si,Al)_2O_6$.

*Osbornite:* Belongs to the native elements group. Its chemical formula is TiN.

*Perovskite:* Belongs to the Oxides and Hydroxides Group. Its chemical formula is $CaTiO_3$.

*Pyrite:* Belongs to the Sulphides Group. Its chemical formula is $FeS_2$.

*Phyllosilicates:* It is a type of silicate minerals, which are differentiated by its silicate ionic group. It contains silicon and oxygen.

*Pigeonite:* It is a mineral that belongs to the Silicates Group. Its general chemical formula is $(Ca,Mg,Fe)(Mg,Fe)Si_2O_6$.

U.PORTO
FACULDADE DE CIÊNCIAS
UNIVERSIDADE DO PORTO

*Plagioclase:* It is a series of solid solutions, also known as the plagioclase feldspar series. The members of this series vary between albite ($NaAlSi_3O_8$) and anorthite ($CaAl_2Si_2O_8$).

*Pyroxene:* Belongs to the Silicates Group. Pyroxenes are found among several igneous and metamorphic rocks. It usual chemical formula is $AB[Si_2O_6]$, where A can be replaced by atoms of calcium or lithium and B can be replaced by atoms of iron, magnesium or aluminum.

*Schreibersite:* Belongs to the native elements group. Its chemical formula is $(Fe,Ni)_3P$.

*Spinel:* Belongs to the Oxides and Hydroxides Group. Its chemical formula is $MgAl_2O_4$.

*Troilite:* Belongs to the Sulphides Group. It is a terminal member of a ferrous sulphide (chemical compound containing sulfur in its lowest oxidation state). Its chemical formula is FeS.

*Whitlockite:* Belongs to the Phosphates, Arsenates and Vanadates Group. Its chemical formula is $Ca_9(Mg,Fe^{2+})(PO_4)_6(PO_3OH)$.

## B.3. Minerals used in this study

In this section a detailed description of the minerals used in this study (orthopyroxenes, clinopyroxenes, olivine and anorthite ) will be provided.

Pyroxenes are a group of important rock-forming inosilicate minerals found in many igneous and metamorphic rocks. They share a common structure consisting of single silica tetrahedral chains and they crystallize in the monocyclic and orthorhombic systems. The monocyclic and orthorhombic systems are two of the 7 lattice point groups. They are described by three vectors of unequal length. In the monocyclic system the vectors form a rectangular prism with a parallelogram as its base, where two pairs of vectors are perpendicular and the third pair makes an angle other than 90º. The orthorhombic lattices are a result of stretching a cubic lattice along two of its orthogonal pairs, by two different factors, resulting in a rectangular prism with a rectangular base. All three bases intersect at angles of 90º.

Pyroxenes have the following general chemical formula: $XY[(Si,Al)_2O_6]$, where X commonly represents calcium, sodium, magnesium and $Fe^{2+}$ and Y commonly

represents ions of smaller size, such as chromium, aluminium, magnesium, manganese, $Fe^{3+}$ or even $Fe^{2+}$.

The chain silicate structure of the pyroxenes offers a high flexibility in the incorporation of several cations. Hence, pyroxenes are named primarily after its chemical composition. Pyroxene minerals are named taking into account the chemical species occupying the X or M1 site, the Y or M2 site and the tetrahedral T site (Fig.B.1).

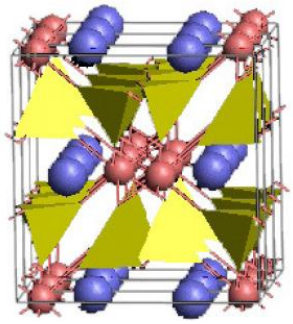

Fig.B.1 - Pyroxene crystal structure. Yellow: $SiO_4$ tetrahedra. Red: position occupied by smaller cations or Y. Blue: position occupied by bigger cations or X. *Source:* M. Font-Altaba, *Atlas de Mineralogia*, Edições Jover, S.A

A common pyroxene has mostly silicon in the tetrahedral site and predominantly ions with a charge of +2 in both X and Y sites, originating the approximate formula $XYT_2O_6$. The names of the common calcium-iron-magnesium pyroxenes are defined in the "pyroxene quadrilateral" (Fig.B.2).

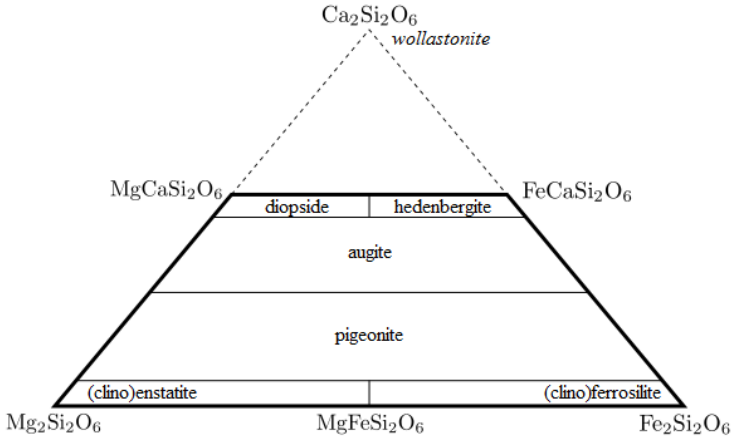


Fig.B.2 - The nomenclature of the calcium, magnesium, iron pyroxenes. *Source:* Morimoto, N. (1989), *Nomenclature of pyroxenes,* Canadian Mineralogist, 27, 84

Another important series of pyroxenes minerals are the sodium-rich pyroxenes, which are named according to Fig.B.3.

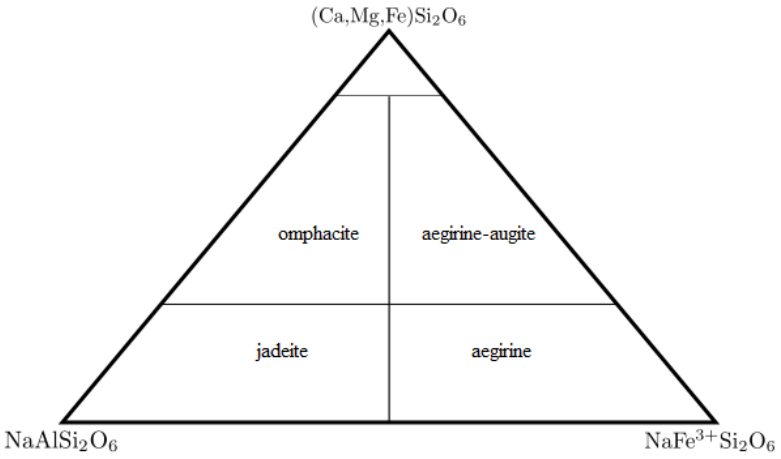


Fig.B.3 - The nomenclature of sodium pyroxenes. *Source:* Morimoto, N. (1989), *Nomenclature of pyroxenes,* Canadian Mineralogist, 27, 85

According to the system under which the pyroxenes crystallize, they can be classed into two groups: clinopyroxenes (monocyclic structure), which is a high-calcium pyroxene; orthopyroxene (orthorhombic structure), which is a low-calcium pyroxene. Belonging to the clinopyroxenes groups there are the following minerals: aegirine, augite, clinoenstatite, diopside, esseneite, hedenbergite, jadeite, jervisite, johannsenite, kanoite, kosmochlor, namansilite, natalyite, omphacite, petedunnite, pigeonite and spodumene. On the other hand, belonging to the orthopyroxenes group there are the following minerals: hypersthenes, donpeacorite, enstatite, ferrosilite and nchwaningite.

Spectrally, both low-calcium and high-calcium pyroxenes are characterized by absorption features near both 1 and 2μm, due to electronic transitions of $Fe^{2+}$ ions in the M2 crystallographic site, in the pyroxene structure. But, in high-calcium pyroxenes, these absorption features can occur at higher wavelengths as the $Ca^{2+}$ ions replace $Mg^{2+}$ ions in the M2 sites. In high-calcium pyroxenes, $Ca^{2+}$ ions preferentially fill the M2 site, while $Fe^{2+}$ ions preferentially fill the M1 site. This can cause additionally absorption features, the strongest of which is found near 1.2μm.

Olivine is a magnesium iron silicate and its general chemical formula is $(Mg,Fe)_2[SiO_4]$. Olivine gives its name to the group of minerals with a related structure (called the olivine group), which includes trephroite ($Mn_2SiO_4$), monticellite ($CaMgSiO_4$)

and kirschsteinite ($CaFeSiO_4$). The minerals in the olivine group crystallize in the orthorhombic system with isolated silicate tetrahedra (Fig.B.4). There are three distinct oxygen sites (marked by O1, O2 and O3), two distinct metal sites (M1 and M2) and only one distinct silicon site (Si), in Fig.B.4.

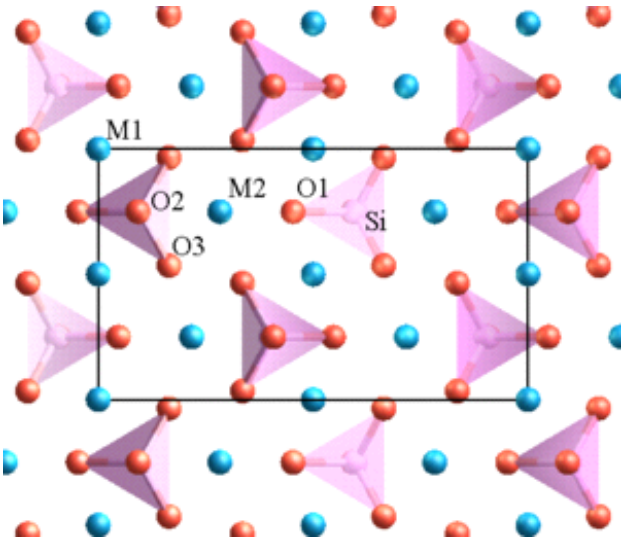


Fig.A.4 - The atomic scale structure of olivine looking along the *a* axis. Oxygen is shown in red, silicon in pink, and magnesium/iron in blue. A projection of the unit cell is shown by the black rectangle. *Source:* Wikipedia.

The olivine spectrum denotes a complex absorption feature near 1000nm, which includes three absorptions originated by transitions of $Fe^{2+}$ crystal site, in the M1 and M2 sites in the olivine structure. Each one of these absorptions moves towards higher wavelengths with the increasing content of $Fe^{2+}$. It is also important to quote that any changes in the Fe/Mg ratio modifies the M1 and M2 absorption intensities. Hence, the shape of total absorption band is altered.

Anorthite is the calcium-rich endmember of the plagioclase feldspar solution series (Fig.B.5). Its general chemical formula is $CaAl_2Si_2O_8$. The plagioclase feldspars have a triclinic structure. In the triclinic system, the crystal is described by vectors of unequal length, which are not mutually orthogonal.

The plagioclase series (Fig.B.5), with anorthite percentage in parentheses, follows: albite (0 to 10), oligoclase (10 to 30), andesine (30 to 50), labradorite (50 to 70), bytownite (70 to 90) and anorthite (90 to 100).

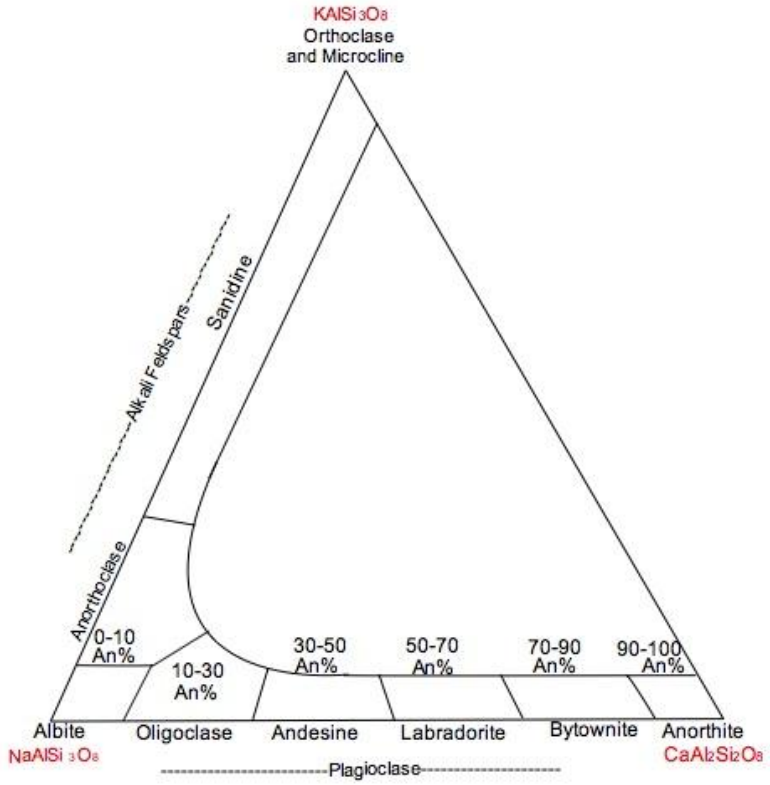


Fig.B.5 - Compositional phase diagram of the different minerals that constitute the feldspar solid solution. *Source:* Wikipedia.

In the plagioclase spectrum, the $Fe^{2+}$ ions also originate a weaker absorption feature than in olivine and pyroxenes, near 1200nm. But, this plagioclase feature can be easily confused with the M1 absorption in high-calcium pyroxenes.

U.PORTO
FACULDADE DE CIÊNCIAS
UNIVERSIDADE DO PORTO

# C. Tables

| Asteroid | Class | Diameter | a(AU) | Family | Predicted Mineralogy[1] |
|---|---|---|---|---|---|
| 3 Juno | S(IV) | 244 | 2.670 | N | px/(ol+px)~0.30 |
| 4 Vesta | V | ~570x460 | 2.362 | Y | pyroxene-plagioclase basalt |
| 6 Hebe | S(IV) | 185 | 2.426 | N | px/(ol+px) ~0.40 and FeNi metal |
| 7 Iris | S(IV) | 203 | 2.386 | N | px/(ol+px) ~0.3; Px~$F_{S42}W_{O7}$ or Cpx-bearing |
| 246 Asporina | A | 64 | 2.695 | N | Olivine+NiFe metal |
| 289 Nenetta | A | 42 | 2.874 | N | Olivine+NiFe metal; px/(ol+px) <0.05 |
| 387 Aquitania | S | 106 | 2.742 | Proposed | Spinel |
| 433 Eros | S(IV) | 39x13x13 | 1.458 | N | px/(ol+px) ~0.36; Px~$F_{S42}W_{O18}$ or Cpx-bearing |
| 446 Aeternitas | A | 43 | 2.788 | Y | Olivine+NiFe metal; px/(ol+px) <0.05 |
| 863 Benkoela | A | 32 | 3.200 | N | Olivine+NiFe metal |
| 980 Anacostia | S | 89 | 2.741 | Proposed | Spinel |
| 3103 Eger | E | 1.5 | 1.406 | N | Iron-free enstatite |

Table C1 – Mineralogy of several asteroids, which have a possible meteorite affinity.

[1] Abbreviations: ol=olivine, px=pyroxene

**Reference:** Gaffey, M.J., Cloutis, E.A., Kelley, M.S., Reed, K.L. (2002), *Mineralogy of asteroids*. In: Bottke, W.F., Cellino, A., Paolicchi, P., Binzel, R.P. (Eds.), Asteroids III. University of Arizona Press, Tucson, p. 195

U.PORTO
FACULDADE DE CIÊNCIAS
UNIVERSIDADE DO PORTO

| Tholen Classification | SMASSII Classification | Description |
|---|---|---|
| B, F | B | Linear, featureless spectrum with bluish to neutral slope |
| | Cb | Similar to B spectrum with neutral to slight reddish slope |
| G | Cg | Strong absorption band (λ<0.55μm), and featureless with neutral to reddish slope (λ>0.55μm) |
| | Cgh | Similar to Cg spectrum, with a shallow absorption centered near 0.7μm |
| C | C | Weak to medium absorption (λ<0.55μm), neutral to slightly reddish and featureless (λ>0.55μm) |
| | Ch | Similar to C spectrum, with shallow absorption centered near 0.7 μm |
| E, M, P | Xc | Slightly reddish spectrum, featureless except for broad convex curvature centered near 0.7μm |
| | Xk | Similar to Xc spectrum, but redder slope (λ<0.7μm), and generally flat (λ>0.7μm) |
| | X | Generally featureless, linear spectrum with slight to moderate reddish slope |
| | Xe | Overall slope slight to moderately red, concave absorption feature centered near 0.5μm, with occasional secondary absorption centered near 0.6μm |
| T | T | Moderately reddish slope (λ<0.75μm), and generally flat (λ>0.85μm) |
| D | D | Relatively featureless spectrum with very steep red slope |
| S | K | Moderately steep red slope (λ<0.75μm) and flat to slightly bluish (λ>0.75μm) |
| | L | Very steep red slope (λ<0.75μm)and flat to slightly bluish (λ>0.75μm) |
| | Ld | Similar to L spectrum, but steeper red slope (λ<0.75μm) |
| | Sa | Similar to S spectrum, but with steeper slope (λ<0.7μm) |
| | Sl | Similar to S spectrum, but with steeper slope (λ<0.7μm) and a shallower absorption band (λ>0.75μm) |
| | S | Moderately steep, reddish slope (λ<0.7μm), and a moderate to deep absorption band (λ>0.75μm) |
| | Sr | Similar to S spectrum, but with very steep red slope (λ<0.7μm) and a deeper absorption (λ>0.75μm) |

U.PORTO
FACULDADE DE CIÊNCIAS
UNIVERSIDADE DO PORTO

| Tholen Classification | SMASSII Classification | Description |
|---|---|---|
| S | Sk | Similar to S spectrum, but with a shallower reddish slope (λ<0.7μm) and a shallower absorption (λ>0.75μm) |
| | Sq | Similar to S spectrum, but with shallower reddish slope (λ<0.7μm) |
| Q | Q | Moderately steep red slope (λ<0.7μm) and a deep, very rounded absorption feature (λ>0.75μm) |
| A | A | Very steep to extremely steep red slope (λ<0.75μm) and a moderately deep absorption (λ>0.75μm). Reflectance maximum or 1μm feature usually more rounded than in S-type spectrum |
| R | R | Very steep red slope (λ<0.7μm) and a deep absorption feature (λ>0.75μm). Reflectance maximum more sharply peaked than in S-type spectra |
| V | V | Moderate to very steep red slope (λ<0.7μm) with an extremely deep absorption band (λ>0.75μm) |
| - | O | Moderately red slope (λ<0.55μm), then less steep (0.55μm<λ<0.7μm). Deep absorption (λ>0.75μm) |

Table C2 – Detailed description about the taxonomic classes of the Tholen and SMASSII classification schemes.

**Reference:** Bus S. J., Vilas F., Barucci M. A., (2002), Visible-Wavelength Spectroscopy of Asteroids, Asteroids III, 169-182

U.PORTO
FACULDADE DE CIÊNCIAS
UNIVERSIDADE DO PORTO

| Asteroid Group | Avg. Distance from Sun (AU) | Perihelion (AU) | Aphelion (AU) |
|---|---|---|---|
| Aten | 0.83-0.97 | 0.46-0.79 | 11.14-1.22 |
| Apollo | 1.24-2.39 | 0.42-0.89 | 1.66-3.91 |
| Amor | 1.46-2.66 | 1.12-1.48 | 1.78-4.07 |
| Inner MAB | 2.20-2.45 | 1.79-2.20 | 2.57-2.93 |
| Middle MAB | 2.58-3.06 | 1.78-2.82 | 2.81-3.60 |
| Outer MAB | 3.13-4.26 | 2.46-4.12 | 3.29-4.40 |
| Trojan | 5.08-5.28 | 4.40-5.00 | 5.20-6.00 |
| Centaur | 13.70-24.90 | 6.60-11.90 | 19.00-37.70 |

Table C3 – Classification of asteroids by the radii of their orbits around the Sun.

**Reference:** Faure, G. and Mensing, T. M. (2007), *Introduction to Planetary Science, The Geological Perspective,* Springer, ISBN-13 978-1-4020-5233-0, 13, 263

| Object | Perihelion | Aphelion |
|---|---|---|
| E | $q \lesssim 4$ | $Q \lesssim 4$ |
| SP | $q \lesssim 4$ | $4 \lesssim Q \lesssim 35$ |
| I | $q \lesssim 4$ | $35 \lesssim Q \lesssim 1000$ |
| L | $q \lesssim 4$ | $Q \gtrsim 1000$ |

Table C4 – Classification scheme for comets based on their aphelion. The Encke-type is defined by E, short period by SP, intermediate-period by I and long-period by L.

**Reference:** Horner, J., Evans, N. W., Bailey, M. E., Asher, D. J. (2003), *The populations of comet-like bodies in the Solar system*, MNRAS, 343, 4, 1060

U.PORTO
FACULDADE DE CIÊNCIAS
UNIVERSIDADE DO PORTO

| Tisserand class | Tisserand parameter |
|---|---|
| Class I | $T_P \lesssim 2.0$ |
| Class II | $2.0 \lesssim T_P \lesssim 2.5$ |
| Class III | $2.5 \lesssim T_P \lesssim 2.8$ |
| Class IV | $2.8 \lesssim T_P$ |

Table C5 – Definition of the Tisserand parameter classification scheme. The upper limit for TP is around 2.8, limit above for which is impossible for an object to be directly injected to a single encounter.

**Reference:** Horner, J., Evans, N. W., Bailey, M. E., Asher, D. J. (2003), *The populations of comet-like bodies in the Solar system*, MNRAS, 343, 4, 1059

U.PORTO
FACULDADE DE CIÊNCIAS
UNIVERSIDADE DO PORTO

Ta

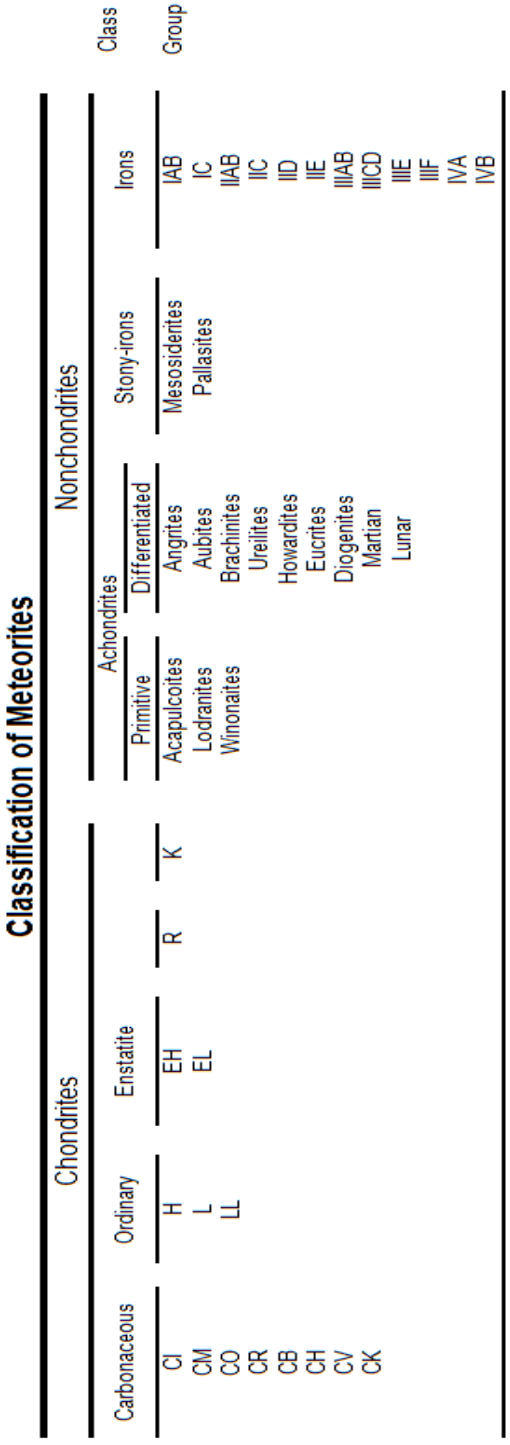


es.

**Reference:** Davies, A. M. (2005), *Meteorites, Comets and Planets*, Elsevier, 1, 84

U.PORTO
FACULDADE DE CIÊNCIAS
UNIVERSIDADE DO PORTO

## Meteorite groups and their numbers

| Chondrites | Falls | Total |
|---|---|---|
| Carbonaceous | | |
| CI | 5 | 5 |
| CM | 15 | 171 |
| CO | 5 | 85 |
| CR | 3 | 78 |
| CB | 0 | 5 |
| CH | 0 | 11 |
| CV | 6 | 49 |
| CK | 2 | 73 |
| Ordinary | | |
| H | 316 | 6962 |
| L | 350 | 6213 |
| LL | 72 | 1048 |
| Enstatite | | |
| EH | 8 | 125 |
| EL | 7 | 38 |
| R | 1 | 19 |
| K | 1 | 3 |

| Nonchondrites | Falls | Total |
|---|---|---|
| Primitive | | |
| Achondrites | | |
| Acapulcoites | 1 | 12 |
| Lodranites | 1 | 14 |
| Winonaites | 1 | 11 |
| Differentiated | | |
| Angrites | 1 | 4 |
| Aubites | 9 | 46 |
| Brachinites | 0 | 7 |
| Ureilites | 5 | 110 |
| Howardites | 20 | 93 |
| Eucrites | 25 | 200 |
| Diogenites | 10 | 94 |
| Martian | 4 | 26 |
| Lunar | 0 | 18 |
| Stony-irons | | |
| Mesosiderites | 7 | 66 |
| Pallasites | 5 | 50 |
| Irons | | |
| IAB | 5 | 131 |
| IC | 0 | 11 |
| IIAB | 6 | 103 |
| IIC | 0 | 8 |
| IID | 3 | 16 |
| IIE | 1 | 18 |
| IIIAB | 11 | 230 |

U.PORTO
FACULDADE DE CIÊNCIAS
UNIVERSIDADE DO PORTO

**Meteorite groups and their numbers**

| Chondrites | Falls | Total | Nonchondrites | Falls | Total |
|---|---|---|---|---|---|
| | | | Irons | | |
| | | | IIICD | 3 | 41 |
| | | | IIIE | 0 | 13 |
| | | | IIIF | 0 | 6 |
| | | | IVA | 4 | 64 |
| | | | IVB | 0 | 13 |

Table C7 – Meteorite groups and numbers of their members. Number of meteorites was taken from Grady (2000).

**Reference:** Grady, M. M. (2000), *Catalogue of meteorites*, Cambridge University Press, London, 689

U.PORTO
FACULDADE DE CIÊNCIAS
UNIVERSIDADE DO PORTO

| Groups | Composition[1] | $\Delta^{17}O$[2] | Genetic Linkages |
|---|---|---|---|
| *Carbonaceous* | | | |
| CI | phy, mag | 0 | |
| CM | phy, toch, ol | -3 | |
| CO | Ol, px, CAIs, met | -4 | |
| CR | phy, px, ol, met | -1.5 | |
| CH | px, met, ol | -1.5 | |
| CV | ol, px, CAIs | -4 | |
| CK | ol, CAIs | -4 | |
| *Ordinary* | | | |
| H | ol, px, plag, met, sul | 0.73 | IIE [1] |
| L | ol, px, plag, met, sul | 1.07 | |
| LL | ol, px, plag, met, sul | 1.26 | |
| *Enstatite* | | | |
| EH | enst, met, sul, plag, ±ol | 0 | |
| EL | enst, met, sul, plag | 0 | |
| *R* | | | |
| R | ol, px, plag, sul | 2.7 | |
| *Primitive Achondrites* | | | |
| Acapulcoites | px, ol, plag, met, sul | -1.04 | Londranites [2] |
| Lodranites | px, ol, met, ±plag, ±sul | -1.18 | Acapulcoites |
| Winonaites | ol, px, plag, met | -0.50 | IAB, IIICD [3] |
| *Differentiated Achondrites* | | | |
| Angrites | $TiO_2$-rich, aug, ol, plag | -0.15 | |
| Aubites | enst,sul | 0.02 | |
| Brachinites | ol, cpx, ±plag | -0.26 | |
| Ureilites | ol, px, graph | -1.20 | |
| Howardites | euritic-diogenetic breccia | -0.26 | Eucrites, Diogenites |

U.PORTO
FACULDADE DE CIÊNCIAS
UNIVERSIDADE DO PORTO

| Groups | Composition[1] | $\Delta^{17}O$[2] | Genetic Linkages |
|---|---|---|---|
| Eucrites | pig, plag | -0.24 | Howardites, Diogenites |
| Diogenites | opx | -0.27 | Eucrites, Howardites |
| *Stony-irons* | | | |
| Mesosiderites | basalt-melt breccia | -0.24 | |
| Pallasites | ol, met | -0.28 | |
| *Irons* | | | |
| IAB | met, sul, ol-px, plag incl | -0.48 | IIICD, Winonaites |
| IC | met, sul | | |
| IIAB | met, sul, schreib | | |
| IIC | met, sul | | |
| IID | met, sul | | |
| IIE | met, sul, ol-px, plag incl | 0.59 | H chondrites |
| IIIAB | met, sul | | |
| IIICD | met, sul, ol-px, plag incl | -0.21 | IAB, Winonaites |
| IIIE | met, sul | -0.43 | |
| IIIF | met, sul | | |
| IVA | met,$SiO_2$-px incl | 1.17 | |
| IVB | met, sul | | |

Table C8 – Meteorite groups and their composition characteristics.

[1] Minerals or components are listed in decreasing order of average abundance. Abbreviations: ol=olivine, px=pyroxene, opx=orthopyroxene, pig=piogenite, enst=enstatite, aug=augite, cpx=clinopyroxene, plag=plagionclase, mag=magnetite, met=metallic iron, sul=sulfides, phy=phyllosilicates, toch=tochilinite, graph=graphite, CAIs=Ca-Al rich refractory inclusions, schreib=schreibersite, incl=inclusions, ±=may be present.

[2] Average values (e.g. Clayton et al. (1991); Clayton and Mayeda (1996, 1999)) for $\Delta^{17}O$, where $\Delta^{17}O=\delta^{17}O-0.52 \times \delta^{18}O$.

**Reference:** Burbine T. H., McCoy T. J., Meibom A., Gladman B., Keil K. (2002), *Meteoritic parent bodies: Their number and identification*. In: Bottke, W. F. Jr., Cellino, A., Paolicchi, P., Binzel, R. P. (Eds), Asteroids III. University of Arizona Press, Tucson, pp. 653–667.

U.PORTO
FACULDADE DE CIÊNCIAS
UNIVERSIDADE DO PORTO

| Group | Fall percentage (%)[1] | Postulated parent body or source body[2] |
|---|---|---|
| L | 38.0 | S(IV) asteroids |
| H | 34.1 | 6 Hebe [S(IV)] |
| LL | 7.9 | S(IV) asteroids |
| Irons | 4.2 | M asteroids |
| Eucrites | 2.7 | 4 Vesta (V) |
| Howardites | 2.1 | 4 Vesta (V) |
| CM | 1.7 | 19 Fortuna |
| Diogenites | 1.2 | 4 Vesta (V) |
| Aubites | 1.0 | 3103 Eger (E) |
| EH | 0.8 | M asteroids |
| EL | 0.7 | M asteroids |
| Mesosiderites | 0.7 | M asteroids |
| CV | 0.6 | K asteroids |
| CI | 0.5 | C asteroids |
| CO | 0.5 | 221 Eros (K) |
| Pallasites | 0.5 | A asteroids |
| Ureilites | 0.5 | S asteroids |
| Martian | 0.4 | Mars |
| CR | 0.3 | C asteroids |
| CK | 0.3 | C asteroids |
| Acapulcoites | 0.1 | S asteroids |
| Angrites | 0.1 | S asteroids |
| Lodranites | 0.1 | S asteroids |
| R | 0.1 | A or S asteroids |
| Winonaites | 0.1 | S asteroids |
| Brachinites | Only finds | A asteroids |
| CH | Only finds | C or M asteroids |

U.PORTO
FACULDADE DE CIÊNCIAS
UNIVERSIDADE DO PORTO

| Group | Fall percentage (%)[1] | Postulated parent body or source body[2] |
|---|---|---|
| Lunar | Only finds | Moon |

Table C9 – Meteorite groups and their postulated parent bodies or source bodies.

[1] Fall percentage were calculated from the 942 classified falls that are listed in Grady (2000), Grossman and Zipfel (2001).

[2] Asteroid classes are a combination of those of Tholen (1984), Graffey et al., (1993) and Bus (1999).

**Reference:** Burbine T. H., McCoy T. J., Meibom A., Gladman B., Keil K. (2002), *Meteoritic parent bodies: Their number and identification*. In: Bottke, W. F. Jr., Cellino, A., Paolicchi, P., Binzel, R. P. (Eds), Asteroids III. University of Arizona Press, Tucson, pp. 653–667

U.PORTO
FACULDADE DE CIÊNCIAS
UNIVERSIDADE DO PORTO

| Asteroid type | Meteoritic Analogs | Mineralogy | Alteration Effects |
|---|---|---|---|
| S | H, L, LL chondrites; stony irons; IAB irons; londratnites; winonites; ureilites | Olivine, pyroxenes, metal | Albedo: up to 50% decrease<br>Red slope: weak to moderate increase<br>Band suppression: 50% decrease |
| V | Basaltic achondrites | Pyroxene, feldspar | Band suppression: 20% |
| A | Brachinites, Pallasites | Olivine | Red slope: moderate increase<br>Band suppression: 20% decrease? |
| Q | H, L, LL chondrites | Olivine, pyroxene, metal | Albedo: 20-20% decrease<br>Band suppression: 20-30% decrease |
| Lunar | Lunar meteorites | Basalt, feldspar | Albedo: 50-75% decrease<br>Red slope: moderate to strong increase<br>Band suppression: 50-75% decrease |

Table C10 – Space weathering and asteroid types.

**Reference:** Clark, B. E., Hapke, B., Pieters, C., Britt, D. (2002), Asteroid Space Weathering and Regolith Evolution, Asteroids III, W. F. Bottke Jr., A. Cellino, P. Paolicchi, and R. P. Binzel (eds), University of Arizona Press, Tucson, 587

U.PORTO
FACULDADE DE CIÊNCIAS
UNIVERSIDADE DO PORTO

# D. Tables of Results

| RELAB sample ID | RELAB File | Grain size proportion | Mixture (Duffard) | Mixture (Results of Solver) | Least Square |
|---|---|---|---|---|---|
| XP-CMP-015 | C1XP15 | 0-45 | Opx:Cpx=85:15 | Opx:Cpx=87:13 | 0,00704 |
| XP-CMP-013 | C1XP13 | 0-45 | Opx:Cpx=75:25 | Opx:Cpx=76:24 | 0,00380 |
| XP-CMP-011 | C1XP11 | 0-45 | Opx:Cpx=60:40 | Opx:Cpx=59:41 | 0,00835 |
| XP-CMP-010 | C1XP10 | 0-45 | Opx:Cpx=50:50 | Opx:Cpx=52:48 | 0,00904 |
| XP-CMP-012 | C1XP12 | 0-45 | Opx:Cpx=40:60 | Opx:Cpx=38:61 | 0,00379 |
| XP-CMP-014 | C1XP14 | 0-45 | Opx:Cpx=25:75 | Opx:Cpx=11:85 | 0,05814 |
| XP-CMP-016 | C1XP16 | 0-45 | Opx:Cpx=15:85 | Opx:Cpx=12:86 | 0,01291 |
| XP-CMP-006 | C1XP06 | 70-145 | Opx:Cpx=85:15 | Opx:Cpx=84:13 | 0,03006 |
| XP-CMP-004 | C1XP04 | 70-145 | Opx:Cpx=75:25 | Opx:Cpx=72:22 | 0,02692 |
| XP-CMP-002 | C1XP02 | 70-145 | Opx:Cpx=60:40 | Opx:Cpx=51:44 | 0,03756 |
| XP-CMP-001 | C1XP01 | 70-145 | Opx:Cpx=50:50 | Opx:Cpx=54:43 | 0,02783 |
| XP-CMP-003 | C1XP03 | 70-145 | Opx:Cpx=40:60 | Opx:Cpx=32:63 | 0,03228 |
| XP-CMP-005 | C1XP05 | 70-145 | Opx:Cpx=25:75 | Opx:Cpx=19:74 | 0,02275 |
| XP-CMP-007 | C1XP07 | 70-145 | Opx:Cpx=15:85 | Opx:Cpx=8:82 | 0,02999 |
| XT-CMP-034 | C1XT34 | 45-75 | Ol:Opx:An=16:66:16 | Ol:Opx:An=23:72:3 | 0,22770 |
| XT-CMP-037 | C1XT37 | 45-75 | Ol:Opx:An=16:41:41 | Ol:Opx:An=20:45:34 | 0,08595 |
| XT-CMP-039 | C1XT39 | 45-75 | Ol:Opx:An=41.41:16 | Ol:Opx:An=43:46:10 | 0,08912 |
| XT-CMP-036 | C1XT36 | 45-75 | Ol:Opx:An=33:33:33 | Ol:Opx:An=33:37:30 | 0,05374 |
| XT-CMP-035 | C1XT35 | 45-75 | Ol:Opx:An=16:16:66 | Ol:Opx:An=16:18:66 | 0,01047 |
| XT-CMP-038 | C1XT38 | 45-75 | Ol:Opx:An=41:16:41 | Ol:Opx:An=38:18:45 | 0,01174 |
| XT-CMP-033 | C1XT33 | 45-75 | Ol:Opx:An=66.16:66 | Ol:Opx:An=61:18:21 | 0,01901 |

Table D1 – Selected Laboratory Mixtures with their grain size proportions and the mineralogical composition derived by Duffard (2005) and the mineralogical compositions derived in this work using the Solver software of Excel, with the residuals of their derivation.

U.PORTO
FACULDADE DE CIÊNCIAS
UNIVERSIDADE DO PORTO

| RELAB sample ID | RELAB File | Grain size proportion | Mineral |
|---|---|---|---|
| PP-CMP-021 | C1PP21 | 0-45 | Clinopyroxene |
| PP-CMP-022 | C1PP22 | 45-75 | Clinopyroxene |
| PP-CMP-023 | C1PP23 | 70-125 | Clinopyroxene |
| PE-CMP-030 | C1PE30 | 0-45 | Orthopyroxene |
| PE-CMP-031 | C1PE31 | 45-75 | Orthopyroxene |
| PE-CMP-032 | C1PE32 | 70-125 | Orthopyroxene |
| OL-JMS-001 | C1OL01 | 45-75 | Olivine |
| PA-CMP-060-B | CBPA60 | 45-75 | Anorthite |

Table D2 – Selected Laboratory minerals with their grain size proportions, to use in the Solver software of Excel to derive the mineralogical compositions of all Laboratory Mixtures presented in Table D1.

U.PORTO
FACULDADE DE CIÊNCIAS
UNIVERSIDADE DO PORTO

| | 4 Vesta | 3908 Nyx | 4055 Magellan | 6611 1993 VW | 5604 1992 FE |
|---|---|---|---|---|---|
| Semi-major axis (AU) | 2,362 | 1,927 | 1,820 | 1,696 | 0,927 |
| Eccentricity | 0,089 | 0,458 | 0,326 | 0,484 | 0,405 |
| Orbital period (Yrs) | 3,630 | 2,680 | 2,460 | 2,210 | 0,890 |
| Inclination | 7,134 | 2,182 | 23,240 | 8,697 | 4,794 |
| Diameter (km) | 530 | 1,000 | 2,490 | | 0,550 |
| Rotational Period (hrs) | 5,342 | 4,426 | 7,475 | 2,5568 | 5,338 |
| Albedo (geometric) | 0,423 | 0,230 | 0,310 | 0,3[1] | 0,480 |
| Absolute magnitude | 3,2 | 17,4 | 14,8 | 16,5[1] | 16,400 |
| Localization | MAB | Amor Group | Amor Group | Apollo Group | Aten Group |

Table D3 – Orbital and physical properties of the five V-type asteroids, considered in this study. Orbital and physical parameters are available at http://ssd.jpl.nasa.gov/sbdb.cgi#top.

Notes:

[1] Data were obtained from R. P. Binzel et al., *Physical Properties of NEO's*, in Asteroids III, Eds. W. F. Bottke et al., 255-271

U.PORTO
FACULDADE DE CIÊNCIAS
UNIVERSIDADE DO PORTO

| Relab File | Sample ID | Sample Name | Meteorite Type | Grain Size Proportion | |
|---|---|---|---|---|---|
| | | | | Min. Size | Max. Size |
| CAMP71 | MP-TXH-071-A | ALHA77256,143 | Diogenite | 0 | 25 |
| CAMP77 | MP-TXH-077-A | LAP91900,27 | Diogenite | 0 | 25 |
| CAMP95 | MP-TXH-095-A | A-881526,90 | Diogenite | 0 | 25 |
| CAMP81 | MP-TXH-081-A | Aioun el Atrouss | Diogenite | 0 | 25 |
| CAMP88 | MP-TXH-088-A | Tatahouine | Diogenite | 0 | 25 |
| CAMP68 | MP-TXH-068-A | GRO95555,22 | Diogenite | 0 | 25 |
| CBMB74 | MB-TXH-074-A | Y-75032,HR | Diogenite | 0 | 25 |
| CBMB73 | MB-TXH-073-A | Y-74013,HR | Diogenite | 0 | 25 |
| CBMB95 | MB-TXH-095-B | Johnstown | Diogenite | 25 | 45 |
| CDMB67 | MB-TXH-067-D | EETA79002,146 | Diogenite | 75 | 125 |
| CAMP84 | MP-TXH-084-A | Cachari | Eucrite | 0 | 25 |
| CAMP86 | MP-TXH-086-A | Moore County | Eucrite | 0 | 25 |
| CAMB97 | MB-TXH-097-A | Stannern | Eucrite | 0 | 25 |
| CAMP87 | MP-TXH-087-A | Pasamonte | Eucrite | 0 | 25 |
| CBMB69 | MB-TXH-069-B | Millbillillie 25-45 um | Eucrite | 25 | 45 |
| CDMB96 | MB-TXH-096-D | Padvarninkai | Eucrite | 25 | 45 |
| CCMB71 | MB-TXH-071-C | Y-74450,92 | Eucrite | 45 | 75 |
| CCMB72 | MB-TXH-072-C | ALH-78132,61 | Eucrite | 45 | 75 |
| CDMB70 | MB-TXH-070-D | Juvinas | Eucrite | 75 | 125 |
| CDMB66 | MB-TXH-066-D | ALHA76005,85 | Eucrite | 75 | 125 |
| CAMP70 | MP-TXH-070-A | Petersburg | Howardite | 0 | 25 |
| CAMP97 | MP-TXH-097-A | Y-7308,142 | Howardite | 0 | 25 |
| CAMP67 | MP-TXH-067-A | GRO95535,12 | Howardite | 0 | 25 |
| CAMP82 | MP-TXH-082-A | Binda | Howardite | 0 | 25 |
| CAMP83 | MP-TXH-083-A | Bununu | Howardite | 0 | 25 |
| CAMP85 | MP-TXH-085-A | Frankfort howardite | Howardite | 0 | 25 |
| CAMP93 | MP-TXH-093-A | Le Teilleul | Howardite | 0 | 25 |

U.PORTO
FACULDADE DE CIÊNCIAS
UNIVERSIDADE DO PORTO

| Relab File | Sample ID | Sample Name | Meteorite Type | Grain Size Proportion | |
|---|---|---|---|---|---|
| | | | | Min. Size | Max. Size |
| CAMP53 | MP-TXH-053-A | Kapoeta | Howardite | 0 | 25 |
| CAMP69 | MP-TXH-069-A | QUE94200,19 | Howardite | 0 | 25 |
| CDMB68 | MB-TXH-068-D | EET87503,97 75-125 um | Howardite | 75 | 125 |

Table D4 – Set of the thirty HED meteorites, considered in this study.

U.PORTO
FACULDADE DE CIÊNCIAS
UNIVERSIDADE DO PORTO

| Relab File | Sample ID | Sample Name | Mineral Subtype | Grain Size Proportion | |
|---|---|---|---|---|---|
| | | | | Min. Size | Max. Size |
| CAPP37 | PP-TXH-037-A | Seven Sisters Is. | Plagioclase | 0 | 25 |
| C1PP46 | PP-EAC-046 | PYX015 | Pyroxene Endiopside | 0 | 45 |
| C1PP21 | PP-CMP-021 | CPX 45 | Pyroxene Clinopyroxene Diopside | 0 | 45 |
| CAPP38 | PP-TXH-038-A | St. Ludger-de-Milot Hypersthene <25 um | Hypersthene | 0 | 25 |
| CAPA60 | PA-CMP-060-A | Split Rock Anorthite | Anorthite | 0 | 25 |
| C1DL08A | DL-CMP-008-A | Wo 5 En 38 Fs 57 (E36-103, 100% opx) < 45 um | Pyroxene Clinopyroxene Pigeonite | 0 | 45 |
| C1DD111 | DD-MDD-111 | DH-231 <45 um | Pyroxene Ferric Clinpyroxene | 0 | 45 |
| C1DD98 | DD-MDD-098 | Fa 100 Fo 0 <45 um | Olivine Fayalite | 0 | 45 |
| C1DD85P | DD-MDD-085-P | Fa 0 Fo 100 <45 um pellet | Olivine Forsterite | 0 | 45 |
| CACR11 | CR-EAC-011 | CHR101 | Chromite | 0 | 45 |
| C1PE30 | PE-CMP-030 | Web 45 | Enstatite | 0 | 45 |
| CJB236 | JB-JLB-236 | NMNH-120414-1 | Pyroxene Orthopyroxene Bronzite | 0 | 45 |
| CAEA09 | EA-EAC-009-A | TRO203A | Troilite | 0 | 45 |
| CBPP37 | PP-TXH-037-B | Seven Sisters Is. | Plagioclase | 25 | 45 |
| CBPP38 | PP-TXH-038-B | St. Ludger-de-Milot Hypersthene 25-45 um | Hypersthene | 25 | 45 |
| CBPA60 | PA-CMP-060-B | Split Rock Anorthite | Anorthite | 25 | 45 |
| CCPP37 | PP-TXH-037-C | Seven Sisters Is. | Plagioclase | 45 | 75 |
| C1PP01 | PP-EAC-001 | PYX005 | Pyroxene Clinopyroxene Endiopside | 45 | 90 |
| C1PP22 | PP-CMP-022 | Cpx 75 | Pyroxene Clinopyroxene Diopside | 45 | 75 |
| CCPP38 | PP-TXH-038-C | St. Ludger-de-Milot Hypersthene 45-75 um | Hypersthene | 45 | 75 |
| C1PA60 | PA-CMP-060-C | Split Rock Anorthite | Anorthite | 45 | 75 |

U.PORTO
FACULDADE DE CIÊNCIAS
UNIVERSIDADE DO PORTO

| Relab File | Sample ID | Sample Name | Mineral Subtype | Grain Size Proportion | |
|---|---|---|---|---|---|
| | | | | Min. Size | Max. Size |
| C1LR180 | LR-CMP-180 | 70035,188 light-brown pyroxene B | Pyroxene Clinopyroxene Pigeonite | 0 | 125 |
| C1PO71 | PO-CMP-071 | St. Peter's Fayalite | Olivine Fayalite | 45 | 75 |
| C1PO77 | PO-CMP-077 | Apache Forsterite | Olivine Forsterite | 45 | 75 |
| C1PE31 | PE-CMP-031 | Web 75 | Enstatite | 45 | 75 |
| C1PP52 | PP-EAC-052 | PYX119 | Pyroxene Orthopyroxene Bronzite | 45 | 90 |
| C1MB06 | MB-CMP-006 | Mundrabilla troilite | Troilite | 0 | 250 |
| C1SR70A | SR-JFM-070-A | BUR-5080 | Pyroxenoid Wollastonite | 45 | 150 |
| CDPP37 | PP-TXH-037-D | Seven Sisters Is. | Plagioclase | 75 | 125 |
| C1PP23 | PP-CMP-023 | Cpx 125 | Pyroxene Clinopyroxene Diopside | 75 | 125 |
| CDPP38 | PP-TXH-038-D | St. Ludger-de-Milot Hypersthene 75-125 um | Hypersthene | 75 | 125 |
| CDPA60 | PA-CMP-060-D | Split Rock Anorthite | Anorthite | 75 | 125 |
| C1SR43A | SR-JFM-043-A | AZ-01 | Olivine Forsterite | 45 | 150 |
| C1PE32 | PE-CMP-032 | Web 125 | Enstatite | 75 | 125 |
| C1LR78 | LR-CMP-178 | 70017,535 ilmenite | Ilmenite | 0 | 125 |
| CJB320 | JB-JLB-320 | Apatite | Apatite | 0 | 90 |
| CASP16 | SP-EAC-016 | SPI116 | Spinel | 0 | 45 |

Table D5 - Set of the reasonable end-members minerals with appropriate grain size proportions, considered in this study.

U.PORTO
FACULDADE DE CIÊNCIAS
UNIVERSIDADE DO PORTO

| RELAB File | Sample ID | End-members Minerals | | | | | |
|---|---|---|---|---|---|---|---|
| | | Plagioclase | Diopside | Hypersthene | Anorthite | Augite | Piogenite |
| CAMP71 | MP-TXH-071-A | 0 | 0 | 0,742973266 | 0 | 0 | 0,186164173 |
| CAMP77 | MP-TXH-077-A | 0 | 0 | 0 | 0 | 0 | 0,151265249 |
| CAMP95 | MP-TXH-095-A | 0 | 0 | 0 | 0 | 0 | 0,133024735 |
| CAMP81 | MP-TXH-081-A | 0 | 0 | 0 | 0 | 0 | 0,148833111 |
| CAMP88 | MP-TXH-088-A | 0 | 0 | 0 | 0 | 0 | 0,148833166 |
| CAMP68 | MP-TXH-068-A | 0 | 0 | 0 | 0 | 0 | 0,146324135 |
| CBMB74 | MB-TXH-074-A | 0 | 0 | 0 | 0 | 0 | 0,217036263 |
| CBMB73 | MB-TXH-073-A | 0 | 0 | 0,028736426 | 0 | 0 | 0,08038543 |
| CBMB95 | MB-TXH-095-B | 0 | 0 | 0,690004974 | 0 | 0 | 0,224310285 |
| CDMB67 | MB-TXH-067-D | 0 | 0 | 0 | 0,3700699 | 0 | 0,053922476 |

| RELAB File | Sample ID | End-members Minerals | | | | | |
|---|---|---|---|---|---|---|---|
| | | Fayalite | Forsterite | Chromite | Enstatite | Bronzite | Troilite |
| CAMP71 | MP-TXH-071-A | 0 | 0 | 0 | 0 | 0 | 0 |
| CAMP77 | MP-TXH-077-A | 0 | 0 | 0 | 0,8487348 | 0 | 0 |
| CAMP95 | MP-TXH-095-A | 0,152201896 | 0 | 0 | 0,5045859 | 0 | 0 |
| CAMP81 | MP-TXH-081-A | 0 | 0 | 0,06477609 | 0,7863908 | 0 | 0 |
| CAMP88 | MP-TXH-088-A | 0 | 0 | 0,06477544 | 0,7863914 | 0 | 0 |
| CAMP68 | MP-TXH-068-A | 0 | 0 | 0 | 0,8536759 | 0 | 0 |
| CBMB74 | MB-TXH-074-A | 0 | 0 | 0 | 0,688196 | 0 | 0,094768 |
| CBMB73 | MB-TXH-073-A | 0 | 0 | 0 | 0 | 0,811803 | 0 |
| CBMB95 | MB-TXH-095-B | 0 | 0 | 0,08568474 | 0 | 0 | 0 |
| CDMB67 | MB-TXH-067-D | 0 | 0 | 0 | 0,4434425 | 0 | 0 |

U.PORTO
FACULDADE DE CIÊNCIAS
UNIVERSIDADE DO PORTO

| RELAB File | Sample ID | End-members Minerals | | | | | |
|---|---|---|---|---|---|---|---|
| | | Wollastonite | Ilminite | Phosphates | Spinel | Piogenite | Enstatite |
| CAMP71 | MP-TXH-071-A | 0 | 0 | 0 | 0 | 0 | 0,070862562 |
| CAMP77 | MP-TXH-077-A | 0 | 0 | 0 | 0 | 0 | 0 |
| CAMP95 | MP-TXH-095-A | 0 | 0 | 0 | 0 | 0 | 0,210187512 |
| CAMP81 | MP-TXH-081-A | 0 | 0 | 0 | 0 | 0 | 0 |
| CAMP88 | MP-TXH-088-A | 0 | 0 | 0 | 0 | 0 | 0 |
| CAMP68 | MP-TXH-068-A | 0 | 0 | 0 | 0 | 0 | 0 |
| CBMB74 | MB-TXH-074-A | 0 | 0 | 0 | 0 | 0 | 0 |
| CBMB73 | MB-TXH-073-A | 0 | 0 | 0 | 0 | 0 | 0,079075383 |
| CBMB95 | MB-TXH-095-B | 0 | 0 | 0 | 0 | 0 | 0 |
| CDMB67 | MB-TXH-067-D | 0 | 0 | 0 | 0 | 0,13256519 | 0 |

| RELAB File | Sample ID | | | | | Sum of the Squares |
|---|---|---|---|---|---|---|
| | | A0 | A1 | A2 | A3 | |
| CAMP71 | MP-TXH-071-A | -0,183806778 | 0,563771661 | -0,3897545 | 0,078456375 | 0,098203448 |
| CAMP77 | MP-TXH-077-A | 0,0417836 | -0,04687413 | 0,01686791 | -0,00266122 | 0,05308105 |
| CAMP95 | MP-TXH-095-A | -0,077342291 | 0,310378669 | -0,213491781 | 0,039882951 | 0,036069279 |
| CAMP81 | MP-TXH-081-A | 0,181643711 | -0,294062026 | 0,173972731 | -0,031001634 | 0,023341244 |
| CAMP88 | MP-TXH-088-A | 0,181642259 | -0,294059126 | 0,173970828 | -0,03100127 | 0,023341244 |
| CAMP68 | MP-TXH-068-A | -0,04269647 | 0,140613905 | -0,092063076 | 0,017838703 | 0,015478918 |
| CBMB74 | MB-TXH-074-A | -0,133820652 | 0,18142642 | -0,102743158 | 0,020162006 | 0,01607913 |
| CBMB73 | MB-TXH-073-A | -0,211440035 | 0,352582395 | -0,273729599 | 0,061132678 | 0,025238177 |
| CBMB95 | MB-TXH-095-B | 0,53426653 | -0,884122894 | 0,484186054 | -0,080837101 | 0,042391743 |
| CDMB67 | MB-TXH-067-D | -0,121828314 | -0,16516171 | 0,050623939 | -0,004397752 | 0,073293687 |

Table D6 – Results of the derived end-members proportions in Diogenites.

Note:

[1]The additional end-members Piogenite and Enstatite found in this table represent the attempt to model the reflectance spectra of Diogenites with different grain size proportions from the ones of the modelled samples. If the grain size

ranges between 0 and 45μm, then samples of Piogenite and Enstatite with grain sizes between 75 and 125μm. If not, samples of Piogenite and Enstatite with grain sizes between 0 and 45μm.

U.PORTO
FACULDADE DE CIÊNCIAS
UNIVERSIDADE DO PORTO

| RELAB File | Sample ID | End-members Minerals | | | | | |
|---|---|---|---|---|---|---|---|
| | | Plagioclase | Diopside | Hypersthene | Anorthite | Augite | Piogenite |
| CAMP84 | MP-TXH-084-A | 0 | 0 | 0 | 0 | 0 | 0,333209507 |
| CAMP86 | MP-TXH-086-A | 0 | 0,21977845 | 0 | 0 | 0 | 0,277720732 |
| CAMB97 | MB-TXH-097-A | 0 | 0 | 0,071806426 | 0 | 0 | 0,228870371 |
| CAMP87 | MP-TXH-087-A | 0 | 0 | 0,541428834 | 0 | 0,309951454 | 0,148619712 |
| CBMB69 | MB-TXH-069-B | 0 | 0 | 0 | 0 | 0 | 0,470234113 |
| CDMB96 | MB-TXH-096-D | 0 | 0 | 0 | 0 | 0 | 0,445345012 |
| CCMB71 | MB-TXH-071-C | 0 | 0 | 0 | 0 | 0 | 0,17042323 |
| CCMB72 | MB-TXH-072-C | 0 | 0 | 0,081941517 | 0 | 0 | 0,229440989 |
| CDMB70 | MB-TXH-070-D | 0 | 0 | 0 | 0 | 0 | 0,470705818 |
| CDMB66 | MB-TXH-066-D | 0 | 0,21715811 | 0,402576797 | 0 | 0 | 0 |

| RELAB File | Sample ID | End-members Minerals | | | | | |
|---|---|---|---|---|---|---|---|
| | | Fayalite | Forsterite | Chromite | Enstatite | Bronzite | Troilite |
| CAMP84 | MP-TXH-084-A | 0 | 0 | 0 | 0,1031154 | 0 | 0 |
| CAMP86 | MP-TXH-086-A | 0 | 0 | 0 | 0,5025008 | 0 | 0 |
| CAMB97 | MB-TXH-097-A | 0 | 0 | 0 | 0,1085039 | 0 | 0,590819 |
| CAMP87 | MP-TXH-087-A | 0 | 0 | 0 | 0 | 0 | 0 |
| CBMB69 | MB-TXH-069-B | 0 | 0,27847933 | 0,11406444 | 0,1372221 | 0 | 0 |
| CDMB96 | MB-TXH-096-D | 0 | 0 | 0,14560524 | 0,0536537 | 0 | 0,355396 |
| CCMB71 | MB-TXH-071-C | 0 | 0,445259065 | 0 | 0,152896 | 0 | 0 |
| CCMB72 | MB-TXH-072-C | 0 | 0 | 0 | 0 | 0 | 0 |
| CDMB70 | MB-TXH-070-D | 0 | 0 | 0 | 0 | 0 | 0,345488 |
| CDMB66 | MB-TXH-066-D | 0 | 0 | 0 | 0 | 0 | 0 |

U.PORTO
FACULDADE DE CIÊNCIAS
UNIVERSIDADE DO PORTO

| RELAB File | Sample ID | End-members Minerals | | | | | |
|---|---|---|---|---|---|---|---|
| | | Wollastonite | Ilminite | Phosphates | Spinel | Piogenite[1] | Enstatite[1] |
| CAMP84 | MP-TXH-084-A | 0 | 0 | 0,56367509 | 0 | 0 | 0 |
| CAMP86 | MP-TXH-086-A | 0 | 0 | 0 | 0 | 0 | 0 |
| CAMB97 | MB-TXH-097-A | 0 | 0 | 0 | 0 | 0 | 0 |
| CAMP87 | MP-TXH-087-A | 0 | 0 | 0 | 0 | 0 | 0 |
| CBMB69 | MB-TXH-069-B | 0 | 0 | 0 | 0 | 0 | 0 |
| CDMB96 | MB-TXH-096-D | 0 | 0 | 0 | 0 | 0 | 0 |
| CCMB71 | MB-TXH-071-C | 0 | 0 | 0 | 0 | 0,231421663 | 0 |
| CCMB72 | MB-TXH-072-C | 0 | 0 | 0 | 0 | 0,253657787 | 0,434959707 |
| CDMB70 | MB-TXH-070-D | 0 | 0 | 0 | 0 | 0,183806166 | 0 |
| CDMB66 | MB-TXH-066-D | 0,060429141 | 0 | 0 | 0 | 0,319835956 | 0 |

| RELAB File | Sample ID | | | | | Sum of the Squares |
|---|---|---|---|---|---|---|
| | | A0 | A1 | A2 | A3 | |
| CAMP84 | MP-TXH-084-A | -0,047118234 | 0,139783337 | -0,090530073 | 0,016585639 | 0,028376683 |
| CAMP86 | MP-TXH-086-A | -0,002047255 | 0,017973724 | -0,014726325 | 0,003201666 | 0,014775261 |
| CAMB97 | MB-TXH-097-A | 0,296267913 | 0,062314279 | -0,047736690 | 0,008190742 | 0,019320824 |
| CAMP87 | MP-TXH-087-A | -0,072781380 | 0,190188832 | -0,125418776 | 0,026111026 | 0,032459098 |
| CBMB69 | MB-TXH-069-B | 0,001134905 | -0,183661183 | 0,098927883 | -0,014154570 | 0,011430869 |
| CDMB96 | MB-TXH-096-D | 0,239172410 | -0,214401889 | 0,119849480 | -0,018464511 | 0,014716237 |
| CCMB71 | MB-TXH-071-C | -0,403360200 | 0,449741291 | -0,320294396 | 0,069625246 | 0,066170323 |
| CCMB72 | MB-TXH-072-C | -0,478912249 | 0,735404140 | -0,494193408 | 0,101053157 | 0,127210997 |
| CDMB70 | MB-TXH-070-D | 0,019368857 | 0,107145859 | -0,057742269 | 0,004266850 | 0,389585972 |
| CDMB66 | MB-TXH-066-D | -0,094071560 | 0,445518383 | -0,360873941 | 0,074499796 | 0,267404538 |

Table D7 – Results of the derived end-members proportions in Eucrites.

Note:

[1]The additional end-members Piogenite and Enstatite found in this table represent the attempt to model the reflectance spectra of Eucrites with different grain size proportions from the ones of the modelled samples. If the grain size ranges

between 0 and 45μm, then samples of Piogenite and Enstatite with grain sizes between 75 and 125μm. If not, samples of Piogenite and Enstatite with grain sizes between 0 and 45μm.

U.PORTO
FACULDADE DE CIÊNCIAS
UNIVERSIDADE DO PORTO

| RELAB File | Sample ID | End-members Minerals | | | | | |
|---|---|---|---|---|---|---|---|
| | | Plagioclase | Diopside | Hypersthene | Anorthite | Augite | Piogenite |
| CAMP70 | MP-TXH-070-A | 0 | 0 | 0,595513169 | 0 | 0 | 0,149842865 |
| CAMP97 | MP-TXH-097-A | 0 | 0 | 0 | 0 | 0 | 0,227608267 |
| CAMP67 | MP-TXH-067-A | 0 | 0 | 0,341209525 | 0 | 0 | 0,174358253 |
| CAMP82 | MP-TXH-082-A | 0 | 0 | 0 | 0 | 0 | 0,283689854 |
| CAMP83 | MP-TXH-083-A | 0 | 0 | 0 | 0 | 0,034181186 | 0,156610181 |
| CAMP85 | MP-TXH-085-A | 0 | 0 | 0 | 0 | 0 | 0,182632176 |
| CAMP93 | MP-TXH-093-A | 0 | 0 | 0 | 0 | 0 | 0,199672759 |
| CAMP53 | MP-TXH-053-A | 0 | 0 | 0 | 0 | 0 | 0,172680073 |
| CAMP69 | MP-TXH-069-A | 0 | 0 | 0 | 0 | 0 | 0,086938898 |
| CDMB68 | MB-TXH-068-D | 0 | 0,14877874 | 0 | 0,4202507 | 0 | 0 |

| RELAB File | Sample ID | End-members Minerals | | | | | |
|---|---|---|---|---|---|---|---|
| | | Fayalite | Forsterite | Chromite | Enstatite | Bronzite | Troilite |
| CAMP70 | MP-TXH-070-A | 0,254643967 | 0 | 0 | 0 | 0 | 0 |
| CAMP97 | MP-TXH-097-A | 0 | 0 | 0 | 0,1653484 | 0 | 0,607043 |
| CAMP67 | MP-TXH-067-A | 0 | 0,288320319 | 0,03539119 | 0,1053228 | 0 | 0,055398 |
| CAMP82 | MP-TXH-082-A | 0 | 0 | 0,07260041 | 0,6437097 | 0 | 0 |
| CAMP83 | MP-TXH-083-A | 0 | 0 | 0 | 0,4330922 | 0 | 0 |
| CAMP85 | MP-TXH-085-A | 0 | 0 | 0,04766534 | 0,6717705 | 0 | 0 |
| CAMP93 | MP-TXH-093-A | 0 | 0 | 0,06216427 | 0,738163 | 0 | 0 |
| CAMP53 | MP-TXH-053-A | 0,021051336 | 0 | 0 | 0,4226851 | 0 | 0,383583 |
| CAMP69 | MP-TXH-069-A | 0 | 0 | 0,06472398 | 0,6801428 | 0,168194 | 0 |
| CDMB68 | MB-TXH-068-D | 0 | 0 | 0 | 0,2346542 | 0 | 0 |

U.PORTO
FACULDADE DE CIÊNCIAS
UNIVERSIDADE DO PORTO

| RELAB File | Sample ID | End-members Minerals | | | | | |
|---|---|---|---|---|---|---|---|
| | | Wollastonite | Ilminite | Phosphates | Spinel | Piogenite[1] | Enstatite[1] |
| CAMP70 | MP-TXH-070-A | 0 | 0 | 0 | 0 | 0 | 0 |
| CAMP97 | MP-TXH-097-A | 0 | 0 | 0 | 0 | 0 | 0 |
| CAMP67 | MP-TXH-067-A | 0 | 0 | 0 | 0 | 0 | 0 |
| CAMP82 | MP-TXH-082-A | 0 | 0 | 0 | 0 | 0 | 0 |
| CAMP83 | MP-TXH-083-A | 0,376116401 | 0 | 0 | 0 | 0 | 0 |
| CAMP85 | MP-TXH-085-A | 0 | 0 | 0 | 0,09793197 | 0 | 0 |
| CAMP93 | MP-TXH-093-A | 0 | 0 | 0 | 0 | 0 | 0 |
| CAMP53 | MP-TXH-053-A | 0 | 0 | 0 | 0 | 0 | 0 |
| CAMP69 | MP-TXH-069-A | 0 | 0 | 0 | 0 | 0 | 0 |
| CDMB68 | MB-TXH-068-D | 0 | 0 | 0 | 0 | 0,196316402 | 0 |

| RELAB File | Sample ID | | | | | Sum of the Squares |
|---|---|---|---|---|---|---|
| | | A0 | A1 | A2 | A3 | |
| CAMP70 | MP-TXH-070-A | -0,504117261 | 1,243959781 | -0,838122524 | 0,167588401 | 0,075073861 |
| CAMP97 | MP-TXH-097-A | 0,287821916 | 0,093606279 | -0,068164979 | 0,012312029 | 0,019632776 |
| CAMP67 | MP-TXH-067-A | 0,000000000 | 0,000000000 | 0,000000000 | 0,000000000 | 0,008495392 |
| CAMP82 | MP-TXH-082-A | 0,101756486 | -0,134610282 | 0,067414295 | -0,009268836 | 0,043800867 |
| CAMP83 | MP-TXH-083-A | -0,105473121 | 0,099346242 | -0,060924326 | 0,011459834 | 0,007790655 |
| CAMP85 | MP-TXH-085-A | -0,003726376 | -0,150988990 | 0,104720961 | -0,020153332 | 0,023909006 |
| CAMP93 | MP-TXH-093-A | -0,036067764 | 0,029784063 | -0,018798892 | 0,005030175 | 0,023411971 |
| CAMP53 | MP-TXH-053-A | 0,163202564 | -0,078848466 | 0,043178240 | -0,008058102 | 0,007727049 |
| CAMP69 | MP-TXH-069-A | 0,026943464 | -0,069895050 | 0,034390999 | -0,004467426 | 0,016354441 |
| CDMB68 | MB-TXH-068-D | -0,191447541 | 0,064947694 | -0,131914865 | 0,033142379 | 0,099794493 |

Table D8 – Results of the derived end-members proportions in Howardites.

Note:

[1]The additional end-members Piogenite and Enstatite found in this table represent the attempt to model the reflectance spectra of Howardites with different grain size proportions from the ones of the modelled samples. If the grain size

ranges between 0 and 45μm, then samples of Piogenite and Enstatite with grain sizes between 75 and 125μm. If not, samples of Piogenite and Enstatite with grain sizes between 0 and 45μm.

U.PORTO
FACULDADE DE CIÊNCIAS
UNIVERSIDADE DO PORTO

| Asteroid/ HED Meteorite | End-members Minerals | | | | | |
|---|---|---|---|---|---|---|
| | Plagioclase | Diopside | Hypersthene | Anorthite | Augite | Piogenite |
| Asteroid 4 Vesta | 0 | 0 | 0 | 0 | 0 | 0,189719189 |
| Howardite MP-TXH-083-A | 0 | 0 | 0 | 0 | 0,034181186 | 0,156610181 |
| Asteroid 3908 Nyx | 0 | 0 | 0,563490472 | 0 | 0 | 0 |
| Diogenite MP-TXH-071-A | 0 | 0 | 0,742973266 | 0 | 0 | 0,186164173 |
| Asteroid 4055 Magellan | 0 | 0 | 0,254865177 | 0,4199505 | 0 | 0,225163605 |
| Eucrite MB-TXH-072-C | 0 | 0 | 0,081941517 | 0 | 0 | 0,229440989 |
| Asteroid (6611) 1993 VW | 0 | 0,309251 | 0 | 0 | 0 | 0,166034535 |
| Howardite MP-TXH-085-A | 0 | 0 | 0 | 0 | 0 | 0,182632176 |
| Asteroid (5604) 1992 FE | 0 | 0 | 0 | 0 | 0 | 0,099260403 |
| Howardite MP-TXH-085-A | 0 | 0 | 0 | 0 | 0 | 0,182632176 |

| Asteroid/ HED Meteorite | End-members Minerals | | | | | |
|---|---|---|---|---|---|---|
| | Fayalite | Forsterite | Chromite | Enstatite | Bronzite | Troilite |
| Asteroid 4 Vesta | 0 | 0 | 0 | 0,29681475 | 0 | 0 |
| Howardite MP-TXH-083-A | 0 | 0 | 0 | 0,433092 | 0 | 0 |
| Asteroid 3908 Nyx | 0 | 0 | 0,2209897 | 0,03800656 | 0 | 0 |
| Diogenite MP-TXH-071-A | 0 | 0 | 0 | 0 | 0 | 0 |
| Asteroid 4055 Magellan | 0 | 0 | 0 | 0 | 0 | 0 |
| Eucrite MB-TXH-072-C | 0 | 0 | 0 | 0 | 0 | 0 |
| Asteroid (6611) 1993 VW | 0,058532646 | 0 | 0,1035305 | 0,36265175 | 0 | 0 |
| Howardite MP-TXH-085-A | 0 | 0 | 0,04766534 | 0,671771 | 0 | 0 |
| Asteroid (5604) 1992 FE | 0 | 0 | 0 | 0,582063 | 0 | 0 |
| Howardite MP-TXH-085-A | 0 | 0 | 0,04766534 | 0,671771 | 0 | 0 |

U.PORTO
FACULDADE DE CIÊNCIAS
UNIVERSIDADE DO PORTO

| Asteroid/ HED Meteorite | End-members Minerals | | | | | |
|---|---|---|---|---|---|---|
| | Wollastonite | Ilminite | Phosphates | Spinel | Piogenite[1] | Enstatite[1] |
| Asteroid 4 Vesta | 0,461459147 | 0 | 0 | 0 | 0,052006915 | 0 |
| Howardite MP-TXH-083-A | 0,376116401 | 0 | 0 | 0 | 0 | 0 |
| Asteroid 3908 Nyx | 0 | 0 | 0 | 0 | 0,177513285 | 0 |
| Diogenite MP-TXH-071-A | 0 | 0 | 0 | 0 | 0 | 0,070863 |
| Asteroid 4055 Magellan | 0 | 0 | 0 | 0 | 0,100020687 | 0 |
| Eucrite MB-TXH-072-C | 0 | 0 | 0 | 0 | 0,253658 | 0,43496 |
| Asteroid (6611) 1993 VW | 0 | 0 | 0 | 0 | 0 | 0 |
| Howardite MP-TXH-085-A | 0 | 0 | 0 | 0,09793197 | 0 | 0 |
| Asteroid (5604) 1992 FE | 0 | 0 | 0 | 0 | 0,318677 | 0 |
| Howardite MP-TXH-085-A | 0 | 0 | 0 | 0,09793197 | 0 | 0 |

| Asteroid/ HED Meteorite | | | | | Sum of the Squares |
|---|---|---|---|---|---|
| | A0 | A1 | A2 | A3 | |
| Asteroid 4 Vesta | -0,699036542 | 0,515762279 | -0,33418037 | 0,07096265 | 0,023103853 |
| Howardite MP-TXH-083-A | -0,10547312 | 0,09934624 | -0,06092433 | 0,01145983 | 0,007790655 |
| Asteroid 3908 Nyx | -0,223295503 | -0,579197528 | 0,325513366 | -0,052592364 | 0,051097563 |
| Diogenite MP-TXH-071-A | -0,18380678 | 0,56377166 | -0,38975450 | 0,07845638 | 0,098203448 |
| Asteroid 4055 Magellan | -0,645993184 | 0,582993021 | -0,45256925 | 0,10338228 | 0,063693765 |
| Eucrite MB-TXH-072-C | -0,47891225 | 0,73540414 | -0,49419341 | 0,10105316 | 0,127210997 |
| Asteroid (6611) 1993 VW | -0,619680317 | 0,278783474 | -0,23057771 | 0,054774974 | 0,013560271 |
| Howardite MP-TXH-085-A | -0,00372638 | -0,15098899 | 0,10472096 | -0,02015333 | 0,023909006 |
| Asteroid (5604) 1992 FE | -0,787504412 | 1,243396369 | -0,86138141 | 0,180526198 | 0,081278286 |
| Howardite MP-TXH-085-A | -0,00372638 | -0,15098899 | 0,10472096 | -0,02015333 | 0,023909006 |

Table D9 – Results of the derived end-members proportions in the selected V-type asteroids and their meteoritic analogs.

U.PORTO
FACULDADE DE CIÊNCIAS
UNIVERSIDADE DO PORTO

Note:

[1]The additional end-members Piogenite and Enstatite found in this table represent the attempt to model the reflectance spectra of Diogenites with different grain size proportions from the ones of the modelled samples. If the grain size ranges between 0 and 45μm, then samples of Piogenite and Enstatite with grain sizes between 75 and 125μm. If not, samples of Piogenite and Enstatite with grain sizes between 0 and 45μm.

U.PORTO
FACULDADE DE CIÊNCIAS
UNIVERSIDADE DO PORTO

| RELAB File | Sample ID | End-members Minerals | | | | | |
|---|---|---|---|---|---|---|---|
| | | Plagioclase | Diopside | Hypersthene | Anorthite | Augite | Piogenite |
| CAMP71 | MP-TXH-071-A | 0,00 | 0,00 | 0,76 | 0,00 | 0,00 | 0,18 |
| CAMP77 | MP-TXH-077-A | 0,00 | 0,00 | 0,00 | 0,00 | 0,00 | 0,16 |
| CAMP95 | MP-TXH-095-A | 0,00 | 0,00 | 0,00 | 0,00 | 0,00 | 0,16 |
| CAMP81 | MP-TXH-081-A | 0,00 | 0,00 | 0,00 | 0,00 | 0,00 | 0,15 |
| CAMP88 | MP-TXH-088-A | 0,00 | 0,00 | 0,00 | 0,00 | 0,00 | 0,15 |
| CAMP68 | MP-TXH-068-A | 0,00 | 0,00 | 0,00 | 0,00 | 0,00 | 0,15 |
| CBMB74 | MB-TXH-074-A | 0,00 | 0,00 | 0,00 | 0,00 | 0,00 | 0,21 |
| CBMB73 | MB-TXH-073-A | 0,00 | 0,00 | 0,03 | 0,00 | 0,00 | 0,08 |
| CBMB95 | MB-TXH-095-B | 0,00 | 0,00 | 0,68 | 0,00 | 0,00 | 0,21 |
| CDMB67 | MB-TXH-067-D | 0,00 | 0,00 | 0,00 | 0,33 | 0,00 | 0,06 |

| RELAB File | Sample ID | End-members Minerals | | | | | |
|---|---|---|---|---|---|---|---|
| | | Fayalite | Forsterite | Chromite | Enstatite | Bronzite | Troilite |
| CAMP71 | MP-TXH-071-A | 0,00 | 0,00 | 0,00 | 0,00 | 0,00 | 0,00 |
| CAMP77 | MP-TXH-077-A | 0,00 | 0,00 | 0,00 | 0,84 | 0,00 | 0,00 |
| CAMP95 | MP-TXH-095-A | 0,00 | 0,00 | 0,00 | 0,59 | 0,00 | 0,00 |
| CAMP81 | MP-TXH-081-A | 0,00 | 0,00 | 0,09 | 0,76 | 0,00 | 0,00 |
| CAMP88 | MP-TXH-088-A | 0,00 | 0,00 | 0,09 | 0,76 | 0,00 | 0,00 |
| CAMP68 | MP-TXH-068-A | 0,00 | 0,00 | 0,00 | 0,85 | 0,00 | 0,00 |
| CBMB74 | MB-TXH-074-A | 0,00 | 0,00 | 0,00 | 0,66 | 0,00 | 0,13 |
| CBMB73 | MB-TXH-073-A | 0,00 | 0,00 | 0,00 | 0,00 | 0,81 | 0,00 |
| CBMB95 | MB-TXH-095-B | 0,00 | 0,00 | 0,11 | 0,00 | 0,00 | 0,00 |
| CDMB67 | MB-TXH-067-D | 0,00 | 0,00 | 0,00 | 0,47 | 0,00 | 0,00 |

U.PORTO
FACULDADE DE CIÊNCIAS
UNIVERSIDADE DO PORTO

| RELAB File | Sample ID | End-members Minerals | | | | | |
|---|---|---|---|---|---|---|---|
| | | Wollastonite | Ilminite | Phosphates | Spinel | Piogenite[1] | Enstatite[1] |
| CAMP71 | MP-TXH-071-A | 0,00 | 0,00 | 0,00 | 0,00 | 0,00 | 0,07 |
| CAMP77 | MP-TXH-077-A | 0,00 | 0,00 | 0,00 | 0,00 | 0,00 | 0,00 |
| CAMP95 | MP-TXH-095-A | 0,00 | 0,00 | 0,00 | 0,00 | 0,00 | 0,25 |
| CAMP81 | MP-TXH-081-A | 0,00 | 0,00 | 0,00 | 0,00 | 0,00 | 0,00 |
| CAMP88 | MP-TXH-088-A | 0,00 | 0,00 | 0,00 | 0,00 | 0,00 | 0,00 |
| CAMP68 | MP-TXH-068-A | 0,00 | 0,00 | 0,00 | 0,00 | 0,00 | 0,00 |
| CBMB74 | MB-TXH-074-A | 0,00 | 0,00 | 0,00 | 0,00 | 0,00 | 0,00 |
| CBMB73 | MB-TXH-073-A | 0,00 | 0,00 | 0,00 | 0,00 | 0,00 | 0,08 |
| CBMB95 | MB-TXH-095-B | 0,00 | 0,00 | 0,00 | 0,00 | 0,00 | 0,00 |
| CDMB67 | MB-TXH-067-D | 0,00 | 0,00 | 0,00 | 0,00 | 0,14 | 0,00 |

Table D10 – Derived mass fractions of the end-members found in Diogenites.

Note:

[1]The additional piogenite and enstatite represent different granulometries. For further details check Table D6.

U.PORTO
FACULDADE DE CIÊNCIAS
UNIVERSIDADE DO PORTO

| RELAB File | Sample ID | End-members Minerals | | | | | |
|---|---|---|---|---|---|---|---|
| | | Plagioclase | Diopside | Hypersthene | Anorthite | Augite | Piogenite |
| CAMP84 | MP-TXH-084-A | 0,00 | 0,00 | 0,00 | 0,00 | 0,00 | 0,34 |
| CAMP86 | MP-TXH-086-A | 0,00 | 0,23 | 0,00 | 0,00 | 0,00 | 0,28 |
| CAMB97 | MB-TXH-097-A | 0,00 | 0,00 | 0,06 | 0,00 | 0,00 | 0,19 |
| CAMP87 | MP-TXH-087-A | 0,00 | 0,00 | 0,55 | 0,00 | 0,30 | 0,14 |
| CBMB69 | MB-TXH-069-B | 0,00 | 0,00 | 0,00 | 0,00 | 0,00 | 0,45 |
| CDMB96 | MB-TXH-096-D | 0,00 | 0,00 | 0,00 | 0,00 | 0,00 | 0,37 |
| CCMB71 | MB-TXH-071-C | 0,00 | 0,00 | 0,00 | 0,00 | 0,00 | 0,17 |
| CCMB72 | MB-TXH-072-C | 0,00 | 0,00 | 0,09 | 0,00 | 0,00 | 0,23 |
| CDMB70 | MB-TXH-070-D | 0,00 | 0,00 | 0,00 | 0,00 | 0,00 | 0,41 |
| CDMB66 | MB-TXH-066-D | 0,00 | 0,22 | 0,42 | 0,33 | 0,00 | 0,00 |

| RELAB File | Sample ID | End-members Minerals | | | | | |
|---|---|---|---|---|---|---|---|
| | | Fayalite | Forsterite | Chromite | Enstatite | Bronzite | Troilite |
| CAMP84 | MP-TXH-084-A | 0,00 | 0,00 | 0,00 | 0,10 | 0,00 | 0,00 |
| CAMP86 | MP-TXH-086-A | 0,00 | 0,00 | 0,00 | 0,49 | 0,00 | 0,00 |
| CAMB97 | MB-TXH-097-A | 0,00 | 0,00 | 0,00 | 0,09 | 0,00 | 0,67 |
| CAMP87 | MP-TXH-087-A | 0,00 | 0,00 | 0,00 | 0,00 | 0,00 | 0,00 |
| CBMB69 | MB-TXH-069-B | 0,00 | 0,26 | 0,16 | 0,13 | 0,00 | 0,00 |
| CDMB96 | MB-TXH-096-D | 0,00 | 0,00 | 0,18 | 0,04 | 0,00 | 0,41 |
| CCMB71 | MB-TXH-071-C | 0,00 | 0,45 | 0,00 | 0,15 | 0,00 | 0,00 |
| CCMB72 | MB-TXH-072-C | 0,00 | 0,00 | 0,00 | 0,00 | 0,81 | 0,00 |
| CDMB70 | MB-TXH-070-D | 0,00 | 0,00 | 0,00 | 0,00 | 0,00 | 0,42 |
| CDMB66 | MB-TXH-066-D | 0,00 | 0,00 | 0,00 | 0,00 | 0,00 | 0,00 |

U.PORTO
FACULDADE DE CIÊNCIAS
UNIVERSIDADE DO PORTO

| RELAB File | Sample ID | End-members Minerals | | | | | |
|---|---|---|---|---|---|---|---|
| | | Wollastonite | Ilminite | Phosphates | Spinel | Piogenite[1] | Enstatite[1] |
| CAMP84 | MP-TXH-084-A | 0,00 | 0,00 | 0,56 | 0,00 | 0,00 | 0,00 |
| CAMP86 | MP-TXH-086-A | 0,00 | 0,00 | 0,00 | 0,00 | 0,00 | 0,00 |
| CAMB97 | MB-TXH-097-A | 0,00 | 0,00 | 0,00 | 0,00 | 0,00 | 0,00 |
| CAMP87 | MP-TXH-087-A | 0,00 | 0,00 | 0,00 | 0,00 | 0,00 | 0,00 |
| CBMB69 | MB-TXH-069-B | 0,00 | 0,00 | 0,00 | 0,00 | 0,00 | 0,00 |
| CDMB96 | MB-TXH-096-D | 0,00 | 0,00 | 0,00 | 0,00 | 0,00 | 0,00 |
| CCMB71 | MB-TXH-071-C | 0,00 | 0,00 | 0,00 | 0,00 | 0,23 | 0,00 |
| CCMB72 | MB-TXH-072-C | 0,00 | 0,00 | 0,00 | 0,00 | 0,26 | 0,42 |
| CDMB70 | MB-TXH-070-D | 0,00 | 0,00 | 0,00 | 0,00 | 0,16 | 0,00 |
| CDMB66 | MB-TXH-066-D | 0,05 | 0,00 | 0,00 | 0,00 | 0,31 | 0,00 |

Table D11 – Derived mass fractions of the end-members found in Eucrites.

Note:

[1]The additional piogenite and enstatite represent different granulometries. For further details check Table D7.

U.PORTO
FACULDADE DE CIÊNCIAS
UNIVERSIDADE DO PORTO

| RELAB File | Sample ID | End-members Minerals | | | | | |
|---|---|---|---|---|---|---|---|
| | | Plagioclase | Diopside | Hypersthene | Anorthite | Augite | Piogenite |
| CAMP70 | MP-TXH-070-A | 0,00 | 0,00 | 0,81 | 0,00 | 0,00 | 0,19 |
| CAMP97 | MP-TXH-097-A | 0,00 | 0,00 | 0,00 | 0,00 | 0,00 | 0,18 |
| CAMP67 | MP-TXH-067-A | 0,00 | 0,00 | 0,35 | 0,00 | 0,00 | 0,16 |
| CAMP82 | MP-TXH-082-A | 0,00 | 0,00 | 0,00 | 0,00 | 0,00 | 0,28 |
| CAMP83 | MP-TXH-083-A | 0,00 | 0,00 | 0,00 | 0,00 | 0,04 | 0,17 |
| CAMP85 | MP-TXH-085-A | 0,00 | 0,00 | 0,00 | 0,00 | 0,00 | 0,18 |
| CAMP93 | MP-TXH-093-A | 0,00 | 0,00 | 0,00 | 0,00 | 0,00 | 0,20 |
| CAMP53 | MP-TXH-053-A | 0,00 | 0,00 | 0,00 | 0,00 | 0,00 | 0,15 |
| CAMP69 | MP-TXH-069-A | 0,00 | 0,00 | 0,00 | 0,00 | 0,00 | 0,09 |
| CDMB68 | MB-TXH-068-D | 0,00 | 0,17 | 0,00 | 0,38 | 0,00 | 0,00 |

| RELAB File | Sample ID | End-members Minerals | | | | | |
|---|---|---|---|---|---|---|---|
| | | Fayalite | Forsterite | Chromite | Enstatite | Bronzite | Troilite |
| CAMP70 | MP-TXH-070-A | 0,00 | 0,00 | 0,00 | 0,00 | 0,00 | 0,00 |
| CAMP97 | MP-TXH-097-A | 0,00 | 0,00 | 0,00 | 0,13 | 0,00 | 0,69 |
| CAMP67 | MP-TXH-067-A | 0,00 | 0,27 | 0,05 | 0,10 | 0,00 | 0,07 |
| CAMP82 | MP-TXH-082-A | 0,00 | 0,00 | 0,10 | 0,62 | 0,00 | 0,00 |
| CAMP83 | MP-TXH-083-A | 0,00 | 0,00 | 0,00 | 0,45 | 0,00 | 0,00 |
| CAMP85 | MP-TXH-085-A | 0,00 | 0,00 | 0,07 | 0,64 | 0,00 | 0,00 |
| CAMP93 | MP-TXH-093-A | 0,00 | 0,00 | 0,09 | 0,71 | 0,00 | 0,00 |
| CAMP53 | MP-TXH-053-A | 0,00 | 0,00 | 0,00 | 0,37 | 0,00 | 0,48 |
| CAMP69 | MP-TXH-069-A | 0,00 | 0,00 | 0,09 | 0,66 | 0,16 | 0,00 |
| CDMB68 | MB-TXH-068-D | 0,00 | 0,00 | 0,00 | 0,25 | 0,00 | 0,00 |

U.PORTO
FACULDADE DE CIÊNCIAS
UNIVERSIDADE DO PORTO

| RELAB File | Sample ID | End-members Minerals | | | | | |
|---|---|---|---|---|---|---|---|
| | | Wollastonite | Ilminite | Phosphates | Spinel | Piogenite[1] | Enstatite[1] |
| CAMP70 | MP-TXH-070-A | 0,00 | 0,00 | 0,00 | 0,00 | 0,00 | 0,00 |
| CAMP97 | MP-TXH-097-A | 0,00 | 0,00 | 0,00 | 0,00 | 0,00 | 0,00 |
| CAMP67 | MP-TXH-067-A | 0,00 | 0,00 | 0,00 | 0,00 | 0,00 | 0,00 |
| CAMP82 | MP-TXH-082-A | 0,00 | 0,00 | 0,00 | 0,00 | 0,00 | 0,00 |
| CAMP83 | MP-TXH-083-A | 0,35 | 0,00 | 0,00 | 0,00 | 0,00 | 0,00 |
| CAMP85 | MP-TXH-085-A | 0,00 | 0,00 | 0,00 | 0,11 | 0,00 | 0,00 |
| CAMP93 | MP-TXH-093-A | 0,00 | 0,00 | 0,00 | 0,00 | 0,00 | 0,00 |
| CAMP53 | MP-TXH-053-A | 0,00 | 0,00 | 0,00 | 0,00 | 0,00 | 0,00 |
| CAMP69 | MP-TXH-069-A | 0,00 | 0,00 | 0,00 | 0,00 | 0,00 | 0,00 |
| CDMB68 | MB-TXH-068-D | 0,00 | 0,00 | 0,00 | 0,00 | 0,21 | 0,00 |

Table D12 – Derived mass fractions of the end-members found in Howardites.

Note:

[1]The additional piogenite and enstatite represent different granulometries. For further details check Table D8.

U.PORTO
FACULDADE DE CIÊNCIAS
UNIVERSIDADE DO PORTO

| Asteroid/ HED Meteorite | End-members Minerals | | | | | |
|---|---|---|---|---|---|---|
| | Plagioclase | Diopside | Hypersthene | Anorthite | Augite | Piogenite |
| Asteroid 4 Vesta | 0,00 | 0,00 | 0,00 | 0,00 | 0,00 | 0,20 |
| Howardite MP-TXH-083-A | 0,00 | 0,00 | 0,00 | 0,00 | 0,04 | 0,17 |
| Asteroid 3908 Nyx | 0,00 | 0,00 | 0,53 | 0,00 | 0,00 | 0,00 |
| Diogenite MP-TXH-071-A | 0,00 | 0,00 | 0,76 | 0,00 | 0,00 | 0,18 |
| Asteroid 4055 Magellan | 0,00 | 0,00 | 0,29 | 0,37 | 0,00 | 0,24 |
| Eucrite MB-TXH-072-C | 0,00 | 0,00 | 0,09 | 0,00 | 0,00 | 0,23 |
| Asteroid (6611) 1993 VW | 0,00 | 0,30 | 0,00 | 0,00 | 0,00 | 0,16 |
| Howardite MP-TXH-085-A | 0,00 | 0,00 | 0,00 | 0,00 | 0,00 | 0,18 |
| Asteroid (5604) 1992 FE | 0,00 | 0,00 | 0,00 | 0,00 | 0,00 | 0,10 |
| Howardite MP-TXH-085-A | 0,00 | 0,00 | 0,00 | 0,00 | 0,00 | 0,18 |

| Asteroid/ HED Meteorite | End-members Minerals | | | | | |
|---|---|---|---|---|---|---|
| | Fayalite | Forsterite | Chromite | Enstatite | Bronzite | Troilite |
| Asteroid 4 Vesta | 0,00 | 0,00 | 0,00 | 0,31 | 0,00 | 0,00 |
| Howardite MP-TXH-083-A | 0,00 | 0,00 | 0,00 | 0,45 | 0,00 | 0,00 |
| Asteroid 3908 Nyx | 0,00 | 0,00 | 0,28 | 0,03 | 0,00 | 0,00 |
| Diogenite MP-TXH-071-A | 0,00 | 0,00 | 0,00 | 0,00 | 0,00 | 0,00 |
| Asteroid 4055 Magellan | 0,00 | 0,00 | 0,00 | 0,00 | 0,00 | 0,00 |
| Eucrite MB-TXH-072-C | 0,00 | 0,00 | 0,00 | 0,00 | 0,00 | 0,00 |
| Asteroid (6611) 1993 VW | 0,07 | 0,00 | 0,14 | 0,33 | 0,00 | 0,00 |
| Howardite MP-TXH-085-A | 0,00 | 0,00 | 0,07 | 0,64 | 0,00 | 0,00 |
| Asteroid (5604) 1992 FE | 0,00 | 0,00 | 0,00 | 0,57 | 0,00 | 0,00 |
| Howardite MP-TXH-085-A | 0,00 | 0,00 | 0,07 | 0,64 | 0,00 | 0,00 |

U.PORTO
FACULDADE DE CIÊNCIAS
UNIVERSIDADE DO PORTO

| Asteroid/ HED Meteorite | End-members Minerals | | | | | |
|---|---|---|---|---|---|---|
| | Wollastonite | Ilminite | Phosphates | Spinel | Piogenite[1] | Enstatite[1] |
| Asteroid 4 Vesta | 0,43 | 0,00 | 0,00 | 0,00 | 0,06 | 0,00 |
| Howardite MP-TXH-083-A | 0,35 | 0,00 | 0,00 | 0,00 | 0,00 | 0,00 |
| Asteroid 3908 Nyx | 0,00 | 0,00 | 0,00 | 0,00 | 0,16 | 0,00 |
| Diogenite MP-TXH-071-A | 0,00 | 0,00 | 0,00 | 0,00 | 0,00 | 0,07 |
| Asteroid 4055 Magellan | 0,00 | 0,00 | 0,00 | 0,00 | 0,11 | 0,00 |
| Eucrite MB-TXH-072-C | 0,00 | 0,00 | 0,00 | 0,00 | 0,26 | 0,42 |
| Asteroid (6611) 1993 VW | 0,00 | 0,00 | 0,00 | 0,00 | 0,00 | 0,00 |
| Howardite MP-TXH-085-A | 0,00 | 0,00 | 0,00 | 0,00 | 0,00 | 0,00 |
| Asteroid (5604) 1992 FE | 0,00 | 0,00 | 0,00 | 0,00 | 0,32 | 0,00 |
| Howardite MP-TXH-085-A | 0,00 | 0,00 | 0,00 | 0,00 | 0,00 | 0,00 |

Table D13 – Derived mass fractions of the end-members found in the selected V-type asteroids and their meteoritic analogs.

Note:

[1]The additional piogenite and enstatite represent different granulometries. For further details check Table D6.

U.PORTO
FACULDADE DE CIÊNCIAS
UNIVERSIDADE DO PORTO

# E. Figures of Results

In this section, it will be presented several figures obtained during this study. This section is divided into two subsections. In the first subsection E.1, the plots of the modeling laboratorial mixtures reflectance spectra and of their respective residuals will be presented. In the second subsection, it will be presented the plots obtained during the study of the V-type asteroids and HED meteorites reflectance spectra.

## E.1. Figures of laboratorial mixtures

In this subsection, the obtained plots of the modeling laboratorial mixtures reflectance spectra are presented. This subsection is divided into subsections according to the specificity of the plots. In subsection E.1.1 are presented the plots obtained for the derived albedo of the mixtures with the corresponding derived albedos of the end-members, with a grain size proportion: 0-45μm. In subsection E.1.2 are presented similar plots to the ones presented in subsection E.1.1, but with a grain size proportion: 45-75μm. In subsection E.1.3 are presented similar plots to the ones presented in subsection E.1.1, but with a grain size proportion: 70-145μm.

U.PORTO
FACULDADE DE CIÊNCIAS
UNIVERSIDADE DO PORTO

## E.1.1. Grain size proportion: 0-45µm

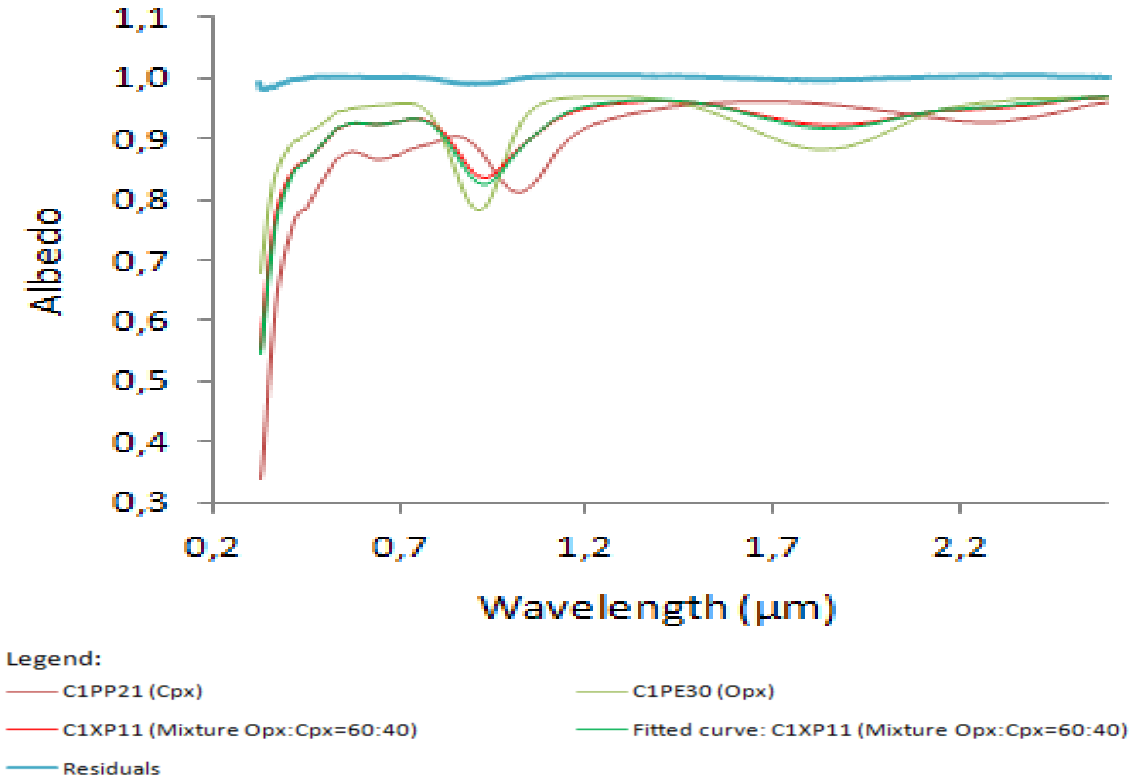


Fig.E1 - Derived albedo for the sample XP-CMP-011 (C1XP11) and for their extreme minerals PP-CMP-021 (C1PP21) and PP-CMP-030 (C1PE30) versus wavelength. The residuals were shifted vertically by one unity.

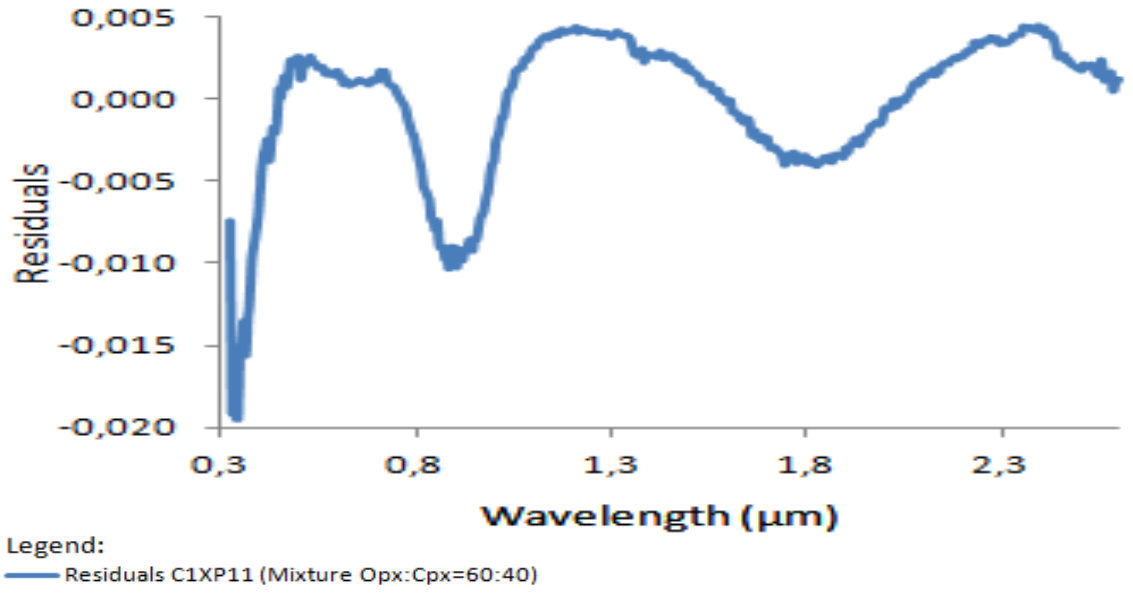


Fig.E2 - Plot of the residuals of the sample C1XP11.

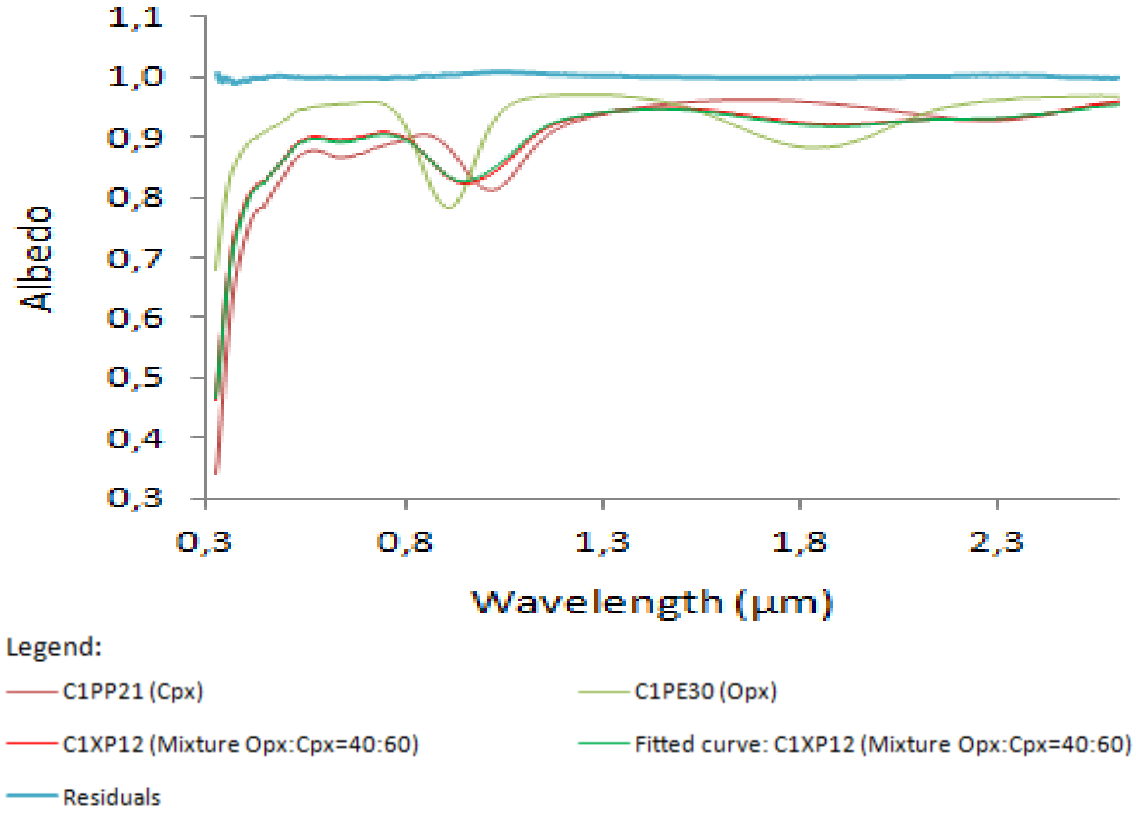


Fig.E3 - Derived albedo for the sample XP-CMP-012 (C1XP12) and for their extreme minerals PP-CMP-021 (C1PP21) and PP-CMP-030 (C1PE30) versus wavelength. The residuals were shifted vertically by one unity.

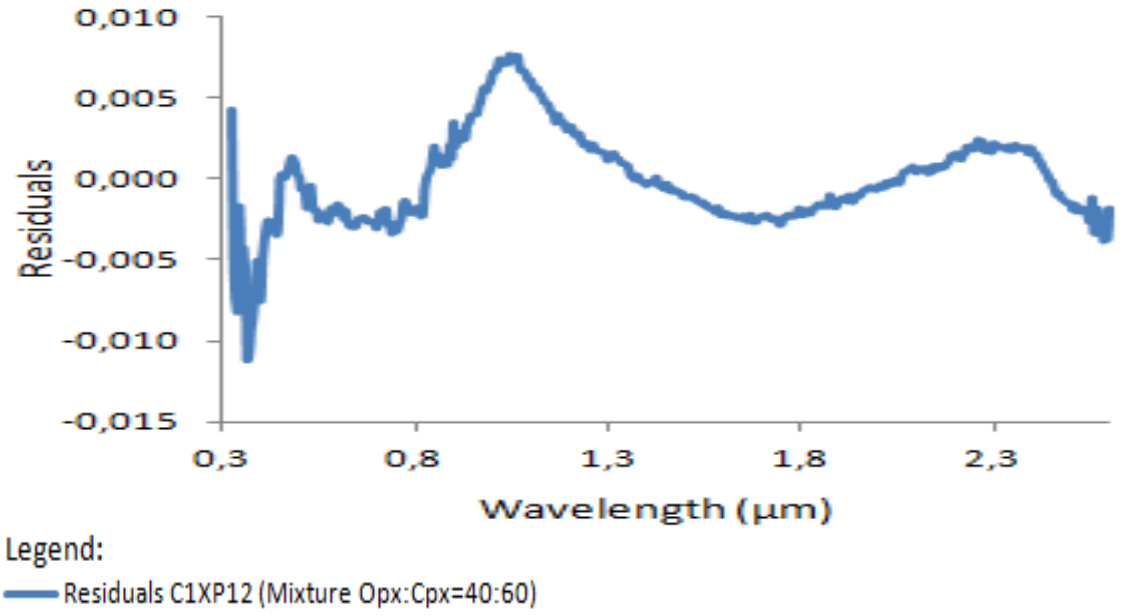


Fig.E4 - Plot of the residuals of the sample C1XP12.

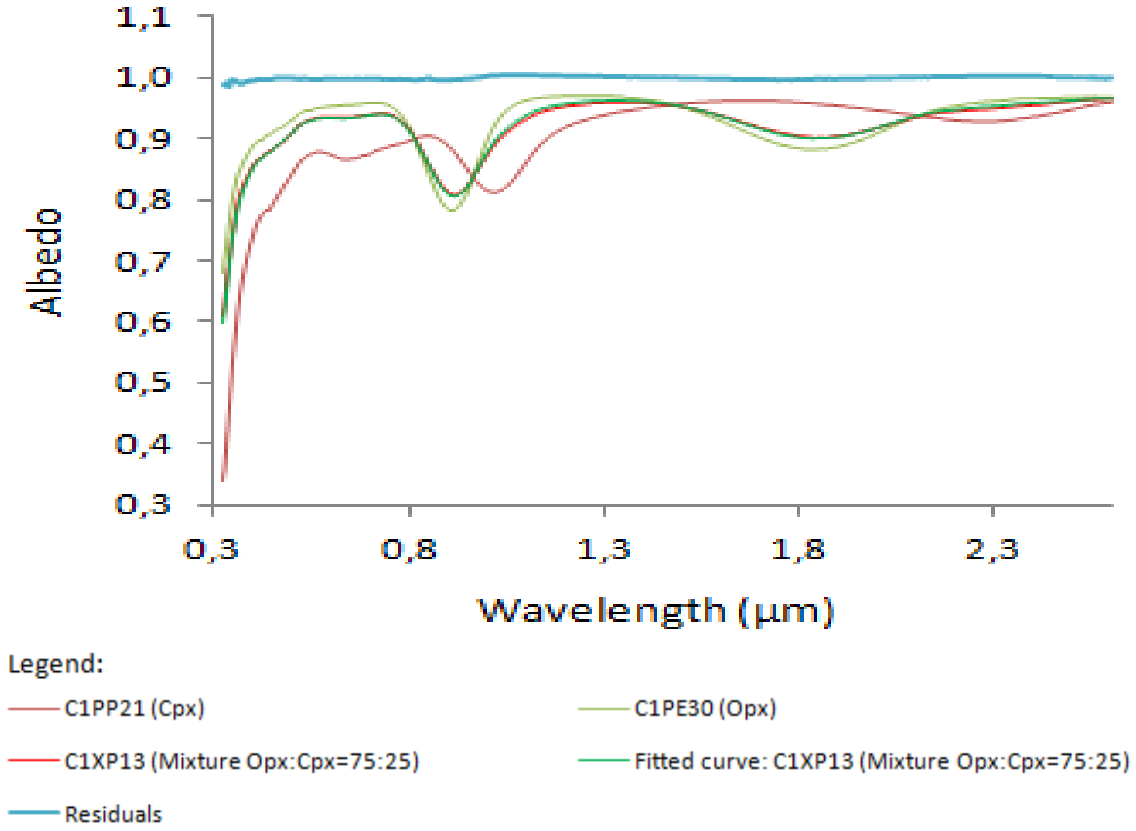


Fig.E5 - Derived albedo for the sample XP-CMP-013 (C1XP13) and for their extreme minerals PP-CMP-021 (C1PP21) and PP-CMP-030 (C1PE30) versus wavelength. The residuals were shifted vertically by one unity.

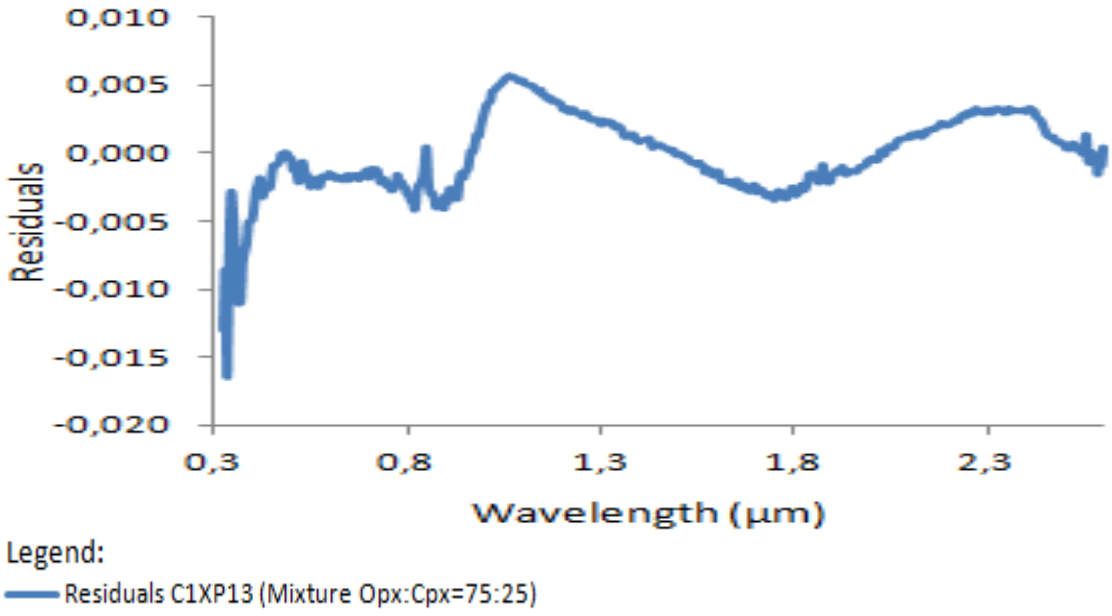


Fig.E6 - Plot of the residuals of the sample C1XP13.

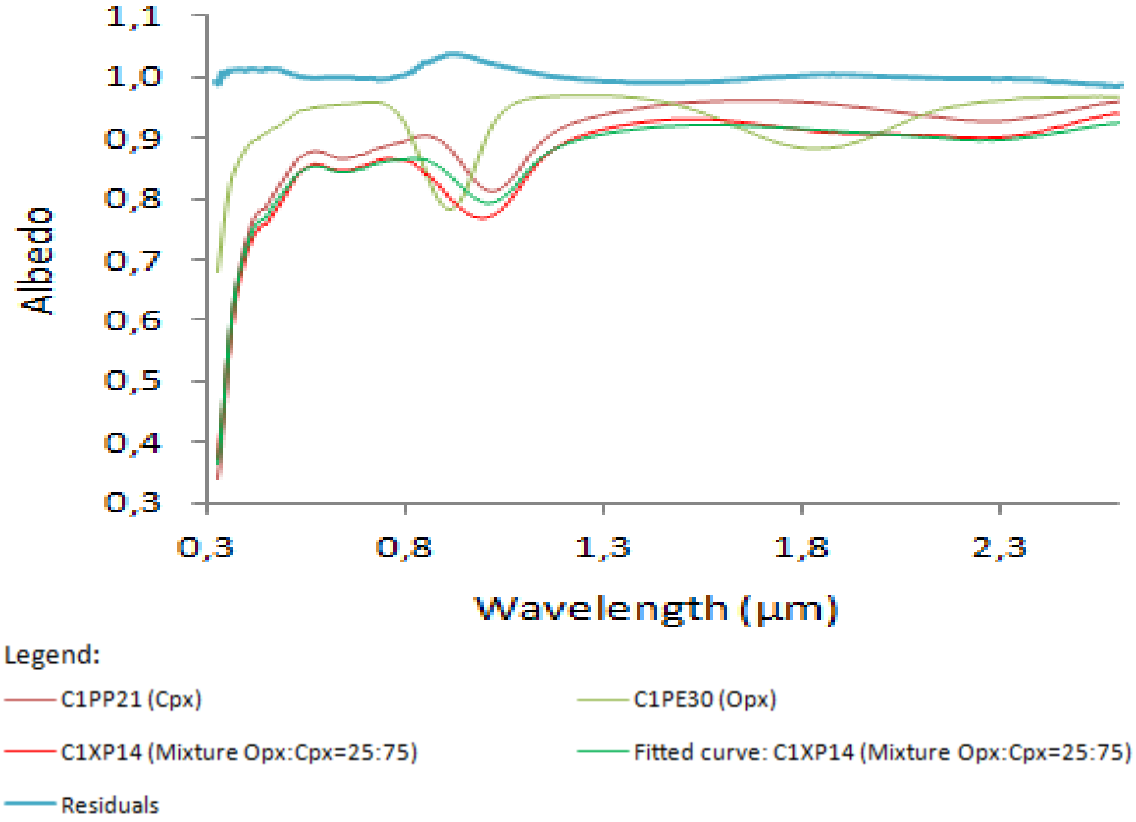


Fig.E7 - Derived albedo for the sample XP-CMP-014 (C1XP14) and for their extreme minerals PP-CMP-021 (C1PP21) and PP-CMP-030 (C1PE30) versus wavelength. The residuals were shifted vertically by one unity.

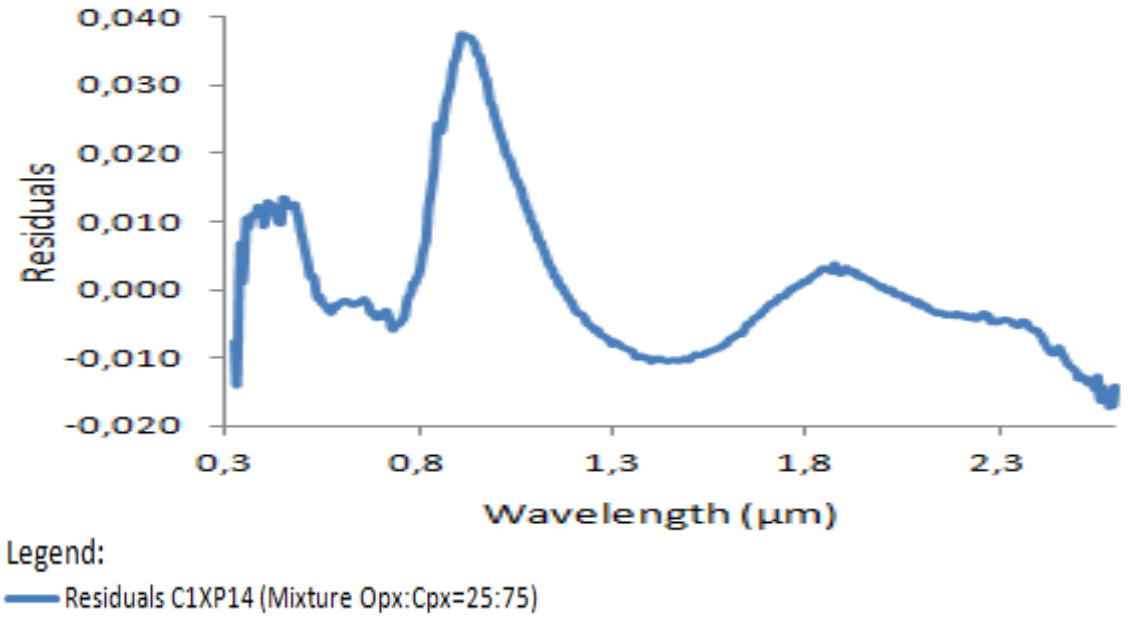


Fig.E8 - Plot of the residuals of the sample C1XP14.

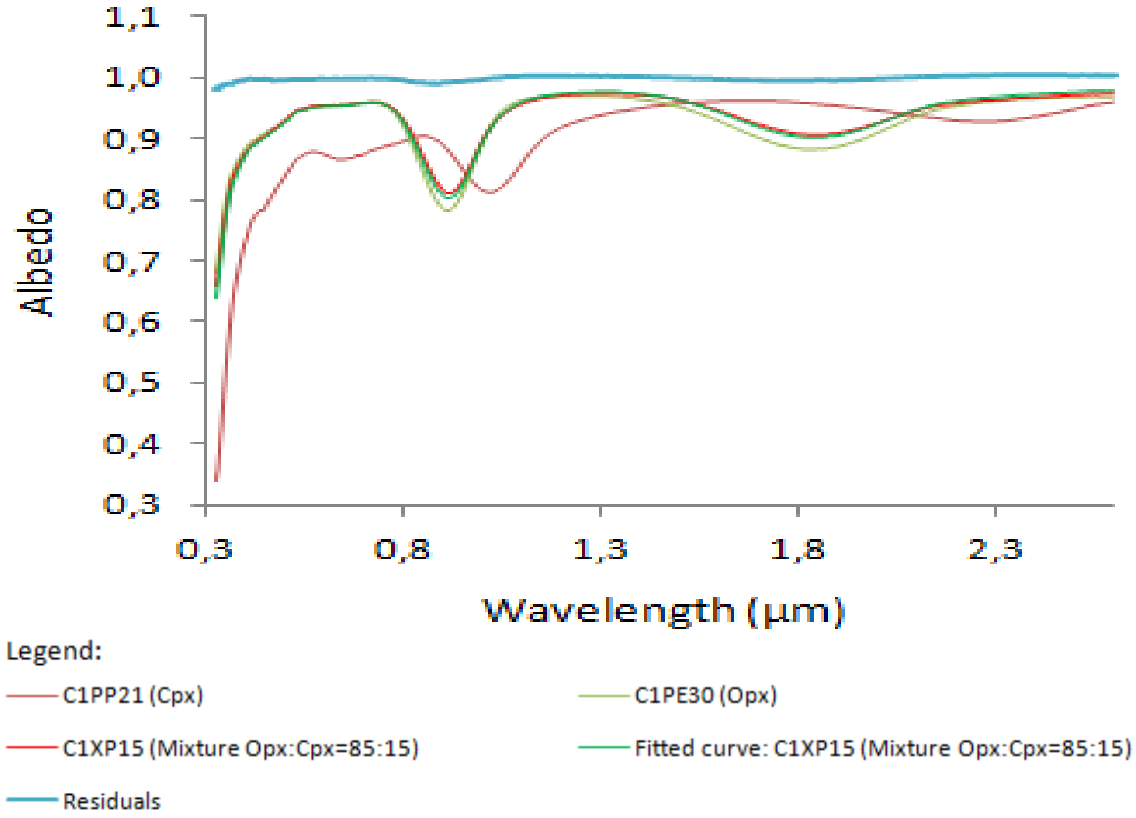


Fig.E9 - Derived albedo for the sample XP-CMP-015 (C1XP15) and for their extreme minerals PP-CMP-021 (C1PP21) and PP-CMP-030 (C1PE30) versus wavelength. The residuals were shifted vertically by one unity.

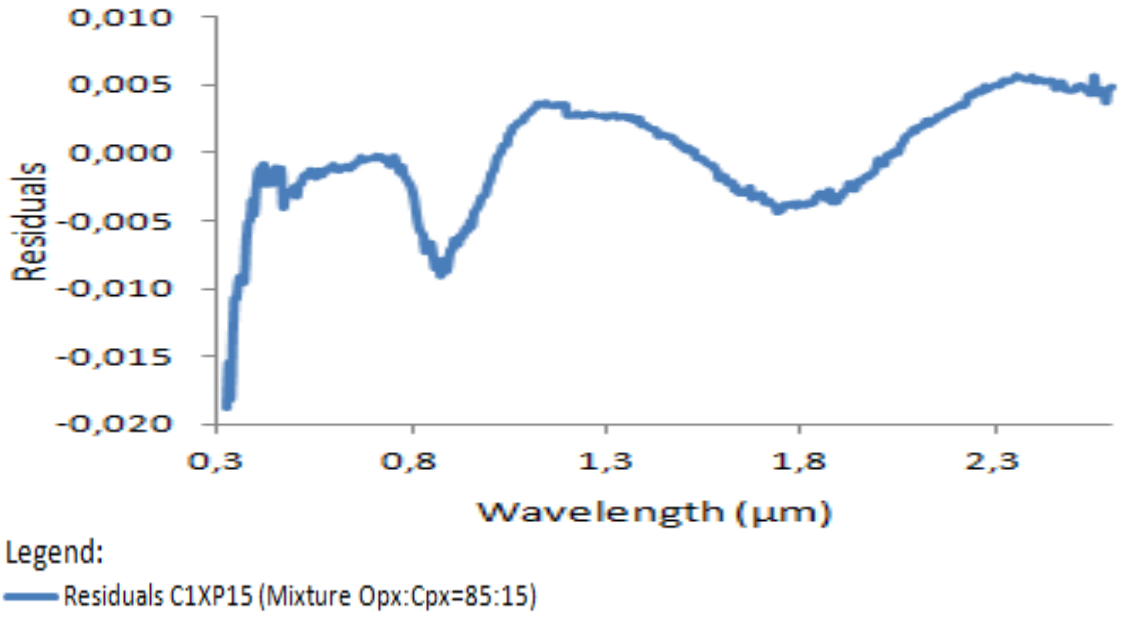


Fig.E10 - Plot of the residuals of the sample C1XP15.

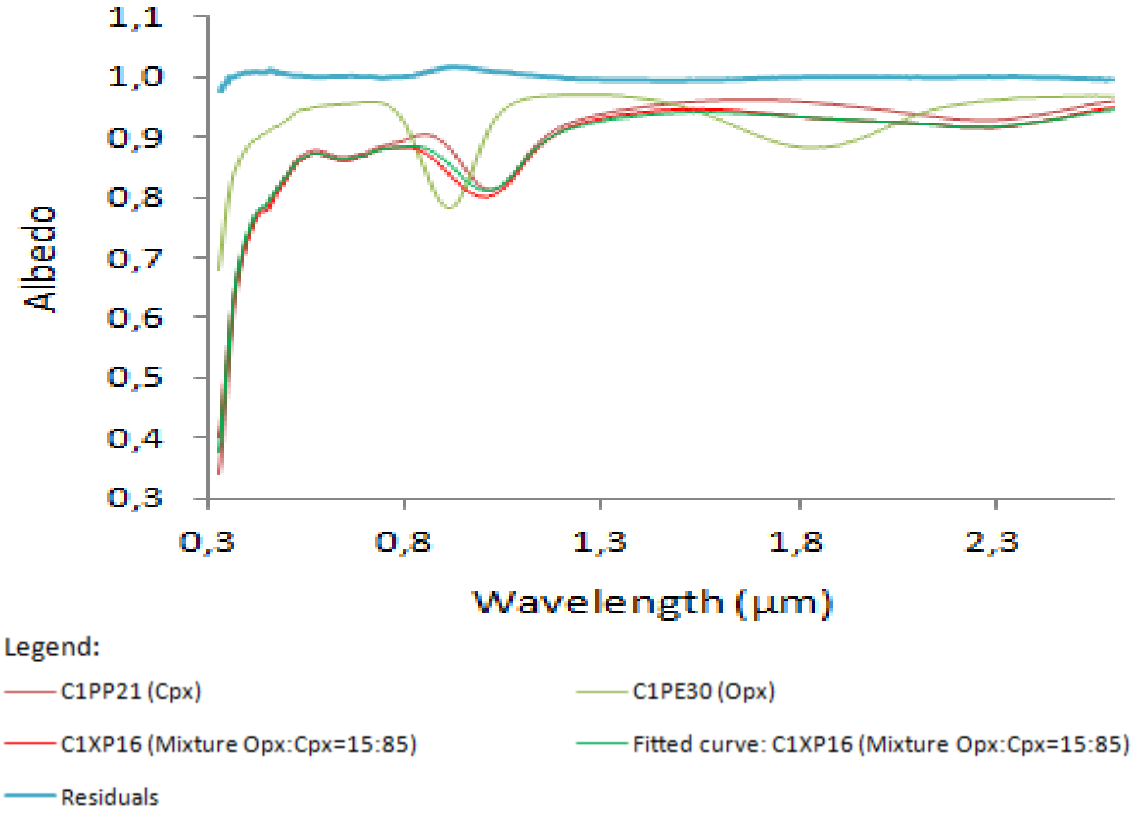


Fig.E11 - Derived albedo for the sample XP-CMP-016 (C1XP16) and for their extreme minerals PP-CMP-021 (C1PP21) and PP-CMP-030 (C1PE30) versus wavelength. The residuals were shifted vertically by one unity.

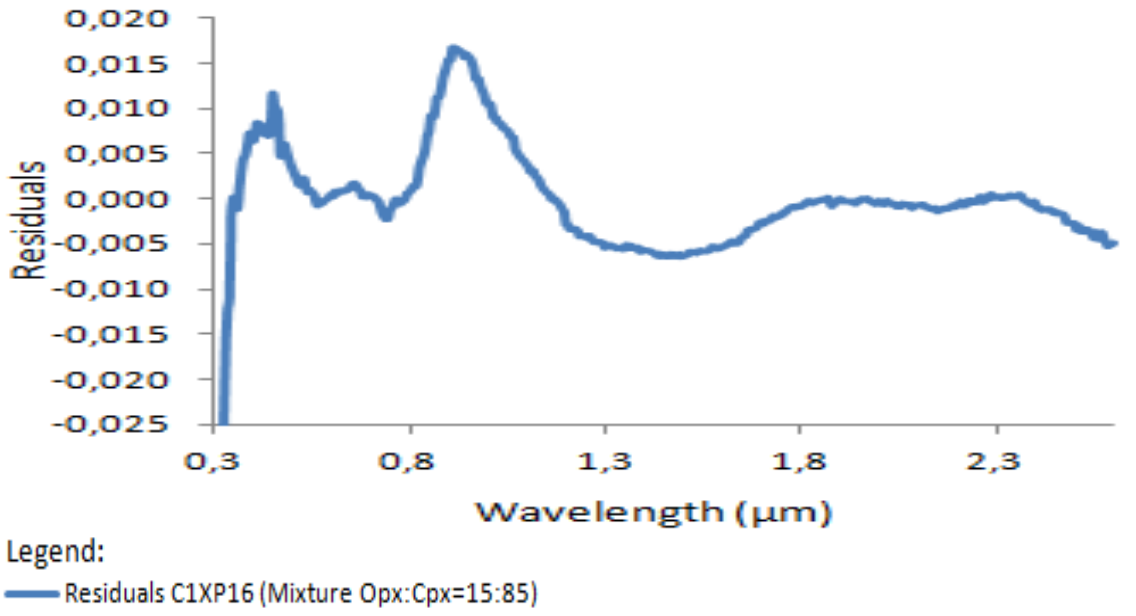


Fig.E12 - Plot of the residuals of the sample C1XP16.

U.PORTO
FACULDADE DE CIÊNCIAS
UNIVERSIDADE DO PORTO

## E.1.2. Grain size proportion: 45-75µm

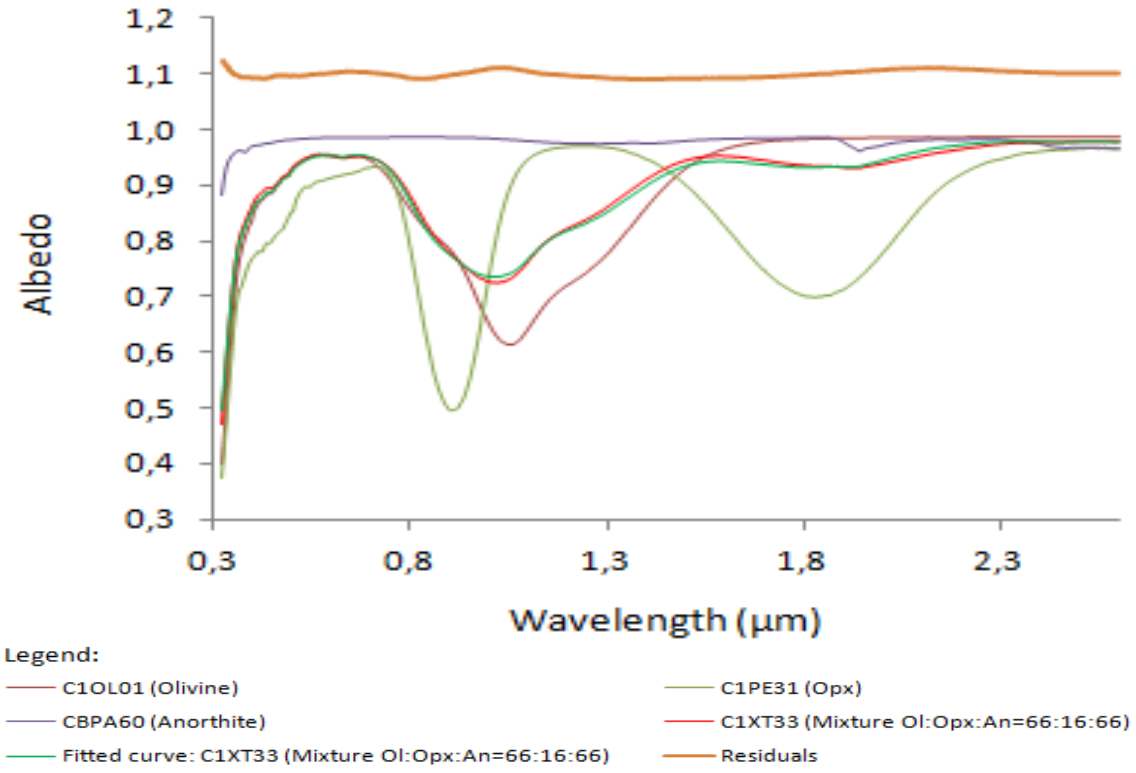


Fig.E13 - Derived albedo for the sample XT-CMP-033 (C1XT33) and for their extreme minerals OL-JMS-001 (C1OL01), PE-CMP-031 (C1PE31) and PA-CMP-060-B (CBPA60) versus wavelength. The residuals were shifted vertically by 1.1 unities.

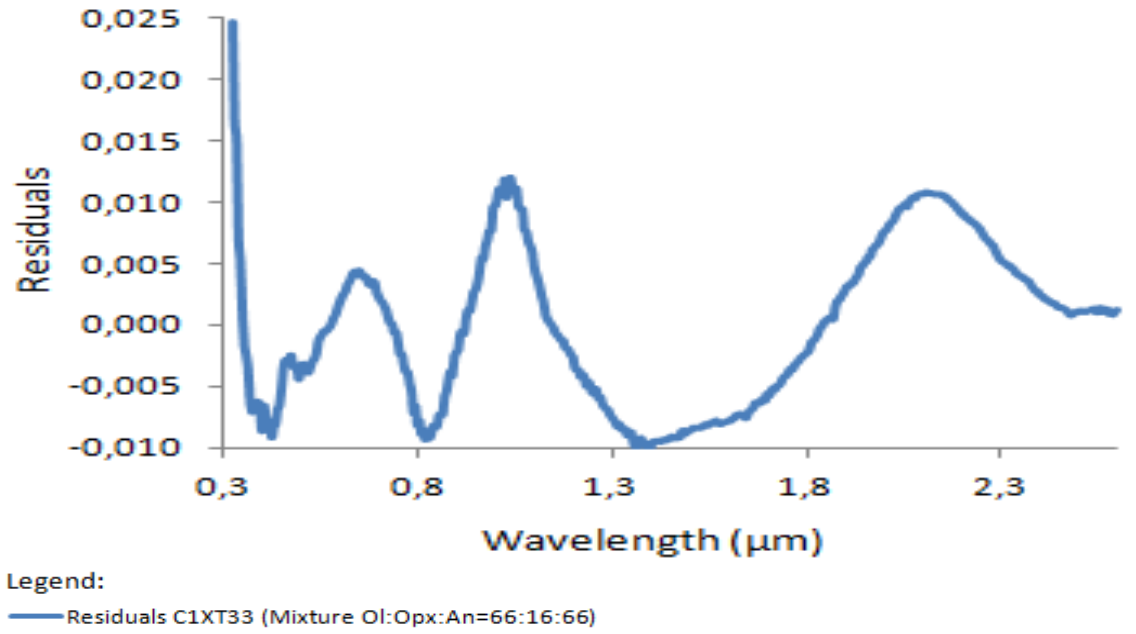


Fig.E14 - Plot of the residuals of the sample C1XT33.

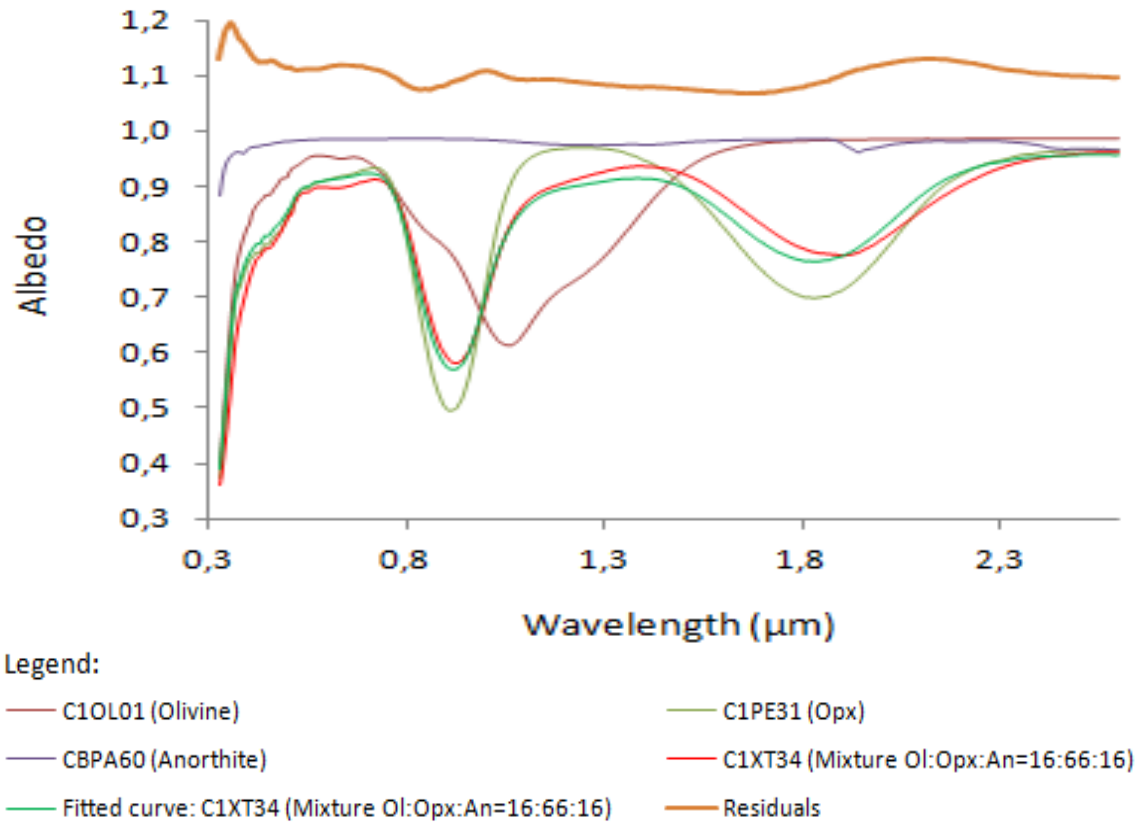


Fig.E15 - Derived albedo for the sample XT-CMP-034 (C1XT34) and for their extreme minerals OL-JMS-001 (C1OL01), PE-CMP-031 (C1PE31) and PA-CMP-060-B (CBPA60) versus wavelength. The residuals were shifted vertically by 1.1 unities.

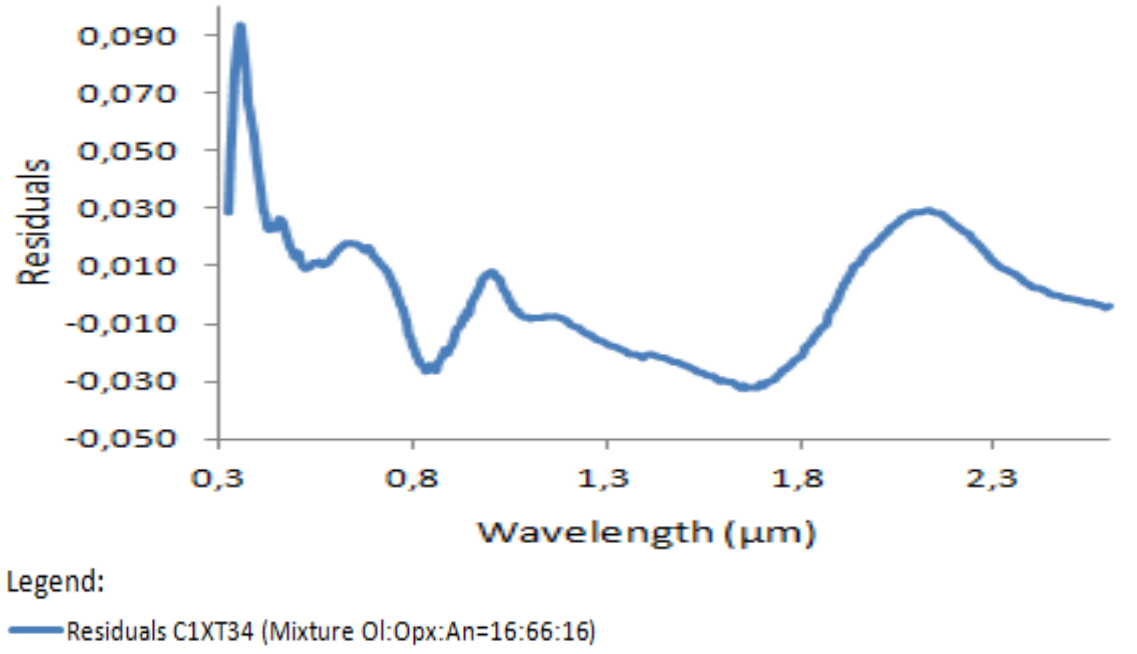


Fig.E16 - Plot of the residuals of the sample C1XT34.

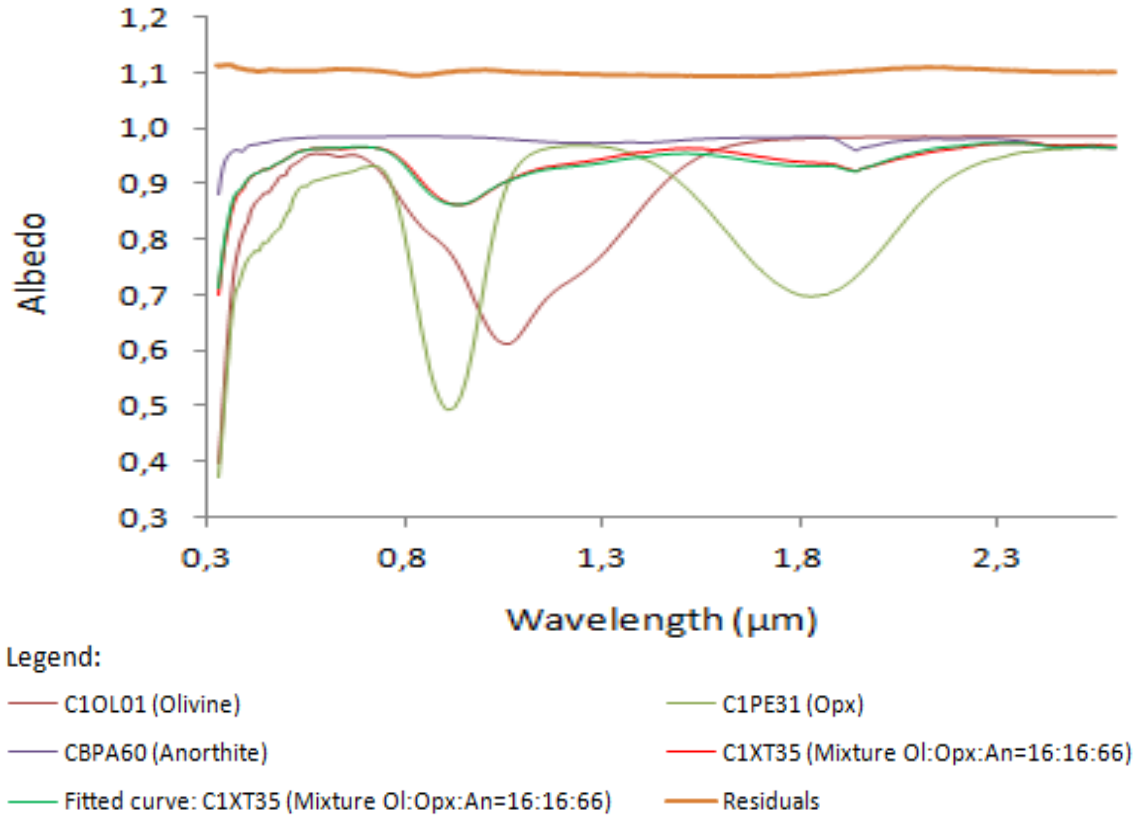


Fig.E17 - Derived albedo for the sample XT-CMP-035 (C1XT35) and for their extreme minerals OL-JMS-001 (C1OL01), PE-CMP-031 (C1PE31) and PA-CMP-060-B (CBPA60) versus wavelength. The residuals were shifted vertically by 1.1 unities.

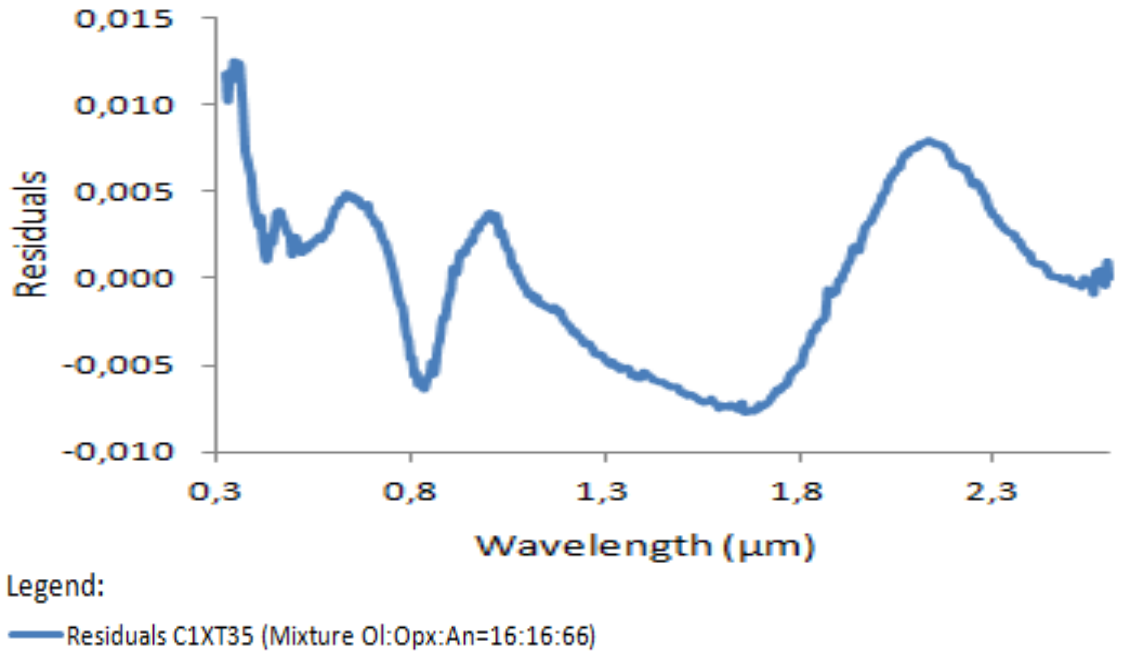


Fig.E18 - Plot of the residuals of the sample C1XT35.

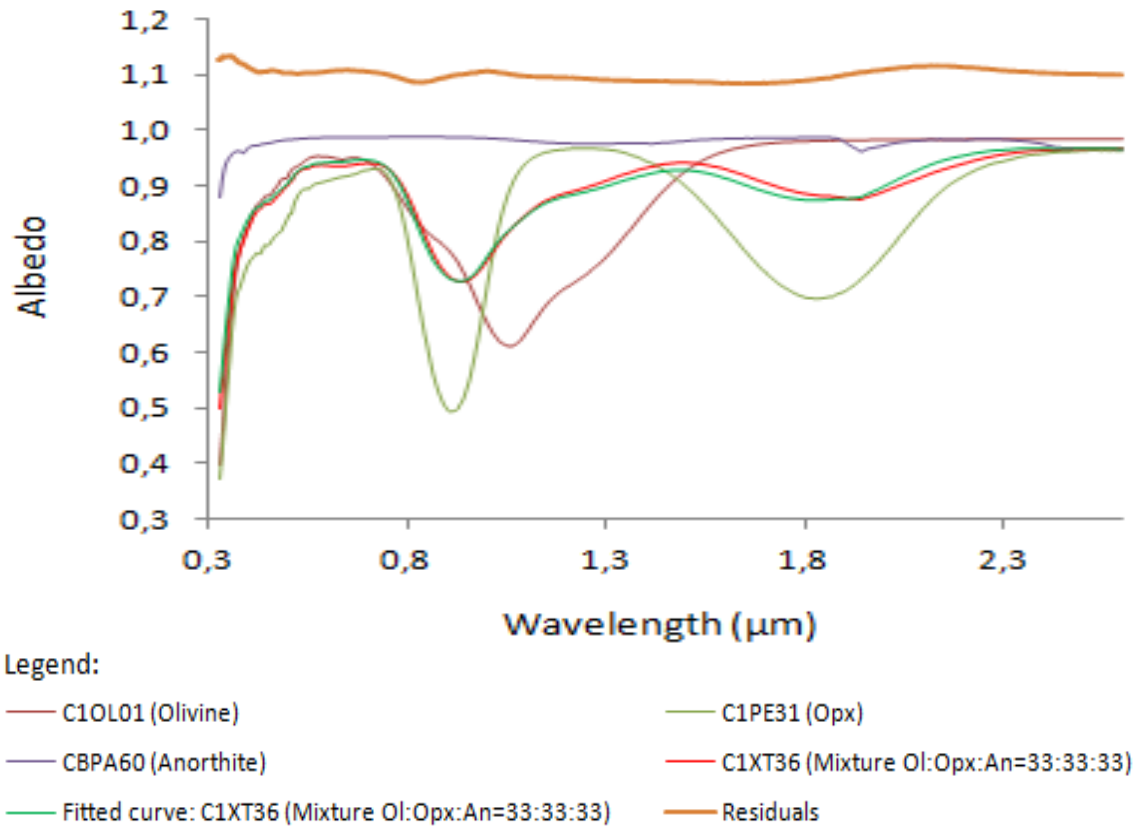


Fig.E19 - Derived albedo for the sample XT-CMP-036 (C1XT36) and for their extreme minerals OL-JMS-001 (C1OL01), PE-CMP-031 (C1PE31) and PA-CMP-060-B (CBPA60) versus wavelength. The residuals were shifted vertically by 1.1 unities.

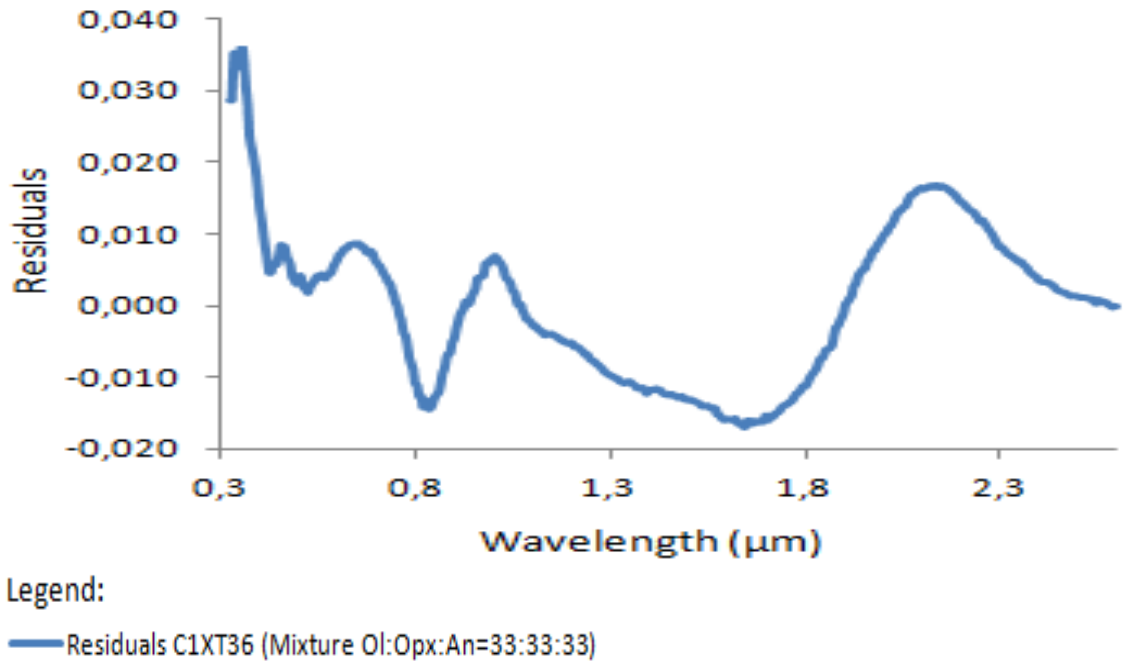


Fig.E20 - Plot of the residuals of the sample C1XT36.

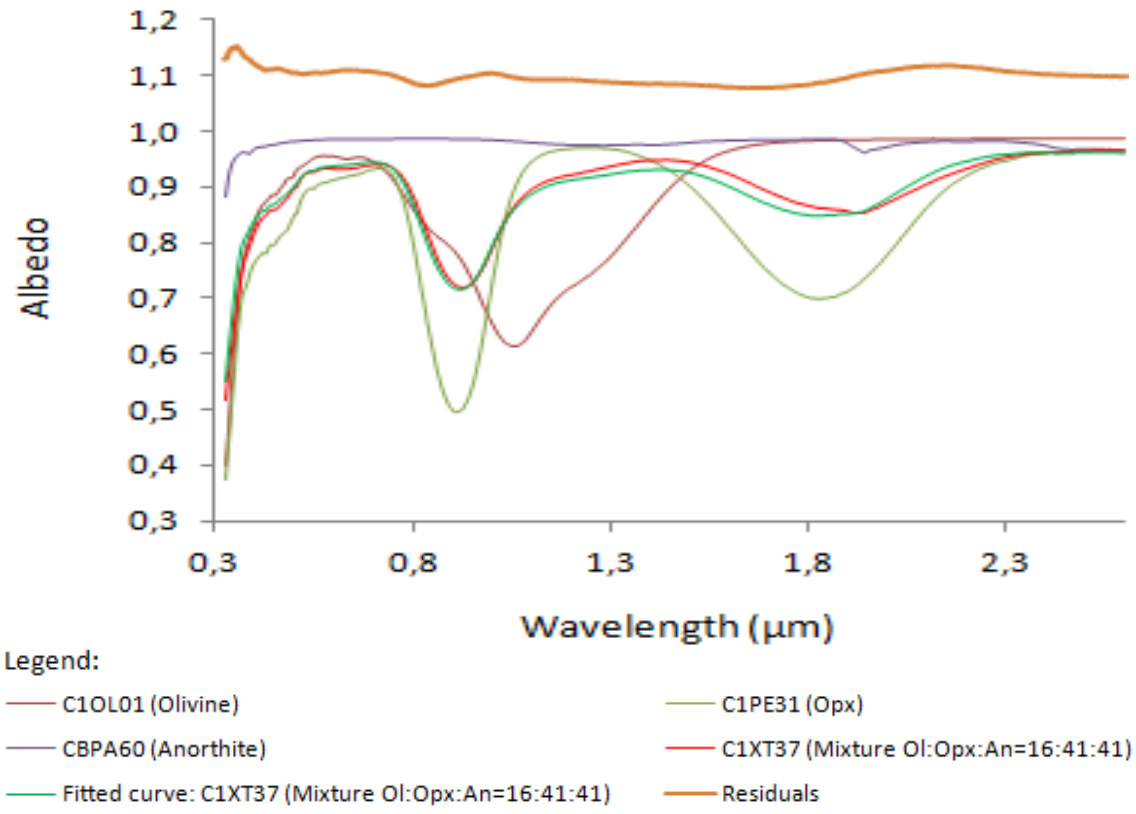


Fig.E21 - Derived albedo for the sample XT-CMP-037 (C1XT37) and for their extreme minerals OL-JMS-001 (C1OL01), PE-CMP-031 (C1PE31) and PA-CMP-060-B (CBPA60) versus wavelength. The residuals were shifted vertically by 1.1 unities.

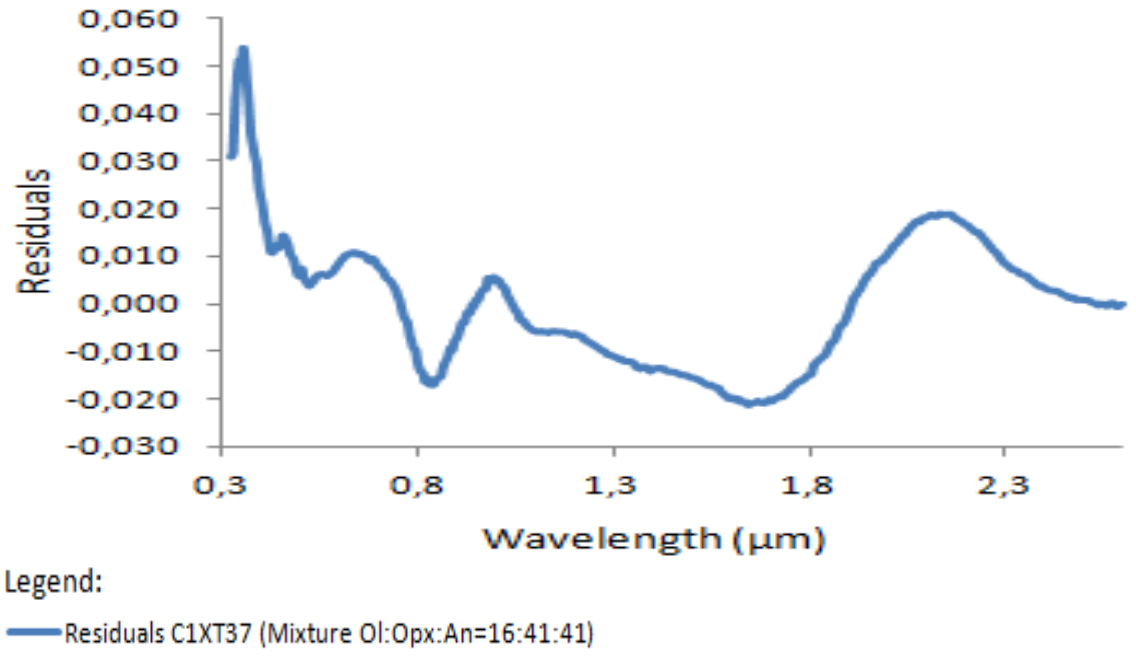


Fig.E22 - Plot of the residuals of the sample C1XT37.

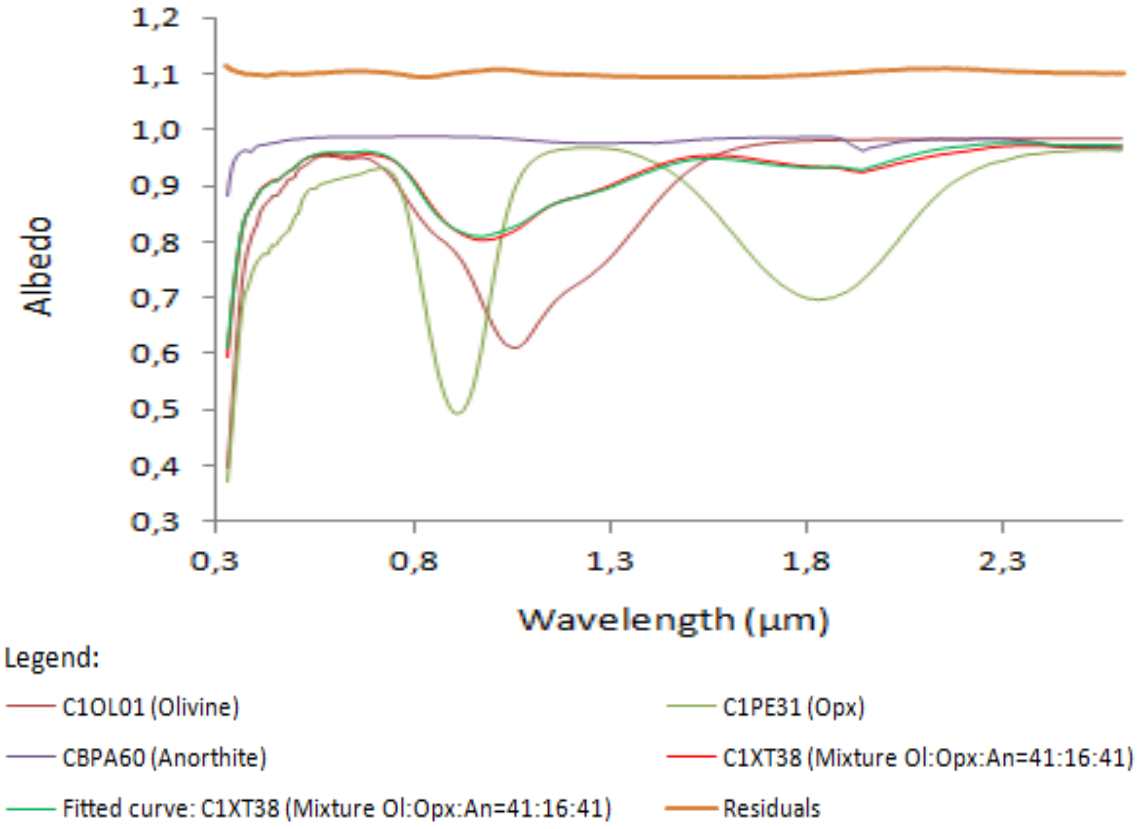


Fig.E23 - Derived albedo for the sample XT-CMP-038 (C1XT38) and for their extreme minerals OL-JMS-001 (C1OL01), PE-CMP-031 (C1PE31) and PA-CMP-060-B (CBPA60) versus wavelength. The residuals were shifted vertically by 1.1 unities.

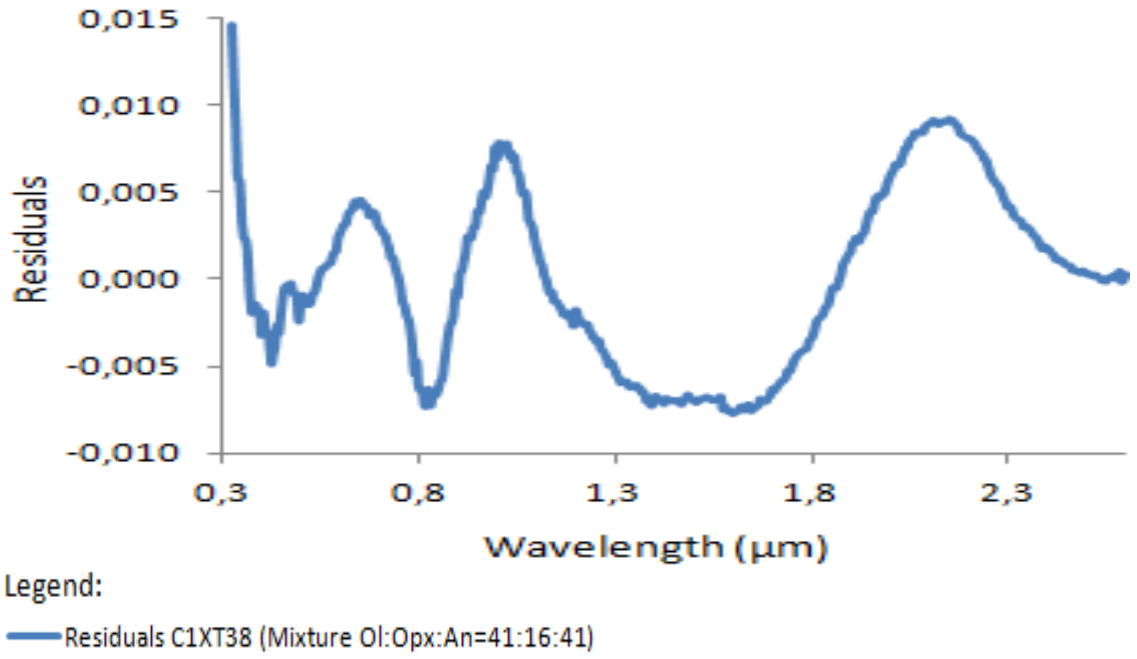


Fig.E24 - Plot of the residuals of the sample C1XT38.

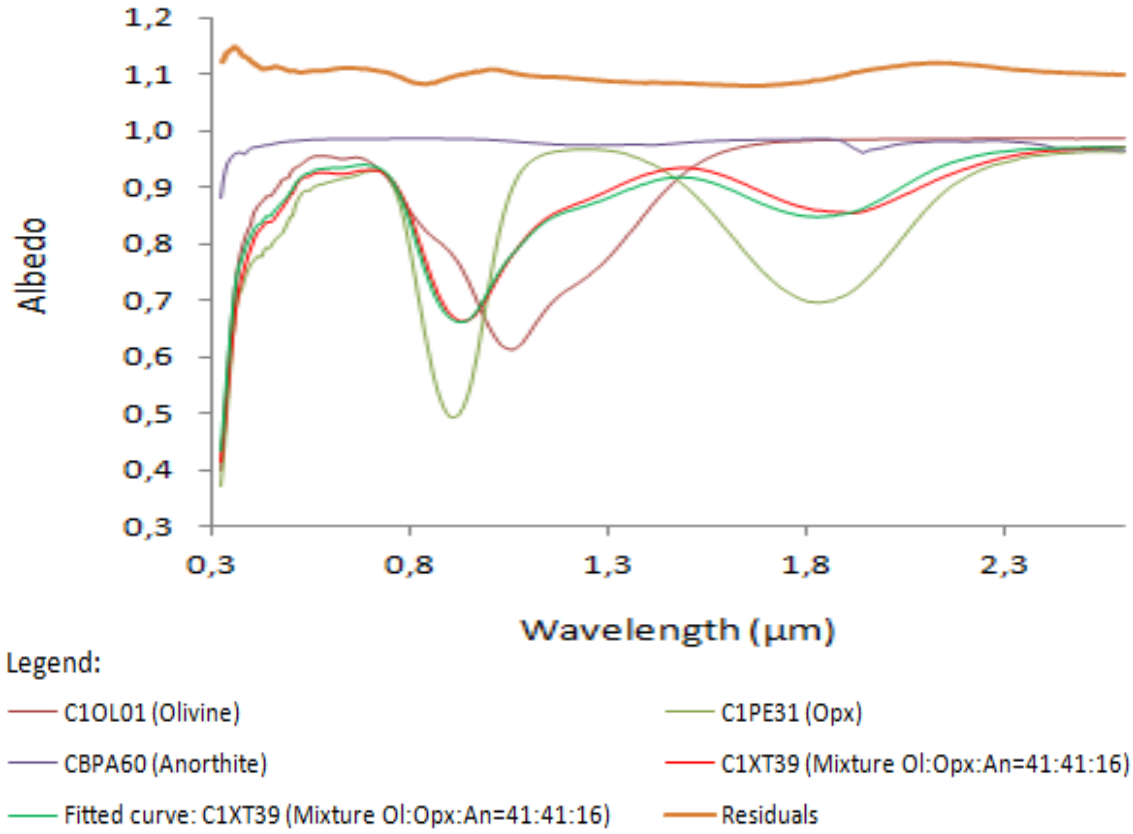


Fig.E25 - Derived albedo for the sample XT-CMP-039 (C1XT39) and for their extreme minerals OL-JMS-001 (C1OL01), PE-CMP-031 (C1PE31) and PA-CMP-060-B (CBPA60) versus wavelength. The residuals were shifted vertically by 1.1 unities.

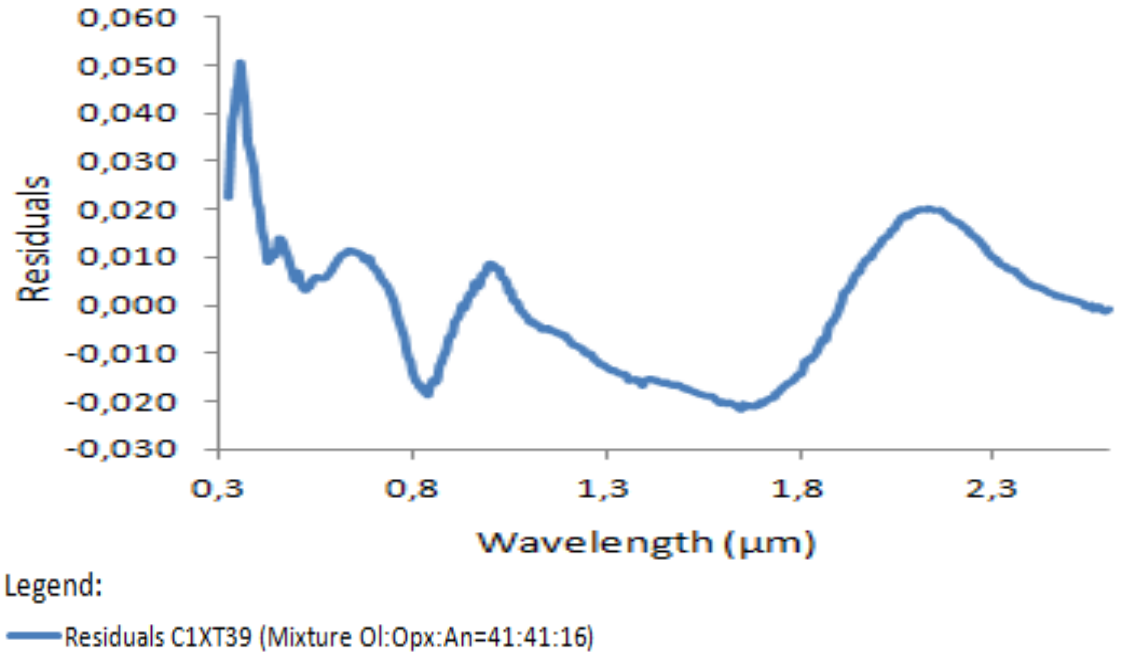


Fig.E26 - Plot of the residuals of the sample C1XT39.

U.PORTO
FACULDADE DE CIÊNCIAS
UNIVERSIDADE DO PORTO

## E.1.3. Grain size proportion: 70-145µm

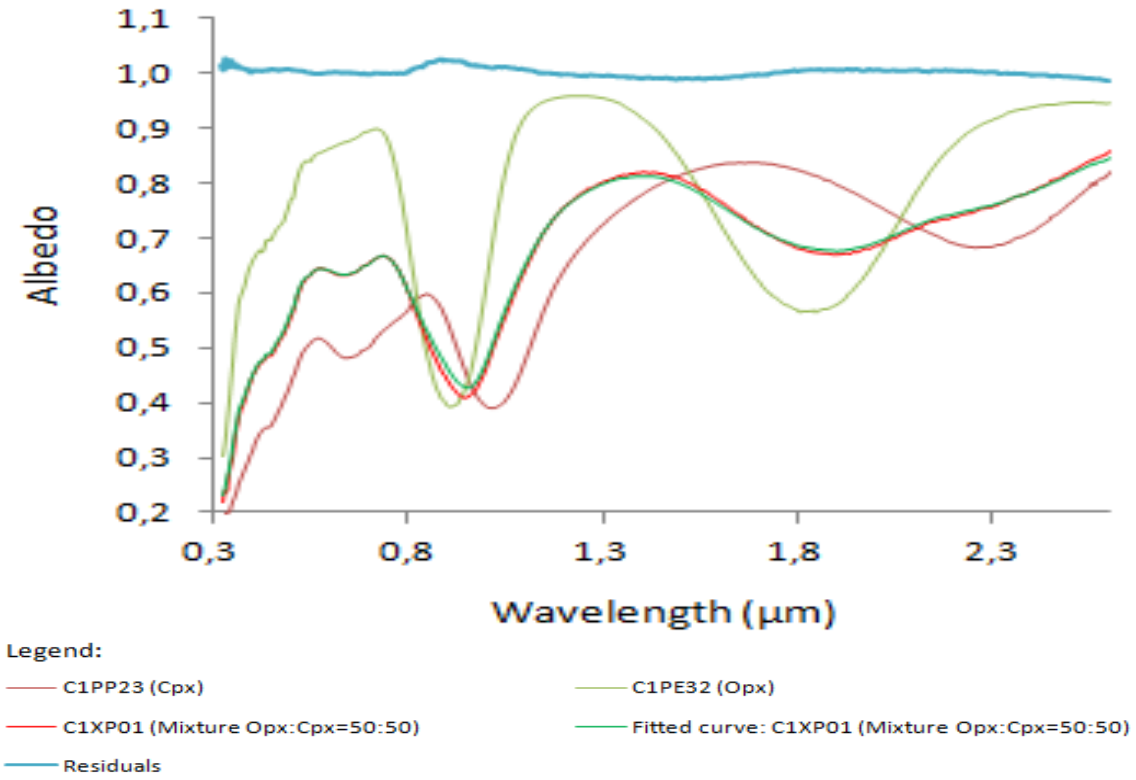


Fig.E27 - Derived albedo for the sample XP-CMP-001 (C1XP01) and for their extreme minerals PP-CMP-023 (C1PP23) and PE-CMP-032 (C1PP32) versus wavelength. The residuals were shifted vertically by one unity.

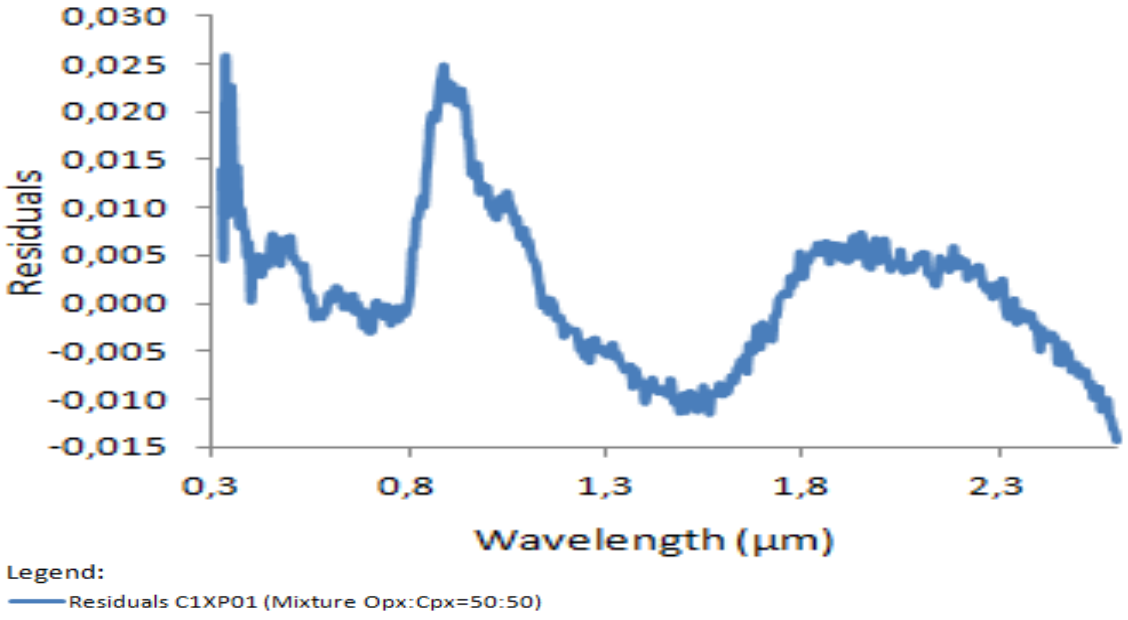


Fig.E28 - Plot of the residuals of the sample C1XP01.

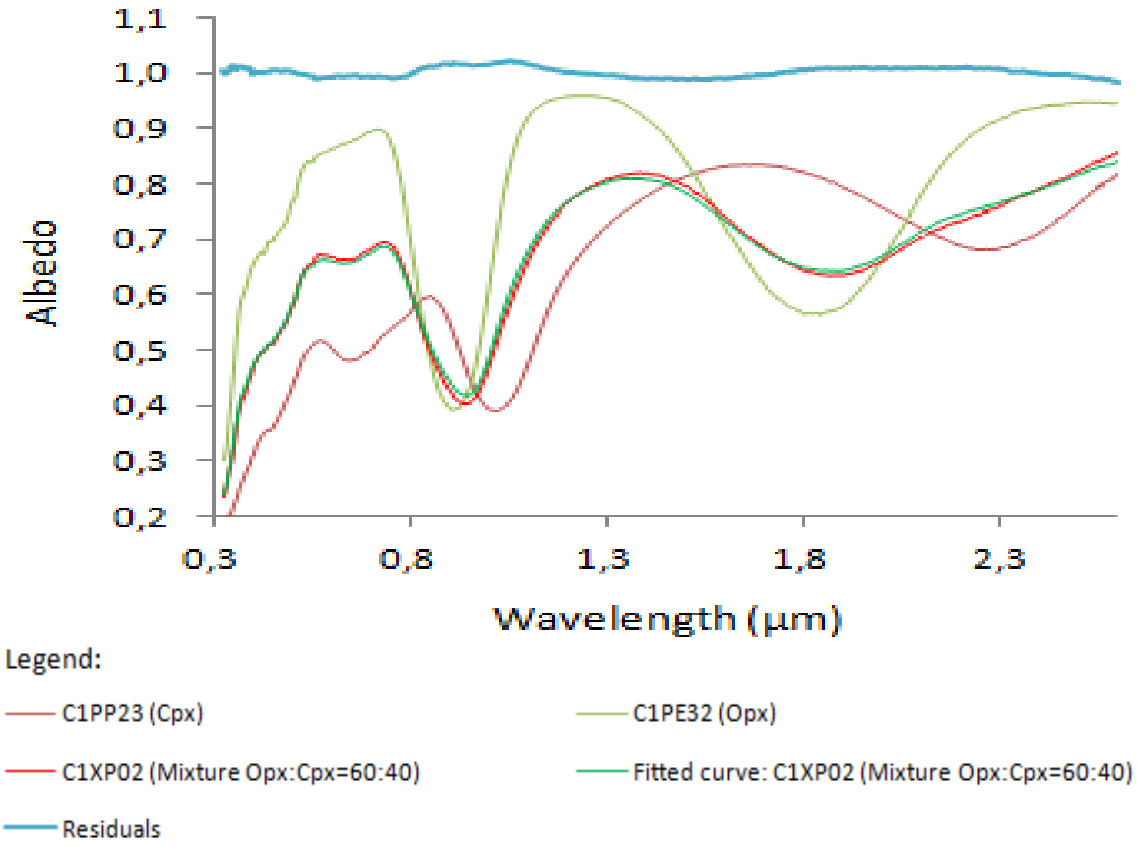


Fig.E29 - Derived albedo for the sample XP-CMP-002 (C1XP02) and for their extreme minerals PP-CMP-023 (C1PP23) and PE-CMP-032 (C1PP32) versus wavelength. The residuals were shifted vertically by one unity.

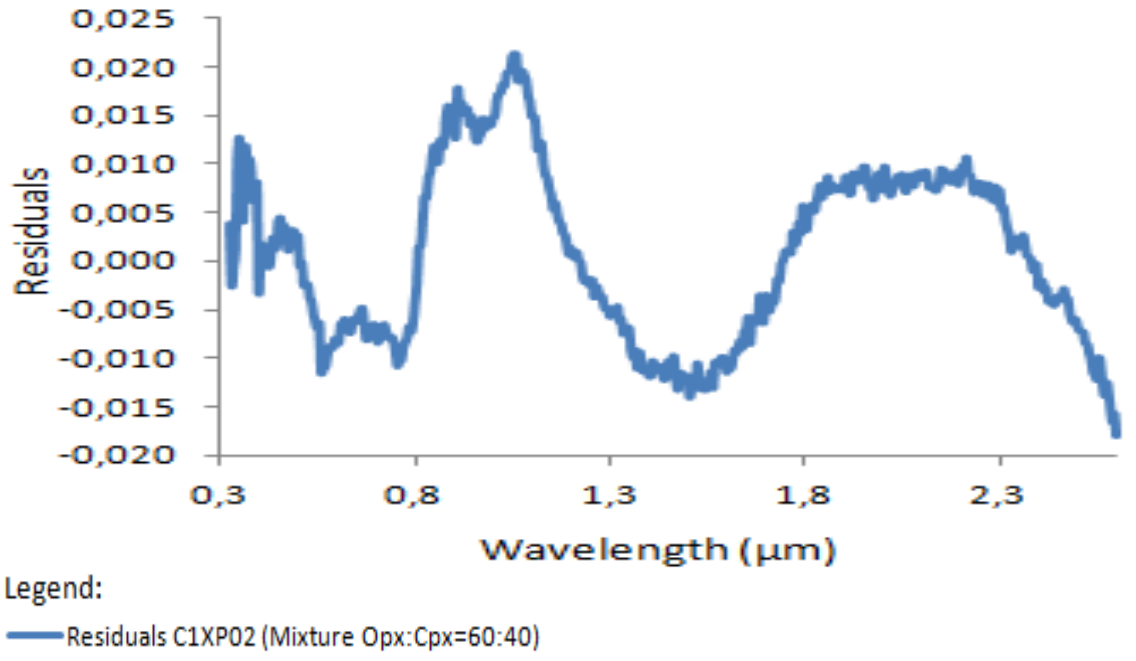


Fig.E30 - Plot of the residuals of the sample C1XP02.

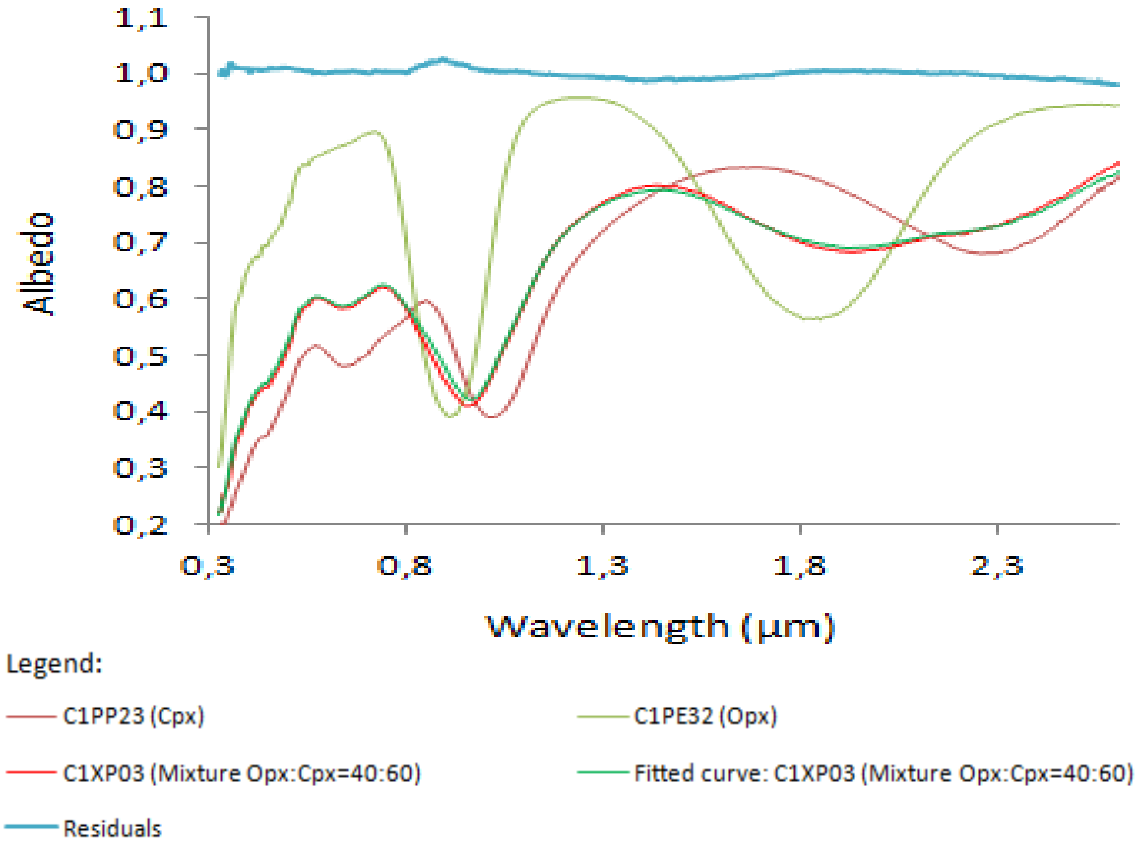


Fig.E31 - Derived albedo for the sample XP-CMP-003 (C1XP03) and for their extreme minerals PP-CMP-023 (C1PP23) and PE-CMP-032 (C1PP32) versus wavelength. The residuals were shifted vertically by one unity.

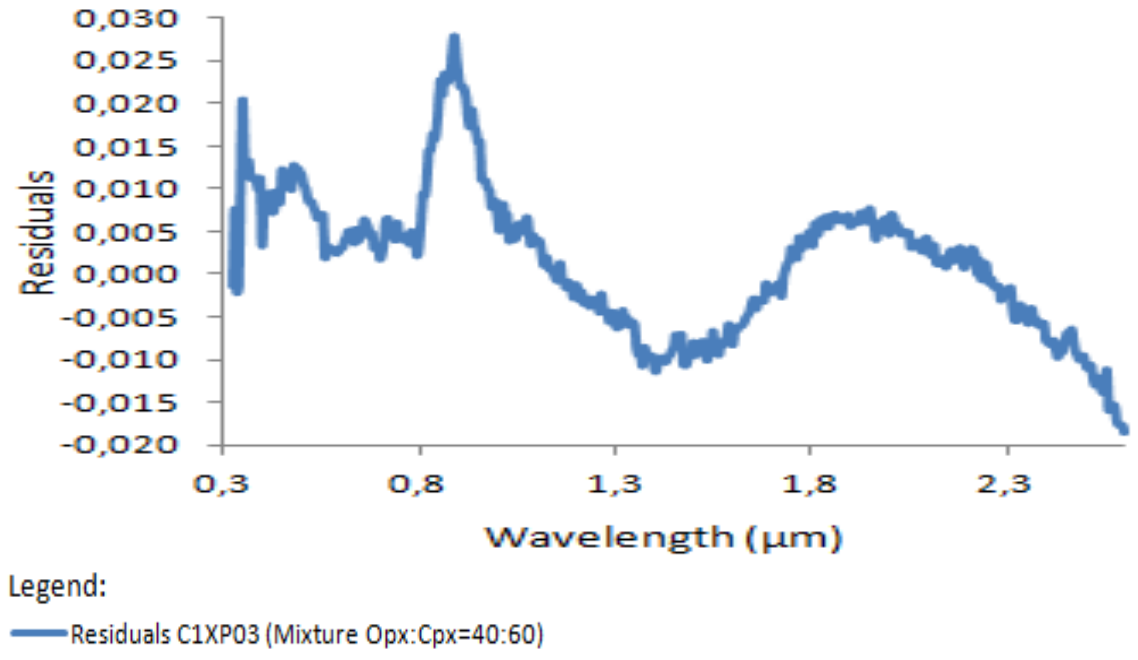


Fig.E32 - Plot of the residuals of the sample C1XP03.

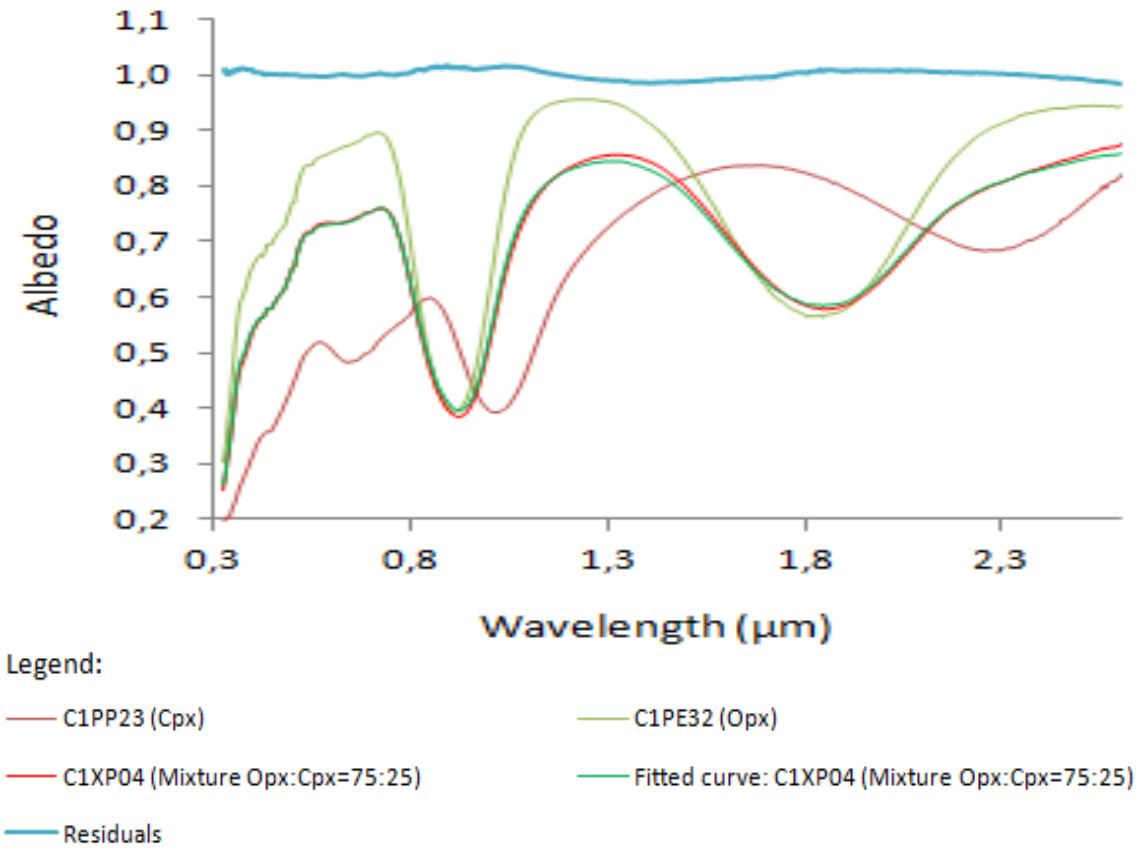


Fig.E33 - Derived albedo for the sample XP-CMP-004 (C1XP04) and for their extreme minerals PP-CMP-023 (C1PP23) and PE-CMP-032 (C1PP32) versus wavelength. The residuals were shifted vertically by one unity.

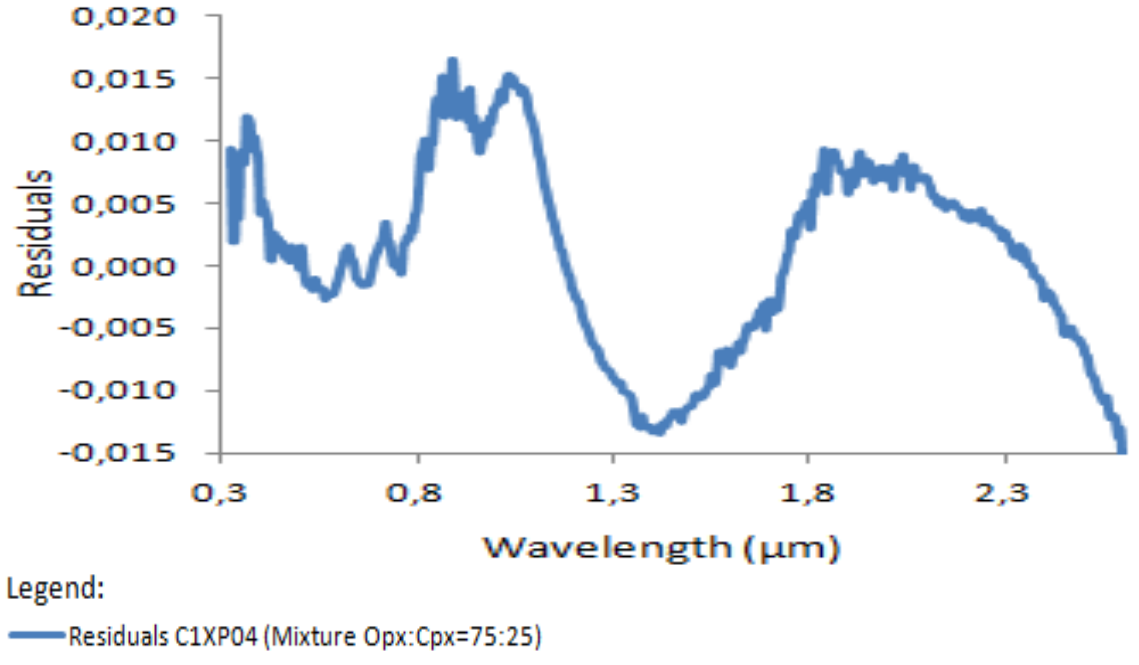


Fig.E34 - Plot of the residuals of the sample C1XP04.

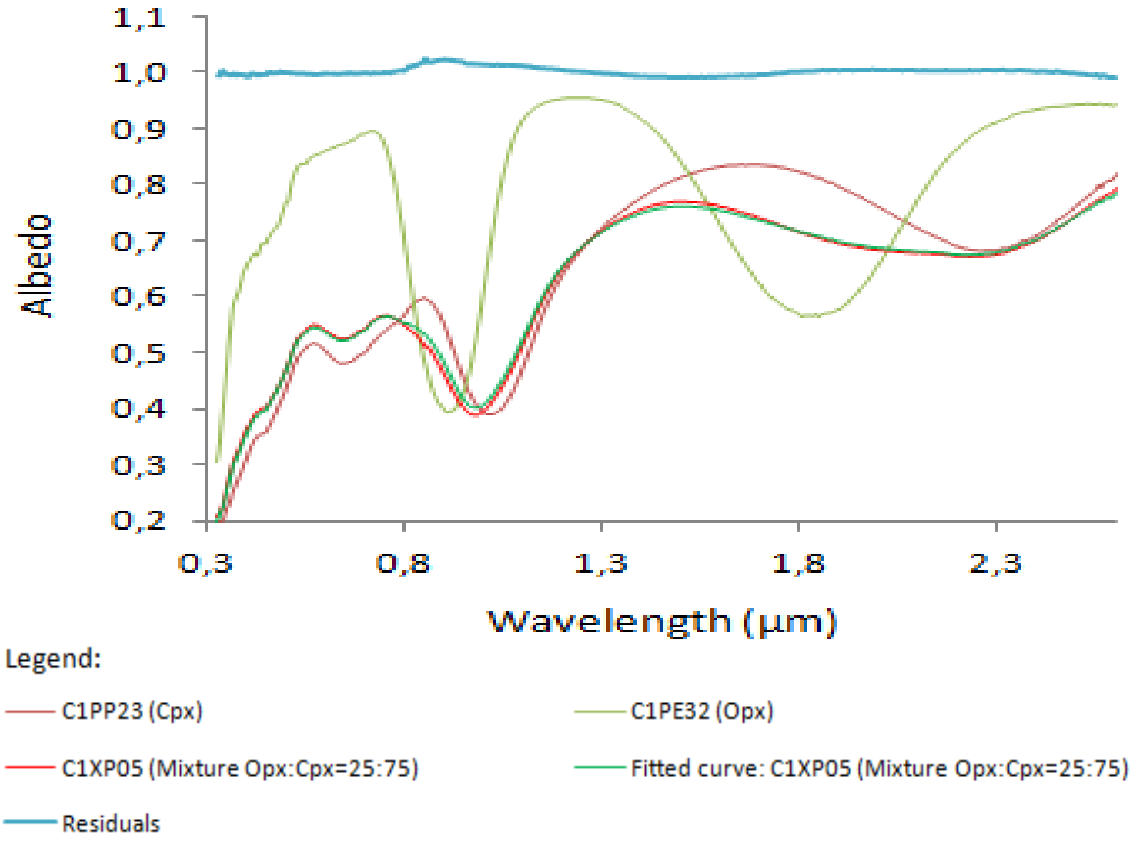


Fig.E35 - Derived albedo for the sample XP-CMP-005 (C1XP05) and for their extreme minerals PP-CMP-023 (C1PP23) and PE-CMP-032 (C1PP32) versus wavelength. The residuals were shifted vertically by one unity.

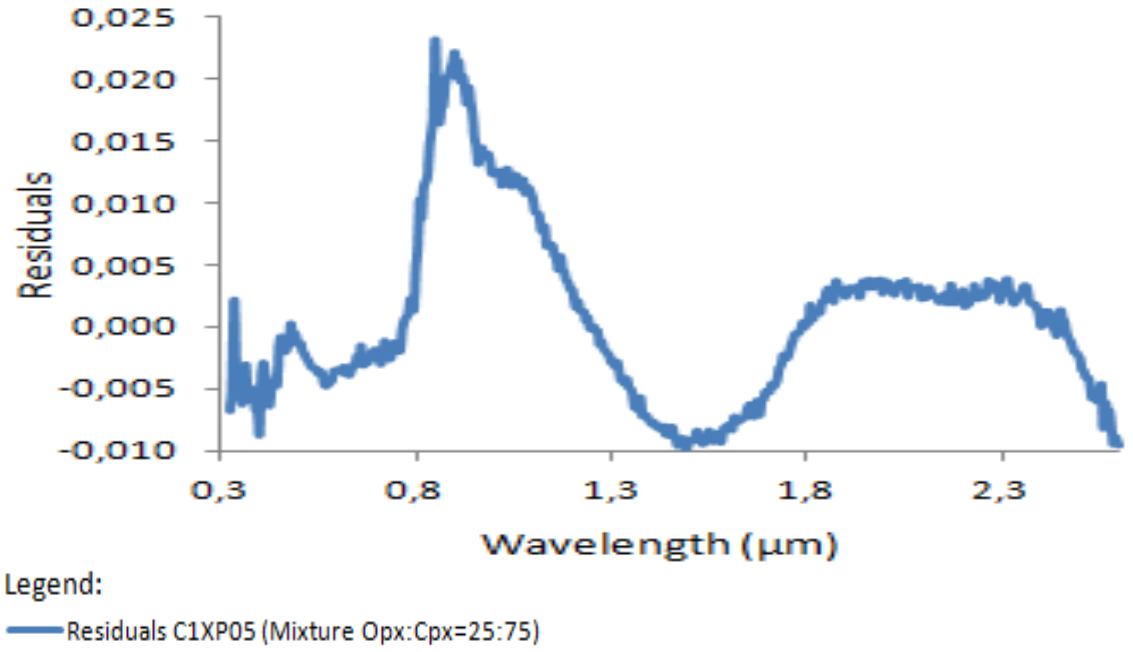


Fig.E36 - Plot of the residuals of the sample C1XP05.

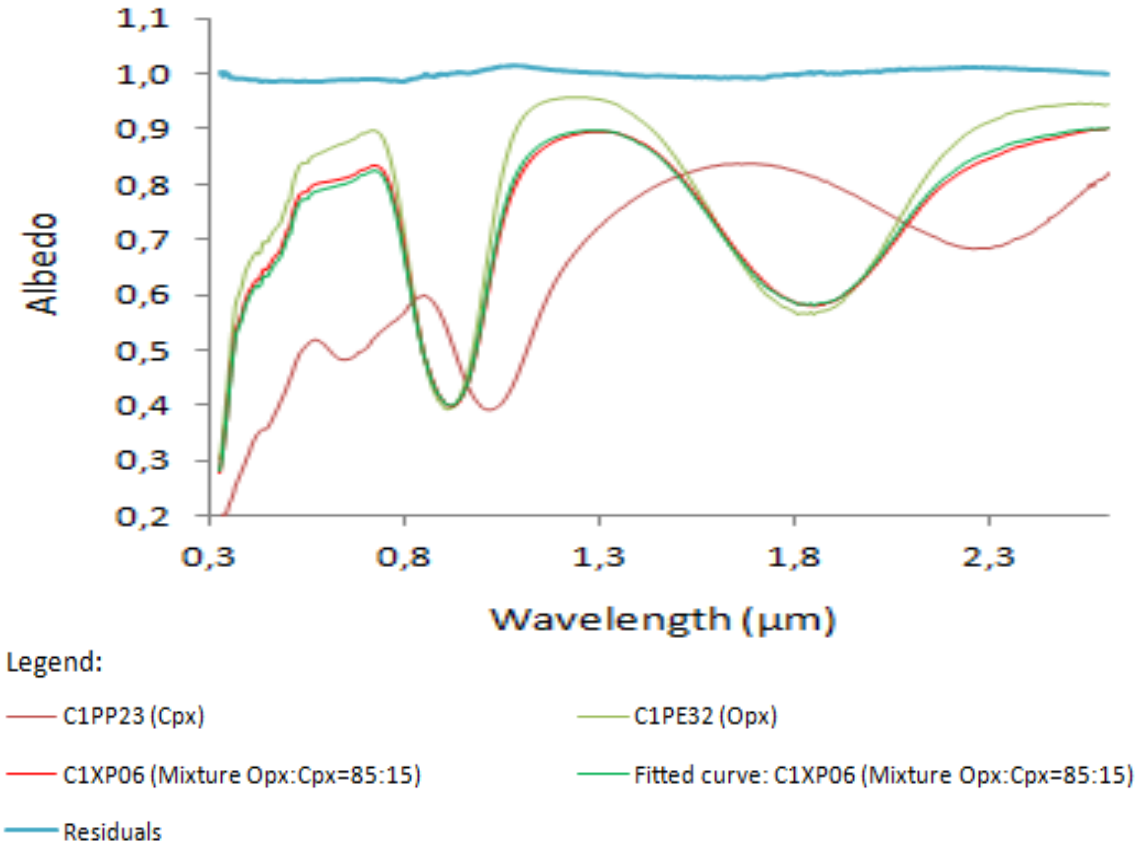


Fig.E37 - Derived albedo for the sample XP-CMP-006 (C1XP06) and for their extreme minerals PP-CMP-023 (C1PP23) and PE-CMP-032 (C1PP32) versus wavelength. The residuals were shifted vertically by one unity.

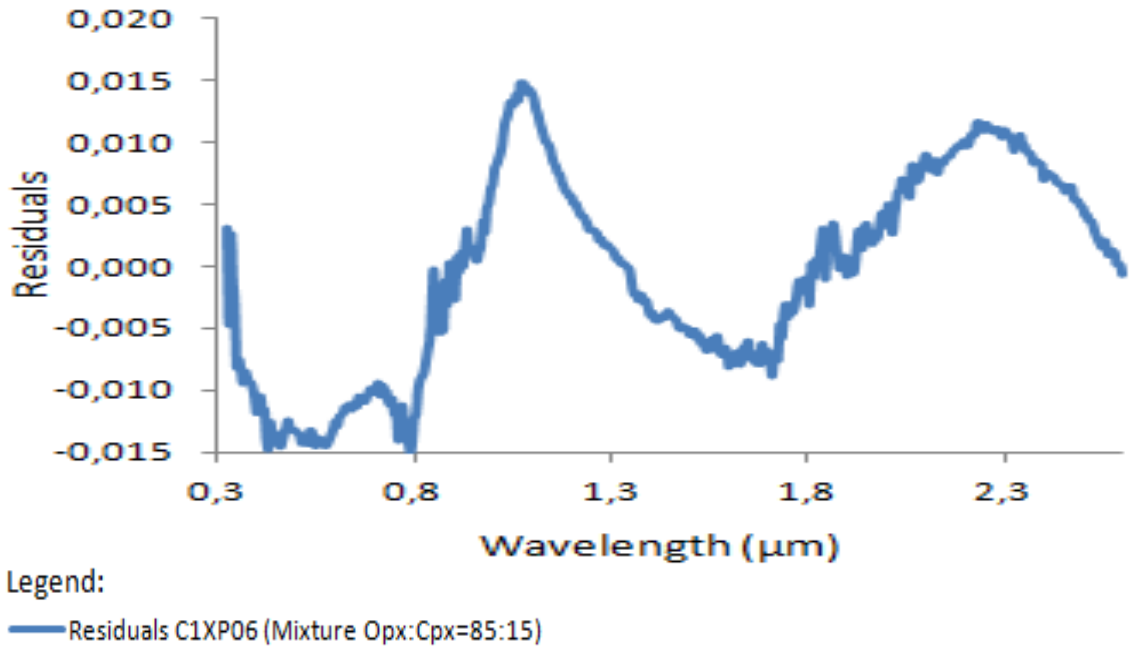


Fig.E38 - Plot of the residuals of the sample C1XP06.

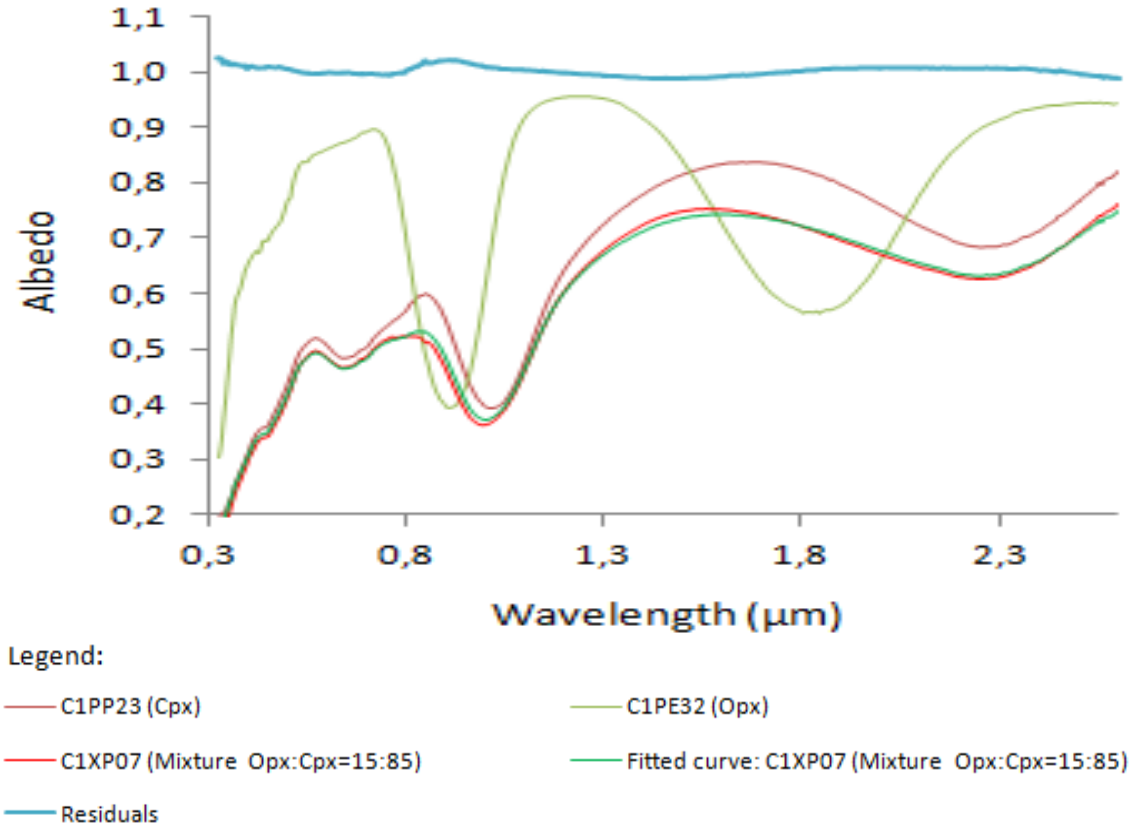


Fig.E39 - Derived albedo for the sample XP-CMP-007 (C1XP07) and for their extreme minerals PP-CMP-023 (C1PP23) and PE-CMP-032 (C1PP32) versus wavelength. The The residuals were shifted vertically by one unity.

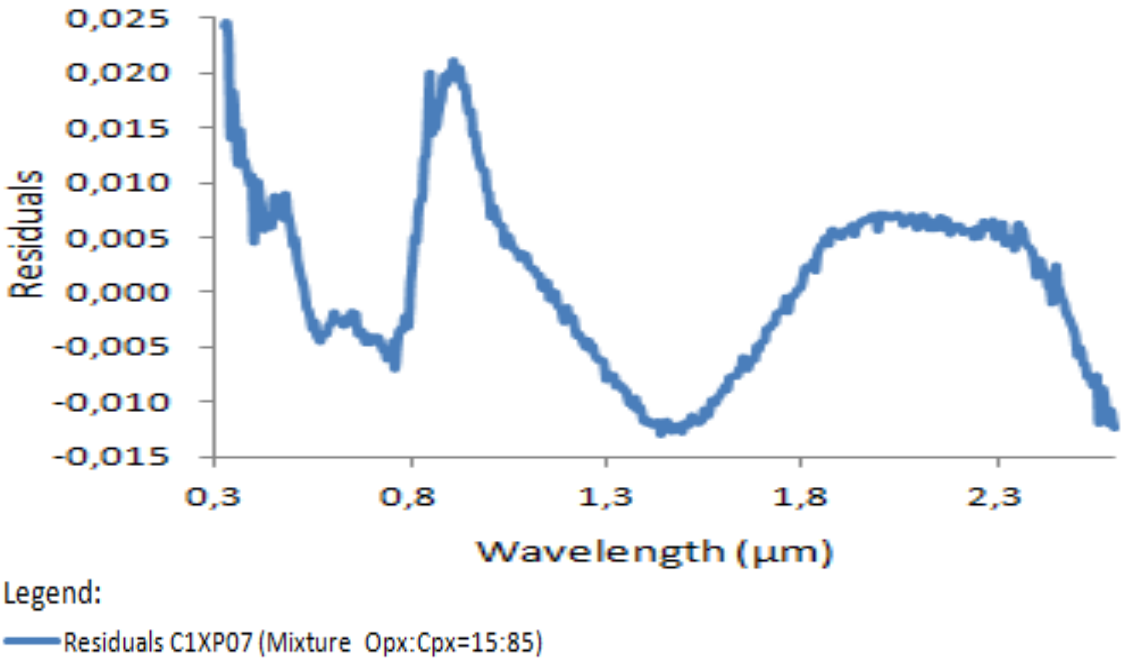


Fig.E40 - Plot of the residuals of the sample C1XP07.

U.PORTO
FACULDADE DE CIÊNCIAS
UNIVERSIDADE DO PORTO

# E.2. Figures of V-type Asteroids and HED Meteorites

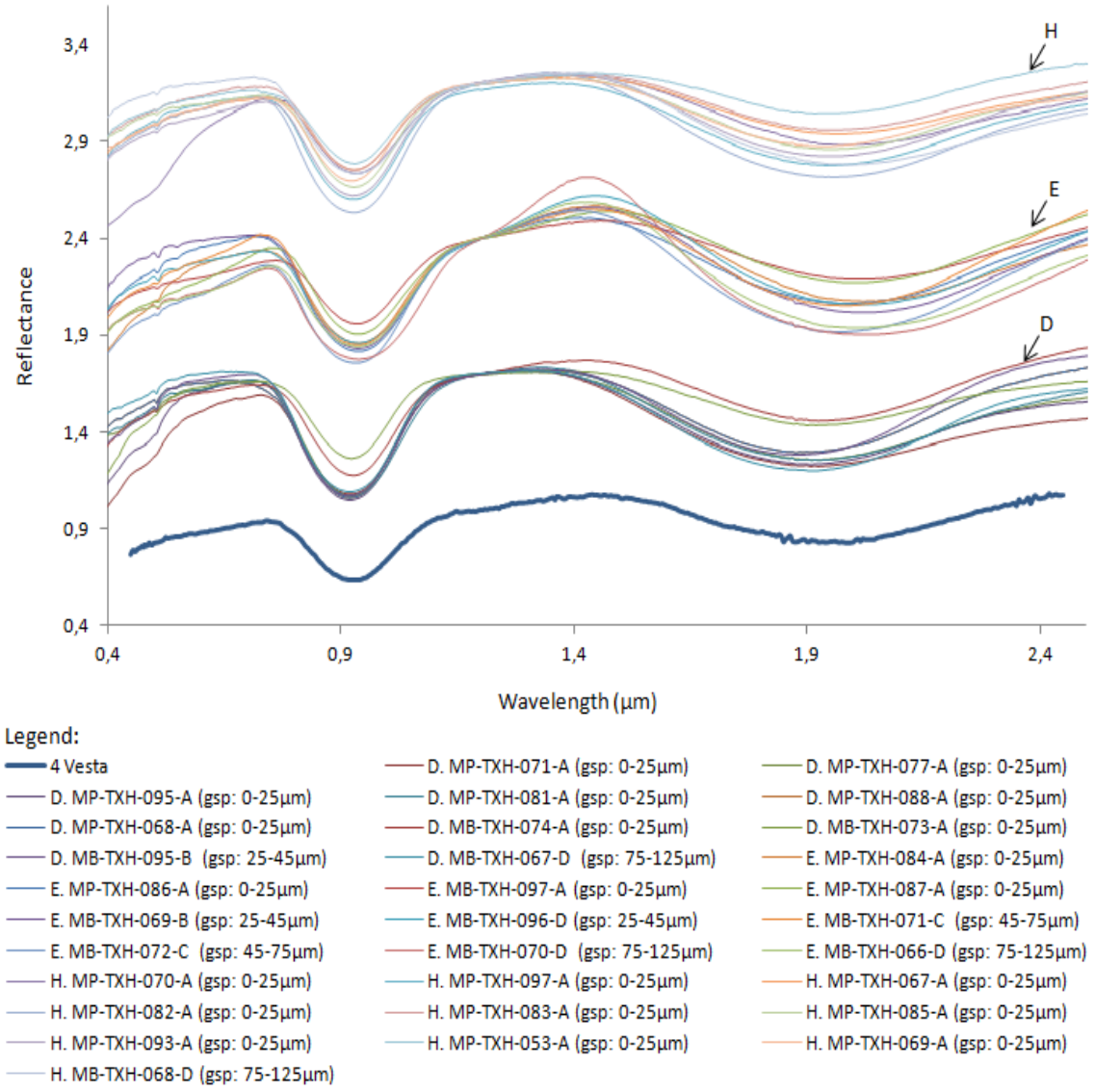


Fig.E41 - Unnormalized reflectance spectrum of 4 Vesta compared with the reflectance spectra of ten diogenites (D), ten eucrites (E) and ten howardites (H). Reflectance spectra of: diogenites (D) are shifted vertically by 0.7; eucrites (E) are shifted vertically by 1.2; howardites (H) are shifted vertically by 2.2. All spectra are normalized by the reflectance value at 1.2µm. The abbreviature "gsp" means grain size proportion.

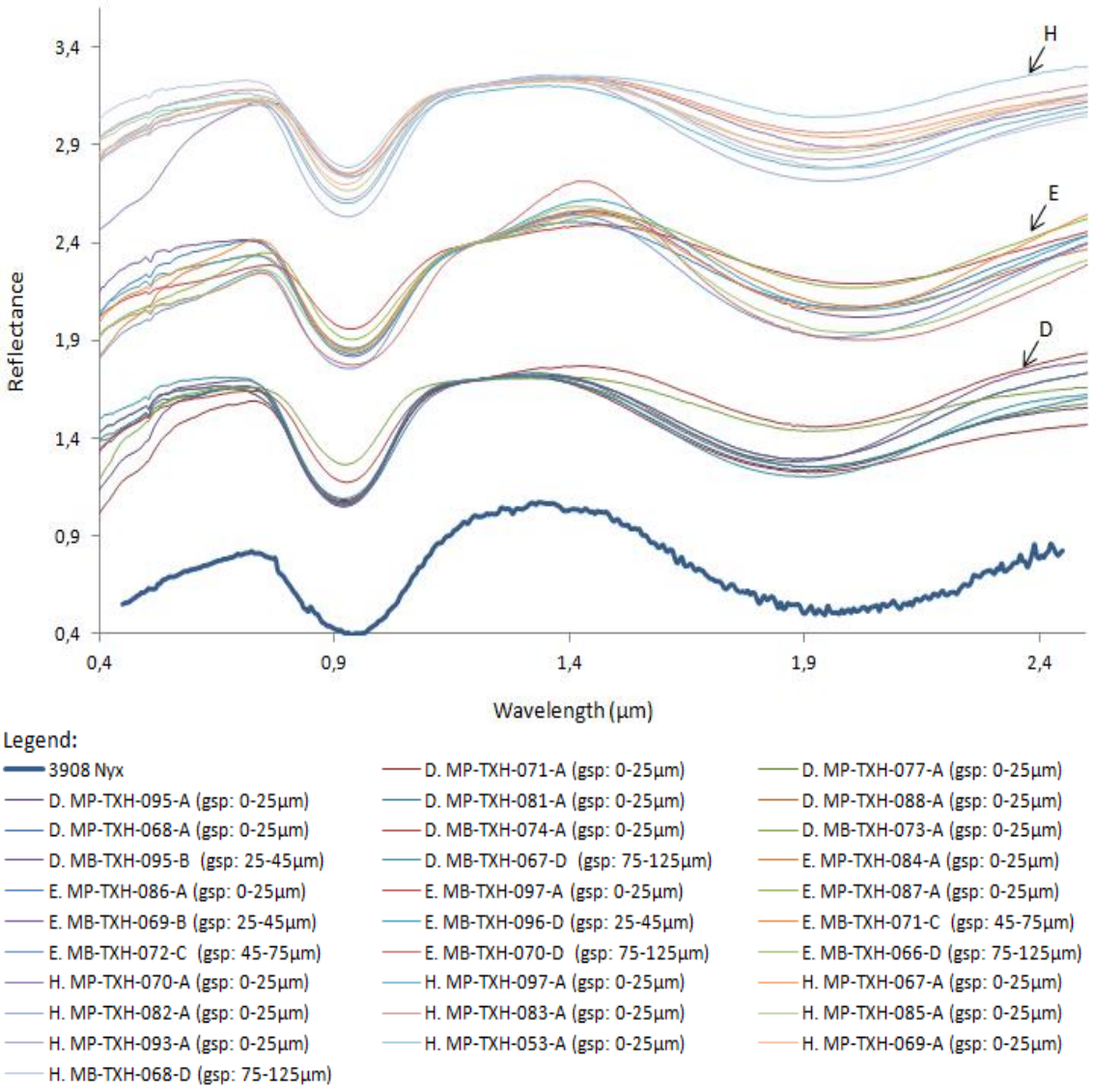


Fig.E42 - Unnormalized reflectance spectrum of 3908 Nyx compared with the reflectance spectra of ten diogenites (D), ten eucrites (E) and ten howardites (H). Reflectance spectra of: diogenites (D) are shifted vertically by 0.7; eucrites (E) are shifted vertically by 1.2; howardites (H) are shifted vertically by 2.2. All spectra are normalized by the reflectance value at 1.2µm. The abbreviature "gsp" means grain size proportion.

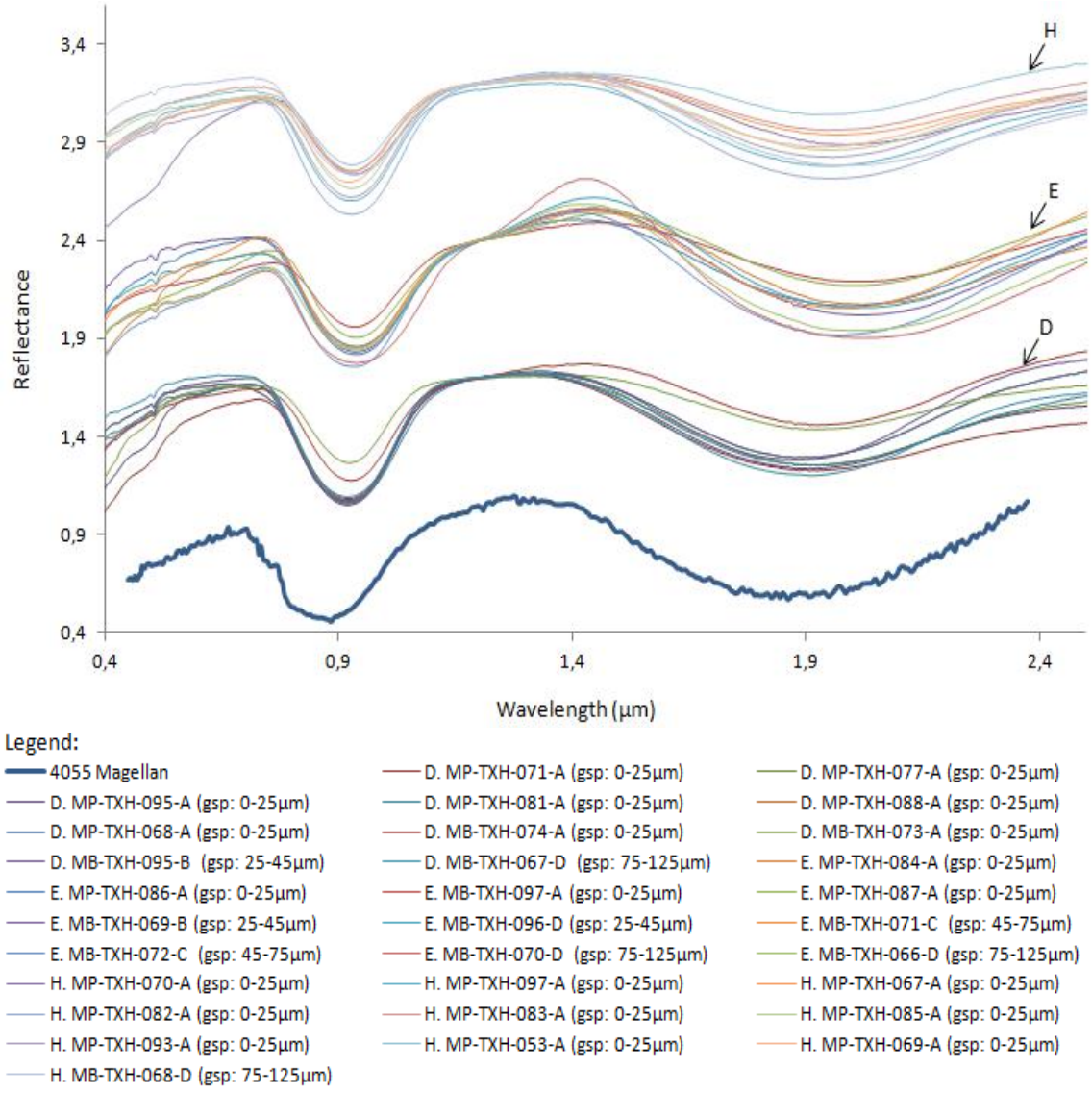


Fig.E43 - Unnormalized reflectance spectrum of 4055 Magellan compared with the reflectance spectra of ten diogenites (D), ten eucrites (E) and ten howardites (H). Reflectance spectra of: diogenites (D) are shifted vertically by 0.7; eucrites (E) are shifted vertically by 1.2; howardites (H) are shifted vertically by 2.2. All spectra are normalized by the reflectance value at 1.2µm. The abbreviature "gsp" means grain size proportion.

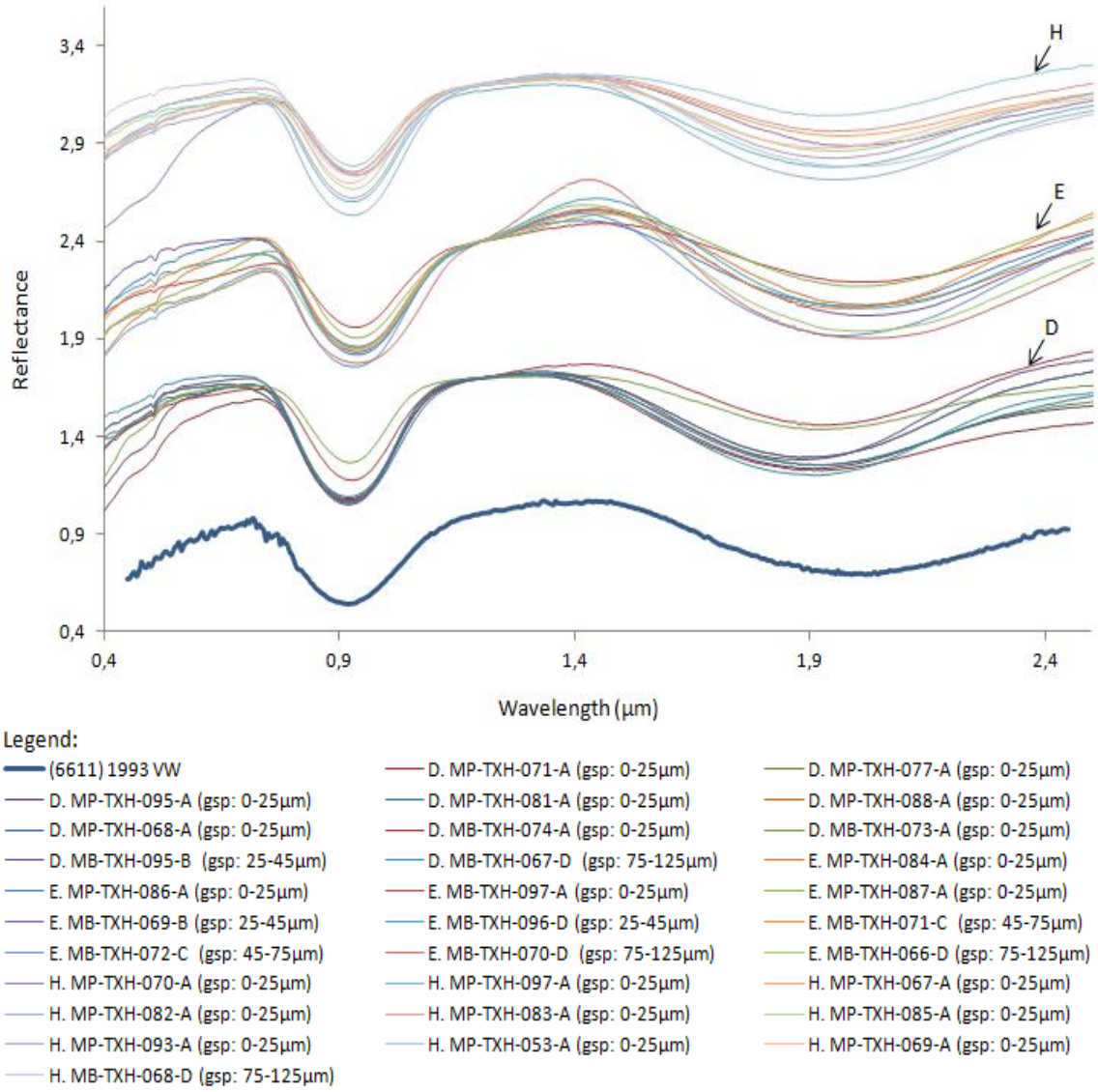


Fig.E44 - Unnormalized reflectance spectrum of (6611) 1993 VW compared with the reflectance spectra of ten diogenites (D), ten eucrites (E) and ten howardites (H). Reflectance spectra of: diogenites (D) are shifted vertically by 0.7; eucrites (E) are shifted vertically by 1.2; howardites (H) are shifted vertically by 2.2. All spectra are normalized by the reflectance value at 1.2µm. The abbreviature "gsp" means grain size proportion.

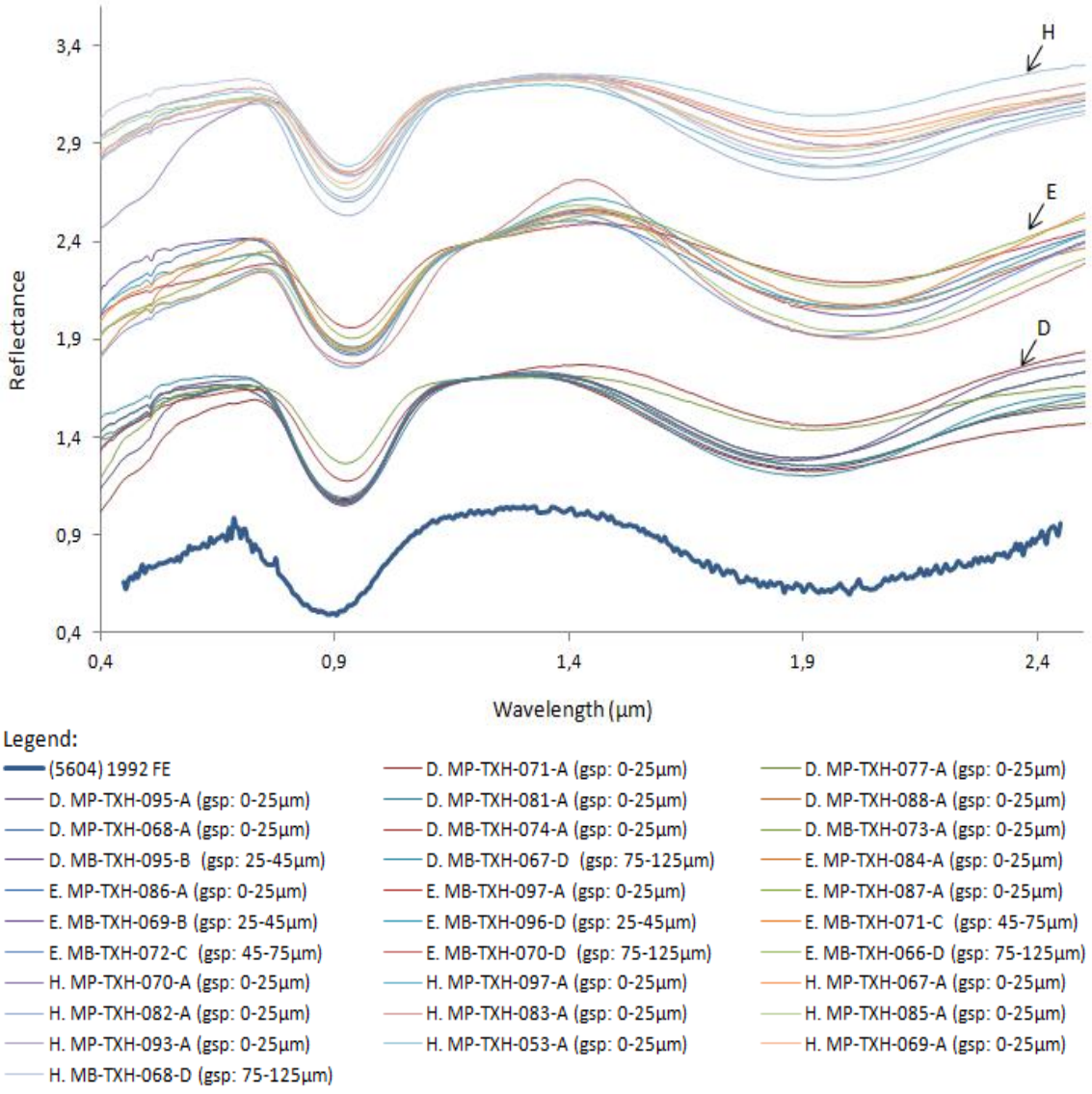


Fig.E45 - Unnormalized reflectance spectrum of (5604) 1992 FE compared with the reflectance spectra of ten diogenites (D), ten eucrites (E) and ten howardites (H). Reflectance spectra of: diogenites (D) are shifted vertically by 0.7; eucrites (E) are shifted vertically by 1.2; howardites (H) are shifted vertically by 2.2. All spectra are normalized by the reflectance value at 1.2µm. The abbreviature "gsp" means grain size proportion.

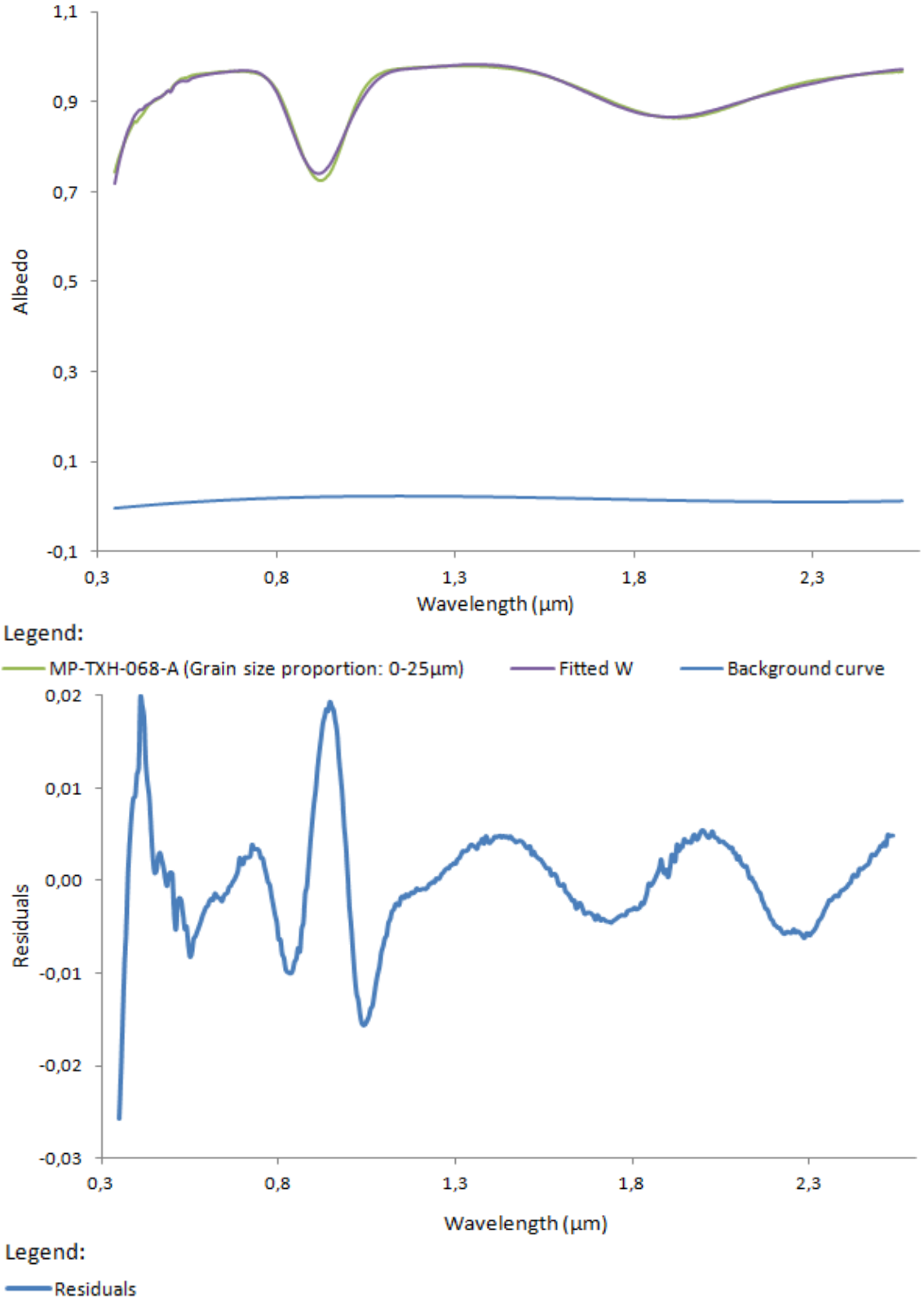


Fig.E46 – Top: Plot of the best fit obtained of a diogenite meteorite (sample MP-TXH-068-A). Down: Residuals plot of the fit of the sample MP-TXH-068-A.

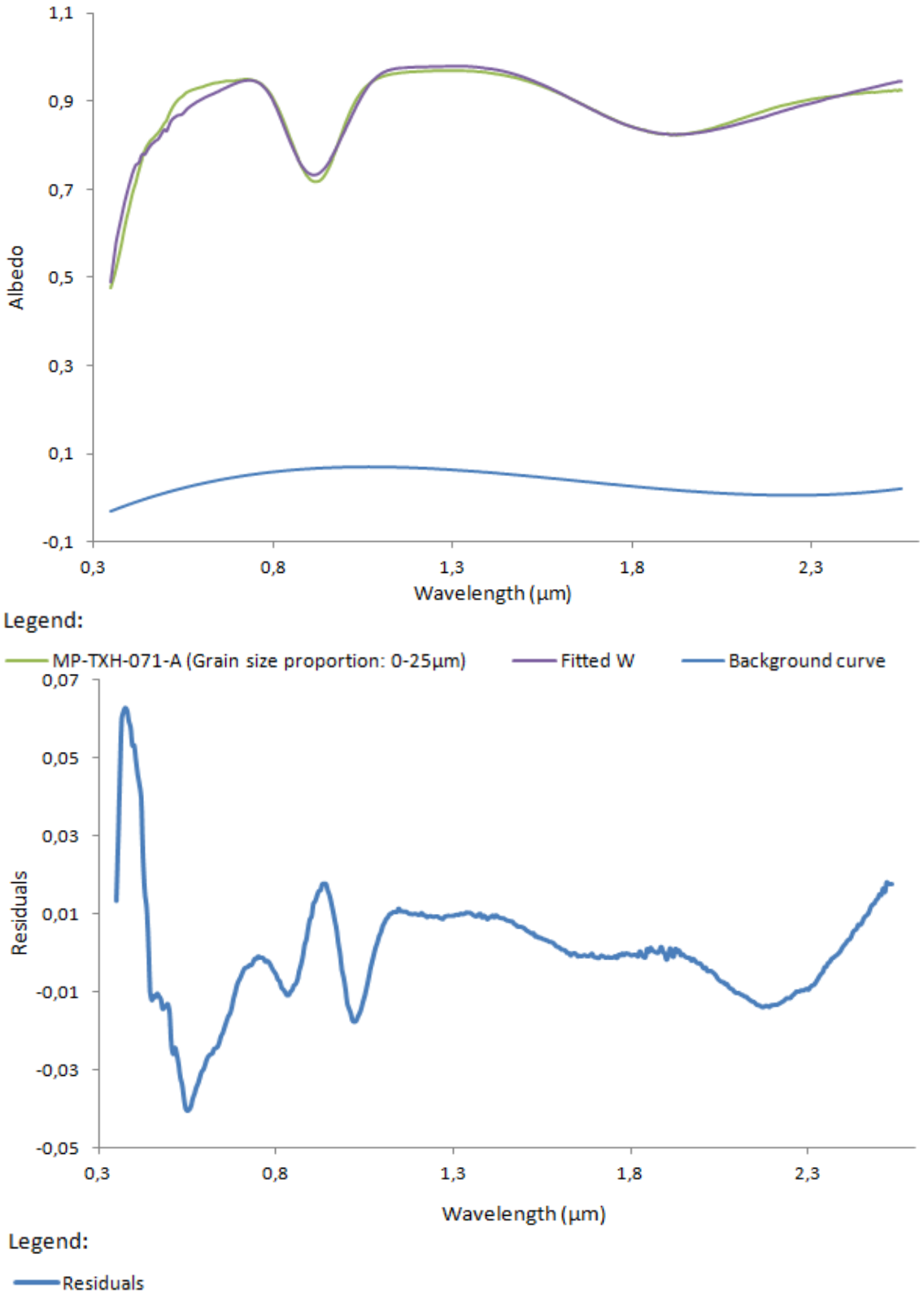


Fig.E47 – Top: Plot of the worst fit obtained of a diogenite meteorite (sample MP-TXH-071-A). Down: Residuals plot of the fit of the sample MP-TXH-071-A.

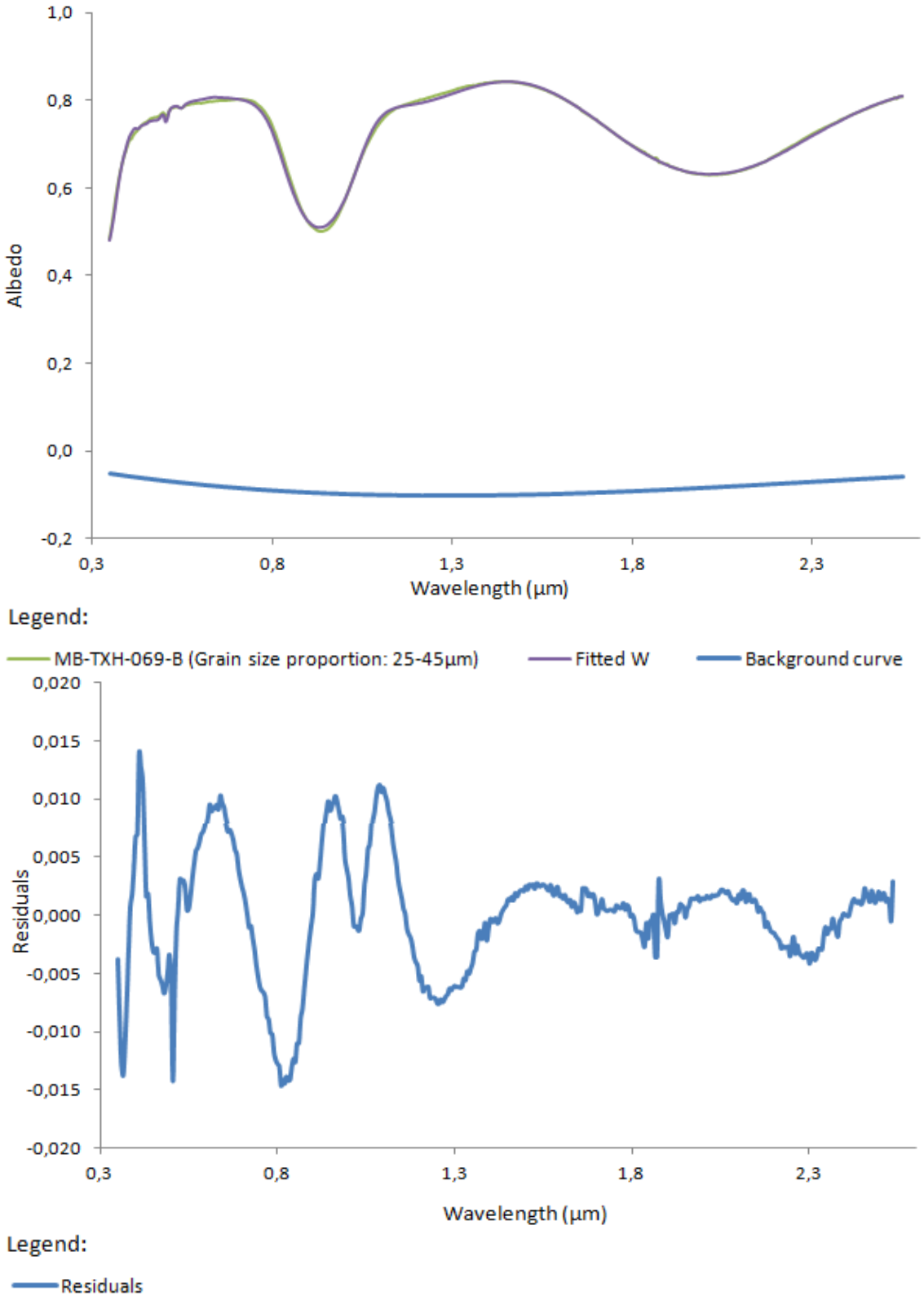


Fig.E48 – Top: Plot of the best fit obtained of a eucrite meteorite (sample MB-TXH-069-B). Down: Residuals plot of the fit of the sample MB-TXH-069-B.

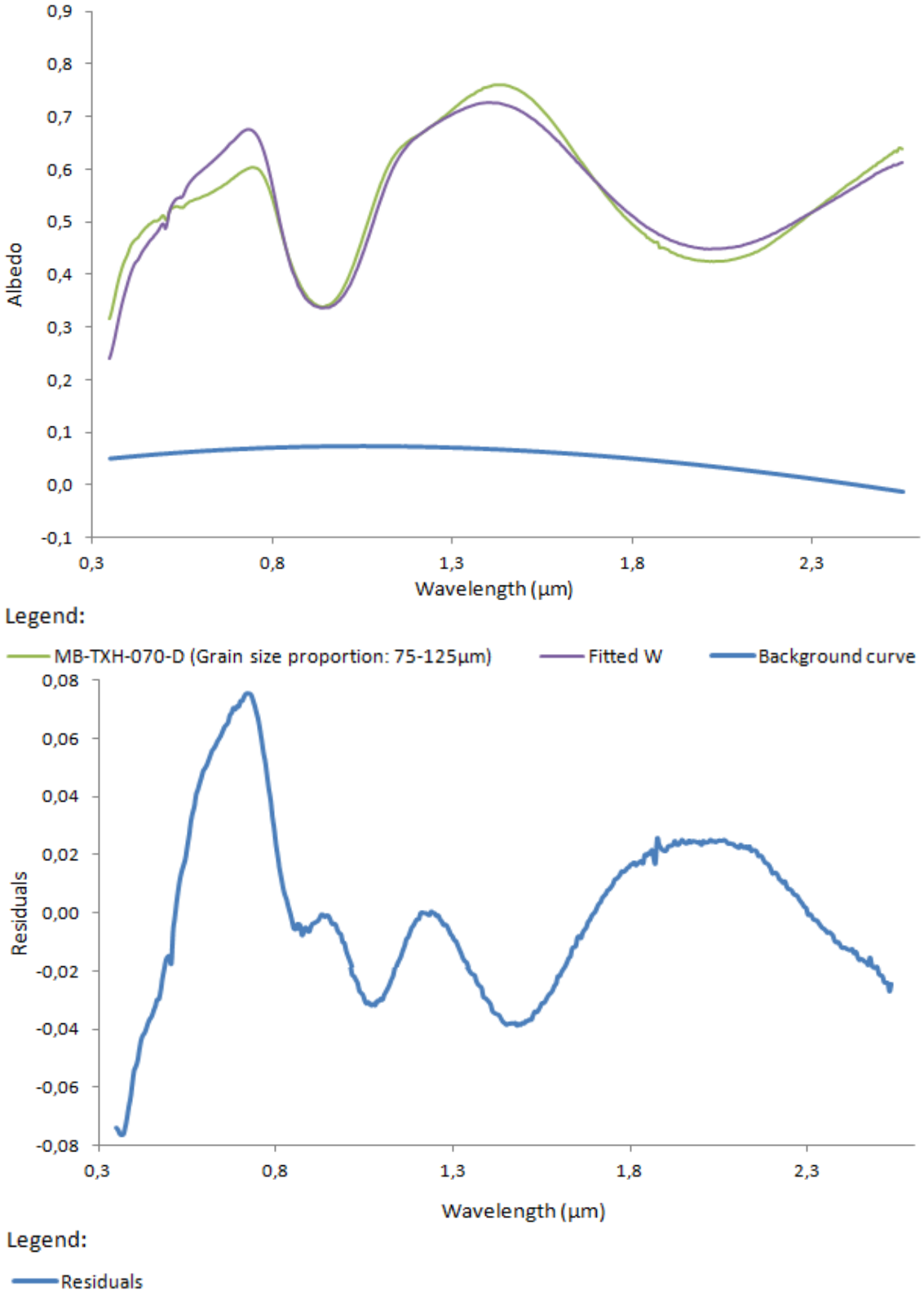


Fig.E49 - Top: Plot of the worst fit obtained of a diogenite meteorite (sample MP-TXH-070-D). Down: Residuals plot of the fit of the sample MP-TXH-070-D.

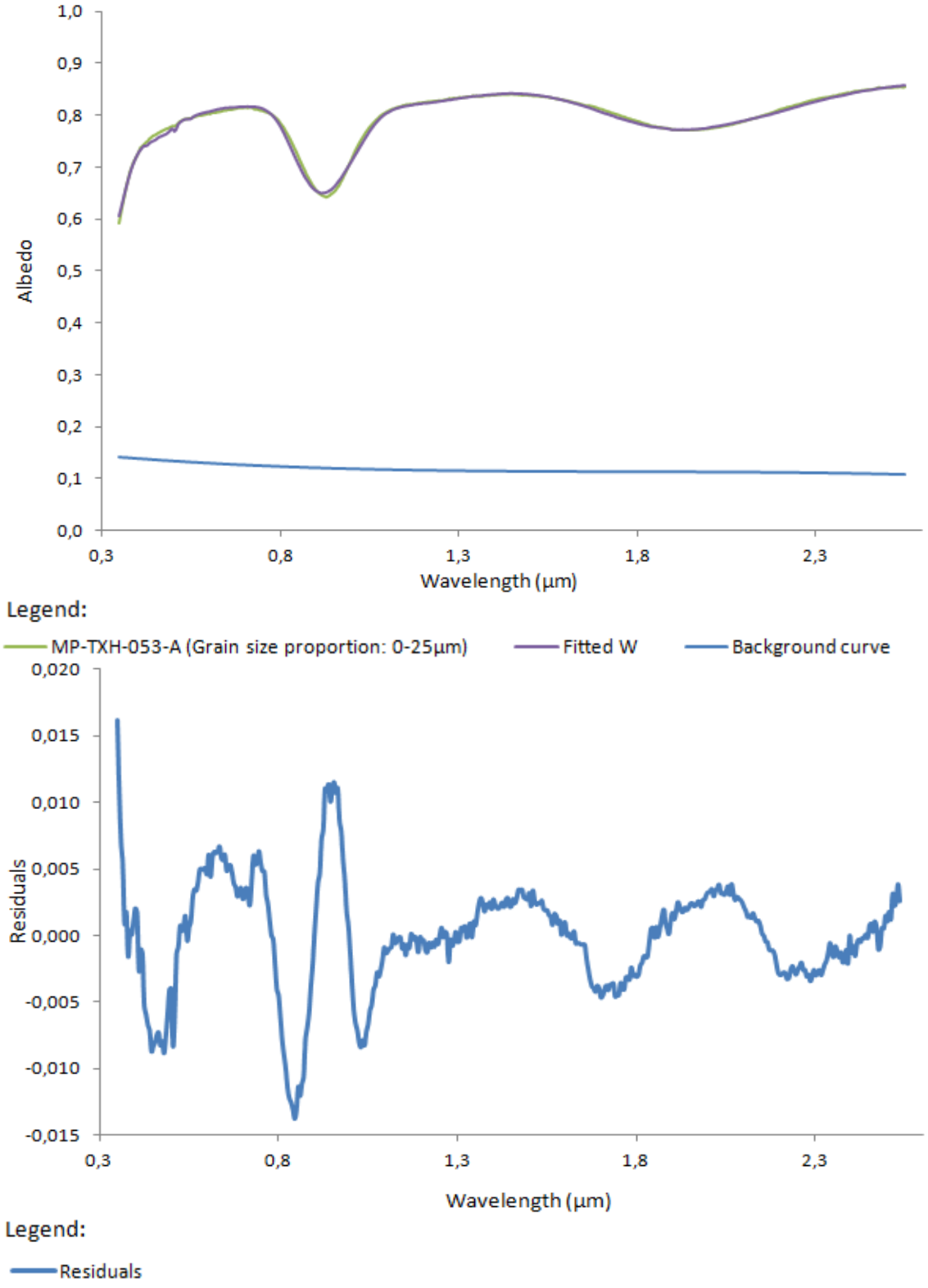


Fig.E50 - Top: Plot of the best fit obtained of a howardite meteorite (sample MB-TXH-053-A). Down: Residuals plot of the fit of the sample MB-TXH-053-A.

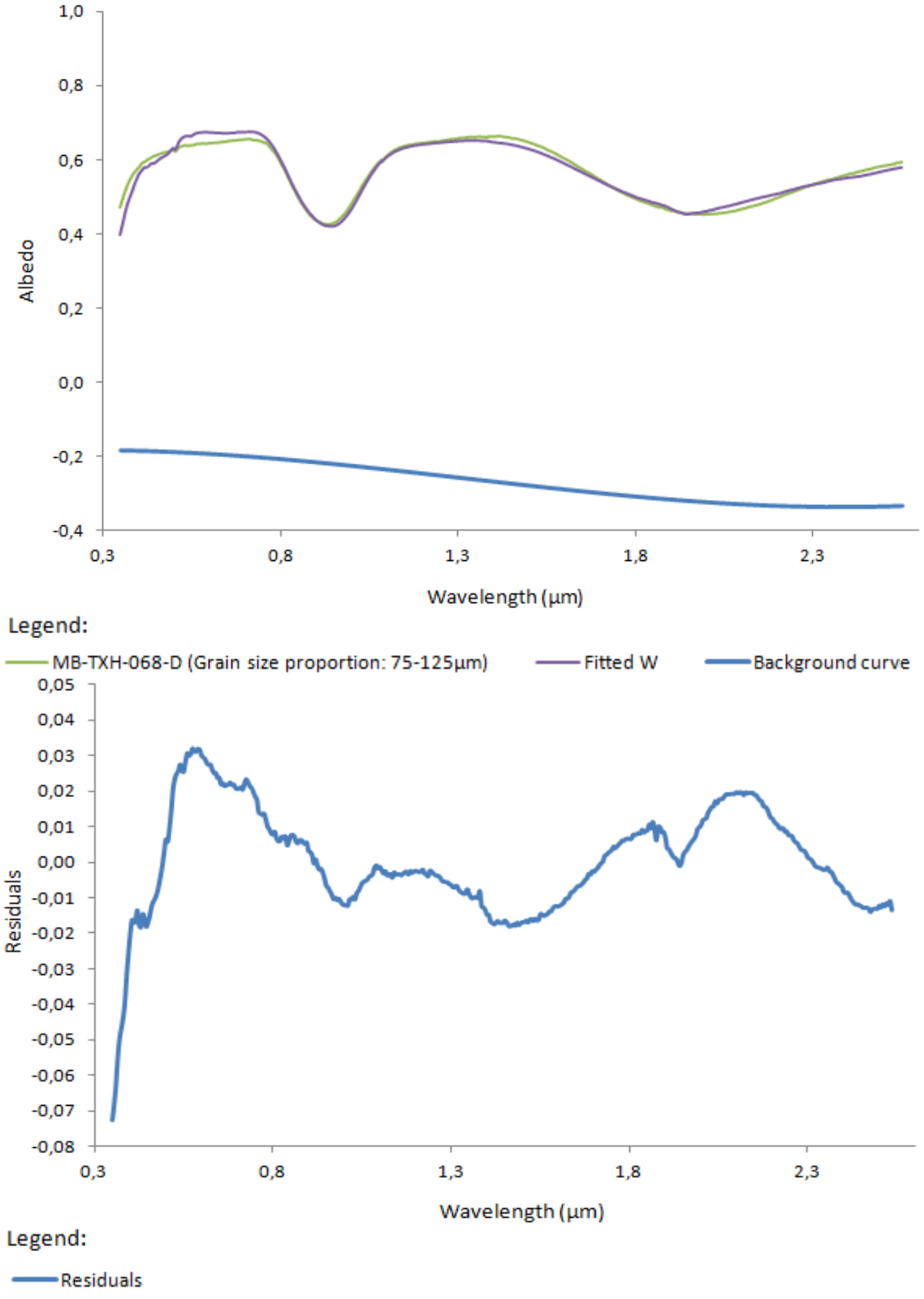


Fig.E51 - Top: Plot of the worst fit obtained of a howardite meteorite (sample MB-TXH-068-D). Down: Residuals plot of the fit of the sample MB-TXH-068-D.

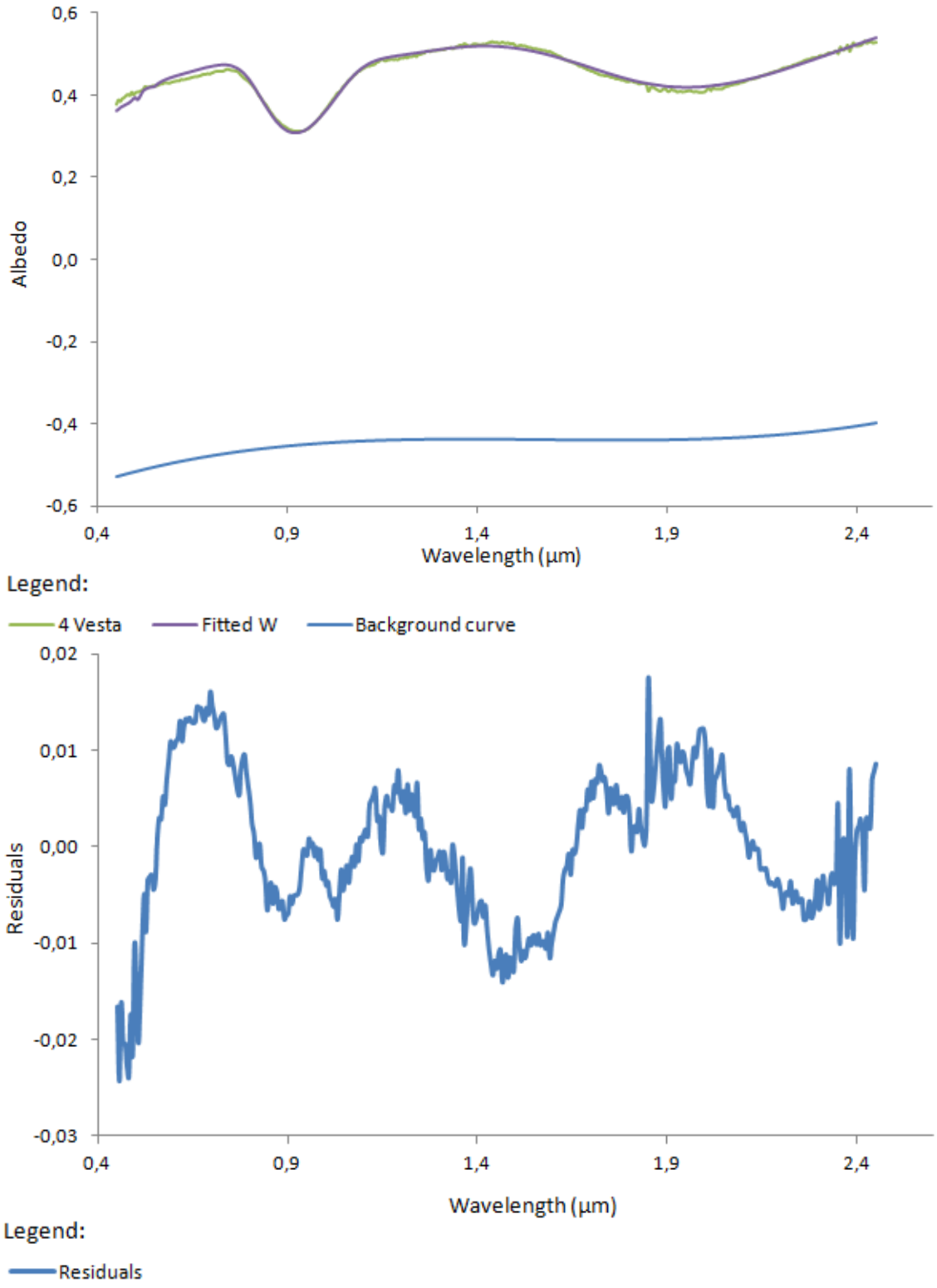


Fig.E52 - Top: 4 Vesta single scattering albedo and its modelled curve. Down: Residuals plot of the fit.

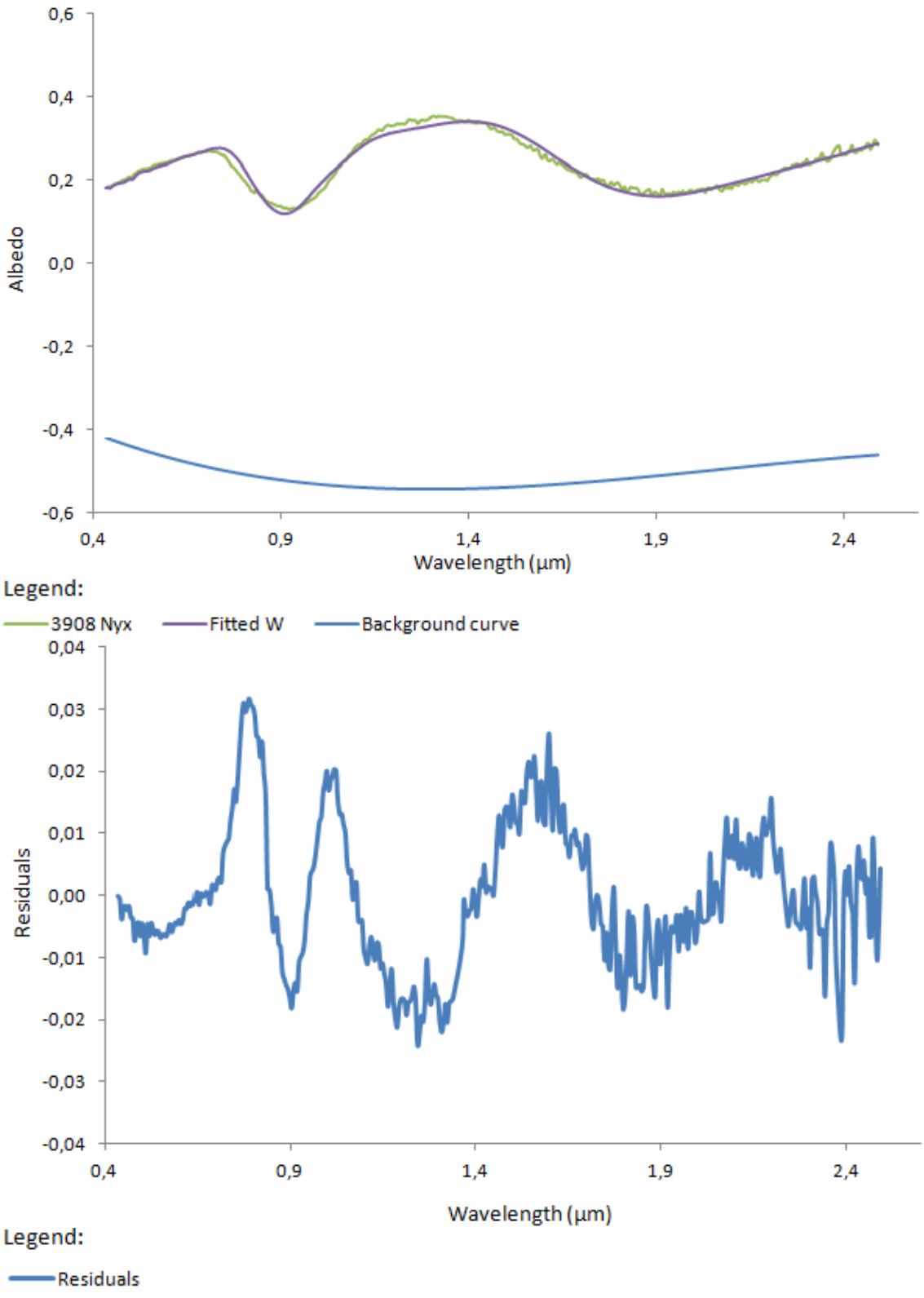


Fig.E53 - Top: 3908 Nyx single scattering albedo and its modelled curve. Down: Residuals plot of the fit.

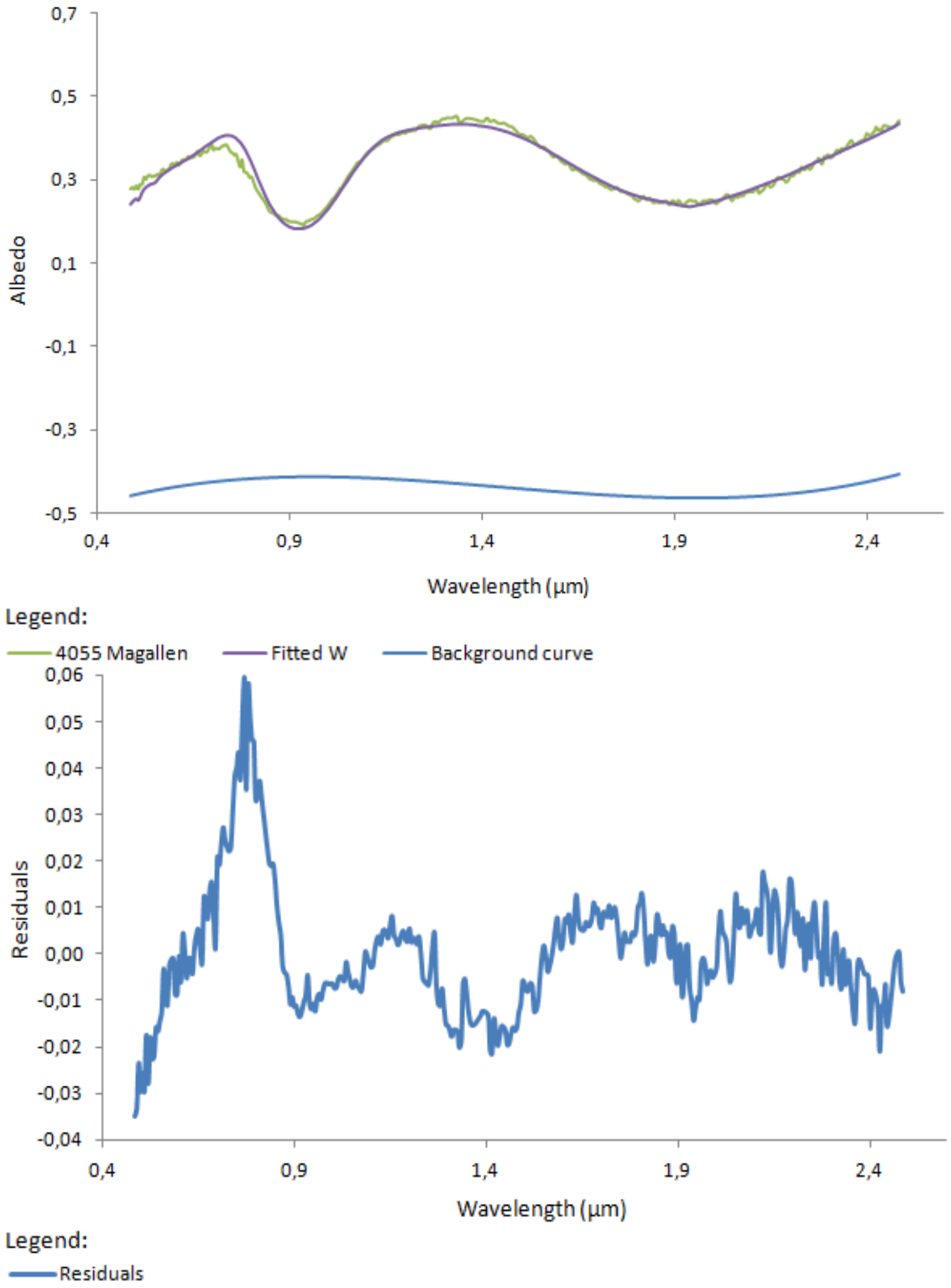


Fig.E54 - Top: 4055 Magellan single scattering albedo and its modelled curve. Down: Residuals plot of the fit.

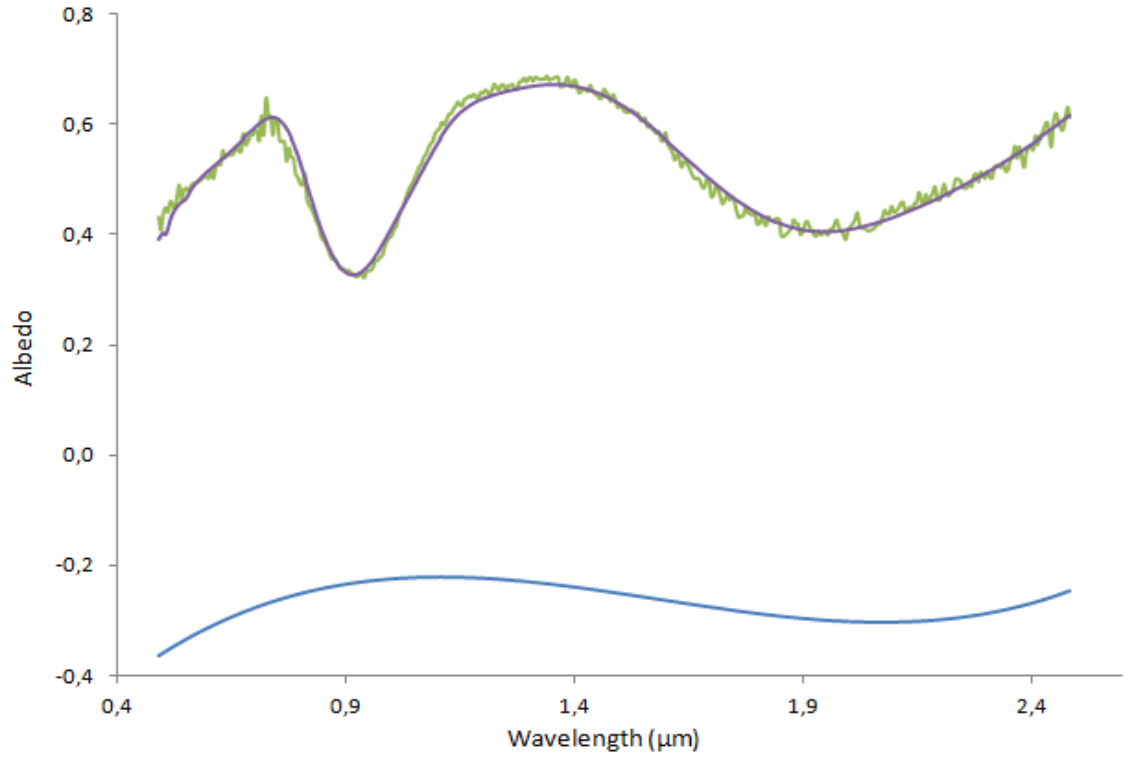


Legend:

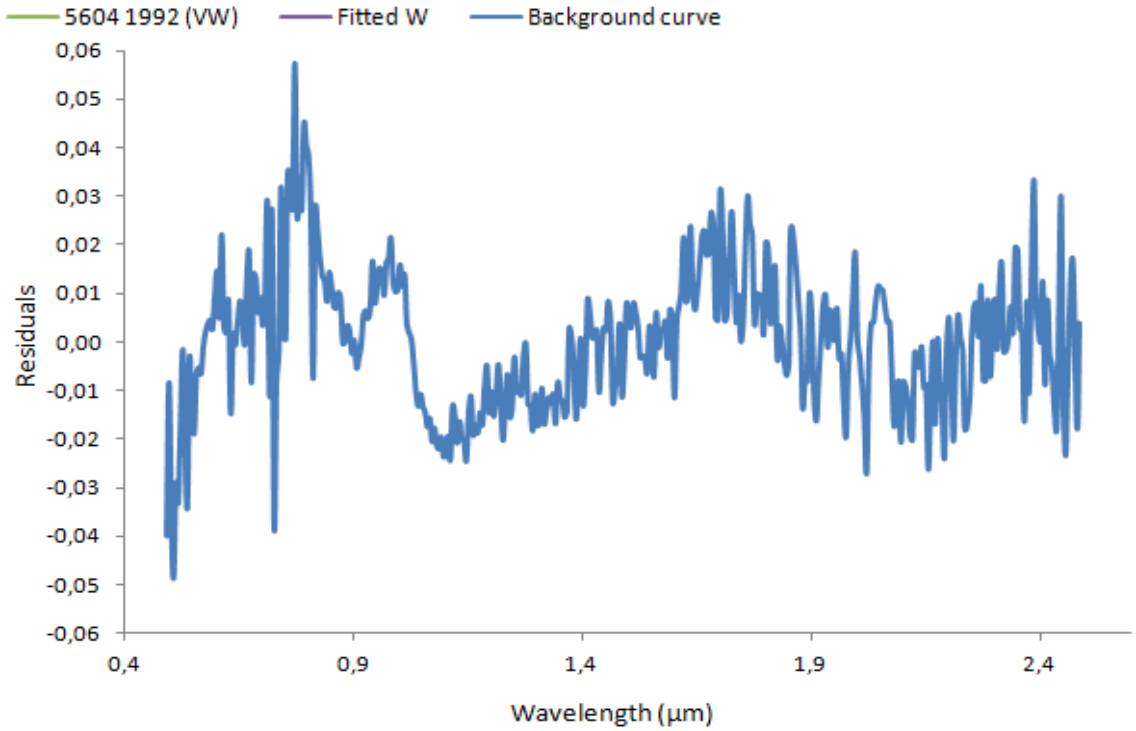


Legend:

Residuals

Fig.E55 - Top: 5604 (1992) FE single scattering albedo and its modelled curve. Down: Residuals plot of the fit.

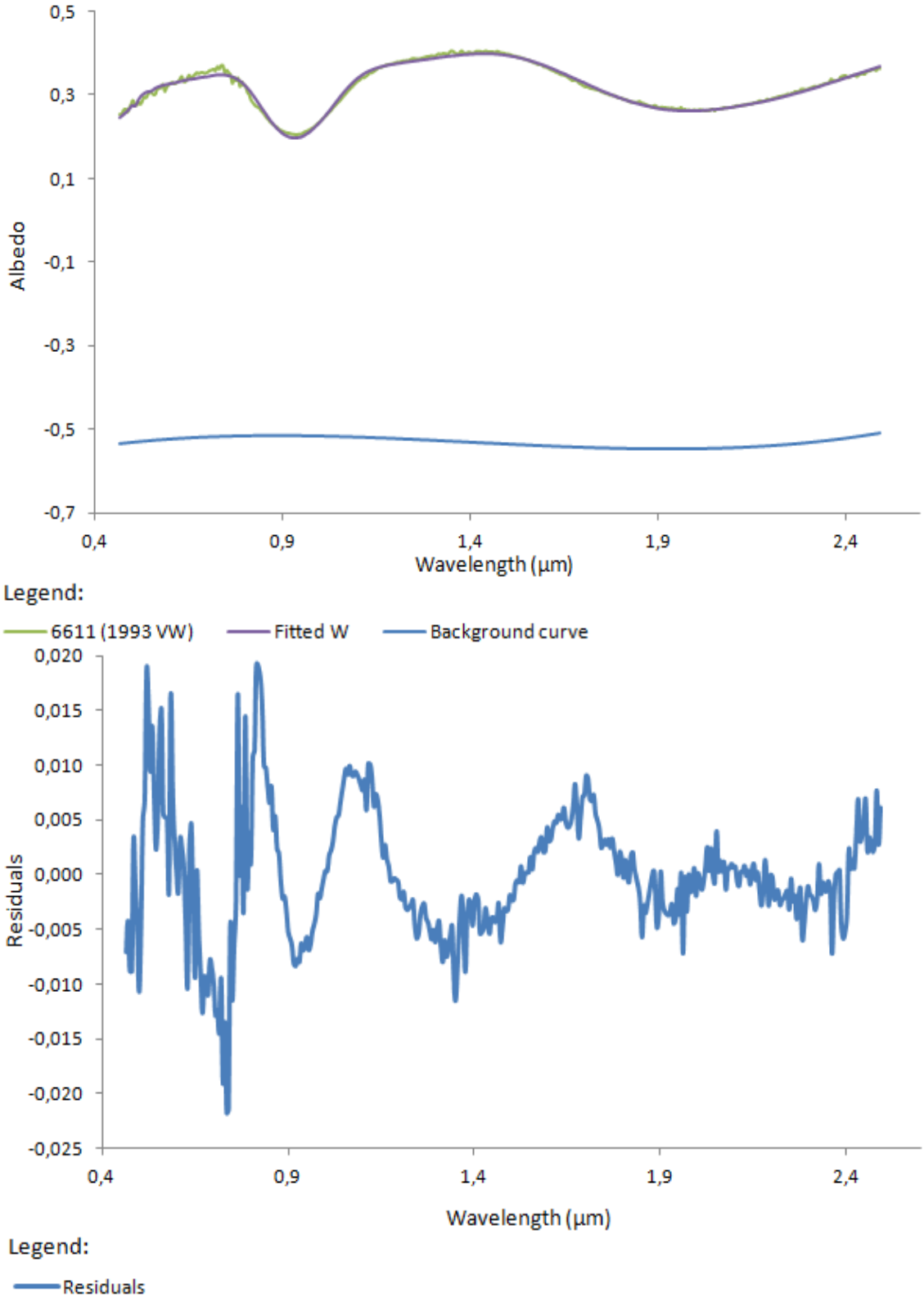


Fig.E56 – Top: 6611 (1993) VW single scattering albedo and its modelled curve. Down: Residuals plot of the fit.

U.PORTO
FACULDADE DE CIÊNCIAS
UNIVERSIDADE DO PORTO

# F. Communications and Extracurricular Internship

In this section, the absctracts of several communications in conferences and the abstract of the extracurricular internship PEEC will be presented. This section will be divided into three subsections: in the first subsection (F.1.), the abstracts of the poster communications will be presented; in the second subsection (F.2.), the absctract of the oral communication will be presented; in the third subsection (F.3.), the absctract of the extracurricular internship PEEC will be presented.

Three poster communications were made. The first poster communication was presented in the IJUP11 (Investigação Júnior da Universidade do Porto 2011) conference and was entitled “Laboratorial Characterization of Meteorites”. This conference took place at Reitoria da Universidade do Porto, between 17 and 19 of February of 2011. Further details about this conference are available at http://ijup.up.pt/2011/. The second poster communication was presented in the XXI ENAA (Encontro Nacional de Astronomia e Astrofísica) conference and was entitled “Laboratorial Characterization of a Campo del Cielo meteorite”. This conference took place at Observatório Astronómico da Universidade de Coimbra, between 7 and 10 of September of 2011. Further details about this conference are available at http://www.uc.pt/congressos/xxienaa. The third poster communication was presented in the IJUP2012 (Investigação Júnior da Universidade do Porto 2012) conference and was entitled “The early stages of the Solar System: constraints from the small icy worlds”. This conference took place at Reitoria da Universidade do Porto, between 22 and 24 of February of 2011. Further details about this conference are available at http://ijup.up.pt/.

The oral communication was presented in the Física2012 conference and was entitled “Mineralogy of V-type near-earth objects”. This conference took place at Universidade de Aveiro between 6 and 8 of September of 2012. Further details about this conference are available at http://www.spf.pt/fisica2012/index.html.

The extracurricular internship was inserted in the 3rd edition of the PEEC (Plano de Estágios Extracurriculares da Faculdade de Ciências da Universidade do Porto) and took place at Departamento de Física e Astronomia da Faculdade de Ciências da

Universidade do Porto, between 1 of February of 2011 and 31 of July of 2011. This extracurricular internship was entitled “Caracterização Laboratorial de Meteoritos”.

U.PORTO
FACULDADE DE CIÊNCIAS
UNIVERSIDADE DO PORTO

# F.1. Abstracts of Poster Communications in Conferences

## F.1.1. Abstract of the Poster Communication in the IJUP11 Conference (17-19 February 2011)

### Laboratorial characterization of meteorites

**S. Batista [1] and T. M Seixas [1]**

[1] Department of Physics and Astronomy, Faculty of Science, University of Porto, Portugal.

Asteroids represent the sole surviving population of early inner solar-system planetesimals [1-2]. They have not formed a planet due to Jupiter's gravity influence and fragmentation produced by several collisions with other asteroids. Nowadays, asteroids provide our only *in situ* record of the conditions and processes that the inner portions (~1.8-3.5 AU) of the late solar nebulae and the infant solar system have experienced [1]. Several advances in our knowledge of the diversity of asteroid mineralogies have been made since the beginning of the use of charge-coupled device (CCD) detectors to obtain the visible and nIF reflectance spectra of small objects [3]. The bulk composition, mineralogy and petrology of a meteorite are functions of the original bulk composition of its parent body and the conditions of heating and melting that it has experienced during its formation.

Our aim in this work is to study several meteorites of different types for investigating meteorite processes and the associated thermophysical history. In a first step, thin sections of the meteorites will be prepared for optical mineralogy studies and electron microprobe analysis. These thin sections will be taken from a layer below the exposed fusion crust. In a second step, powder samples are to be prepared by milling slices of the original meteorites for X-ray diffractometry. In a third step, thin sections previously prepared will be analysed by optical mineralogy using a petrographic microscope, allowing the identification of the component minerals and their microtexture. Electron microprobe analysis in the same samples will help to complement this information by providing chemical composition profiles along selected paths such as grains boundaries, shearing planes and chondrules internal structures. Finally, X-ray diffractometry on powder samples will be performed in order to determine the crystal structure of the constituent phases and to discriminate eventual polymorphic phases.

References:

[1] Gaffey, M.J., Cloutis, E.A., Kelley, M.S., Reed, K.L. (2002), *Mineralogy of asteroids*. In: Bottke, W.F., Cellino, A., Paolicchi, P., Binzel, R.P. (Eds.), Asteroids III. University of Arizona Press, Tucson, pp. 183–204.
[2] Safronov, V. S. (1969), *Evolution of the Protoplanetary Cloud and Formation of the Earth and Planets*, Moscow: Nauka; English transl. NASA TTF-677 [1972].
[3] Burbine T. H., McCoy T. J., Meibom A., Gladman B., Keil K. (2002), *Meteoritic parent bodies: Their number and identification*. In: Bottke, W. F. Jr., Cellino, A., Paolicchi, P., Binzel, R. P. (Eds), Asteroids III. University of Arizona Press, Tucson, pp. 653–667.

U.PORTO
FACULDADE DE CIÊNCIAS
UNIVERSIDADE DO PORTO

# F.1.2. Abstract of the Poster Communication in the XXIENAA Conference (7-10 September 2011)

## LABORATORIAL CHARACTERIZATION OF A *CAMPO DEL CIELO* METEORITE

S. Batista[1], T. M. Seixas[1], M. A. Salgueiro da Silva[1], A. B. Lopes[2], J. M. Vieira[2], B. Almeida[2], D. Flores[3] and F. Noronha[3]

[1] *Department of Physics and Astronomy, Faculty of Science, University of Porto, Rua do Campo Alegre 687, 4169-007 Porto, Portugal*
[2] *Department of Ceramics and Glass Engineering/CICECO, University of Aveiro, Campus de Santiago, 3810-193 Aveiro, Portugal*
[3] *Department of Geosciences, Environment and Land Management, Faculty of Science, University of Porto, Rua do Campo Alegre 687, 4169-007 Porto, Portugal*

**Session:** Sun, stars and planets — **Communication:** Poster

**Abstract:** During the last few years, the number of known meteorites is rapidly growing up through the discovery of large concentrations of meteorites in cold [1] and hot deserts [2]. Meteorites are bodies that were fragmented due to several collisions from their parent body or were completely shielded by cosmic rays from their source body [3]. A parent body, which can be an asteroid or a comet, is the body from which the meteorite acquired its current chemical composition and mineralogical characteristics [3]. The bulk composition, mineralogy and petrology that a meteorite acquires, are functions of the original bulk composition of its parent body and the conditions of heating and melting that it has experienced during its formation. Mineralogy, texture and chemical composition of meteorites are essential for their classification and provide us important clues about the planet formation processes as well as important keys towards the main processes occurred on the evolution of the solar nebula [4].

Nowadays, asteroids represent the sole surviving population of early inner solar-system planetesimals [5-6]. Asteroids provide our only *in situ* record of the conditions and processes that the inner portions (~1.8-3.5 AU) of the late solar nebulae and the infant solar system have experienced [4]. Several advances in our knowledge about the diversity of asteroidal mineralogies have been made since the beginning of the use of charge-coupled device (CCD) detectors to obtain the visible and NIF reflectance spectra of small objects [3].

Our aim in this work is to study a meteorite recovered in *Campo del Cielo* (Argentina) for investigating meteorite processes and the associated thermophysical history. For this purpose, thin sections were taken from a layer below the exposed fusion crust and were prepared for optical mineralogy and electron microprobe analysis. Exploratory XRD measurements were performed at room temperature, in order to identify the component mineral phases. Here we report results of this study including a preliminary classification of this meteorite.

U.PORTO
FACULDADE DE CIÊNCIAS
UNIVERSIDADE DO PORTO

**References:**

[1] Sephton, M. A.; Bland, P. A.; Pillinger, C. T.; Gilmou, I., *The preservation state of organic matter in meteorites from Antarctica.*, Meteoritics & Planetary Science, Vol. 39, No. 5, p.747-754.
[2] Bischoff, A. & Geiger, T. (1995), *Meteorites for the Sahara: Find locations, shock classification, degree of weathering and pairing.*, Meteoritics (ISSN 0026-1114), vol. 30, no. 1, p. 113-122.
[3] Burbine T. H., McCoy T. J., Meibom A., Gladman B., Keil K. (2002), *Meteoritic parent bodies: Their number and identification*. In: Bottke, W. F. Jr., Cellino, A., Paolicchi, P., Binzel, R. P. (Eds), Asteroids III. University of Arizona Press, Tucson, pp. 653–667.
[4] P. Vernazza, R. P. Binzel, A. Rossi, M. Fulchignoni, M. Birlan, *Solar wind as the origin of rapid reddening of asteroid surfaces*, Nature 458 (2009) 993-95.
[5] Gaffey, M.J., Cloutis, E.A., Kelley, M.S., Reed, K.L. (2002), *Mineralogy of asteroids*. In: Bottke, W.F., Cellino, A., Paolicchi, P., Binzel, R.P. (Eds.), Asteroids III. University of Arizona Press, Tucson, pp. 183–204.
[6] Safronov, V. S. (1969), *Evolution of the Protoplanetary Cloud and Formation of the Earth and Planets*, Moscow: Nauka; English transl. NASA TTF-677 [1972].

U.PORTO
FACULDADE DE CIÊNCIAS
UNIVERSIDADE DO PORTO

## F.1.3. Abstract of the Poster Communication in the IJUP12 Conference (22-24 February 2012)

# The early stages of the Solar System Evolution: constraints from the small icy worlds

**S. Batista[1,2,3] R. Albuquerque[1,3] and T. Seixas[1,3]**

[1] Department of Physics and Astronomy, Faculty of Sciences, University of Oporto, Portugal

[2] Department of Mathematics, Faculty of Sciences, University of Oporto, Portugal

[3] Center for Geophysics of the University of Coimbra, University of Coimbra, Portugal

The birth environment of the Sun has been subject of several studies [1]. It known that stars born in clusters [2], as it is thought the Sun also did [3]. Nowadays, the architecture of the Solar System is well known: its eight planets and the small icy worlds, which are sculpted by the force of gravity and by the phenomenon of resonances [4]. However, understanding several steps in the early Solar System is a puzzling task. In this scenario, asteroids provide our only *in situ* record of the conditions and processes that the inner portions (~1.8-3.5 AU) of the late solar nebula and the infant solar system have experienced [5]. In addition, comets can also play an important role in this scenario. However, the only way that Humankind can access this material is thought meteorites, i.e extraterrestrial material that comes from the small icy worlds such as asteroids or comets. Trying to link a specific meteorite with a particular asteroid or class of asteroids can help us to understand a bit better the early stages of our Solar System. Actually, as the number of known exoplanets has recently been increasing in the last decade [6], understanding the steps evolved in the formation and evolution of the Solar System can then be extrapolated to understand others planetary systems.

Our aim in this work is to try to establish possible genetic linkages between asteroids and meteorites [7]. We hope to link a specific meteorite to a certain parent or source body. For this purpose, the reflectance spectra of meteorite samples will be compared to spectra of known asteroids available at the Brown University RELAB database.

References:

[1] Adams, F. C. (2010), *The Birth Environment of the Solar System*, ARAA, 48, 47-85

[2] Lada, C. J. and Lada, E. A. (2003), *Embedded Clusters in Molecular Clouds*, ARAA, 41, 57-115

[3] Bobylev, V., V., Bajkova, A. T., Myllari, A. and Valtonen, M. (2010), *Searching for possible siblings of the sun from a common cluster based on stellar space velocities*, Astronomy Letters, 37, 8, 550-562

[4] Jewitt, D. (2009), *Icy bodies in the New Solar System*, Proceedings of the International Astronomical Union, IAU Symposium, 263, 3-16

[5] Gaffey, M.J., Cloutis, E.A., Kelley, M.S., Reed, K.L. (2002), *Mineralogy of asteroids*. In: Bottke, W.F., Cellino, A., Paolicchi, P., Binzel, R.P. (Eds.), Asteroids III. University of Arizona Press, Tucson, pp. 183–204.
[6] Butler, R. P., Wright, J. T., Marcy, G. W., Fischer, D. A., Vogt, S. S., Tinney, C. G., Jones, H. R. A., Carter, B. D., Johnson, J. A., McCarthy, C., Penny, A. J. (2006), *Catalog of nearby Exoplanets*, ApJ, 646, 1, 505-522
[7] Burbine T. H., McCoy T. J., Meibom A., Gladman B., Keil K. (2002), *Meteoritic parent bodies: Their number and identification*. In: Bottke, W. F. Jr., Cellino, A., Paolicchi, P., Binzel, R. P. (Eds), Asteroids III. University of Arizona Press, Tucson, pp. 653–667.

U.PORTO
FACULDADE DE CIÊNCIAS
UNIVERSIDADE DO PORTO

# F.2. Abstract of the Oral communication in the Física 2012 Conference (6-8 September 2012)

## MINERALOGY OF V-TYPE NEAR EARTH OBJECTS

**S. Batista**[1,3], **T. Seixas**[1,3], **M. Silva**[1,3] **e E. Alves**[2,3]

[1] Departamento de Física e Astronomia da Faculdade de Ciências da Universidade do Porto, Rua do Campo Alegre, 687, 4169-007 Porto
[2] Departamento de Ciências da Terra da Faculdade de Ciências e Tecnologia da Universidade de Coimbra, Largo Marquês de Pombal, 3000-272 Coimbra
[3] Centro de Geofísica da Universidade de Coimbra, Av. Dr. Dias da Silva, 3000-134 Coimbra
tmseixas@fc.up.pt

### ABSTRACT

In this work, we present part of our study on the possible genetic linkage between HED meteorites and V-type asteroids through the analysis of asteroid NIR reflectance spectra taken from the publically available MIT-UH-IRTF Joint Campaign for NEO Reconaissance and correlated spectra of HED meteorites and intimate mineral mixtures from the RELAB database. Five V-type asteroids were considered: 4 Vesta, 3908 Nyx, 4055 Magellan, 5379 Abehiroshi and 6611 (1993 VW). We report on the spectral analysis performed through the Hapke radiative transfer model and the resulting estimation of asteroids surface composition, mineralogy and grain size.

U.PORTO
FACULDADE DE CIÊNCIAS
UNIVERSIDADE DO PORTO

## F.3. Extracurricular Internship PEEC (3rd edition)

## Programa PEEC-Programa de Estágios da FCUP (2010-11)

**Plano de Estágio (resumo)**

**Estagiário:** Sérgio Batista

**Tutor científico**: Teresa M. Seixas (DFA – FCUP)

**Duração**: 6 meses

**Laboratorial characterization of meteorites**

In this work we intend to study several meteorites of different types for investigating meteorite formation processes and the associated thermophysical history. The experimental work is to be performed at facilities of the universities of Porto (UP) and Aveiro (UA) according to the following sequence of activities:

**a) Meteorite samples preparation**

Thin sections of the meteorites will be prepared for optical mineralogy studies, electron microprobe analysis (UA). The thin sections will be taken from a layer below the exposed fusion crusts. For X-ray diffractometry, powder samples are to be prepared by milling slices of the original meteorites.

**b) Meteorite samples characterization**

Thin sections previously prepared will be analysed by optical mineralogy using a petrographic microscope (UA, UP). This will allow the identification of the component minerals and their microtexture. Electron microprobe analysis (UP, UA) of the same samples will help to complement this information by providing chemical composition profiles along selected paths such as grain boundaries, shearing planes and chondrules internal structures.

X-ray diffractometry (UA) on powder samples will be performed in order to determine the crystal structure of the constituent phases and to discriminate eventual polymorphic phases.